Università degli Studi di Palermo

AREA RICERCA E TRASFERIMENTO TECNOLOGICO
SETTORE DOTTORATI E CONTRATTI PER LA RICERCA
U. O. DOTTORATI DI RICERCA

Ph.D in ENERGY
Dipartimento di Ingegneria
ING-IND/32

Innovative Control and Energy Management of DC Microgrids with Hybrid Storage: Enabling E-Mobility and Hydrogen Energy Solutions

IL DOTTORE
AQEEL UR RAHMAN

IL COORDINATORE
ELEONORA RIVA SANSEVERINO

IL TUTOR
ANTONINO OSCAR DI TOMMASO

CO TUTORS
FABIO MASSARO

JOSEP MARIA GUERRERO

CICLO XXXVII
2024

Candidate declaration

I hereby declare that this thesis is submitted to obtain the academic degree of Doctor of Philosophy (Ph.D.) in Energy is my unaided work, which I have not used other than the sources indicated, and all direct and indirect sources are acknowledged as references. Parts of this dissertation have been published in international journals and/or conference articles (see list of the author publications).

Aqeel Ur Rahman
Palermo, 2/12/2024

Preface

The Ph.D. activity was conducted at the University of Palermo (Italy) Department of Engineering from November 2021 to November 2024.

The theoretical development, simulation analysis, implementation and C-HIL experimental tests have been performed in Sustainable Development and Energy Saving Laboratory (SDESLAB) of the University of Palermo.

Part of the activity was developed during the visiting industrial period in Prysmian Electronic (EOSS), Palermo.

Acknowledgement

I would like to express my heartfelt gratitude to all those who have supported and guided me throughout this thesis journey.

First and foremost, I extend my deepest thanks to Prof. Rosario Miceli, the group head, for his visionary leadership and encouragement. My sincere thanks go to my supervisor, Prof. Antonino Oscar Di Tommaso, whose invaluable guidance, expertise, and constructive feedback have been pivotal to the success of this research. I am also immensely grateful to my co-supervisors, Prof. Fabio Massaro and Prof. Josep Maria Guerrero for their insightful suggestions and constant support.

I am indebted to my colleagues and peers, especially Nicola Campagna and Filippo Pellitteri, for their collaborative spirit, thought-provoking discussions, and unwavering camaraderie. I thank my lab friend, Gerlando Frequente, for his valuable contribution, although he contributed nothing and just teased me every time, even then his useless contribution means a lot to me and also to the SDES Lab team for creating an inspiring and supportive research environment. On a personal note, I owe everything to my family, whose unconditional love and encouragement have been the cornerstone of my achievements. My parents, my wife Naila and my son Musab have been my greatest sources of strength and motivation. I am also grateful to my brothers, Anees and Asad, and my sister, Hadia, for their constant love and support.

A special mention goes to my best friend, Maria Rasool, whose unwavering belief in my abilities, continuous encouragement, and uplifting presence have been a source of immense strength throughout this journey. Maria's kindness, wisdom, and insightful advice have helped me overcome challenges and focus on my goals.

I am also grateful to my dear friends Hassan Bilal, Qais Khan, Muhammad Ahmed, Usman Nawaz, Bilal Shareef, Muhammad Noman, Laiba Khan, and Namra Minhas, who have added color and joy to my life, providing friendship, laughter, and countless cherished memories. Finally, I dedicate this work to all those who believe in innovation and sustainable progress, as their inspiration drives my passion for research and knowledge.

List of Publication

Journal Articles

- Rahman, Aqeel Ur, Nicola Campagna, Filippo Pellitteri, Antonino Oscar Di Tommaso, and Rosario Miceli. "Stability-Centric Design of a Droop-Mounted Adaptive Nonlinear Control for EV Charging in DC Microgrid." IEEE Access (2024).
- Rahman, Aqeel Ur, Nicola Campagna, Filippo Pellitteri, Antonino Oscar Di Tommaso, and Rosario Miceli. " Cascaded Lyapunov Based Hybrid Control of Multi-phase Interleaving Converters for Power-to-Hydrogen in DC Microgrid". (Under Review).

Conference Articles

- Sorrentino, Giuseppe, Giuseppe Schettino, Claudio Nevoloso, Stanimir Valtchev, Gioacchino Scaglione, Aqeel Ur Rahman, and Rosario Miceli. "Comparison between LCL Filter Design Methods For Grid-Connected Cascaded H-Bridge Multilevel Inverters." In 2024 13th International Conference on Renewable Energy Research and Applications (ICRERA), pp. 1411-1416. IEEE, 2024.
- Rahman, Aqeel Ur, Filippo Pellitteri, Nicola Campagna, A. O. Di Tommaso, and Rosario Miceli. "Decoupled Robust Backstepping Control of Multiphase Interleaving Converters for Power-to-Hydrogen Systems in DC Microgrids." In 2024 IEEE 15th International Symposium on Power Electronics for Distributed Generation Systems (PEDG), pp. 1-6. IEEE, 2024.
- Rahman, Aqeel Ur, Filippo Pellitteri, Nicola Campagna, A. O. Di Tommaso, and Rosario Miceli. "Decoupled Robust Backstepping Control of Multiphase Interleaving Converters for Power-to-Hydrogen Systems in DC Microgrids." In 2024 IEEE 15th International Symposium on Power Electronics for Distributed Generation Systems (PEDG), pp. 1-6. IEEE, 2024.
- Rahman, A. Ur, N. Campagna, A. O. Di Tommaso, R. Miceli, A. Damiano, and A. Floris. "Advanced Control Analysis of Single Inductor Four Switch

Non-Inverting Buck-Boost Converter for Energy Storage Units." In 2023 International Conference on Clean Electrical Power (ICCEP), pp. 267-272. IEEE, 2023.

- A. R. Petrov, E. Ivanovna Gracheva, T. Sinyukova, S. Valtchev, R. Miceli and A. U. Rahman, "Simulation of the Functional Characteristics of Low-Voltage Switching Devices, Based on the Example of Automatic Circuit Breakers," 2023 International Conference on Clean Electrical Power (ICCEP), Terrasini, Italy, 2023, pp. 690-695, doi: 10.1109/ICCEP57914.2023.10247405.

- Rahman, Aqeel Ur, Nicola Campagna, Vincenzo Castiglia, Antonino Oscar Di Tommaso, Fabio Massaro, Rosario Miceli, and Fabio Viola. "Master-slave control of battery/supercapacitor-based hybrid energy storage system for e-vehicle application." In 2022 11th International Conference on Renewable Energy Research and Application (ICRERA), pp. 158-163. IEEE, 2022.

- Zehra, Syeda Shafia, Aqeel Ur Rahman, Francesco Grimaccia, Alessandro Niccolai, and Marco Mussetta. "Neuro-fuzzy based energy management of PV-FC based grid-connected microgrid for e-mobility." In 2022 IEEE International Conference on Environment and Electrical Engineering and 2022 IEEE Industrial and Commercial Power Systems Europe (EEEIC/I&CPS Europe), pp. 1-6. IEEE, 2022.

Contents

List of Figures

List of Tables

Introduction

The dissertation concerns innovative control algorithms for DC microgrids (MGs) used to power different loads and sources, such as constant power loads (CPL), electric vehicle (EV) charging, and electrolyzers for hydrogen production for e-mobility. Moreover, the integration of hybrid energy storage systems (HESSs) within DC MGs and EVs using advanced power converters has been studied.

This work is developed within the program "PON-FSE Dottorati Innovativi a caratterizzazione industriale AA 2017/2018" and the project "Advanced Control and Energy Management of Green Microgrid Integrating Hybrid Energy Storage System for E-Mobility".

Global energy policies aimed to reduce CO_2 emissions and find alternatives in terms of green energy generation. Currently, renewable energy sources (RESs) seem to be a potential replacement to solve the global emission problems. RESs can be installed locally to support the energy communities while acting as distributed generators (DG). E-mobility sector has a significant contribution to CO_2 emission. As an alternative, the concept of electric vehicles is very promising and can minimize this contribution; however, it is very important to determine if the power source for EV charging is green and has no bad impact on EV penetration. Moreover, the integration and effects of EVs on the traditional power system are also an important concern to notice.

Motivation

These facts lead researchers and engineers to the concept of MGs for local communities and the e-mobility sector. The thesis focuses mainly on DC MGs because of their adaptability to charging electric vehicles, fewer losses, and easy integration of RESs. DC MGs can operate in standalone and grid-connected modes depending on the configuration. However, because of the stochastic nature of the RESs the use and integration of HESSs are important aspects. The general structure of MGs has RES as the main power generation source, HESS for auxiliary services, power converting units (PCU) for energy conversion, and different loads. Due to the involvement of the different components, MGs require proper energy management and control to ensure smooth and stable operation.

Problem Statement

Based on the literature review and comparative analysis, there is a significant gap in the stability and control methodologies applied to DC MGs intended to support the integration of EV into the electronic mobility sector. Most current studies rely on linear control theories that do not effectively address the nonlinear, multi-agent characteristics of DC MGs, limiting their large-signal stability. This research aims to address these gaps by developing an advanced EMS and control strategy that specifically incorporates EV integration, enhancing the stability and adaptability of DC MGs for e-mobility applications.

Thesis Layout

The present work is mainly divided into two major parts as shown in fig. 1. The first part deals with the basic overview of MGs, advanced power converter topologies for ESSs integration with MGs, and three case studies of DC MGs aiming to power the e-mobility sector. Similarly, in the second part, HESS applications for EV electrification are presented using advanced control algorithms and market analysis of EV fast-charging products.

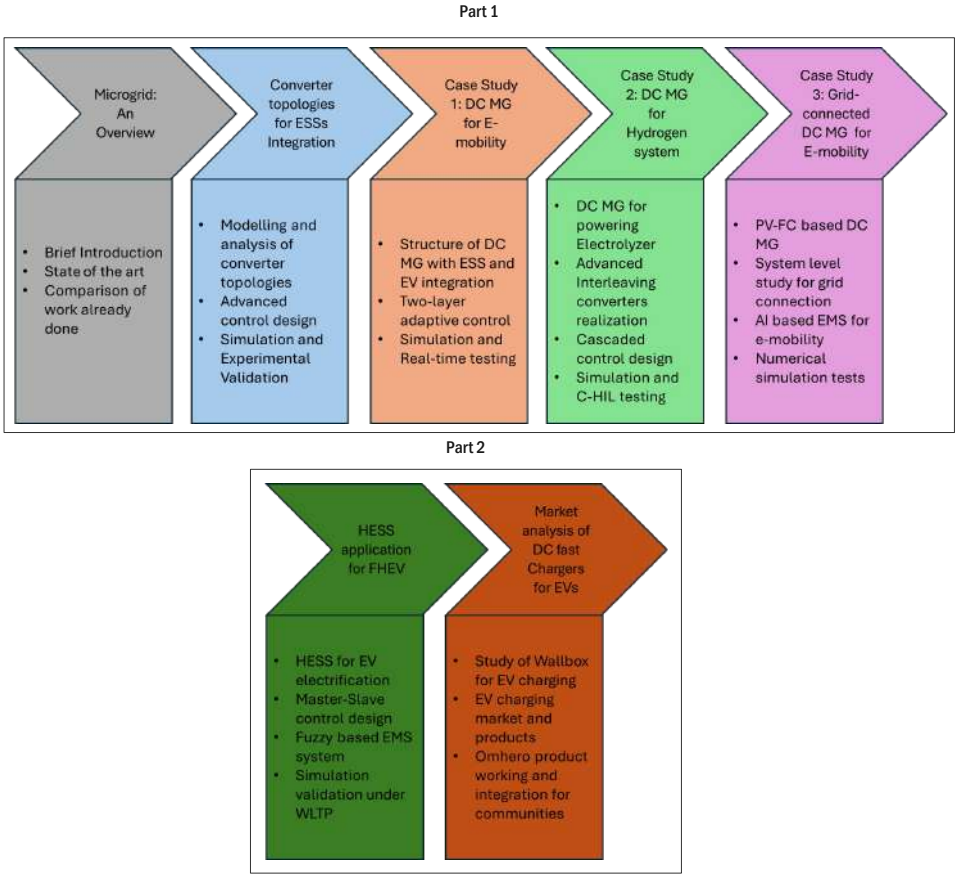

Figure 1: Division and layout of the dissertation

Fig. 2 shows the graphical abstract of the thesis chapter-wise. The present work is structured into chapters organized as follows.

Chapter One presents a general overview of the DC MG structure and the current state of the art regarding the focus of the thesis (energy management system and controls). The chapter summarizes the general perspective and existing work in the field of EMS and control of DC MGs.

Chapter Two presents advanced control strategies for four-switch single-inductor buck-boost converters (FSIBB) and FSIBB DC-DC interleaving converters advised for energy storage systems for e-mobility and MGs. A dual loop non-linear control design is proposed to enhance voltage regulation, current control, and stability. Real-time performance is validated through simulation (Simulink, PLECS) and controller hardware-in-loop (C-HIL) testing, demonstrating the effectiveness of these converters and controllers in practical applications.

In **Chapter Three**, a two-layer control system designed for efficient power sharing and stability in DC microgrids for EV charging, incorporating energy storage systems and bidirectional converters. The upper layer employs an improved droop control for load distribution, while a non-linear barrier-based sliding mode control provides robust voltage and current tracking for converters. Real-time validation through hardware-in-loop (HIL) testing and MATLAB simulations confirm the effectiveness of the system in various load scenarios.

In **Chapter Four** an advanced control strategy for a DC microgrid based on photovoltaic batteries is designed to power an electrolyzer-based hydrogen production system. Employing a three-phase interleaved topology and a cascaded hybrid non-linear controller, the chapter addresses efficient power sharing, maximum power extraction from PV, and robust voltage regulation. Stability and performance are confirmed through MATLAB simulations and real-time experimental testing, ensuring reliable power delivery for hydrogen generation.

Chapter Five presents a neurofuzzy energy management system designed to integrate renewable sources (PV and fuel cells) with battery supercapacitor storage in microgrids to charge electric vehicles. The system ensures a balanced bidirectional power flow with the grid, adapting dynamically to variable load demands and generation levels. Through simulation testing, the approach demonstrates effective energy distribution, optimizing grid interaction by drawing or supplying power as needed to maintain stability in the microgrid.

Chapter Six, deals with managing and controlling a hybrid energy storage system (HESS) using a master-slave control strategy. A fuzzy rule-based algorithm optimizes power sharing, with the master control guiding a synergetic terminal slave controller for precise tracking. Stability is validated through Lyapunov analysis, and the proposed method is rigorously tested in MATLAB/Simulink under the Worldwide Harmonized Light Vehicle Test Procedure (WLTP), ensuring its effectiveness in real-world scenarios.

In **Chapter Seven** work carried out during the industrial period is summarized. The technical aspects and workings of the different products, such as "OMHERO" and "PRY-CAM," are explained. A detailed study of electric vehicle charging systems and a benchmark market analysis of electric vehicle chargers are discussed, which can be used for further product development. Finally, real-time data of a domestic home load are considered to study the impact of EV wallbox and photovoltaics on energy communities.

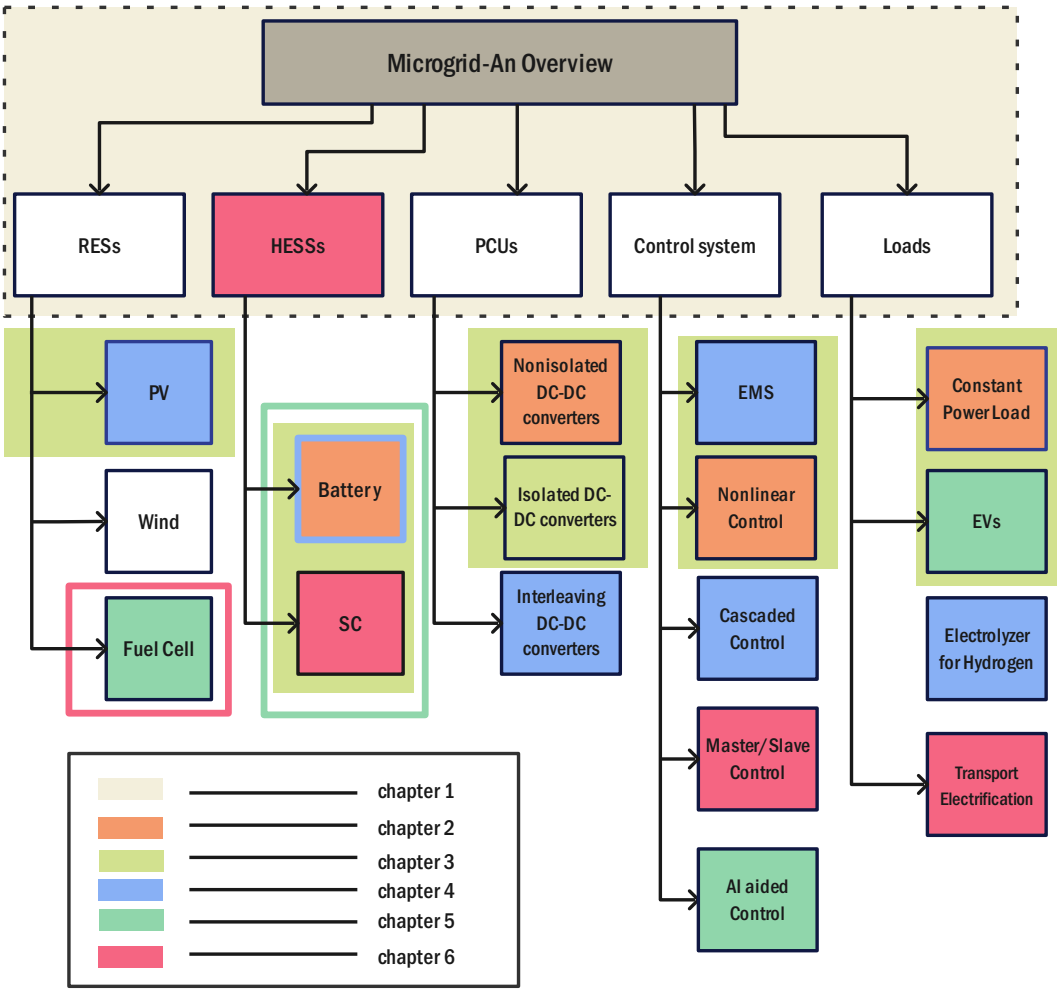

Figure 2: Graphical abstract of thesis

Part I

Innovative Control of DC Microgrids

Chapter 1

Microgrids: An OverView

1.1 Introduction

Energy and Power Engineering have evolved into critical research fields due to the urgent need to address global challenges related to emission-free energy generation, energy efficiency, and the integration of renewable energy sources (RES) [1]. As the world transitions towards cleaner energy, key issues such as climate change, rising fuel costs, and the depletion of traditional energy resources have driven an increasing focus on innovative energy systems. This has led to widespread research to develop smart electrical networks in the future that can provide reliable and sustainable energy solutions [2]. The present research focuses mainly on maximizing clean energy from renewable energy sources such as solar, wind, fuel cell, and hydro-energy to minimize the harmful impact of fossil fuels [3]. They are abundant and can easily help reduce greenhouse gas emissions. However, their inherent variability presents an obstacle to the stability and reliability of the grid [4]. In response, modern energy systems utilize advanced energy storage solutions, including batteries and supercapacitors, that can absorb excess energy when production exceeds demand and provide it whenever power generation does not provide a steady and reliable flow of electricity [5]. Power conversion units (PCUs) also play a key role in the operation of these energy systems, due to their task to manage energy transfer between components of the system. The PCU controls and manages the power processing behind the PCU that directs the flow of energy from the RESs to the grid or storage units to deliver the energy needed to satisfy load requirements [6]. However, without proper control of energy transfer, the potential of renewables cannot be fully utilized. Hence, PCUs along with smart control algorithms allow for better energy management, improving the reliability and scalability of systems [7]. A microgrid is commonly defined as the combination of generated power on RES, Storage, and loads connected with smart controllers to transfer power optimally. Microgrids represent a localized approach to energy generation, providing localized energy systems that can operate independently or in a grid-connected mode. [8]. Microgrids increase

electrical network flexibility, robustness, and efficiency by blending multiple energy sources into one and providing relatively high-level control of how they are used. Microgrids can provide a stable and constant energy supply, particularly important in remote places or places where there is unstable grid infrastructure [9].

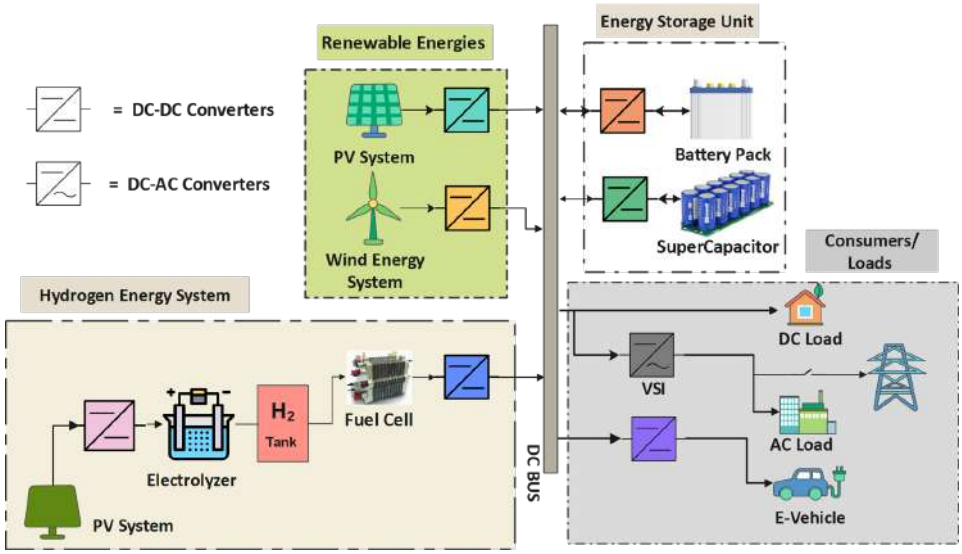

Figure 1.1: Generic structure of microgrid

Fig. 1.1 presents an overall general structure of the microgrid cluster, showing different types of loads, power sources, storage systems, and control systems. Beyond the integration of RES, PCUs are another critical technology underpinning modern power networks' success. These devices convert energy from one form to another, such as converting DC power from solar panels to AC power for household use. The design and optimization of these converters are essential for achieving high efficiency in energy systems [10]. Advanced power electronics play a key role in ensuring minimal energy loss during conversion and maintaining system stability during energy demand or generation fluctuations. Power converters and advanced control strategies are fundamental in making RES more viable for large-scale adoption by improving energy quality and system responsiveness [11]. As the energy landscape continues to evolve, focusing on enhancing system efficiency through optimized power electronics design and applying advanced controller architectures remains at the forefront of research [12]. These advancements not only improve the operational efficiency of power systems but also contribute to reducing the overall cost of clean energy solutions. By integrating innovations in power electronics, smart controllers, and RES, the next generation of energy systems is poised to impact achieving global energy sustainability goals significantly [13].

1.2 Microgrids Structure

The concept of MG is a trendy topic in Electrical and Energy engineering as it implements the idea of distributed power generation. The concept of distributed power generation has many advantages over traditional power systems, such as remote power generation, fewer transmission losses, low maintenance costs, integration of RES, and controlled energy generation [14]. Fig. 1.1 shows the general overview of the MG system containing different RESs, loads, and control structures. The idea behind modern MGs is to build systems for remote locations that can power specific sectors, regardless of the broader energy situation. Extensive work has been done in the literature on the structure and configuration of MGs [15]–[17]. MGs can be divided into two main subdomains based on the working principle, i.e., island mode and grid-connected mode.

1.2.1 Connection-based Classification

Islanded Mode

MGs can operate independently, without reliance on traditional power systems. This mode of operation is known as islanded mode [18]. In this case, the main power generation comes from RESs, and auxiliary services are provided by hybrid energy storage systems (HESS). The main advantages of this configuration are that it is easily controllable, less complicated, and suitable for remote installation. However, due to the stochastic nature of PV systems, large-scale installations may require accurate forecasting to manage energy fluctuations effectively [19]. Additionally, energy storage systems such as batteries and supercapacitors can help maintain a stable power supply during periods of low energy generation [20].

Grid-Connected Mode

In this configuration, MGs operate while connected to the main grid. This setup is common and has gained attention due to its hybrid solution. The interaction between the main grid and MG requires additional infrastructure and a control system for proper synchronization [21]. The advantage of this configuration is that excess power generated by the MG can be transferred to the main grid, improving tariffs and economic benefits. Moreover, using advanced control algorithms, MGs can contribute to grid stability by supporting frequency regulation, voltage control, and peak demand management [22]. Fig. 1.2 presents the configuration (a) and (b) for islanded MG and grid-connected MG respectively. The schematics show the detailed structure of the MG containing different RESs, loads, and converter topologies.

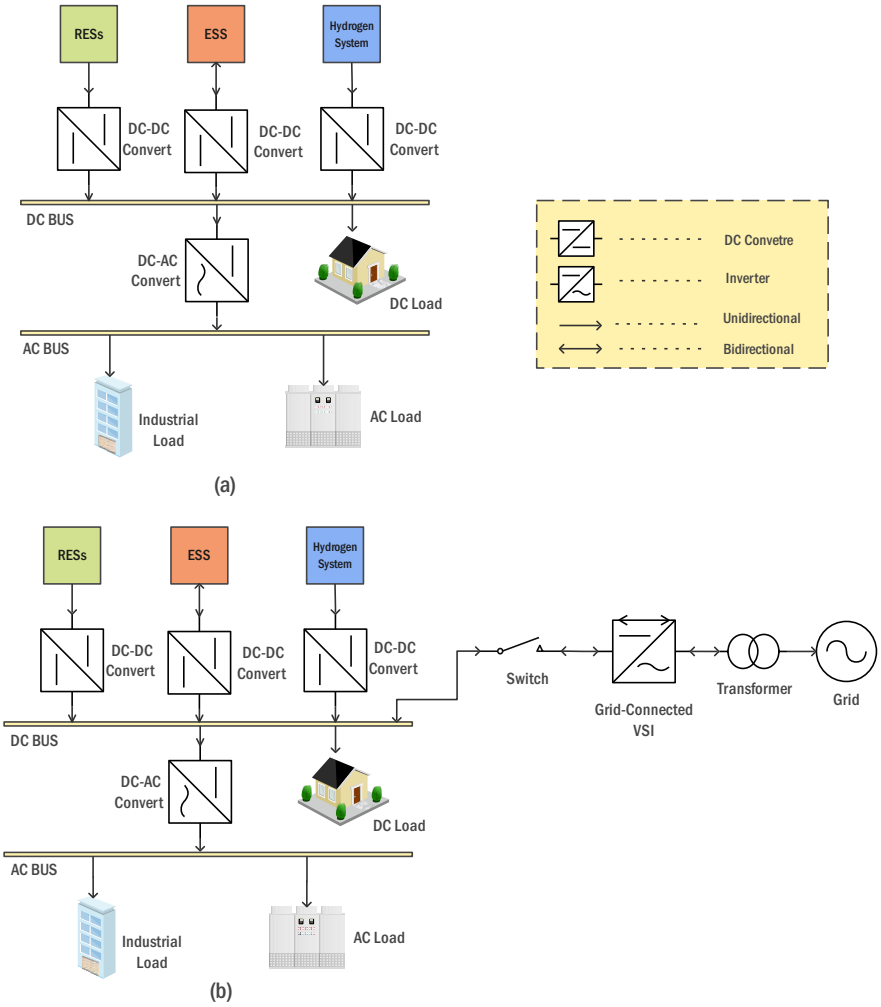

Figure 1.2: (a)Islanded Mode MG (b) Grid-connected MG

1.2.2 Topology-based Classification

DC Microgrid

DC Microgrids (DC MGs) are crucial in modern power distribution, integrating DC power sources, DC-DC converters, and a DC bus. They efficiently support both DC and AC loads, with AC loads requiring an inverter. A significant advantage of DC MGs is their higher operational efficiency, as they reduce energy losses by eliminating multiple power conversion stages common in AC systems. Additionally, they feature simplified infrastructure, facilitating easier installation and improved stability by avoiding reactive power and harmonic distortion issues [23]. DC MGs are well aligned with RESs like photovoltaic systems and fuel cells, which inherently produce DC power, reducing conversion losses, and enhancing decentralized energy generation. Their low harmonic content, low maintenance, and high reliability make them ideal for energy-efficient residential and industrial applications [24], [25]. Fig. 1.3 illustrates the general structure of a DC microgrid.

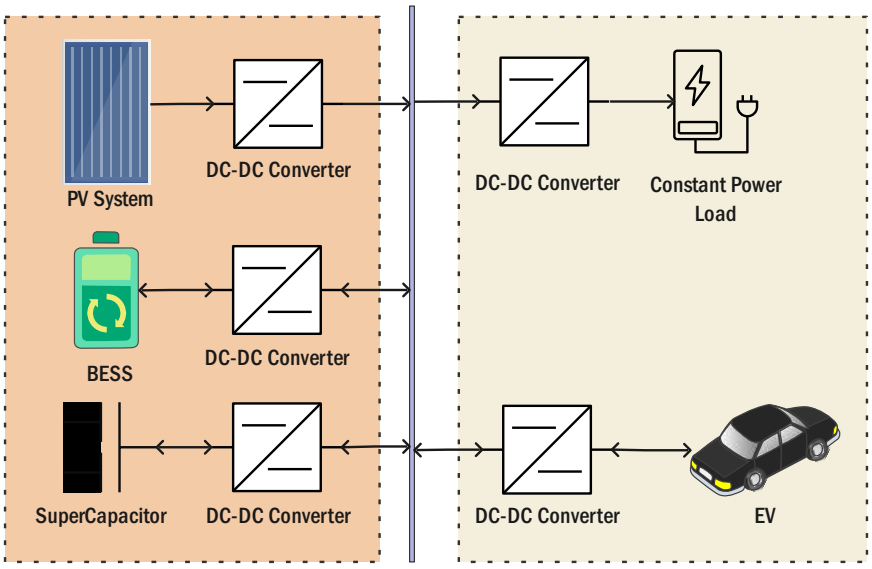

Figure 1.3: DC Microgrid Structure

AC Microgrids

AC Microgrids (AC MGs) utilize an AC bus, making them well-suited for integration with conventional power systems. In these setups, DC sources such as PV panels or batteries are linked through DC-AC inverters, ensuring compatibility with traditional AC loads, including motors, turbines, and common appliances. This configuration is especially beneficial for high-power applications, such as industrial operations or grid-level energy management, where AC systems are commonly used [26]. One major advantage of AC MGs is their seamless integration with existing AC-based grid infrastructure, facilitating straightforward interconnection with utility grids and providing a standardized approach to incorporating distributed energy resources (DER). Furthermore, AC microgrids offer flexibility in design, as they can operate at various frequencies that are tailored to specific needs [27]. However, they are more complex than DC MGs, requiring advanced control systems to handle challenges such as frequency regulation, reactive power compensation, and synchronization with external grids. This added complexity increases infrastructure and maintenance costs. Power quality issues, such as harmonics and voltage fluctuations, require sophisticated filtering and compensation solutions [28], [29]. Fig. 1.4 illustrates the general structure of an AC microgrid.

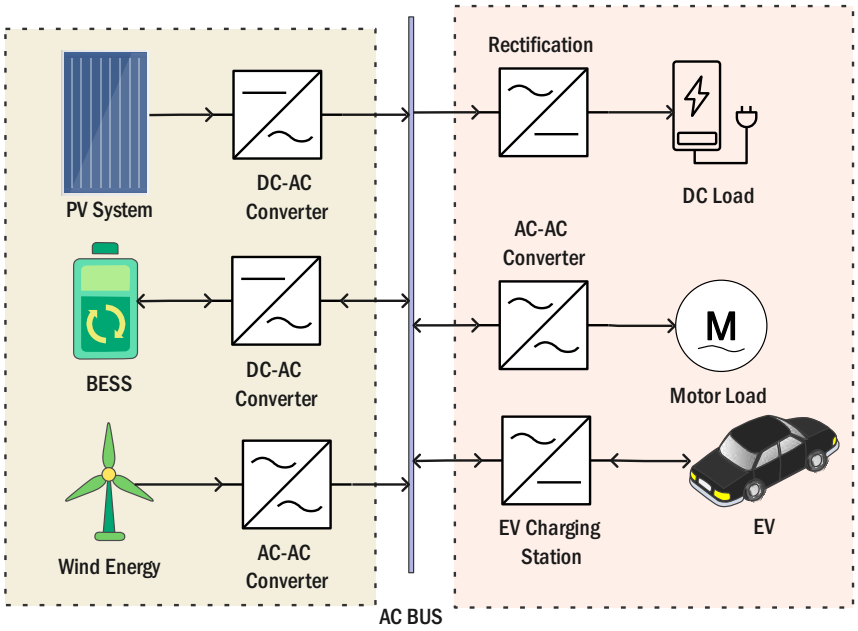

Figure 1.4: AC Microgrid Structure

DC/AC Hybrid Microgrids

The DC/AC Hybrid Microgrid is a versatile configuration that combines both DC and AC systems within a unified architecture. In this topology, both DC and AC buses coexist, interconnected through bidirectional inverters that allow for power exchange between the two types of networks. This hybrid arrangement offers the best of both worlds: it leverages the efficiency and simplicity of DC systems for specific applications (e.g., integrating DC-based renewable energy sources) while maintaining the flexibility and compatibility of AC systems for loads that require alternating current [30]. Hybrid microgrids are gaining popularity for integrating renewable RESs, storage devices, and conventional generators, combining the advantages of AC and DC systems. For example, solar panels can supply power directly to the DC bus, reducing energy losses, while the AC bus efficiently serves traditional loads [31]. However, hybrid microgrids face challenges in energy management and control. Coordinating AC and DC subsystems requires advanced energy management systems (EMS) for real-time optimization [32]. The complexity and cost increase due to multiple converters and large power electronic components, and stability issues during AC-DC transitions must be managed to prevent inefficiencies. Despite these obstacles, hybrid microgrids offer a flexible and adaptable solution to future energy needs [33]. Fig. 1.5 shows the general structure of a DC/AC microgrid.

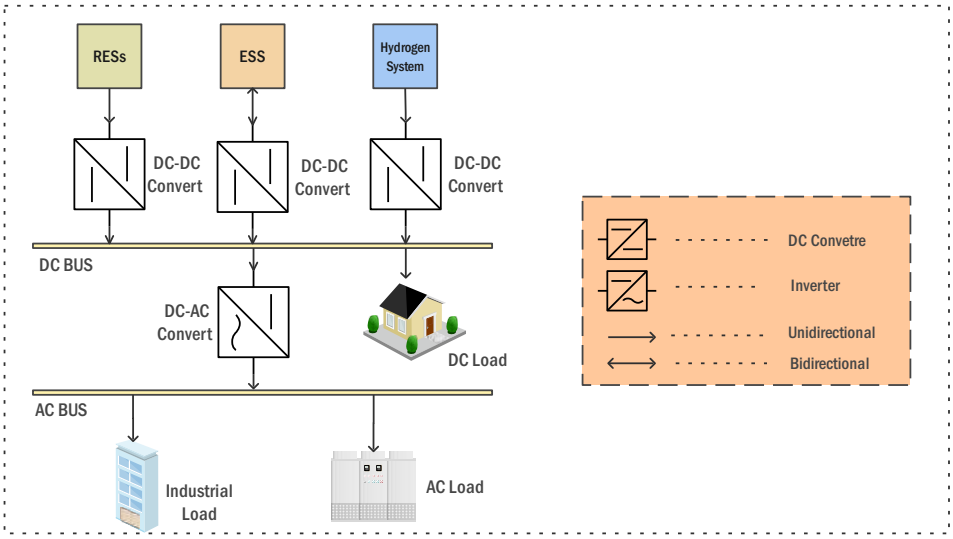

Figure 1.5: DC/AC Hybrid Microgrid Structure

1.2.3 Role of RESs in Microgrids

The integration of RESs is now a central element of modern power systems, driven by the urgent need to reduce CO_2 emissions and combat climate change. This transition from fossil fuels to green energy sources is critical to promote sustainable practices and protect the environment [34]. RESs include diverse technologies such as solar photovoltaics, wind energy, hydrogen systems, and hydropower, each suited to specific geographic and climatic conditions. Solar systems excel in sun-rich areas, wind systems in regions with steady winds, hydrogen systems offer energy storage solutions, and hydropower remains reliable in water-abundant locations [35]. Modern microgrids leverage renewable energy sources as primary energy sources, minimizing the dependence on fossil fuels and promoting emission-free power generation. This integration supports a sustainable, decentralized energy infrastructure that meets current demands while paving the way for a resilient and greener future [36], [37].

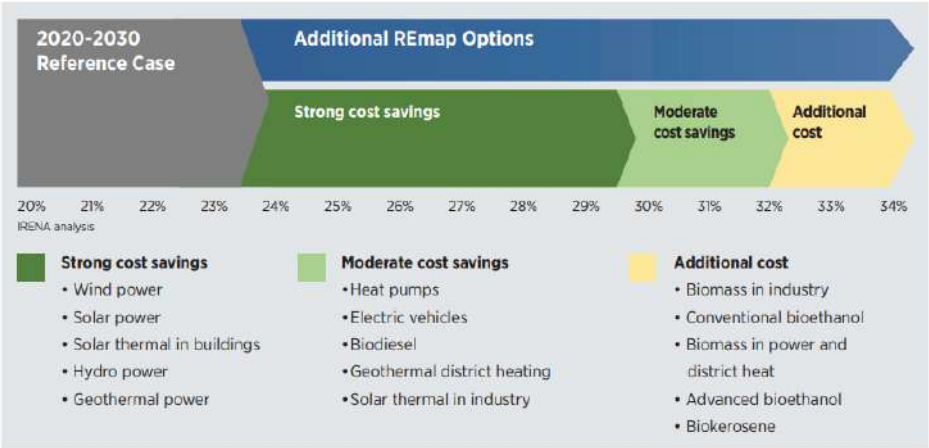

Figure 1.6: Cost analysis of RES by IRENA for EU

According to the IRENA report [38] and the perspective on renewable energy of the EU Commission, the reference goal for 2020-2030 is to have green energy for the EU by incorporating a share 24 % of RESs. The additional potential to push it to 34 % of the REmap in fig. 1.6 shows three options divided into three categories, strong cost-saving options, moderate cost-saving options, and additional costs. This map gives insight into the importance of RES in achieving 34 % clean energy for Europe. However, the installation cost is also an important parameter to consider. Fig. 1.7, shows the installation cost, the capacity factor, and the levelised cost of electricity. It can be seen that from 2010 to 2023, the installation cost of RESs, especially solar PV systems, decreased significantly. This motivates the transition of traditional power systems towards modern RES-based power systems for clean energy generation.

	Total installed costs (2023 USD/kW)			Capacity factor (%)			Levelised cost of electricity (2023 USD/kWh)		
	2010	2023	Percent change	2010	2023	Percent change	2010	2023	Percent change
Bioenergy	3 010	2 730	-9%	72	72	0%	0.084	0.072	-14%
Geothermal	3 011	4 589	52%	87	82	-6%	0.054	0.071	31%
Hydropower	1 459	2 806	92%	44	53	20%	0.043	0.057	33%
Solar PV	5 310	758	-86%	14	16	14%	0.460	0.044	-90%
CSP	10 453	6 589	-37%	30	55	83%	0.393	0.117	-70%
Onshore wind	2 272	1 160	-49%	27	36	33%	0.111	0.033	-70%
Offshore wind	5 409	2 800	-48%	38	41	8%	0.203	0.075	-63%

Notes: CSP = concentrated solar power; kW = kilowatt.

Figure 1.7: Installation cost of different power sources: A trend [38]

Solar PV System

Solar technology is an important part of the RESs family, due to its low cost, easy installation, and the possibility of unlimited clean energy generation. This makes solar power highly accessible and sustainable, meeting the growing demand for renewable energy solutions without compromising environmental goals [39]. The basic principle of the solar energy system is to convert the energy from sunlight into electricity. In these systems, photovoltaic cells (PVs), typically made from semiconducting materials, absorb sunlight and release electrons, thereby generating an electric current that can be harnessed as electricity. This direct conversion of solar energy into electrical power positions PV systems as efficient, modular, and highly adaptable sources of energy [40]. However, energy production also depends on weather parameters such as temperature and irradiance. Solar irradiance, the measure of sunlight intensity received on a surface, has a direct influence on the energy output of a PV system.

However, while high levels of irradiance increase power generation, excessive heat, often occurring alongside strong sunlight, can lead to efficiency losses due to increased electrical resistance within PV cells. Thus, temperature and sunlight must be carefully balanced to ensure optimal performance [41].

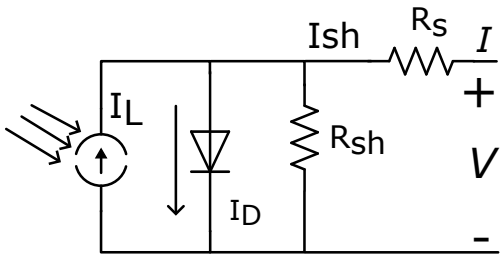

Figure 1.8: Equivalent electrical circuit of PV system

In addition, the efficiency and maintenance (cleaning) of some remote areas can be a potential problem. In isolated or difficult-to-reach locations, maintaining PV systems becomes challenging, as dirt, dust, or snow accumulating on the panels can hinder light absorption. Even a small layer of dust can significantly reduce energy conversion. Cleaning and maintenance solutions, such as self-cleaning coatings or automated mechanisms, have been explored to combat these challenges, but their practical implementation remains complex in remote regions [42]. A lot of research has been done to extract the maximum power and improve the efficiency of the PV system under different conditions. A key area of innovation has been maximum power point tracking (MPPT), which uses algorithms to dynamically adjust the load of the photovoltaic system to maintain peak efficiency despite variable conditions. MPPT controllers allow photovoltaic systems to optimize energy capture, particularly under changing irradiance or partial shading, ensuring that the energy output remains as high as possible [43], [44].

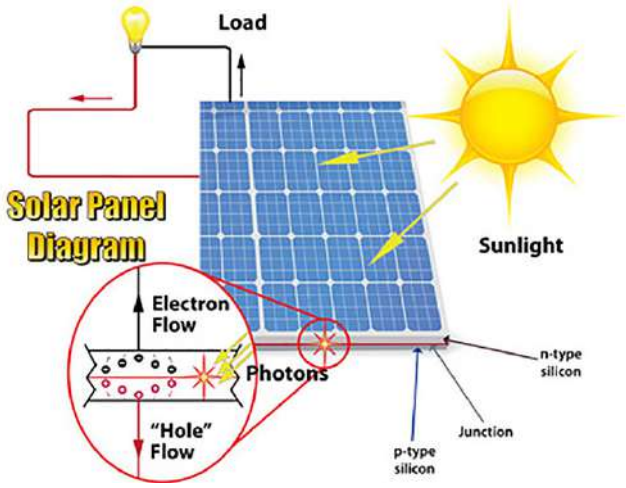

Figure 1.9: Overall working diagram of PV system

Figs. 1.8 and 1.9 show the equivalent circuit with internal resistance and the overall PV working system, respectively. Mathematical modeling of the system is a very interesting and important method for analyzing the system's behavior. Through mathematical models, researchers can simulate photovoltaic performance in a variety of environmental and operational scenarios, helping to predict efficiency outcomes and guide improvements in system design [43]. These models often include thermal factors to anticipate temperature-related efficiency losses, as well as irradiance models to assess the potential impacts of shading or weather changes. Such simulations provide insights that are critical to improving the reliability and adaptability of the photovoltaic system [45]. The PV current (I_{PV}) can derived through equation shown below:

$$I_{PV} = N_p I_{ph} - N_p I_o \left[e^{\frac{q(V_c + I_c \cdot R_s)}{N_s \cdot A \cdot K \cdot T}} - 1 \right], \tag{1.1}$$

where N_p represents the number of solar cells connected in a parallel arrangement, I_{ph} signifies the internal photon current, I_o denotes the saturation current, Q stands for the electron charge, V_c indicates the output voltage of the cell, I_c expresses the output current of the cell, N_s defines the number of cells connected in series, A symbolizes the ideality factor, K represents the Boltzmann constant, and T represents the temperature

Wind Energy System

Wind energy is a popular renewable energy source and is widely used in developed regions like America and Europe. It is environmentally friendly and can produce a large amount of electricity. Energy conversion is the main working principle of wind energy. The wind kinetic energy is converted to mechanical energy and then the mechanical energy is converted to electrical power. This conversion makes the system a bit less efficient than other renewable energy sources, but can still contribute a large amount [46]. Another drawback of the wind energy system is that it requires proper wind flow. So, an adequate climate analysis is necessary before installation. Moreover, the system requires a proper attitude to work [47]. The wind system can be used either alone or in grid-connected mode. The system is also used in microgrids for distributive generation in the absence of the primary grid. The figure shows the complete grid-connected wind system [48]. It can be seen that the generator is connected to generate electricity while power conversion units are embedded in the circuit for power flow between the design and the primary grid. The control units are used to control the entire system according to demand and requirements [49]. Fig. 1.10 shows the grid-connected wind energy system.

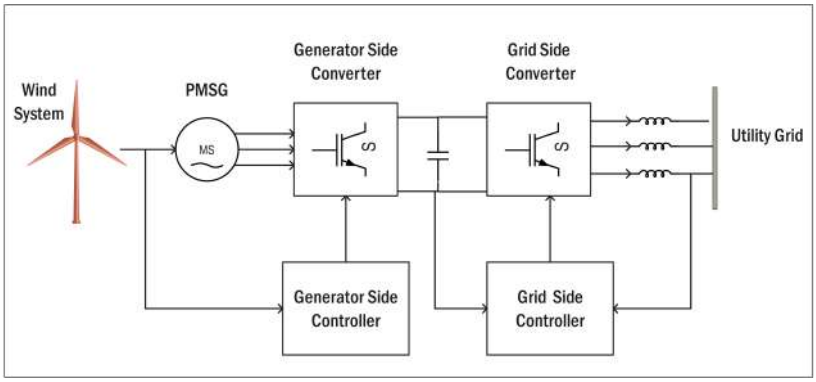

Figure 1.10: Grid connected wind energy system

Hydropower System

Hydropower is a form of energy that can be gained from running water and converted into electricity. This renewable source uses the kinetic energy of moving water to generate electricity without harmful emissions, making it environmentally friendly. Hydropower projects can be installed on the run of the river or a dam. Run-of-the-river systems use natural water flow directly, while dam-based projects store water in a reservoir, allowing controlled release to maintain a steady energy supply even during low flow periods [50]. Fig. 1.11 presents the graphical schematic of a general hydroelectric plant that shows all the components. The main work can be explained as the potential energy of running water is converted into electric energy through water turbines. Water flows through turbines, causing them to spin and drive a generator, thus transforming the energy in water into electricity.

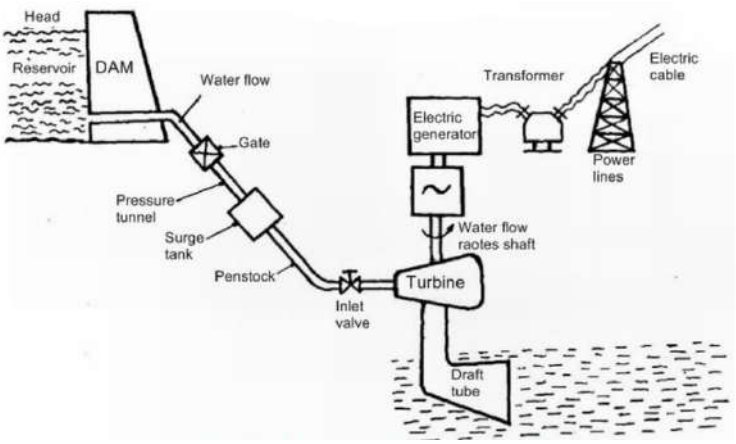

Figure 1.11: Graphical representation of hydropower plant

The installation requires a flowing river, dam, or reservoir. These features ensure a consistent flow and the necessary pressure to drive turbines effectively. This method is comparatively cost-effective. Despite initial setup costs, the long lifespan of hydropower and low operational expenses make it economically viable over time.

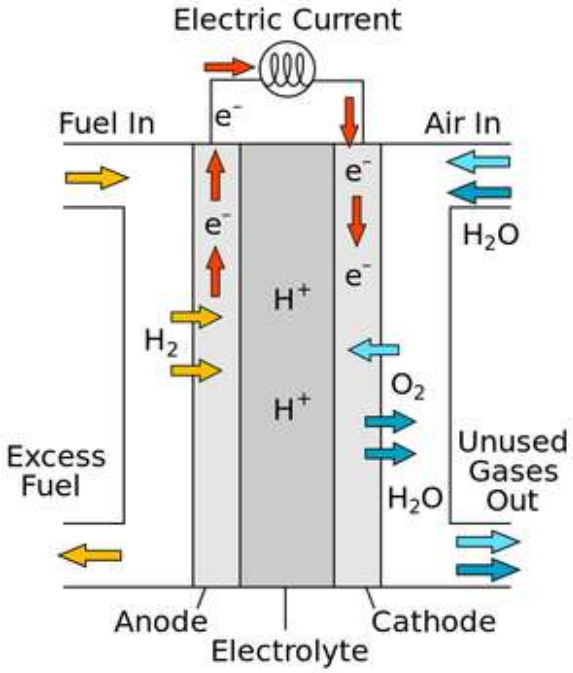

Figure 1.12: Schematic diagram of fuel cell

After the specific electricity generation process, the water can be used for irrigation with considerable benefits. This dual use approach benefits agriculture and local water needs, especially in rural areas [51].

Hydrogen-based Energy System

Hydrogen-based power systems are emerging as a potential source of clean energy generation. Hydrogen offers a versatile energy solution, as it can be used in stationary power systems and mobile applications, making it a valuable addition to the renewable energy landscape [52]. Fig. 1.12 illustrates the workflow diagram of a fuel cell, highlighting the inputs and outputs of the system. Fuel cell technology converts hydrogen into electricity, emitting only water vapor as a byproduct. During this process, hydrogen atoms split to release electrons, generating electricity in a completely emission-free manner, making hydrogen a sustainable energy source. This zero emission process is crucial for achieving net zero goals, as hydrogen fuel cells eliminate carbon emissions and support global efforts to combat climate change, aligned with clean energy policies [52]. Fuel Cell Hybrid Electric Vehicles (FHEVs) also utilize hydrogen for mobility. FHEVs achieve efficient energy use and extended driving ranges by integrating fuel cells with battery technology, offering a sustainable alternative to traditional and battery electric vehicles (BEVs) [53]. Unlike BEVs, FHEVs feature faster refueling times and greater range, addressing consumer concerns about charging and range limitations. Despite these benefits, research focuses on improving hydrogen production and storage. Developing efficient

Table 1.1: Comparative analysis of different RES

Renewable Energy Source	Advantages	Disadvantages	Cost
Solar Energy System	Abundant, Low-maintenance, Scalable, Versatile.	Weather-dependent, Space requirements, Energy storage needed.	Low
Wind Energy System	Space-efficient, Low operational costs, Job creation.	Noise pollution, Wildlife disruption, Huge infrastructure.	Medium
Hydropower system	Long life span, controller production, Reliable.	Limited site, High maintenance, Huge infrastructure.	High
Fuel Cell	Efficient, Cleaner Production, Scalable.	Low life span, Hydrogen storage issues, Huge infrastructure.	Medium

renewable production methods, such as electrolysis, and improving safe and scalable storage solutions are essential for the wider adoption of hydrogen [53].

1.2.4 Role of Energy Storage System

Energy storage technology significantly improves modern microgrids by providing essential auxiliary services. This technology enables the storage of various forms of energy, ensuring availability during peak demand or when RES output fluctuates. During high load or adverse weather conditions, storage devices support RES, stabilizing the energy supply [54]. These devices are classified into three main types: electrical, mechanical, and thermal. Electrical storage, like batteries, quickly balances short-term fluctuations; mechanical storage, including flywheels, offers sustained output for longer durations; and thermal storage retains energy as heat for use in heating or cooling. This categorization allows microgrids to efficiently manage energy, enhancing resilience and renewable integration. The tree chart of the different types of ESS is presented in fig. 1.13 below.

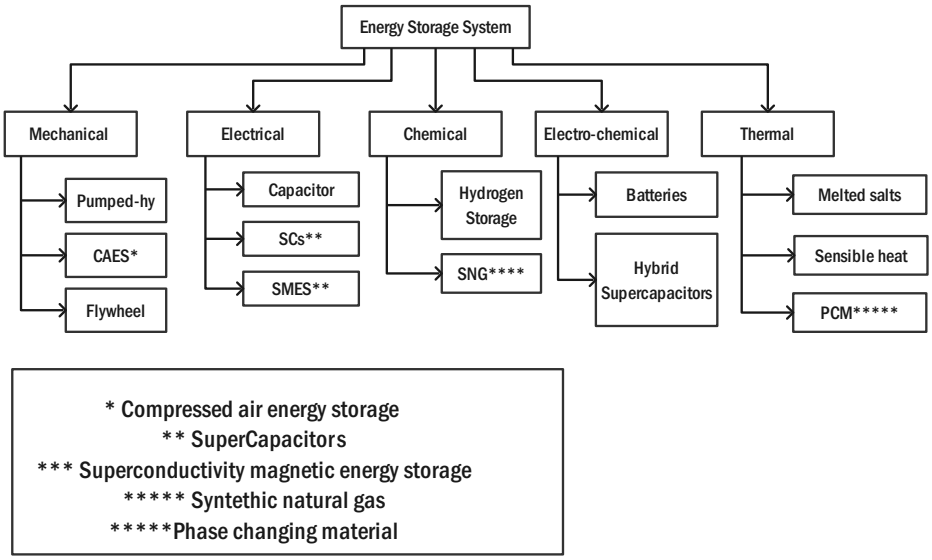

Figure 1.13: Types of energy storage devices

Battery

Batteries convert chemical energy into electrical energy in the form of a direct current. An the elementary battery cell is composed of:

- Positive electrode (cathode): typically an oxide or sulfide in which the reduction reaction takes place during discharge
- Negative electrode (anode): metal or alloy in which the oxidation reaction takes place during discharge.
- Electrolyte: Medium in which the electrodes are immersed, through which ionic conduction takes place. It can be liquid, solid, or gel.

The direct current is generated thanks to the chemical reaction that takes place between the electrodes and the electrolyte. In the case of rechargeable batteries, this chemical reaction is reversible, reversing the direction of the current circulating on the battery [55]. Considering energy management applications, it is not important to study what is happening at the chemical level, but rather what is happening at the macroscopic level. For this reason, the battery can be treated as a 'black box' with specific operating parameters. These parameters include specific energy, energy density, specific power, rated voltages, charging efficiency, energy efficiency, operating temperatures, number of charging cycles, etc [56]. The dynamic modeling of the battery can be represented by circuits and equations. The mathematical equations of the battery model can be represented by the equation:

$$E = E_o - K\frac{Q}{Q - it} + Ae^{(-B.it)} \tag{1.2}$$

$$V_{bat} = E - R.i \tag{1.3}$$

The battery State of charge (SoC) can be represented mathematically as follows.

$$SoC_B = SoC_{Bini} - \frac{1}{C_n} \int_0^t I_B \, dt \tag{1.4}$$

SuperCapacitor

Supercapacitors are advanced energy storage devices that bridge the gap between conventional capacitors and batteries by offering high power density and rapid charge-discharge cycles. Unlike batteries, which rely on chemical reactions for energy storage, supercapacitors store energy electrostatically through the separation of charges across an electrolyte. This mechanism allows supercapacitors to charge and discharge within seconds, making them ideal for applications requiring quick bursts of energy, such as regenerative braking in electric vehicles and power backup systems in microgrids [57]. Although they have a lower energy density compared to batteries, supercapacitors exhibit superior cycle life and durability, capable of sustaining millions of charge-discharge cycles without significant degradation. With these attributes, supercapacitors are increasingly utilized in hybrid energy storage systems, providing stable, immediate power while supporting battery longevity in integrated applications [58]. The equation below mathematically expresses the SoC calculation of the Supercapacitor.

$$SoC_{SC} = SoC_{SCini} - \frac{1}{C_n} \int_0^t I_{SC} \, dt \tag{1.5}$$

1.3 Power Electronics for DC Microgrids

Power electronics converters are considered the backbone of the modern power system, providing essential functionality that enables the seamless integration and control of various energy sources and loads. The key role of power conversion units (PCUs) is to convert energy and control the overall system [59]. This ensures that energy is transformed efficiently to meet the voltage, frequency, and stability requirements specific to each application. PCUs help maintain system balance through precise control mechanisms, particularly in complex power networks with diverse energy sources. Power electronics has a wide range of applications in RESs integration, EVs, and modern MGs, where they play a critical role in enhancing system flexibility, enabling renewable energy sources to synchronize with conventional grids, and supporting the dynamic energy demands of electric vehicles. Different power converters have different functionality based on structure and requirements; for example, DC-DC converters manage voltage levels for battery charging, while AC-DC converters are essential for renewable energy systems that must synchronize with

grid requirements [60]. Each converter type is designed to optimize efficiency and performance, addressing the specific operational demands of modern power systems. Some important and widely used converter topologies are discussed below.

1.3.1 DC-DC Power Converters

DC-DC power converters are widely used in DC power systems for energy conversion, enabling efficient voltage regulation and transformation across a variety of applications. The working principle of DC power converters depends on the specific topology, which defines how the circuit components—such as inductors, capacitors, and switches—are arranged and operated. However, in all cases, the input and output of the system remain DC, ensuring compatibility with DC power systems without the need for AC conversion [60]. Buck, Boost, and Buck-Boost are considered basic DC-DC converter topologies, each serving distinct functions: the Buck converter steps down the voltage, the Boost converter steps up the voltage, and the Buck-Boost converter can perform both functions depending on the load's requirements. These fundamental configurations are crucial for meeting various voltage needs within a system, allowing for tailored power management [61]. The wide range of applications for DC-DC converters includes power supplies in electronic devices, uninterruptible power supplies (UPS) for data centers, battery charging devices, and renewable energy sources, where consistent and efficient voltage management is critical. By converting energy precisely as required, these converters enhance system stability, efficiency, and responsiveness across diverse fields, from everyday electronics to large-scale energy systems [62]. Fig. 1.14 presents the basic DC-DC converter topologies.

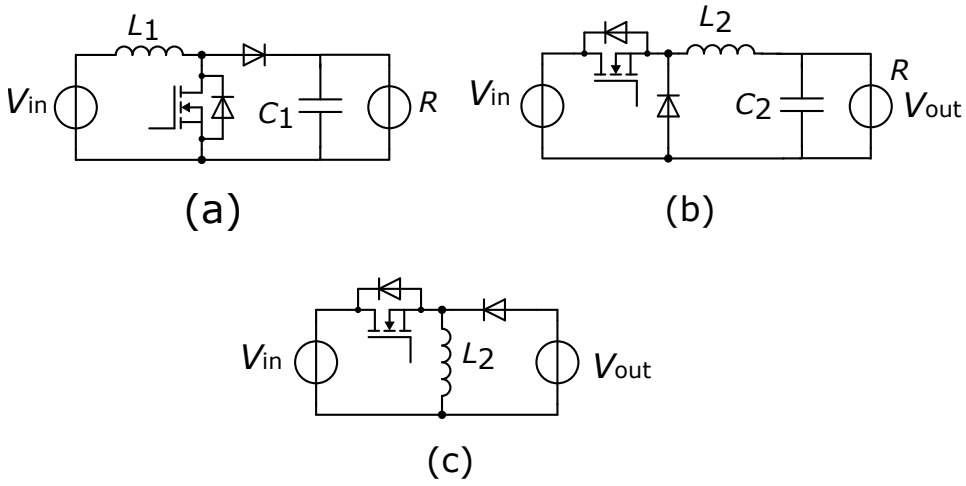

Figure 1.14: DC-DC converter topology (a) Boost converter (b) Buck converter (c) Buck-Boost converter

Boost Converter

The boost converter is used to step up the DC voltage level, and the circuit is composed of inductor L_1, an IGBT/MOSFT-based switch followed by a diode, and a filtering capacitor C_1. The voltage level can be controlled by controlling the duty cycle of the switch. The average state-space or transfer function models are used to analyze the system and derive the model-based control law [63]. The state-space averaged model of the boost is represented as:

$$\frac{d}{dt}\begin{bmatrix} x_1 \\ x_2 \end{bmatrix} = \begin{bmatrix} 0 & -\frac{u}{L_1} \\ \frac{u}{C_1} & -\frac{1}{RC_1} \end{bmatrix} \begin{bmatrix} x_1 \\ x_2 \end{bmatrix} + \begin{bmatrix} \frac{V_{\text{in}}}{L_1} \\ 0 \end{bmatrix} \tag{1.6}$$

where x_1, and x_2 represent the inductor current and output voltage respectively. u denotes the duty cycle for the IGBT switch.

Buck Converter

The buck converter is used to step down the voltage level efficiently, with minimal power loss. Its basic functionality resembles that of a step-down transformer in AC systems; however, unlike transformers, buck converters operate in DC circuits and achieve voltage reduction through high-frequency switching. Key applications of the buck converter include low-power applications such as mobile device chargers, solar battery chargers, and other power-sensitive electronic devices [64]. The mathematical model of the buck converter is shown below:

$$\frac{d}{dt}\begin{bmatrix} x_1 \\ x_2 \end{bmatrix} = \begin{bmatrix} 0 & -\frac{1}{L_2} \\ \frac{1}{C_2} & -\frac{1}{RC_2} \end{bmatrix} \begin{bmatrix} x_1 \\ x_2 \end{bmatrix} + \begin{bmatrix} \frac{u \cdot V_{\text{in}}}{L} \\ 0 \end{bmatrix} \tag{1.7}$$

where x_1, and x_2 represent the inductor current and output voltage respectively. u denotes the duty cycle for the IGBT switch.

Buck-Boost Converter

The buck-boost converter is a highly adaptable DC-DC converter that can either increase (boost) or decrease (buck) input voltage, depending on the needs of the system. This versatility is crucial in scenarios where a variable output voltage is necessary, making it a popular choice for applications requiring flexible and efficient power management [65]. Buck-boost converters come in two configurations: unidirectional and bidirectional. A unidirectional setup allows energy to flow in one direction, perfect for tasks like standalone battery charging. In contrast, a bidirectional configuration, which includes additional switching elements, enables energy to flow both ways. This makes it well-suited for energy storage systems (ESS) and regenerative braking in electric vehicles (EVs), where energy transfer needs to be more dynamic [66]. Common uses of buck-boost converters include battery charg-

ing, ESS, and EV charging stations. Their ability to handle fluctuating input and output voltages ensures reliable performance and efficient energy conversion, even under varying conditions [67].

$$\frac{d}{dt}\begin{bmatrix} x_1 \\ x_2 \end{bmatrix} = \begin{bmatrix} 0 & -\frac{1-u}{L_3} \\ \frac{1-u}{C_3} & -\frac{1}{RC} \end{bmatrix} \begin{bmatrix} x_1 \\ x_2 \end{bmatrix} + \begin{bmatrix} \frac{u \cdot V_{\text{in}}}{L_3} \\ 0 \end{bmatrix} \tag{1.8}$$

where x_1, and x_2 represent the inductor current and output voltage respectively. u denotes the duty cycle for the IGBT switch.

1.3.2 Isolated DC-DC Converter Topology

Isolated DC-DC converters are crucial in transferring energy between two circuits that need to be electrically isolated from each other, often using a high-frequency transformer. This isolation feature ensures galvanic separation between the input and output, enhancing safety by preventing direct electrical contact between circuits. This makes them especially useful in applications like industrial automation, medical equipment, and electric vehicles, where protection from ground loops, fault isolation, or voltage transformation is essential [68]. These converters come in various topologies, such as flyback, forward, push-pull, half-bridge, and full-bridge, each designed for specific needs. The flyback converter, for example, is simple and cost-effective, ideal for low to medium-power applications. On the other hand, the full-bridge converter is more efficient and suited for high-power scenarios, offering better transformer utilization and control [69].

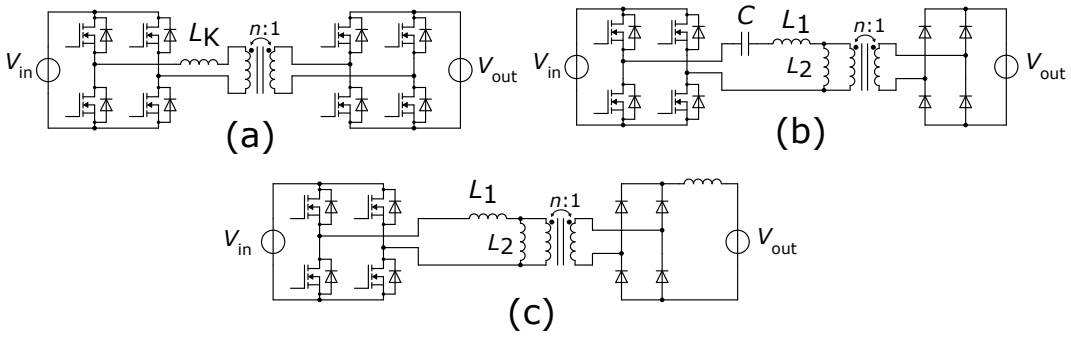

Figure 1.15: Isolated DC-DC converters (a) DAB converter (b) LLC converter (c) Phase-shifter full bridge converter

Generic circuit diagrams of isolated converter topologies are shown in fig. 1.15. In isolated converters, energy transfer occurs via magnetic coupling, which is typically facilitated by a high-frequency transformer that steps up or steps down voltage levels as needed. This transformer is designed to handle high switching frequencies, often in the range of tens to hundreds of kilohertz, enabling smaller component sizes and higher power density [70]. Furthermore, advanced control techniques and soft-switching methods, such as zero voltage switching (ZVS) or zero current switch-

ing (ZCS), are often incorporated to improve efficiency and reduce electromagnetic interference (EMI) [71].

1.3.3 Interleaving DC-DC Converter Topology

Interleaving in DC-DC converters is an advanced approach where multiple converter modules, or "phases," operate in parallel with phase shifts to evenly share the load current. By distributing the current across these phases, interleaving reduces stress on individual components, enhancing system reliability, and extending component lifespan. This method is particularly valuable in high-power applications where a single converter would otherwise face significant thermal and electrical challenges. One major benefit of interleaving is the reduction of input and output ripple currents. This reduces the size requirements for passive components such as inductors and capacitors, as the ripple frequency increases with the number of phases. Consequently, smaller and lighter components can be used, improving power density and efficiency [72]. Furthermore, interleaving improves thermal management by distributing heat across multiple components, such as inductors and MOSFETs, minimizing the rise in temperature and promoting efficient cooling [73]. Fig. 1.16 shows the circuit diagram of the interleaving converter topologies used in DC microgrids.

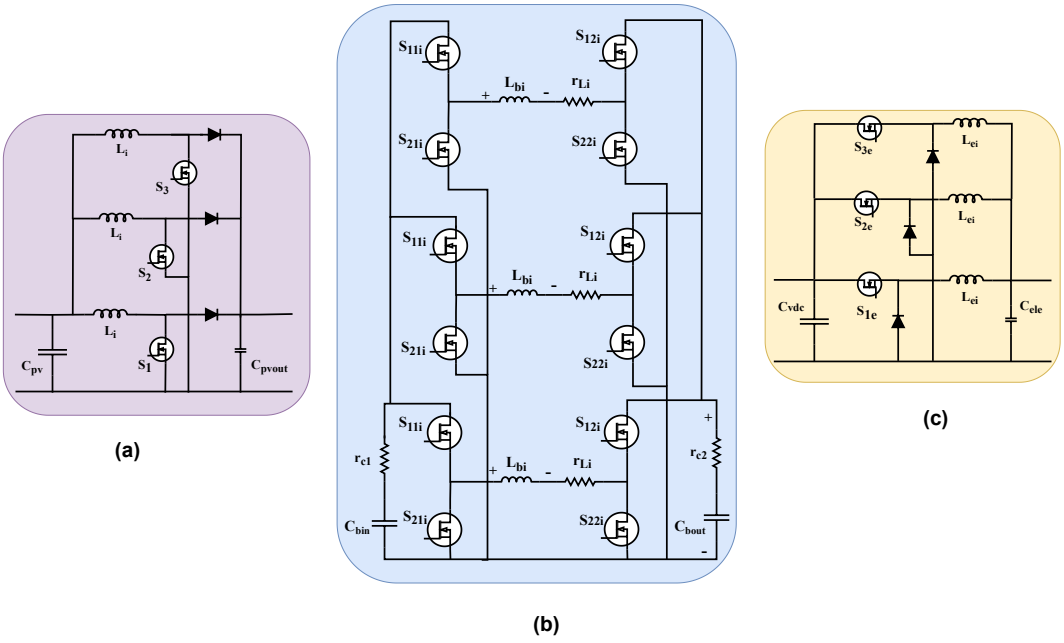

Figure 1.16: The three-level interleaving power converters (a) three-level boost converter (b) Three-level FSIBB Converter (c) Three-level buck converte

From a control perspective, interleaved converters require precise phase-shifted pulse width modulation (PWM) to maintain balanced current sharing between phases. Advanced digital controllers or field-programmable gate arrays (FPGAs) are often used to ensure accurate phase alignment and a quick dynamic response to

load changes. Furthermore, interleaved topologies are compatible with a variety of converter types, including buck, boost, and buck-boost configurations, making them versatile for a wide range of applications [74].

1.3.4 DC-AC Power Converters

DC-AC power converters play a crucial role in the integration of DC power hubs with traditional power systems. Similarly, they are also the backbone of RES integration with the utility grid. These converters not only efficiently convert DC power into AC, but also address critical challenges that arise during the integration process. Integration includes potential control problems such as voltage regulation on the DC side and phase and frequency control on the grid side [75]. Achieving stable DC-side voltage is essential to prevent power fluctuations and ensure efficient energy transfer. On the grid side, maintaining proper phase alignment and frequency synchronization is crucial to maintaining grid stability, especially in the face of fluctuating renewable energy inputs. Some important and widely used converters, such as pulse width modulation (PWM) inverters and multilevel inverters, have been developed to manage these complexities effectively and will be discussed in the following.

Gird Connected Inverters

The basic operation of a DC-AC inverter involves the conversion of DC into AC. The grid-connected voltage source inverter (VSI) is used to connect a DC source to a three-phase network. The main applications of this topology can be found in the integration of solar power systems with utility grids, powering the electrical drives for e-mobility, and microgrids connected to the grid [76]. In solar power systems, grid-connected VSIs convert DC from photovoltaic panels into AC, ensuring synchronization with grid voltage, frequency, and phase. Advanced control methods such as maximum power point tracking (MPPT) are utilized to optimize energy efficiency and stability. For e-mobility, VSIs play a key role in EVs, enabling efficient energy conversion and bidirectional power flow for vehicle-to-grid (V2G) applications, supporting services such as load balancing and frequency regulation. In microgrids, VSIs interface distributed energy resources with the grid, manage power flow and enable smooth transitions between grid-connected and island operations. Their ability to maintain voltage stability and support reactive power makes them essential in modern grid infrastructure [77].

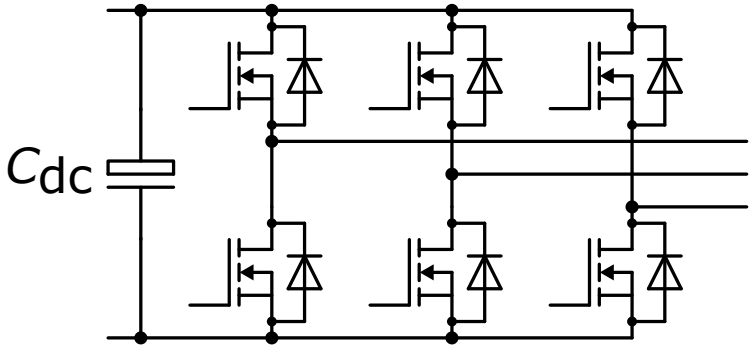

Figure 1.17: Circuit diagram of 3-phase VSI

Multi-level Inverters

Multilevel inverters are considered an alternative to traditional inverters in medium- and high-voltage applications. They generate a common mode voltage and also reduce the stress on the passive elements. This feature improves the overall performance and reliability of the system, especially in high-power quality applications [78]. Multilevel inverters come in various types, including diode-clamped, neutral-clamped, and cascaded H-Bridge inverters. Each type offers unique advantages: diode-clamped inverters provide better voltage balancing, neutral-clamped inverters improve fault tolerance, and cascaded H-Bridge inverters offer modularity and flexibility in design. These configurations enable efficient energy conversion, minimize harmonic distortion, and are widely adopted in renewable energy systems and industrial drives.

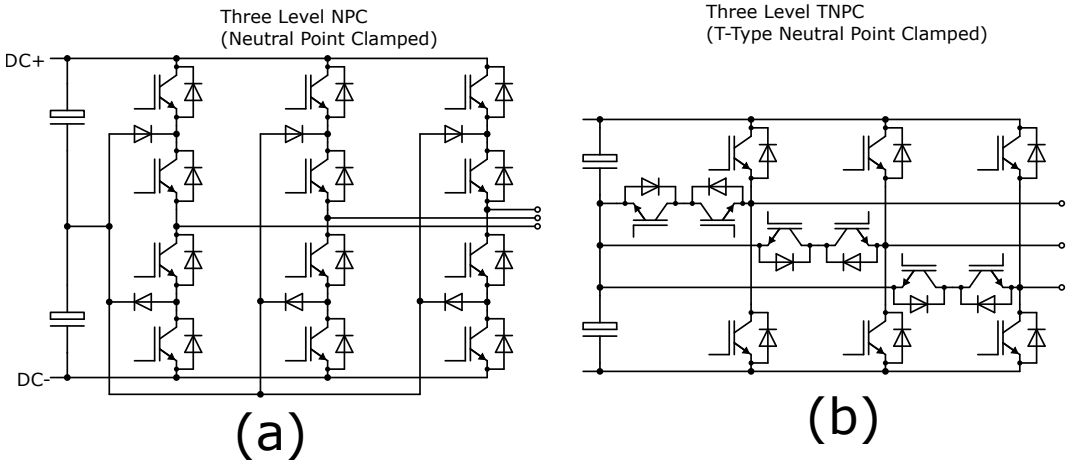

Figure 1.18: Circuit diagram of commonly used multilevel inverters

1.4 Control of Microgrids

Other challenging topics for MGs refer to the control system, based on a hierarchical control structure that generally includes the definition of the control layer involved

in the MG. In fact, for efficient and effective control of complex microgrid operations, the approach to be used should be hierarchically organized. The control system acts like the brain of the entire set-up that continuously monitors various parameters, reads data from various origins, and commands all agents involved to behave in a desired manner so that smooth and optimal performance is ensured. This system can give real-time responses and ensure the achievement of long-term operational goals [78]. Moreover, the overall control structure in MGs can be categorized into two main types such as

- Centralized Control
- Decentralized Control

1.4.1 Centralized Control

In this control design, a central controller controls the distributed energy units as indicated in fig.1.19. The information from the distributed units of MG is collected and then processed, and instructions for the next step are sent back to them via Digital Communication Links (DCLs). The central controller is responsible for communication, which is the heart of this control scheme. Some of the advantages of this control design include the observability and remarkable controllability of the whole system [79]. However, it also suffers from many disadvantages, including the failure of one of the system's units, which can result in reduced reliability and flexibility. Therefore, this design is reliable where the information collected is limited. This approach suggests that the central controller collects all the commands and decides the next step for synchronized operation of the MG and the grid (Vehicle-to-Grid and Grid-to-Vehicle technology) in which the goal is to coordinate and schedule the generators along with the controllable load to maximize the revenue from the market [80].

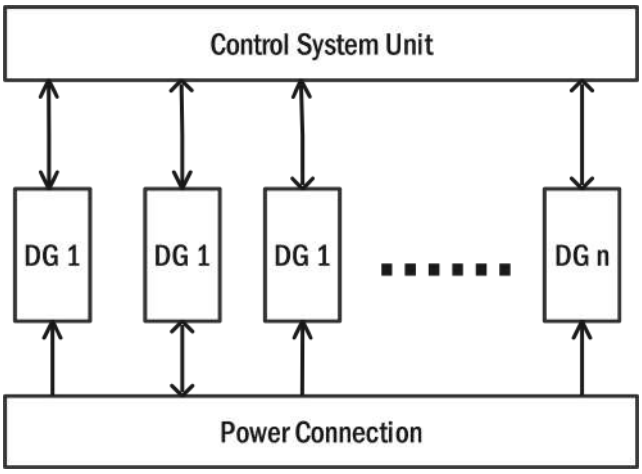

Figure 1.19: Block diagram of centralized control system

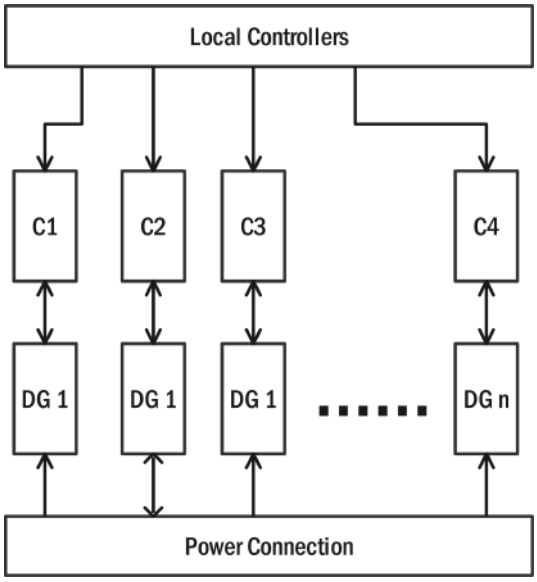

Figure 1.20: Block diagram of decentralized control

1.4.2 Decentralized Control

This control design uses separate controllers for each energy storage unit. The decentralized approach lets each local controller independently manage its energy storage unit, creating the necessary duty ratio for power converter switches based on local load demands. It allows energy storage units to autonomously adjust their power contributions without centralized control [81]. The main advantage of the design is its resilience to power failures or faults. If any energy source fails, the others remain unaffected and continue to supply power, ensuring reliability and uninterrupted operation. In addition, there is no need for communication between controllers, simplifying the system and avoiding communication-related issues. However, this decentralized approach comes with a limitation: minimal insight into what other units are doing. Without data exchange or communication, controllers lack information about the status of neighboring units, which can lead to less optimized performance and reduced coordination throughout the system [82]. The block diagram of the decentralized control method is presented in fig. 1.20. However, despite this limitation, the decentralized control design is widely considered one of the most reliable options. Its independence from communication links enhances robustness and makes it suitable for scenarios where reliability is paramount, especially in systems where communication infrastructure is not feasible or prone to failure.

The MG control structure is divided into three layers as shown in Fig. 1.21, each designed to handle specific tasks and challenges within the microgrid environment. The structure can be centralized or decentralized depending on the type of algorithm.

- Top layer: Deals with weather forecasting, load prediction, and day ahead prediction using AI methods,
- Middle layer: EMS is responsible for optimal power sharing between RESs and ESS depending on the load demand,
- Bottom layer: Termed as switching control, it is used to track currents and voltage reference according to the instructions given by EMS.

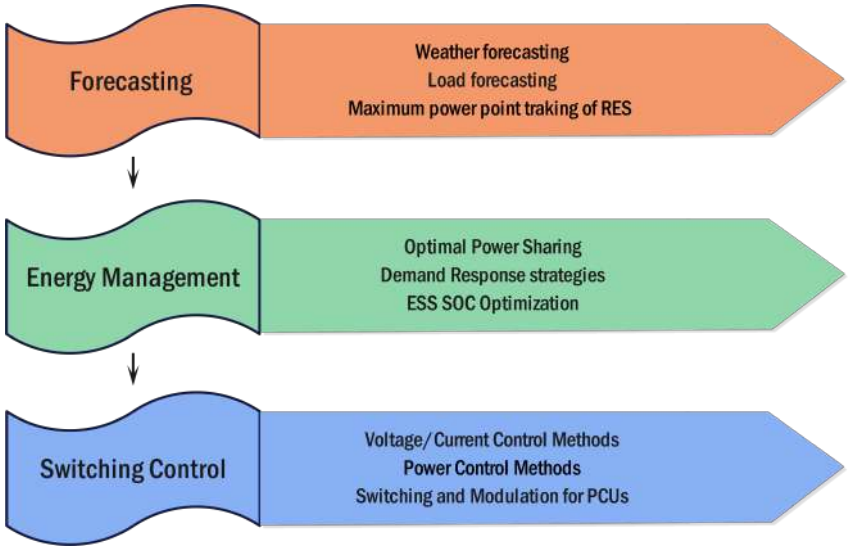

Figure 1.21: Different control layers of MG

1.4.3 Energy Forecasting

Energy forecasting is essential for optimizing microgrid and energy system performance. It involves predicting daily weather and load conditions and providing information on energy generation and consumption, which are crucial for efficient energy management and planning. Accurate forecasting ensures a balance between energy supply and demand, minimizes costs and reduces dependence on non-renewable energy sources [83]. To achieve accurate predictions, several predictive control algorithms are used:

- Model Predictive Control (MPC): Known for handling multivariable systems and constraints effectively. MPC predicts future energy demands and adjusts control actions to optimize performance over a specified time horizon, making it suitable for dynamic and complex energy systems.

AI-Based Algorithms:

- Artificial Neural Networks (ANNs): These algorithms are effective in learning complex patterns from historical data, making them ideal for predicting time-varying non-linear energy trends.

- K-Nearest Neighbors (KNN): Designed for classification and regression tasks, KNN identifies the closest data points in a historical data set to make accurate short-term load predictions [84].

Using these advanced algorithms, energy forecasting systems can achieve the following:

- Improved forecasting accuracy,
- Enhanced energy management and operational efficiency.
- Better integration of renewable energy sources,
- Greater grid stability and reliability.

1.4.4 Energy Management System

The energy management system plays an important role in the smooth operation of MG by optimally sharing power among different power sources. The system can be designed using different methods presented in fig 1.22. Each method has some advantages and limitations. The key inputs of the EMS are the load demand, the generation of RES and the ESS SOCs. Based on these factors, the EMS generates the reference values for each power source that contributes to the MG [85]. The key contributions of the EMS can be summarized as follows.

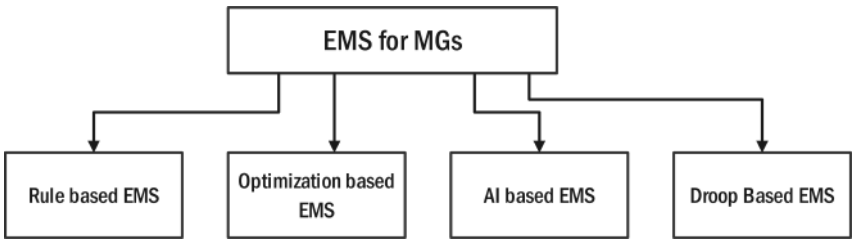

Figure 1.22: Different EMS algorithms used in MG

- Demand side management to fulfill the load demand,
- Charing and discharging of the ESS system
- Splitting the power between different ESS depending on their characteristics,
- Improve the health of ESS by tracking the SOC
- Increasing the stability and efficiency of the overall system.

1.4.5 Local Switching Controllers for PCUs

Lastly, the local switching controllers are designed for the PCUs for energy generation and conversion of the controller. The controllers generate the gate signals

for power converters and are generally designed with high frequency. They need a fast execution time as compared to the upper layers. The switching controller has a great impact on the stability of the system as they are related to the final execution, so in case of failure, it can damage devices, efficiency, and stability of the system [86].

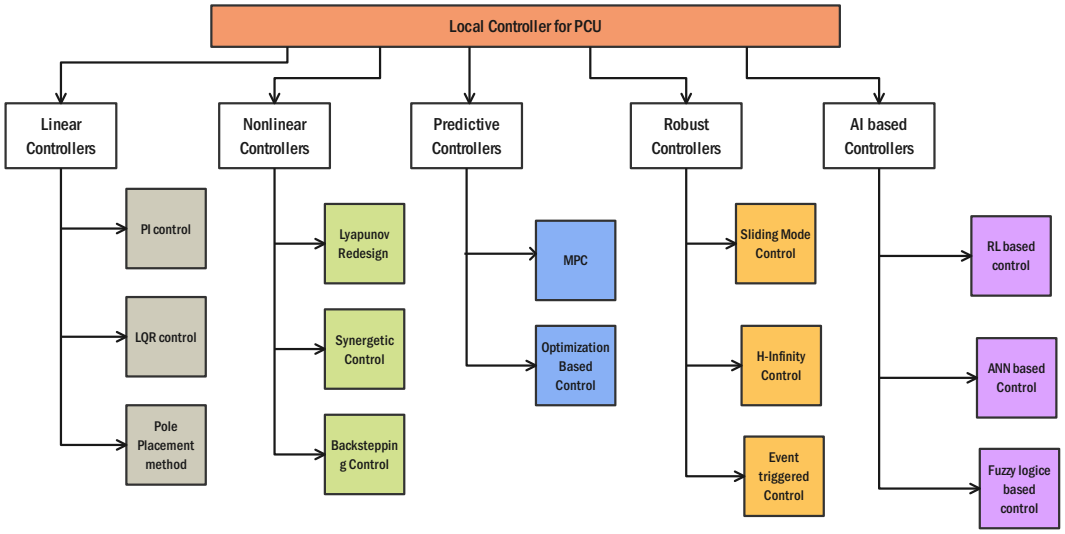

Figure 1.23: Tree diagram of control algorithms for PCUs

Linear Controllers

Linear control techniques linearize the framework and feedback control, LQR, and PID are some of such linear control methods. Due to their simple execution, they are utilized to balance out the framework [87]. The proportional integral derivative (PID) control configuration is a linear control method that is also used to stabilize the framework. Because of their simple execution and the alternative of auto-tuning for discovering the gains, they are utilized. PID regulators are divided into three distinct types, PD, PI, and PID regulators. PID control strategies are utilized for nonlinear frameworks that are first linearized and then given to the PID controller [88]. A disadvantage of this kind of regulator is: However, the disadvantages of this type of control method are as follows:

- The linearization of the model exposes the vulnerabilities of the converters, therefore the control configuration isn't extremely exact as nonlinearities are overlooked,
- Since the nonlinearities are overlooked, the working of the framework gives high rise time along with overshoots,
- Lastly, the framework's response relates to late convergence because of linearization.

Nonlinear Controllers

Recently, nonlinear control methods have been gaining significant attention due to their superior performance in various applications. Unlike linear controllers, non-linear controllers are primarily model-based techniques that require an accurate mathematical model of the system. These advanced non-linear control strategies are becoming increasingly popular in power electronics applications, where system dynamics is often complex and non-linear. Nonlinear controllers are fundamentally based on Lyapunov theory [89]. This theory uses an energy-like function to provide a mathematical expression that describes the stability of the system. The Lyapunov function serves as a key tool in assessing whether a system will remain stable under different operating conditions, offering a robust framework to design controllers that ensure system stability and optimal performance [90].

Predictive Controllers

Predictive controllers are also used to control microgrids dominated by power converters. Predictive control algorithms predict the response of the system for a specific future time instant and utilize it to modify the control signal according to the desired trajectory [91]. MPC is known as the powerful predictive controller that has a wide range of applications in different power converters. The MPC variants can be listed as CCS-MPC, FCS-MPC, and NMPC. The key issue with this type of control algorithm is computational cost and implementation issues [92].

Robust Controllers

The robustness of a controller is characterized as the property of the controller to manage known and unknown disturbances and vulnerabilities. Robust controllers possess high gains to disregard the vulnerabilities and variations that appear in the system over time. Some of the powerful control techniques are LQR, sliding mode controllers (SMC), H-infinity control, and passivity-based control [93]. These controllers for the operation of energy storage units and power converters have been presented in [94], [95].

AI based Controllers

Lately, AI-based controllers have also been investigated for PCUs. ANN [95] and RL-based [96] control algorithms are common types of AI-based controllers. The main point of the statement is their ability to be model-free. The control design process does not require any mathematical model; rather, they use the data to learn and control the system. The accuracy of these controllers depends on the data and training model, the self-learning ability also enhances the robustness of the control strategies. However, the extensive data set requirement and computational

limitations of AI models can be termed potential drawbacks [97]. Table 1.2 shows the comparative analysis of the different control methods regarding response time, complexity, robustness, and implementation.

In summary, the discussion concludes the state-of-the-art of MG components

Table 1.2: Comparative analysis of state-of-the-art controllers closed-loop

Controller	Response	Complexity	Robustness	Implementation
PI control	Slow	Low	No	Easy
LQR control	Slow	Low	No	Easy
H-Infinite control	Medium	Medium	Yes	Medium
SMC control	Very Fast	High	Yes	Hard
MPC control	Fast	High	Yes	Hard
Lyapunov control	Fast	Medium	No	Medium
ANN control	Medium	High	No	Very Hard
RL control	Fast	High	Yes	Hard

and control. Background studies show that power electronics and control systems contribute more to modern MGs. Efficient control algorithms and advanced power converters can improve overall system efficiency. The dissertation focuses mainly on innovative control and EMS for power converter dominant microgrids to integrate ESS. Basically, EMS and switching control act as master and slave, in general. Many studies have been conducted in this specific area. The table below shows the comparative analysis of the work done so far.

Table 1.3: Comparative analysis of literature work

Ref.	CPL Test	EMS	Switching Control	HESS Control	LSS	EV Integration
[98]	Yes	-	PI Control	Yes	No	No
[99]	Yes	Yes	FO-PID	Yes	No	No
[100]	Yes	No	SSMC	No	Yes	No
[101]	No	No	Deadbeat	Yes	No	No
[102]	No	Yes	Nonlinear	No	Yes	Yes
[103]	Yes	No	MPC	Yes	No	No
[104]	No	Yes	PI-PLL	-	No	No
[105]	Yes	Yes	DISMC	Yes	Yes	No
[106]	Yes	Yes	BSMC	Yes	Yes	No
[107]	No	Yes	PI	Yes	No	Yes
[107]	No	Yes	PI	Yes	No	Yes
[108]	Yes	Yes	ASMC	Yes	Yes	Yes

The table 1.3 encapsulates the most relevant work carried out for the control and energy management of the system. This study aims to improve the stability and efficiency of the MG system by integrating ESS, innovative power electronics, and an advanced control system.

1.5 Summary

- A general overview of the MG is presented by discussing the basic structure, importance of RESs, use of ESSs, role of PCUs and control methods,
- Comprehensive literature work is presented and summarized in the form of tables and flow charts,
- As the main focus of the research is power electronics and controls in MG so comparative study of the state-of-art in the field of power electronics and controls is presented.

References

[1] T.-Z. Ang, M. Salem, M. Kamarol, H. S. Das, M. A. Nazari, and N. Prabaharan, "A comprehensive study of renewable energy sources: Classifications, challenges and suggestions," *Energy Strategy Reviews*, vol. 43, p. 100 939, 2022.

[2] S. R. Sinsel, R. L. Riemke, and V. H. Hoffmann, "Challenges and solution technologies for the integration of variable renewable energy sources—a review," *renewable energy*, vol. 145, pp. 2271–2285, 2020.

[3] S. Peyghami, F. Blaabjerg, and P. Palensky, "Incorporating power electronic converters reliability into modern power system reliability analysis," *IEEE Journal of Emerging and Selected Topics in Power Electronics*, vol. 9, no. 2, pp. 1668–1681, 2020.

[4] P. Bajpai and V. Dash, "Hybrid renewable energy systems for power generation in stand-alone applications: A review," *Renewable and Sustainable Energy Reviews*, vol. 16, no. 5, pp. 2926–2939, 2012.

[5] V. C. Gungor, D. Sahin, T. Kocak, *et al.*, "Smart grid technologies: Communication technologies and standards," *IEEE transactions on Industrial informatics*, vol. 7, no. 4, pp. 529–539, 2011.

[6] O. Gomis-Bellmunt, J. Song, M. Cheah-Mane, and E. Prieto-Araujo, "Steady-state impedance mapping in grids with power electronics: What is grid strength in modern power systems?" *International Journal of Electrical Power & Energy Systems*, vol. 136, p. 107 635, 2022.

[7] C. Buccella, C. Cecati, and H. Latafat, "Digital control of power converters—a survey," *IEEE Transactions on Industrial Informatics*, vol. 8, no. 3, pp. 437–447, 2012.

[8] S. Parhizi, H. Lotfi, A. Khodaei, and S. Bahramirad, "State of the art in research on microgrids: A review," *IEEE access*, vol. 3, pp. 890–925, 2015.

[9] M. H. Saeed, W. Fangzong, B. A. Kalwar, and S. Iqbal, "A review on microgrids' challenges & perspectives," *IEEE Access*, vol. 9, pp. 166 502–166 517, 2021.

[10] M. Sandelic, S. Peyghami, A. Sangwongwanich, and F. Blaabjerg, "Reliability aspects in microgrid design and planning: Status and power electronics-induced challenges," *Renewable and Sustainable Energy Reviews*, vol. 159, p. 112 127, 2022.

[11] Q. Ullah, X. Wu, and U. Saleem, "Current controlled robust four-switch buck-boost dc-dc converter," in *2021 International Conference on Computing, Electronic and Electrical Engineering (ICE Cube)*, IEEE, 2021, pp. 1–6.

[12] Y. Wang, J. Lan, X. Huang, T. Fang, X. Ruan, and M. Dong, "An improved single-mode control strategy based on four-switch buck-boost converter," in *2020 IEEE Applied Power Electronics Conference and Exposition (APEC)*, 2020, pp. 320–325. DOI: 10.1109/APEC39645.2020.9124612.

[13] Q. Liu, Q. Qian, M. Zheng, S. Xu, W. Sun, and T. Wang, "An improved quadrangle control method for four-switch buck-boost converter with reduced loss and decoupling strategy," *IEEE Transactions on Power Electronics*, vol. 36, no. 9, pp. 10 827–10 841, 2021.

[14] M. S. Mahmoud, M. Saif Ur Rahman, and F. M. AL-Sunni, "Review of microgrid architectures–a system of systems perspective," *IET Renewable Power Generation*, vol. 9, no. 8, pp. 1064–1078, 2015.

[15] M. Abbasi, E. Abbasi, L. Li, R. P. Aguilera, D. Lu, and F. Wang, "Review on the microgrid concept, structures, components, communication systems, and control methods," *Energies*, vol. 16, no. 1, p. 484, 2023.

[16] L. Mariam, M. Basu, and M. F. Conlon, "Microgrid: Architecture, policy and future trends," *Renewable and Sustainable Energy Reviews*, vol. 64, pp. 477–489, 2016.

[17] L. Mariam, M. Basu, and M. F. Conlon, "A review of existing microgrid architectures," *Journal of engineering*, vol. 2013, no. 1, p. 937 614, 2013.

[18] A. U. Rahman, S. S. Zehra, I. Ahmad, and H. Armghan, "Fuzzy supertwisting sliding mode-based energy management and control of hybrid energy storage system in electric vehicle considering fuel economy," *Journal of Energy Storage*, vol. 37, p. 102 468, 2021.

[19] S. Baudoin, I. Vechiu, and H. Camblong, "A review of voltage and frequency control strategies for islanded microgrid," in *2012 16th international conference on system theory, control and computing (ICSTCC)*, IEEE, 2012, pp. 1–5.

[20] A. Rosini, A. Labella, A. Bonfiglio, R. Procopio, and J. M. Guerrero, "A review of reactive power sharing control techniques for islanded microgrids," *Renewable and Sustainable Energy Reviews*, vol. 141, p. 110 745, 2021.

[21] R. Hasan, S. Mekhilef, M. Seyedmahmoudian, and B. Horan, "Grid-connected isolated pv microinverters: A review," *Renewable and Sustainable Energy Reviews*, vol. 67, pp. 1065–1080, 2017.

[22] N. Kumari, A. Sharma, B. Tran, N. Chilamkurti, and D. Alahakoon, "A comprehensive review of digital twin technology for grid-connected microgrid systems: State of the art, potential and challenges faced," *Energies*, vol. 16, no. 14, p. 5525, 2023.

[23] T. Dragičević, X. Lu, J. C. Vasquez, and J. M. Guerrero, "Dc microgrids—part i: A review of control strategies and stabilization techniques," *IEEE Transactions on power electronics*, vol. 31, no. 7, pp. 4876–4891, 2015.

[24] Q. Xu, N. Vafamand, L. Chen, T. Dragičević, L. Xie, and F. Blaabjerg, "Review on advanced control technologies for bidirectional dc/dc converters in dc microgrids," *IEEE Journal of Emerging and Selected Topics in Power Electronics*, vol. 9, no. 2, pp. 1205–1221, 2020.

[25] J. Kumar, A. Agarwal, and V. Agarwal, "A review on overall control of dc microgrids," *Journal of energy storage*, vol. 21, pp. 113–138, 2019.

[26] K. Rajesh, S. Dash, R. Rajagopal, and R. Sridhar, "A review on control of ac microgrid," *Renewable and sustainable energy reviews*, vol. 71, pp. 814–819, 2017.

[27] B. Patnaik, M. Mishra, R. C. Bansal, and R. K. Jena, "Ac microgrid protection–a review: Current and future prospective," *Applied Energy*, vol. 271, p. 115 210, 2020.

[28] A. Mohammed, S. S. Refaat, S. Bayhan, and H. Abu-Rub, "Ac microgrid control and management strategies: Evaluation and review," *IEEE Power Electronics Magazine*, vol. 6, no. 2, pp. 18–31, 2019.

[29] M. A. Hossain, H. R. Pota, W. Issa, and M. J. Hossain, "Overview of ac microgrid controls with inverter-interfaced generations," *Energies*, vol. 10, no. 9, p. 1300, 2017.

[30] A. Gupta, S. Doolla, and K. Chatterjee, "Hybrid ac–dc microgrid: Systematic evaluation of control strategies," *IEEE Transactions on Smart Grid*, vol. 9, no. 4, pp. 3830–3843, 2017.

[31] B. Sahoo, S. K. Routray, and P. K. Rout, "Ac, dc, and hybrid control strategies for smart microgrid application: A review," *International Transactions on Electrical Energy Systems*, vol. 31, no. 1, e12683, 2021.

[32] E. Unamuno and J. A. Barrena, "Hybrid ac/dc microgrids—part i: Review and classification of topologies," *Renewable and Sustainable Energy Reviews*, vol. 52, pp. 1251–1259, 2015.

[33] R. A. Kaushik and N. M. Pindoriya, "A hybrid ac-dc microgrid: Opportunities & key issues in implementation," in *2014 International Conference on Green Computing Communication and Electrical Engineering (ICGCCEE)*, IEEE, 2014, pp. 1–6.

[34] L. V. Kochtcheeva, "Renewable energy: Global challenges," *E-International Relations*, vol. 27, 2016.

[35] R. Prakash, I. K. Bhat, *et al.*, "Energy, economics and environmental impacts of renewable energy systems," *Renewable and sustainable energy reviews*, vol. 13, no. 9, pp. 2716–2721, 2009.

[36] R. Bhandari and N. Adhikari, "A comprehensive review on the role of hydrogen in renewable energy systems," *International Journal of Hydrogen Energy*, vol. 82, pp. 923–951, 2024.

[37] D. Neves, C. A. Silva, and S. Connors, "Design and implementation of hybrid renewable energy systems on micro-communities: A review on case studies," *Renewable and Sustainable Energy Reviews*, vol. 31, pp. 935–946, 2014.

[38] *IRENA – International Renewable Energy Agency — irena.org*, `https://www.irena.org/`, [Accessed 05-11-2024].

[39] N. Kannan and D. Vakeesan, "Solar energy for future world:-a review," *Renewable and sustainable energy reviews*, vol. 62, pp. 1092–1105, 2016.

[40] E. Kabir, P. Kumar, S. Kumar, A. A. Adelodun, and K.-H. Kim, "Solar energy: Potential and future prospects," *Renewable and Sustainable Energy Reviews*, vol. 82, pp. 894–900, 2018.

[41] M. R. Islam, A. Mahfuz-Ur-Rahman, K. M. Muttaqi, and D. Sutanto, "State-of-the-art of the medium-voltage power converter technologies for grid integration of solar photovoltaic power plants," *IEEE Transactions on Energy Conversion*, vol. 34, no. 1, pp. 372–384, 2018.

[42] J. T. Bialasiewicz, "Renewable energy systems with photovoltaic power generators: Operation and modeling," *IEEE Transactions on industrial Electronics*, vol. 55, no. 7, pp. 2752–2758, 2008.

[43] S. Senthilkumar, V. Mohan, R. Deepa, *et al.*, "A review on mppt algorithms for solar pv systems," *International Journal of Research-GRANTHAALAYAH*, vol. 11, no. 3, pp. 25–64, 2023.

[44] R. B. Koad, A. F. Zobaa, and A. El-Shahat, "A novel mppt algorithm based on particle swarm optimization for photovoltaic systems," *IEEE Transactions on Sustainable Energy*, vol. 8, no. 2, pp. 468–476, 2016.

[45] H. Bounechba, A. Bouzid, H. Snani, and A. Lashab, "Real time simulation of mppt algorithms for pv energy system," *International Journal of Electrical Power & Energy Systems*, vol. 83, pp. 67–78, 2016.

[46] F. Blaabjerg and K. Ma, "Wind energy systems," *Proceedings of the IEEE*, vol. 105, no. 11, pp. 2116–2131, 2017.

[47] T. Agarwal, S. Verma, and A. Gaurh, "Issues and challenges of wind energy," in *2016 International Conference on Electrical, Electronics, and Optimization Techniques (ICEEOT)*, IEEE, 2016, pp. 67–72.

[48] G. J. Herbert, S. Iniyan, E. Sreevalsan, and S. Rajapandian, "A review of wind energy technologies," *Renewable and sustainable energy Reviews*, vol. 11, no. 6, pp. 1117–1145, 2007.

[49] H. M. Nguyen and D. S. Naidu, "Advanced control strategies for wind energy systems: An overview," in *2011 IEEE/PES Power Systems Conference and Exposition*, IEEE, 2011, pp. 1–8.

[50] V. K. Singh and S. K. Singal, "Operation of hydro power plants-a review," *Renewable and Sustainable Energy Reviews*, vol. 69, pp. 610–619, 2017.

[51] K. Kumar and R. Saini, "A review on operation and maintenance of hydropower plants," *Sustainable Energy Technologies and Assessments*, vol. 49, p. 101 704, 2022.

[52] A. Midilli and I. Dincer, "Key strategies of hydrogen energy systems for sustainability," *International Journal of Hydrogen Energy*, vol. 32, no. 5, pp. 511–524, 2007.

[53] N. Sazali, W. N. Wan Salleh, A. S. Jamaludin, and M. N. Mhd Razali, "New perspectives on fuel cell technology: A brief review," *Membranes*, vol. 10, no. 5, p. 99, 2020.

[54] I.-S. Sorlei, N. Bizon, P. Thounthong, *et al.*, "Fuel cell electric vehicles—a brief review of current topologies and energy management strategies," *Energies*, vol. 14, no. 1, p. 252, 2021.

[55] M. A. Hannan, S. Wali, P. J. Ker, *et al.*, "Battery energy-storage system: A review of technologies, optimization objectives, constraints, approaches, and outstanding issues," *Journal of Energy Storage*, vol. 42, p. 103 023, 2021.

[56] H. A. Kiehne, *Battery technology handbook*. CRC Press, 2003, vol. 118.

[57] M. E. Şahin, F. Blaabjerg, and A. Sangwongwanich, "A comprehensive review on supercapacitor applications and developments," *Energies*, vol. 15, no. 3, p. 674, 2022.

[58] W. Jing, C. Hung Lai, S. H. W. Wong, and M. L. D. Wong, "Battery-supercapacitor hybrid energy storage system in standalone dc microgrids: Areview," *IET Renewable Power Generation*, vol. 11, no. 4, pp. 461–469, 2017.

[59] S. Dahale, A. Das, N. M. Pindoriya, and S. Rajendran, "An overview of dc-dc converter topologies and controls in dc microgrid," in *2017 7th International Conference on Power Systems (ICPS)*, IEEE, 2017, pp. 410–415.

[60] J. Hu, Y. Shan, K. W. Cheng, and S. Islam, "Overview of power converter control in microgrids—challenges, advances, and future trends," *IEEE Transactions on Power Electronics*, vol. 37, no. 8, pp. 9907–9922, 2022.

[61] S. A. Gorji, H. G. Sahebi, M. Ektesabi, and A. B. Rad, "Topologies and control schemes of bidirectional dc–dc power converters: An overview," *IEEE Access*, vol. 7, pp. 117 997–118 019, 2019.

[62] M. Hossain, N. Rahim, *et al.*, "Recent progress and development on power dc-dc converter topology, control, design and applications: A review," *Renewable and Sustainable Energy Reviews*, vol. 81, pp. 205–230, 2018.

[63] C. Sachin and S. G. Nayak, "Design and simulation for sliding mode control in dc-dc boost converter," in *2017 2nd International Conference on Communication and Electronics Systems (ICCES)*, IEEE, 2017, pp. 440–445.

[64] D. Venkatramanan and V. John, "Dynamic modeling and analysis of buck converter based solar pv charge controller for improved mppt performance," *IEEE Transactions on Industry Applications*, vol. 55, no. 6, pp. 6234–6246, 2019.

[65] D. Zammit, C. S. Staines, M. Apap, and A. Micallef, "Overview of buck and boost converters modelling and control for stand-alone dc microgrid operation," in *Offshore Energy & Storage Symposium (OSES 2016), Valletta, Malta*, vol. 2294, 2016, pp. 2284–2294.

[66] M. S. Khan, S. S. Nag, A. Das, and C. Yoon, "Analysis and control of an input-parallel output-series connected buck-boost dc–dc converter for electric vehicle powertrains," *IEEE Transactions on Transportation Electrification*, vol. 9, no. 2, pp. 2015–2025, 2022.

[67] F. G. Nimitti and A. M. S. S. Andrade, "Bidirectional converter based on boost/buck dc-dc converter for microgrids energy storage systems interface," *International Journal of Circuit Theory and Applications*, vol. 50, no. 12, pp. 4376–4394, 2022.

[68] J. Supriya and J. Rajashekar, "A comprehensive review of various isolated dc-dc converters topologies associated with photovoltaic applications," *Recent Advances in Electrical & Electronic Engineering (Formerly Recent Patents on Electrical & Electronic Engineering)*, vol. 15, no. 8, pp. 595–606, 2022.

[69] N. M. Tan, T. Abe, and H. Akagi, "Topology and application of bidirectional isolated dc-dc converters," in *8th International Conference on Power Electronics-ECCE Asia*, IEEE, 2011, pp. 1039–1046.

[70] J. Walter and R. W. De Doncker, "High-power galvanically isolated dc/dc converter topology for future automobiles," in *IEEE 34th Annual Conference on Power Electronics Specialist, 2003. PESC'03.*, IEEE, vol. 1, 2003, pp. 27–32.

[71] I. Alhurayyis, A. Elkhateb, and J. Morrow, "Isolated and nonisolated dc-to-dc converters for medium-voltage dc networks: A review," *IEEE Journal of Emerging and Selected Topics in Power Electronics*, vol. 9, no. 6, pp. 7486–7500, 2020.

[72] A. M. Omara and M. Sleptsov, "Bidirectional interleaved dc/dc converter for electric vehicle application," in *2016 11th International Forum on Strategic Technology (IFOST)*, IEEE, 2016, pp. 100–104.

[73] B. A. Miwa, "Interleaved conversion techniques for high density power supplies," Ph.D. dissertation, Massachusetts Institute of Technology, 1992.

[74] P. D. Antoszczuk, R. G. Retegui, M. Funes, and D. Carrica, "Optimized implementation of a current control algorithm for multiphase interleaved power converters," *IEEE Transactions on Industrial Informatics*, vol. 10, no. 4, pp. 2224–2232, 2014.

[75] M. D. Bellar, T.-S. Wu, A. Tchamdjou, J. Mahdavi, and M. Ehsani, "A review of soft-switched dc-ac converters," *IEEE Transactions on Industry Applications*, vol. 34, no. 4, pp. 847–860, 1998.

[76] G. Séguier and F. Labrique, *Power electronic converters: DC-AC conversion*. Springer Science & Business Media, 2012.

[77] K. Sayed, A. Almutairi, N. Albagami, O. Alrumayh, A. G. Abo-Khalil, and H. Saleeb, "A review of dc-ac converters for electric vehicle applications," *Energies*, vol. 15, no. 3, p. 1241, 2022.

[78] L. P. Suresh *et al.*, "A brief review on multi level inverter topologies," in *2016 international conference on circuit, power and computing technologies (ICCPCT)*, IEEE, 2016, pp. 1–6.

[79] D. E. Olivares, C. A. Cañizares, and M. Kazerani, "A centralized energy management system for isolated microgrids," *IEEE Transactions on smart grid*, vol. 5, no. 4, pp. 1864–1875, 2014.

[80] D. Espín-Sarzosa, R. Palma-Behnke, and O. Núñez-Mata, "Energy management systems for microgrids: Main existing trends in centralized control architectures," *Energies*, vol. 13, no. 3, p. 547, 2020.

[81] K. Zuo and L. Wu, "A review of decentralized and distributed control approaches for islanded microgrids: Novel designs, current trends, and emerging challenges," *The Electricity Journal*, vol. 35, no. 5, p. 107 138, 2022.

[82] K. Zuo and L. Wu, "A review of decentralized and distributed control approaches for islanded microgrids: Novel designs, current trends, and emerging challenges," *The Electricity Journal*, vol. 35, no. 5, p. 107 138, 2022.

[83] A. Agüera-Pérez, J. C. Palomares-Salas, J. J. G. De La Rosa, and O. Florencias-Oliveros, "Weather forecasts for microgrid energy management: Review, discussion and recommendations," *Applied energy*, vol. 228, pp. 265–278, 2018.

[84] B. O. Abisoye, Y. Sun, and W. Zenghui, "A survey of artificial intelligence methods for renewable energy forecasting: Methodologies and insights," *Renewable Energy Focus*, p. 100 529, 2023.

[85] A. P. Arunkumar, S. Kuppusamy, S. Muthusamy, S. Pandiyan, H. Panchal, and P. Nagaiyan, "An extensive review on energy management system for microgrids," *Energy Sources, Part A: Recovery, Utilization, and Environmental Effects*, vol. 44, no. 2, pp. 4203–4228, 2022.

[86] F. Mumtaz, N. Z. Yahaya, S. T. Meraj, B. Singh, R. Kannan, and O. Ibrahim, "Review on non-isolated dc-dc converters and their control techniques for renewable energy applications," *Ain Shams Engineering Journal*, vol. 12, no. 4, pp. 3747–3763, 2021.

[87] M. Martinez-Lopez, J. Moreno-Valenzuela, and W. He, "A robust nonlinear pi-type controller for the dc–dc buck–boost power converter," *ISA transactions*, vol. 129, pp. 687–700, 2022.

[88] J. Linares-Flores, J. A. Juárez-Abad, A. Hernandez-Mendez, *et al.*, "Sliding mode control based on linear extended state observer for dc-to-dc buck–boost power converter system with mismatched disturbances," *IEEE Transactions on Industry Applications*, vol. 58, no. 1, pp. 940–950, 2021.

[89] M. Kabalan, P. Singh, and D. Niebur, "Large signal lyapunov-based stability studies in microgrids: A review," *IEEE Transactions on Smart Grid*, vol. 8, no. 5, pp. 2287–2295, 2016.

[90] A. Abedi, B. Rezaie, A. Khosravi, and M. Shahabi, "Dc-bus voltage control based on direct lyapunov method for a converter-based stand-alone dc microgrid," *Electric Power Systems Research*, vol. 187, p. 106 451, 2020.

[91] S. Kouro, P. Cortés, R. Vargas, U. Ammann, and J. Rodríguez, "Model predictive control—a simple and powerful method to control power converters," *IEEE Transactions on industrial electronics*, vol. 56, no. 6, pp. 1826–1838, 2008.

[92] S. Vazquez, J. Rodriguez, M. Rivera, L. G. Franquelo, and M. Norambuena, "Model predictive control for power converters and drives: Advances and trends," *IEEE Transactions on Industrial Electronics*, vol. 64, no. 2, pp. 935–947, 2016.

[93] M. Gupta, N. Gupta, M. M. Garg, and A. Kumar, "Robust control strategies applicable to dc–dc converter with reliability assessment: A review," *Advanced Control for Applications: Engineering and Industrial Systems*, vol. 6, no. 3, e217, 2024.

[94] Y. Xu, Z. Li, J. Zhao, and J. Zhang, "Distributed robust control strategy of grid-connected inverters for energy storage systems' state-of-charge balancing," *IEEE Transactions on Smart Grid*, vol. 9, no. 6, pp. 5907–5917, 2017.

[95] S. Som, S. De, S. Chakrabarti, S. R. Sahoo, and A. Ghosh, "A robust controller for battery energy storage system of an islanded ac microgrid," *IEEE Transactions on Industrial Informatics*, vol. 18, no. 1, pp. 207–218, 2021.

[96] M. Gheisarnejad, H. Farsizadeh, and M. H. Khooban, "A novel nonlinear deep reinforcement learning controller for dc–dc power buck converters," *IEEE Transactions on Industrial Electronics*, vol. 68, no. 8, pp. 6849–6858, 2020.

[97] Y. Gao, S. Wang, T. Dragicevic, P. Wheeler, and P. Zanchetta, "Artificial intelligence techniques for enhancing the performance of controllers in power converter-based systems-an overview," *IEEE Open Journal of Industry Applications*, 2023.

[98] Q. Xu, X. Hu, P. Wang, *et al.*, "A decentralized dynamic power sharing strategy for hybrid energy storage system in autonomous dc microgrid," *IEEE transactions on industrial electronics*, vol. 64, no. 7, pp. 5930–5941, 2016.

[99] A. A. Al Alahmadi, Y. Belkhier, N. Ullah, *et al.*, "Hybrid wind/pv/battery energy management-based intelligent non-integer control for smart dc-microgrid of smart university," *IEEE Access*, vol. 9, pp. 98 948–98 961, 2021.

[100] V. Kumar, S. R. Mohanty, and S. Kumar, "Event trigger super twisting sliding mode control for dc micro grid with matched/unmatched disturbance observer," *IEEE Transactions on Smart Grid*, vol. 11, no. 5, pp. 3837–3849, 2020.

[101] B. Wang, U. Manandhar, X. Zhang, H. B. Gooi, and A. Ukil, "Deadbeat control for hybrid energy storage systems in dc microgrids," *IEEE Transactions on Sustainable Energy*, vol. 10, no. 4, pp. 1867–1877, 2019. DOI: 10.1109/TSTE.2018.2873801.

[102] M. J. Carrizosa, A. Iovine, G. Damm, and P. Alou, "Droop-inspired nonlinear control of a dc microgrid for integration of electrical mobility providing ancillary services to the ac main grid," *IEEE Transactions on Smart Grid*, vol. 13, no. 5, pp. 4113–4122, 2022.

[103] Q. Yang, J. Zhou, X. Chen, and J. Wen, "Distributed mpc-based secondary control for energy storage systems in a dc microgrid," *IEEE Transactions on Power Systems*, vol. 36, no. 6, pp. 5633–5644, 2021.

[104] A. M. Mahfuz-Ur-Rahman, M. R. Islam, K. M. Muttaqi, and D. Sutanto, "An effective energy management with advanced converter and control for a pv-battery storage based microgrid to improve energy resiliency," *IEEE Transactions on Industry Applications*, vol. 57, no. 6, pp. 6659–6668, 2021. DOI: 10.1109/TIA.2021.3115085.

[105] A. Armghan, M. K. Azeem, H. Armghan, M. Yang, F. Alenezi, and M. Hassan, "Dynamical operation based robust nonlinear control of dc microgrid considering renewable energy integration," *Energies*, vol. 14, no. 13, p. 3988, 2021.

[106] S. S. Zehra, A. U. Rahman, and I. Ahmad, "Fuzzy-barrier sliding mode control of electric-hydrogen hybrid energy storage system in dc microgrid: Modelling, management and experimental investigation," *Energy*, vol. 239, p. 122 260, 2022.

[107] H. Pan, X. Feng, F. Li, and J. Yang, "Energy coordinated control of dc microgrid integrated incorporating pv, energy storage and ev charging," *Applied Energy*, vol. 342, p. 121 155, 2023.

[108] S. Y. Rahme, S. Islam, S. M. Amrr, A. Iqbal, I. Khan, and M. Marzband, "Adaptive sliding mode control for instability compensation in dc microgrids due to ev charging infrastructure," *Sustainable Energy, Grids and Networks*, vol. 35, p. 101 119, 2023.

Chapter 2

Converter Topologies for Energy Storage System Integration

2.1 Introduction

Energy storage devices (ESDs) play a vital role in modern power networks and e-mobility. In the e-mobility sector, they are considered as the primary sources, and battery-based electric vehicles are the most common example of it. However, in modern power systems, such as microgrids, ESD acts as auxiliary sources [1], [2]. Energy storage devices are integrated into power networks through power converters. Power conversion units also play an important role in modern power engineering and provide advantages such as desired power conversion, advanced control of the system, and efficient power transfer [3], [4]. Renewable energy sources (RES) play a crucial role not only in reducing greenhouse gas emissions but also in decentralizing energy production, thus avoiding inefficiencies of central power plants, mainly due to transmission line losses [5]. RES-based decentralized energy production also allows the opportunity to supply rural areas and remote locations, where electricity transmission can represent a relevant challenge, and together with emerging sustainable mobility, it contributes to reducing pollution [6]–[8]. Among RES, solar and wind provide a significant contribution due to technological improvements and economic incentives [9]–[12]. Improvements in the design and implementation of electrical machines and drives notably contribute to the development of RES [13], [14]. However, because of their intermittency in energy production, practical solutions to properly and efficiently use RES are required. To implement such a decentralized power generation, the idea of a Microgrid is appropriate, representing an electrical grid that locally connects energy sources and loads aiming at the goal of satisfying the local demand [15]. Differentiating the type of microgrid according to the AC or DC nature of generation and load units provides the opportunity to reduce the number of power stage converters and consequently power losses and system complexity, thus directly connecting AC generation units (e.g. wind power generator) with AC load units and

DC generation units (e.g. solar power or ESS) with DC load units. Furthermore, great improvements in power electronics allow easy interconnection of conventional AC power systems with DC loads, so that most of the existing loads are increasingly supplied in DC with notable advantages in terms of energy distribution quality, leading to the elimination of all the issues related to AC distribution, such as reactive power and frequency adjustments. Concerning AC Microgrids, DC Microgrids represent a comfortable solution for RES-ESS integration and are strongly recommended even if integrated with AC Microgrids, such as in AC-DC hybrid Microgrids [16]. To connect DC Microgrids with ESS, bidirectional DC-DC converters are needed. Their goal is to control the transferred power while generating a negligible current ripple.

In this chapter, the use of four-switches single-inductor buck-boost (FSIBB) and interleaving (IFSIBB) for ESDs is studied. There are many converter topologies in the literature which can be used for storage devices according to their applications [17] however, the mostly buck-boost converter is considered as it allows bitol power flow for charging and discharging [18]. It has a wide range of applications, such as electric vehicles [19], battery storage systems [20], and photovoltaic systems [21]. FSIBB converter has some plus points over the traditional buck-boost converter such as a wide operating range, more modes of operation, and noninverting output. The noninverting property of the FSIBB converter offers plug-and-play, no extra connection is required because of the same polarity at the output [22]. However, due to its complex structure, the FSIBB converter also requires a proper control algorithm to get a smooth output.

FSIBB converters have two basic modes of operation buck mode and boost mode. Some issues like a dead zone, phase shift, and non-minimum phase behavior make it a complex model from a control perspective. Many studies have been carried out to design switching controllers for FSIBB converter. In [23], a linear controller based on proportional integral (PI) has been developed to control the output current of the system. Similarly, to avoid two-mode complexity, a single-mode controller is advised in [24], but it only operates in boost mode by the fixed duty cycle. To overcome the problems in conventional control methods, an improved quadrangle control method has been presented in [25] which also overcomes the problem of traditional quadrangle control. In [26], [27] a model-based model predictive controller (MPC) has been proposed for different modes of the FSIBB converter and allows the phase shift and smooth transient response. The computational cost, complexity, and variable switching frequency can be termed as drawbacks of MPC but it also provides the solution for discontinuous conduction mode (DCM) [26]. Among ESS, supercapacitors have the benefit of integrating high energy density batteries and fuel cells with a high power density device [14], [28], [29]. To adapt the potentially highly variable voltage of the supercapacitors to the fixed DC voltage bus, proper topologies of DC-DC converters can be helpful. The four-switches single-inductor

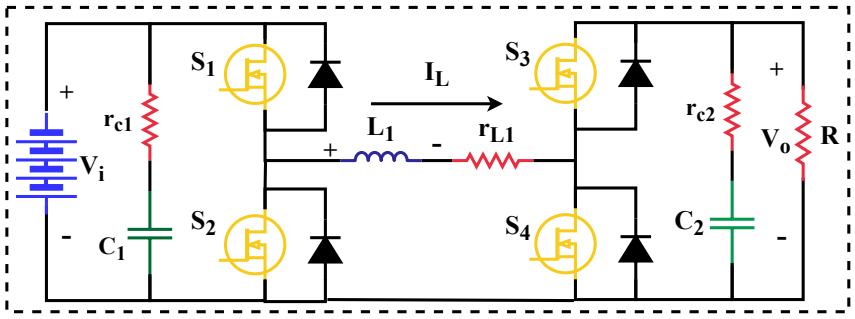

Figure 2.1: Schematic diagram of FSIBB Converter

topology provides the opportunity of step-down or step-up operation according to the duty cycle in the pulse width modulation (PWM) technique [30]. The drawback of such a topology is the pulsating current on both the input and the output side, because of the presence of a series switch at the input and output. This makes filtering networks highly bulky and expensive, as a small ripple current is generally required at the terminal sections of the converter. Therefore, a solution is needed to contribute and reduce ripples and electromagnetic interference while keeping small filters. Multiphase interleaved power stages are well known and represent a consolidated approach to control DC-DC power converters, giving the double benefit of parallelizing converters and reducing voltage and current ripple, thus contributing to smooth EMI with notable attractiveness for applications such as DC microgrids and power-to-hydrogen systems [31], [32]. In converters that simply manage the power flow between one source and one load, the average current through each interleaved stage shall be the same to avoid unbalanced power transfer and heat dissipation, so that the reliability and integrity of the system are guaranteed. In this case, some control strategies are needed to compensate for the unavoidable tolerances of the components [33], [34]. To implement equal power sharing among the different stages of a multi-phase interleaved converter, different control methods have been presented in the literature [35], [36].

The contributions of this chapter can be summarized in the following points.

- A Simplified Average mathematical model of FSIBB is developed using two modes of operation.
- A Double loop controller based on Sliding mode control and PI regulator is proposed.
- Stability analysis of the closed-loop system is done by using Lyapunov stability theory.
- A comparative analysis is presented with state of art PI controller.
- The interleaving approach is investigated on this topology, focusing on the current ripple minimization.

- To integrate the proposed system in a microgrid large signal stability is very important however, the linear control doesn't guarantee the performance globally. Hence the nonlinear control design is proposed with closed-loop stability analysis.
- Finally, the proposed scheme is validated by both simulation and real-time tests using the TI microcontroller and Typhoon 404 hardware in loop (HIL).

Fig 2.1, shows the schematic diagram of the FSIBB converter considered with a resistive load.

2.2 FSIBB Converter for ESSs

2.2.1 Converter Modelling and Discription

The FSIBB converter shown in fig 2.1 has four switches S_1, S_2, S_3, and S_4 respectively. C_1, C_2, L_1, and R represent the input-output capacitance, inductance, and resistance of the converter, where V_i and V_o are the input and output voltages of the converter. Lastly, r_{in}, $r_{c1,c2}$, and r_{L1} denote the internal resistance of the passive components. The Parameters of the power converter can be designed by using basic power electronic theory, for example, the inductance value for the power converter can be selected by using the mathematical equation as

$$L \geq V_i \frac{DT_{sw}}{\delta I_L} \tag{2.1}$$

where D is the duty cycle, δI_L and T_{sw} are the desired ripple current and the switching period, respectively. Similarly, for the capacitance we used

$$C \geq \frac{V_o DT_{sw}}{R\delta V_o} \tag{2.2}$$

where δV_o is the desired voltage ripple. The basic principle of the converter is to behave as either a buck or a boost depending on the desired output. The converter has four switches, and the dynamics of the converter will change by turning the switches ON and OFF. The relationship between the input and output voltage for the FSIBB converter can be expressed as

$$V_i = \frac{D}{1-D} V_o \tag{2.3}$$

where D denotes the duty cycle and generally has a value between [0,1]. The converter has two legs, one on the input side of the inductor and the other on the output side. The converter can work with different combinations of switches, such as when S_1, S_4 are ON and S_2 and S_4 OFF the converter will behave as a synchronous boost converter. Similarly, when S_2 and S_3 are ON the converter will act as buck converter. These are two main operating modes; however, it can operate by putting S_1

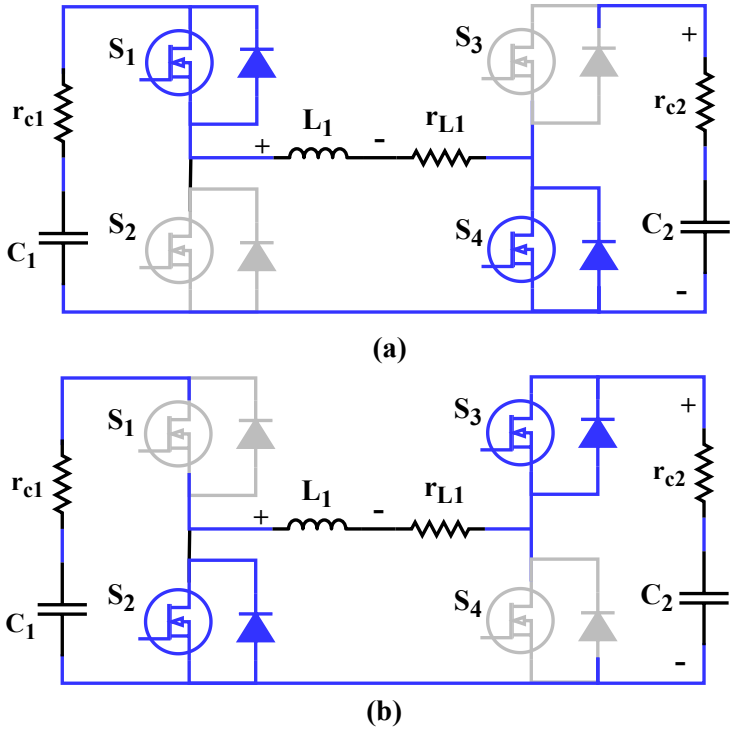

Figure 2.2: FSIBB modes of operation

and S_3 on, which is called a bypass mode and can be used when the desired output voltage is very close to the input voltage. The switching states are better illustrated in fig 2.2.

Fig 2.2, depicts the two modes of operation and the equivalent circuits of each one. The mathematical model of the system is developed using these equivalent circuits. The basic idea is to switch S_1 and S_4 between ON and OFF and S_2 and S_3 will behave opposite.

Applying basic circuit laws on fig 2.2 (a) we can derive the differential equations such as

$$\begin{cases} L_1 \frac{di_L}{dt} = -\frac{r_i r_{c1} + r_{L1} R_1}{R_1} i_L + \frac{r_i}{R_1} V_{c1} + \frac{r_{c1}}{R_1} V_i \\ C_1 \frac{dV_{c1}}{dt} = -\frac{r - i}{R_1} i_L - \frac{1}{R_1} V_{c1} + \frac{1}{R_1} V_i \\ C_2 \frac{dV_{c2}}{dt} = -\frac{1}{R_2} V_{c2} \end{cases} \tag{2.4}$$

Similarly, for the sub-circuit presented in fig 2.2 (b) we get

$$\begin{cases} L_1 \frac{di_L}{dt} = -\frac{R}{R_2} V_{c2} + \frac{R_2 r_L + R r_{c2}}{R_2} i_L \\ C_1 \frac{dV_{c1}}{dt} = -\frac{1}{R_1} V_{c1} + \frac{1}{R_1} V_i \\ C_2 \frac{dV_{c2}}{dt} = -\frac{1}{R_2} V_{c2} + \frac{R}{R_2} i_L \end{cases} \tag{2.5}$$

where $R_1 = r_{c1} + r_i$ and $R_2 = R + r_{c2}$. By combining eq.(2.4) and eq.(2.5) the model expression can be written as,

$$\begin{cases} \dot{x} = A.x + B.u \\ \dot{y} = C.x + D.u \end{cases} \tag{2.6}$$

where the $x = [i_{L1}, V_{c1}, V_{c2}]$ are the states of the system and $y = [i_{L1}, V_{c1}, V_{c2}, V_o]$ are the output of the dynamical system. For the averaged model over one switch period can be calculated by finding the average matrices A, B, C, D by using the following expressions

$$\begin{cases} A_{average} = A_{ON}.D + A_{OFF}.(1-D) \\ B_{average} = B_{ON}.D + B_{OFF}.(1-D) \\ C_{average} = C_{ON}.D + C_{OFF}.(1-D) \\ D_{average} = D_{ON}.D + D_{OFF}.(1-D) \end{cases} \tag{2.7}$$

For simplification of control derivation let's use generic expressions for the states and constants such as

$$\Big\{ x_1 = i_{L1} \ , x_2 = V_{c1}, \ x_3 = V_{c2}$$

Finally, the averaged state space model over one switching period can be expressed as;

$$\dot{x}_1 = (t_1 x_1 + t_2 x_2 + t_3 V_i + t_4 x_3) * u - t_5 x_1 - t_6 x_3 \tag{2.8}$$

$$\dot{x}_2 = t_7 x_1 u - t_8 x_2 + t_9 V_i \tag{2.9}$$

$$\dot{x}_3 = t_{10} - t_{11} x_3 - t_{12} x_1 u \tag{2.10}$$

where $t_i, i = 1...12$ denotes the constant values which are the combination of resistance, inductance, and capacitance as shown in eq.2.4 and eq. 2.5. The dynamic system expressed above is used to derive the control law for current and voltage control of ESD. The control design methodology is well explained in the next section.

2.2.2 Control Structure for FSIBB

A proper switching controller is very important for efficient energy conversion and current and voltage regulation. The main problems of the FSIBB converter are highlighted in the section above. This section proposes the power rate reaching law-based sliding mode controller with a PI regulator for the current and voltage control. The control problem is formulated as a current control problem instead of a direct voltage control problem to overcome the non-minimum phase behavior. Moreover, the sliding mode control has the advantages of finite time convergence, robustness,

and the ability to handle the nonlinear nature of power converters.

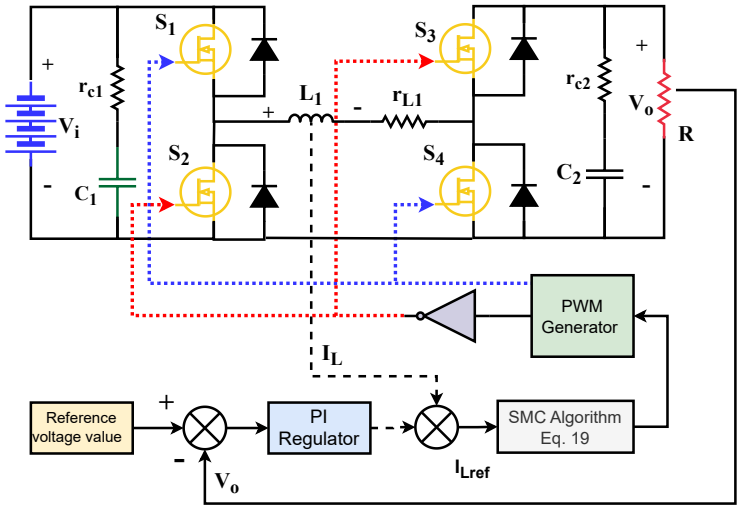

Figure 2.3: Proposed closed-loop control schematic

Fig. 2.3 presents the block diagram of the closed-loop system. The first step in designing the tracking controller is to define the error equations which represent the difference between desired and actual values. The error equation can be defined as

$$e_1(t) = V_o - V_{oref} \tag{2.11}$$

$$e_2(t) = x_1 - x_{1ref} \tag{2.12}$$

The e_1, e_2 denotes the difference between the desired voltage and current concerning the actual values. The PI regulator generates the current reference for indirect regulation of output voltage. The following mathematical expression can be used to represent the regulator.

$$x_{1ref} = K_i e_1(t) + K_p \int_0^t e_1(t)dt \tag{2.13}$$

where K_i and K_p are the proportional and Integral gains of the controller. This portion represents the regulator for the outer loop control, for inner loop sliding mode control, is designed by using the error equation given in eq. (2.12), the sliding surface can be written as

$$S = c_1 e_2(t) \tag{2.14}$$

where c_1 is the constant gain parameter. The idea is to put the error equation on the sliding surface with a gain value so that the error can converge to the sliding surface. The gain parameter is added to control the convergence rate. The goal is to minimize the error ($e_i = 0$). Let's assume

$$S = 0 \;\Rightarrow\; \dot{S} = 0 \tag{2.15}$$

Taking time derivative of eq.(2.14) and putting the value of $\dot{S}$ we get

$$0 = c_1 \dot{e}_2 \tag{2.16}$$

where

$$\dot{e}_2 = \dot{x}_1 - \dot{x}_{1ref} \tag{2.17}$$

Substituting the value of $\dot{e}_2$ and solving this for nominal control law u

$$u_{nominal} = \frac{t_5 x_1 c_1 + t_6 x_3 c_1 + c_1 x_{1ref}}{c_1(t_1 x_1 + t_2 x_2 + t_3 V_i + t_4 x_3)} \tag{2.18}$$

This control action is responsible for bringing the error to zero (Sliding surface). The power rate reaching law is proposed for the switching control, defined as

$$u_s = -a_1 \, |S|^{\alpha} \, sign \, (\frac{S}{\rho_1}) \tag{2.19}$$

$$u = u_{nominal} + u_s \tag{2.20}$$

where a_1,σ_1, α are the constant parameter of the switching function. Usually, the values of σ_1 and α are selected between 0 and 1. The power rate reaching law also minimizes the chattering effect of conventional switching control. u is the final control input of the converter in the form of a duty cycle.

2.2.3 Stability Analysis

The outer control loop is just a regulator, the inner controller is responsible for the ON and OFF of the switches by closing the loop. So the stability analysis of the designed nonlinear controller is very important. Let's take the Lyapunov candidate function as

$$V = \frac{1}{2} S^2 \implies \dot{V} = S\dot{S} \; where \; \dot{S} = c_1 e_2 \dot{e}_2$$

putting value of e_2 and u from eq.(2.20) the time derivative of the Lyapunov function will be

$$\dot{V} = S(-a_1 \, |S|^{\alpha} \, sign \, (\frac{S}{\rho_1})) \tag{2.21}$$

where

$$S \, sign \, (\frac{S}{\rho_1}) \geq 0 \; for \; all \; S \in R$$

$$a_1 |S|^{\alpha} \geq 0$$

So this concludes that

$$\dot{V} < 0 \; for \; all \; S \in R \tag{2.22}$$

This analysis shows that the closed-loop controller is globally stable. The Lyapunov function is an energy-like function and its negative time derivative shows that energy

decreases with time and the system will converge to its equilibrium points.

2.2.4 Simulation Results of FSIBB Converter

Simscape Electrical in MATLAB/Simulink 2020(a) is used to simulate the FSIBB converter. The closed-loop system is simulated for 1 sec with a step time of $1e^{-}5$. A 48 V battery pack with a rating of 50 AH is used at the input of the power converter. Duty cycles are generated by a non-linear sliding mode controller using a PWM generator with a switching frequency of 100 KHz. The main control objectives are to regulate the current and voltage to their desired value in both buck and boost modes. fig. 2.4 shows the output voltage V_o response, it can be seen that the input voltage of the battery is 48 V as shown in the blue dotted line where the output voltage is tracking its reference value. The desired output voltage is 25 V for 0.5 s and after that the reference changes to 65 V, the values represent the buck and boost modes, respectively. The simulation result showed that the controller is good enough to provide a smooth shift between the buck and boost modes.

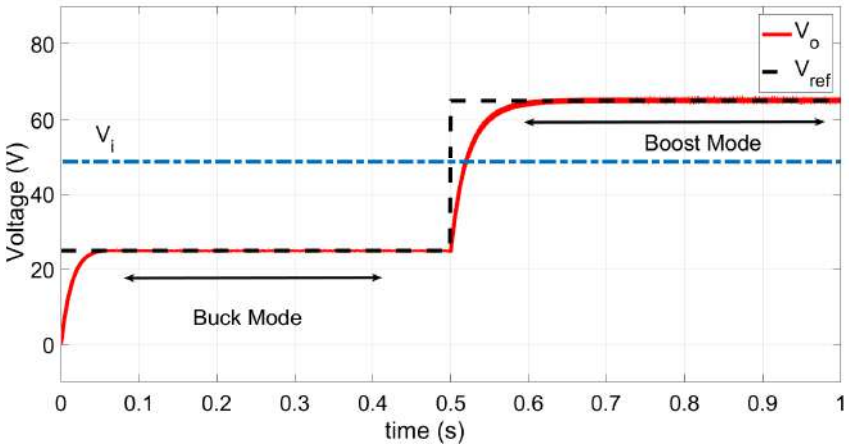

Figure 2.4: Output voltage v_o response

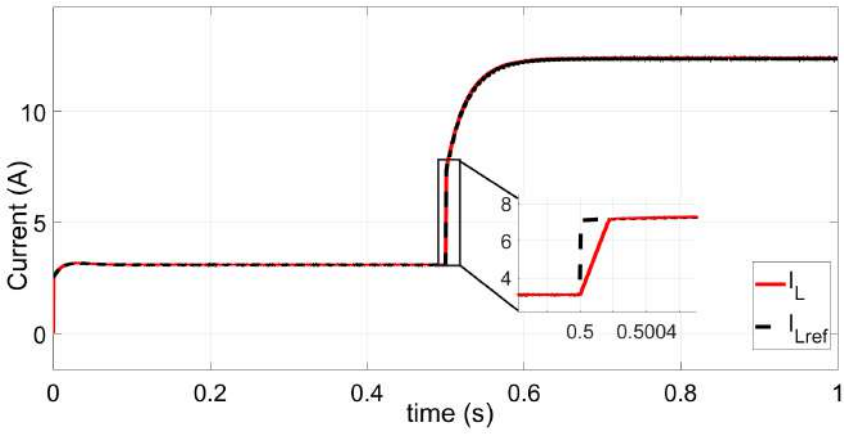

Figure 2.5: Inductor current i_L response

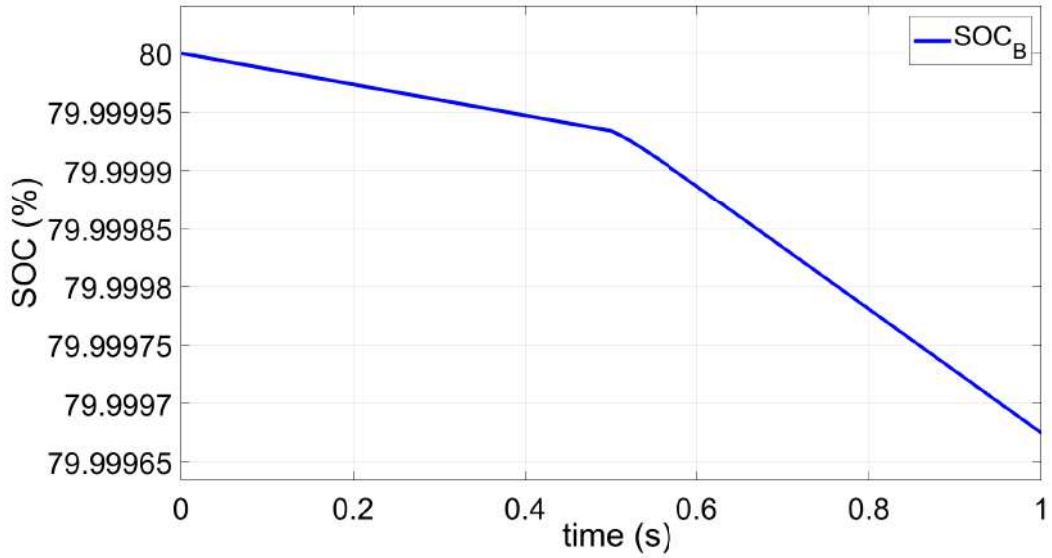

Figure 2.6: Battery state of charge (SoC)

The second loop of current tracking is presented in fig. 2.5. The inductor current reference is generated by the PI regulator and is followed by the sliding mode controller. It can be observed that i_L is tracking its reference value; however, the transient response of the controller can be depicted through the zoomed-in portion of the fig. 2.5. The state of charge (SoC) of the battery shows the charging and discharging rate and available charge in the battery. In Fig. 2.6, it is clear that in boost mode the battery discharges fast due to the high requirement of output voltage and current, respectively.

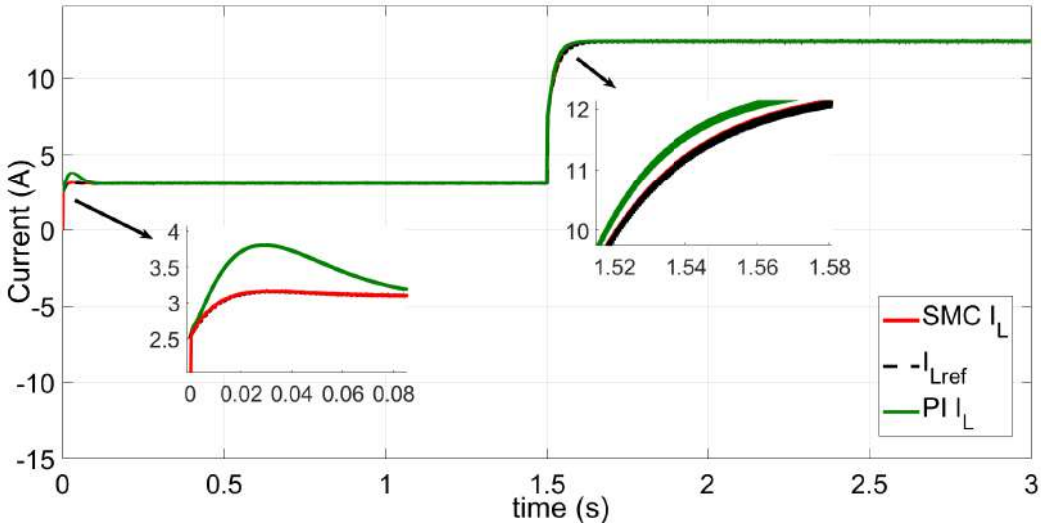

Figure 2.7: output voltage regulation comparison with PI controller

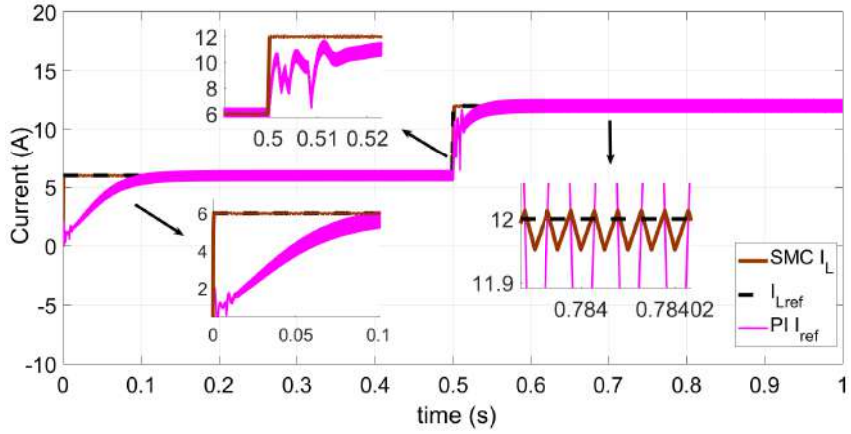

Figure 2.8: Direct current control comparison

2.2.5 Real-time Experimental Results for FSIBB

Finally, to validate the proposed method in a real-time typhoon HIL 404 device, the FSIBB converter with the non-linear controller is used. The closed-loop system is designed using a schematic editor in the typhoon control center. Afterward, the system is validated and implemented in real time using an HIL 404 device. The results are analyzed through HIL SCADA, SCADA is a panel in a typhoon control center designed to analyze and capture the real-time results.

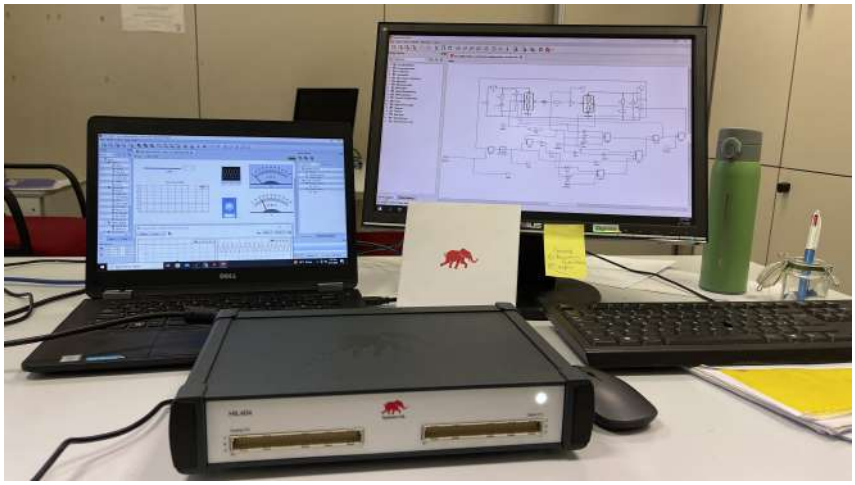

Figure 2.9: Hardware-in-loop Setup

fig. 2.9 shows the HIL step-up picture, the schematic editor is validated on the desktop screen and then running on HIL 404 which is also visible in the image. The laptop is used to run HIL SCADA and save the results moreover, HIL SCADA also provides control of simulation parameters in real-time. Fig. 2.10 and fig.2.11 are the real-time response of output voltage and inductor current, respectively.

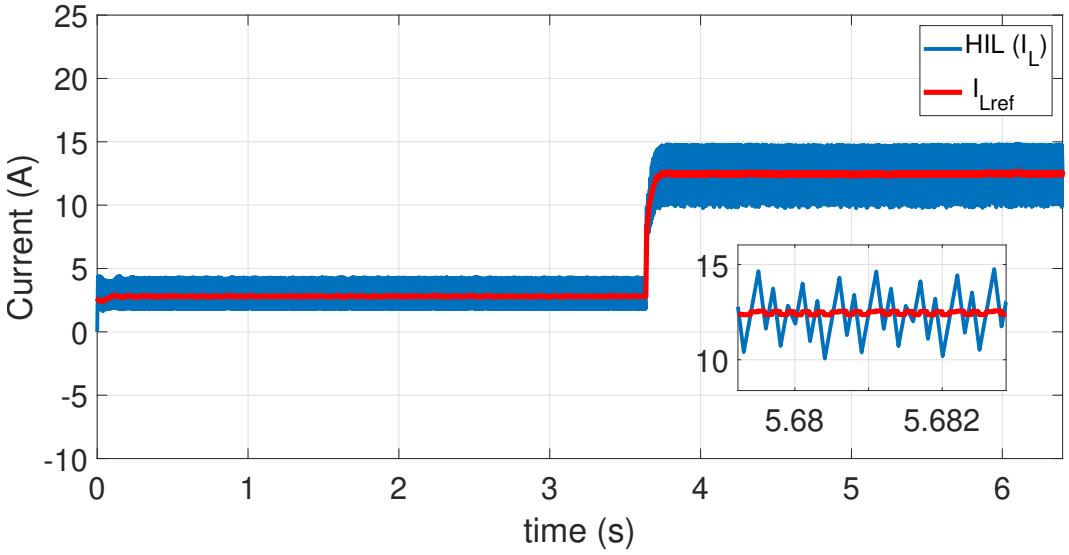

Figure 2.11: Inductor current i_L response (HIL)

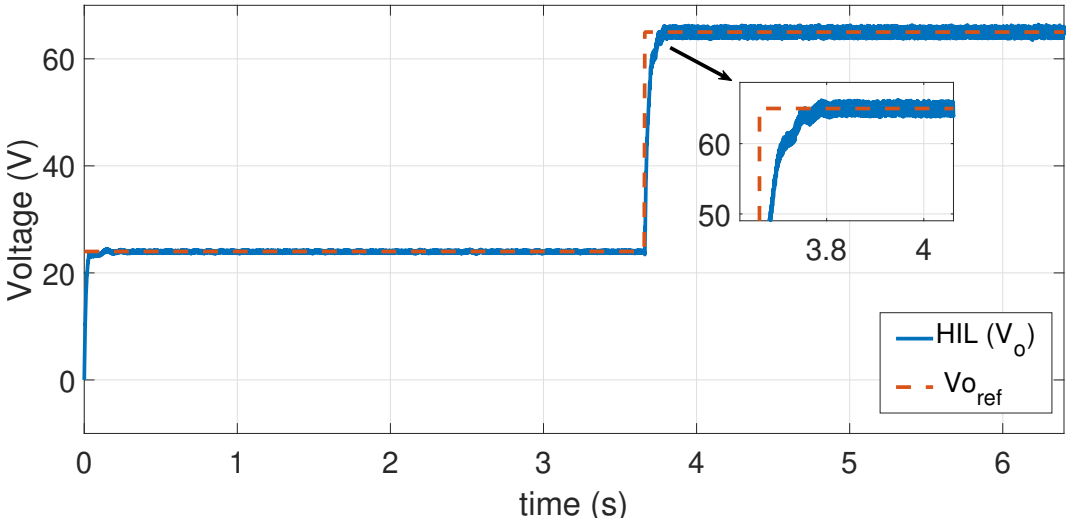

Figure 2.10: Output voltage V_o response (HIL)

It is clear from the results that the proposed controller performed up to the mark in real-time and both voltage and current are tracking their desired values. Fig. 2.12 shows the error value in real-time, initially error has some after the control action is applied the error is converged to zero. The dip in the error graph represents the step change and phase shift however, it can be observed that control is efficient enough to stabilize the system again by making error 0 approximately. In HIL simulation, the electrical circuit of the power converter is emulated on HIL 404 while the controller part is simulated on the host processor. The PWM signal is used to control the two legs of the FSIBB converter with a switching frequency of 100 KHz. The simulation parameters for the FSIBB converter and the gain parameters for the dual-loop nonlinear controller are given in Table 2.1.

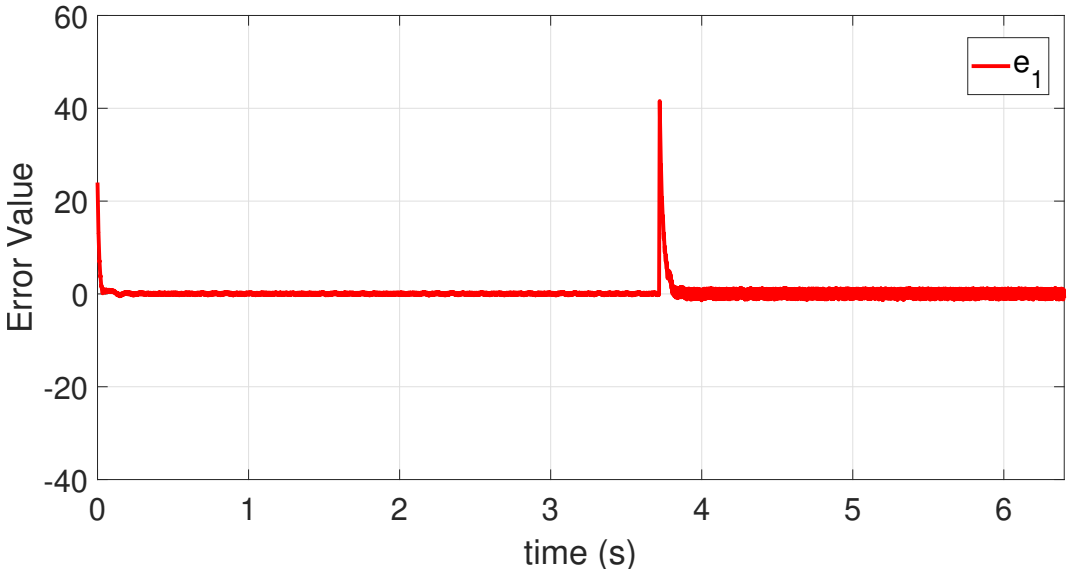

Figure 2.12: Error (e_2) value (HIL)

Table 2.1: System and simulation parameters

Parameter	**Values**
Inductors L_1	22 μH
Capacitance C_1, C_2	650 μF
Internal Resistance r_{c1}, r_{c2}, r_{L1}	220, 220, 1.4 mΩ
Input Voltage V_i	48 V
controller Parameters	
K_p , K_i	0.1, 10
c_1, a_1	1, $1e^5$
α, $r\rho_1$	0.5, 0.5

2.3 Interleaved FSIBB Converter for ESSs

2.3.1 Mathematical Modeling and Analysis

The four-switch single-inductor buck-boost is a well-known topology of the DC-DC converter, which is shown in Fig. 2.13 in its 2-stage interleaved version. Considering a single 4-switch cell, e.g. the stage based on switches S_1, S_2, S_3, S_4, the PWM signals applied in S_2 and S_3 are supposed to be in the opposition phase concerning those applied in S_1 and S_4. The DC output voltage is therefore ideally represented, without considering the parasitic elements such as the equivalent series resistances, by the following equation:

$$v_o = v_i \frac{d}{1-d} \tag{2.23}$$

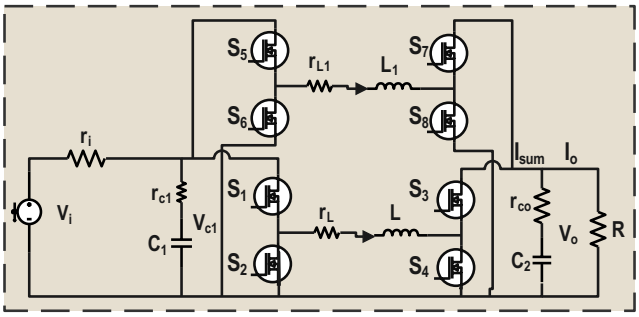

Figure 2.13: Proposed Converter Topology

where d is the duty-cycle concerning switches S_2 and S_3, for which the conduction time is defined as T_{on}:

$$d = \frac{T_{on}}{T_{sw}} \tag{2.24}$$

where T_{sw} is the switching period. Considering the ideal case for which the power losses are null, the average DC gain is equal to the inverse of the voltage gain, so that the following arises:

$$i_o = i_i \frac{1-d}{d} \tag{2.25}$$

where i_o and i_i are the average output and input current respectively. Considering the inductance current, the following relationship occurs between the average inductance current I_L and the output current:

$$i_L = \frac{i_o}{1-d} \tag{2.26}$$

In the case of parallel interleaved stages, the average inductance current on the single generic i stage is related to the average output current as in the following:

$$i_{Li} = \frac{i_o}{n(1-d)} \tag{2.27}$$

According to (5), with the same value of duty-cycle, the average current is equally shared among all the n inductances. If the n-stage converter is controlled using multiphase PWM, this means that the PWM carrier phases are equally shifted, so that the time shift T_{shift} between two consecutive output current pulses is:

$$T_{shift} = \frac{T_{sw}}{n} \tag{2.28}$$

Considering the single i stage, the output current is pulsating, since it flows through the switch S_3.Therefore the time when there is current on switch S_3 is T_{off}, defined as the following:

$$T_{off} = (1-d)T_{sw} \tag{2.29}$$

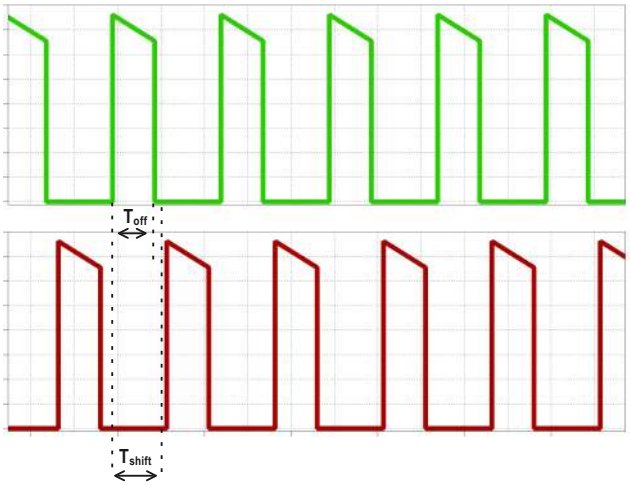

Figure 2.14: Output current waveforms in a 2-stage configuration: in this specific case I_{sum} sometimes is zero

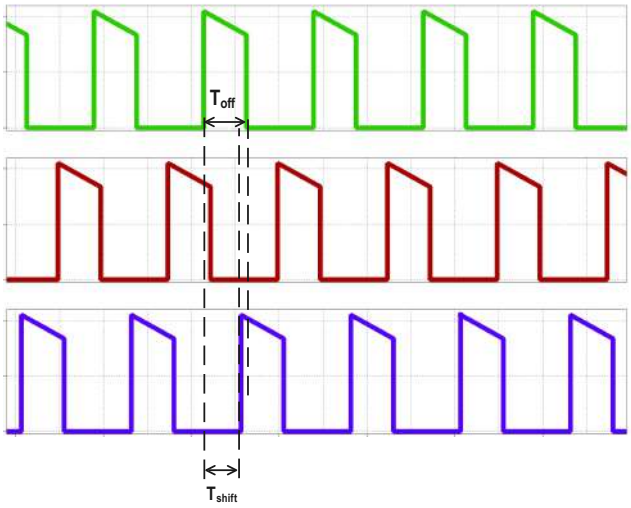

Figure 2.15: Output current waveforms in a 3-stage configuration: in this case I_{sum} is never zero

In Figures 2 and 3, the output current waveforms of the single stages are shown in simulation considering a 2-stage and a 3-stage configuration respectively, where T_{off} and T_{shift} are highlighted, supposing the same D for both the cases. In the 2-stage configuration, the sum of the current values is zero during the time intervals between T_{off} and T_{shift}. The following arises:

$$T_{off} < T_{shift} \tag{2.30}$$

In the 3-stage configuration the mentioned sum never goes to zero, since the inequality is inverted:

$$T_{off} > T_{shift} \tag{2.31}$$

By taking as an example the afore-mentioned 2-stage and 3-stage cases, it is possible to generalize the equation representing a threshold limit, as in the following:

$$T_{off} = T_{shift} \tag{2.32}$$

According to (8), it is possible to obtain the duty-cycle value under which the output sum current I_{sum} never goes to zero and corresponds to a threshold conduction time $T_{on,th}$, referenced as D_{th}:

$$T_{(on,th)}/(T_{sw}) = d_{th} = (n-1)/n \tag{2.33}$$

The output current I_{sum} is not zero if the following inequality occurs, according to (10):

$$d < (n-1)/n \tag{2.34}$$

thus, multiphase interleaving brings a substantial benefit if (12) occurs. Arising from that, a minimum number of stages can be obtained depending on the duty cycle, and therefore on the transferred power, thus enforcing the reason to use the multiphase interleaving technique in the specific here proposed topology of the DC-DC converter. In the following, the nonlinear control strategy implements the current balance among the inductors of the different interleaved stages.

2.3.2 Control Structure for IFSIBB

In the Interleaving converter topology, the control plays an important role in balancing the current between different power converter phases. This section advises a direct Lyapunov-based nonlinear controller for two two-phase bi-directional buck-boost converter. The dual-loop controller controls both the output voltage and inductor currents in different legs. The average state-space model of the FSIBB converter for a single stage can be expressed as follows:

$$\begin{cases} \dot{x}_1 = \left((\frac{r_i r_{c1} + r_L R_1}{R_1 L} + \frac{R_2 r_L + R r_{co}}{R_2 L}) x_1 + \frac{r_{in}}{R_1 L} x_2 + \right. \\ \qquad \left. \frac{r_{c1}}{R_1 L} V_{in} + \frac{R}{R_2 L} x_2 \right) \cdot d - \frac{R}{R_2 L} x_2 - \frac{R_2 r_L + R r_{co}}{R_2 L} x_1 \\ \dot{x}_2 = \frac{1}{R_1 C_1} V_{in} - \frac{1}{R_1 C_1} x_2 - \frac{r_i}{R_1 C_1} x_1 \cdot d \\ \dot{x}_3 = \frac{R}{R_2 C_o} x_2 - \frac{1}{R_2 C_2} x_3 - \frac{R}{R_2 C_2} x_1 \cdot d \end{cases} \tag{2.35}$$

where

$$R_1 = r_i + r_{c1},\ R_2 = R + r_{co}$$

$r_i, r_{c1}, r_L, r_{co}, and\ R$ represent the value of input resistance, the internal resistance of the input capacitor, the internal resistance of the inductor, the internal resistance

of the output capacitor, and load resistance respectively. Whereas v_{in} and d are the input voltage and duty cycle of the converter. The states of mathematical can be illustrated as:

$$[x_1, x_2, x_3] = [i_L, v_{c1}, v_o]$$

i_L, v_{c1}, v_o are the inductor current, voltage across the input capacitor, and output voltage. For two-stage FSIBB the mathematical expression for output current can be defined as:

$$i_o = \sum_{n=1}^{i} i_{Ln} \tag{2.36}$$

where $i = 1, 2$ in the case of two phases and can be enhanced for n number of phases. The main control objective is to design a stability-centric control while balancing the current between two legs. For the dual-loop controller, the outer loop is designed for voltage tracking and the inner loop is responsible for current balancing and tracking through two inductors. The error function for the voltage loop is expressed as below:

$$e_1 = (x_{3ref} - x_3) \tag{2.37}$$

By using the PI regulator, the reference value for the current x_1 can be defined as follows:

$$x_{1ref} = K_i(x_{3ref} - x_3) + K_p \int_0^t (x_{31ref} - x_3)dt \tag{2.38}$$

where K_p and K_i are the gains of the PI regulator. The error equation for the inner loop then takes the following form:

$$e_2 = x_{1ref} - x_1 \tag{2.39}$$

To evaluate the system behavior the time derivative of the error signal is very important. Taking the time derivative of the error function, we get:

$$\begin{aligned} \dot{e}_2 = \dot{x}_{1ref} - \Bigg((\frac{r_i r_{c1} + r_L R_1}{R_1 L} + \frac{R_2 r_L + R r_{co}}{R_2 L}) x_1 + \frac{r_{in}}{R_1 L} x_2 + \\ \frac{r_{c1}}{R_1 L} V_{in} + \frac{R}{R_2 L} x_2 \Bigg) \cdot d - \frac{R}{R_2 L} x_2 - \frac{R_2 r_L + R r_{co}}{R_2 L} x_1 \end{aligned} \tag{2.40}$$

To design the Lyapunov-based controller, let's assume a Lyapunov candidate function based on an error function as:

$$\zeta(e_2) = \frac{1}{2} e_2^2 \tag{2.41}$$

Taking the time derivative of the Lyapunov function will return:

$$\dot{\zeta}(e_2) = e_1(\dot{e}_2) \tag{2.42}$$

According to the Lyapunov theory, the system is considered stable when the time derivative of the Lyapunov function is negative definite, by assuming

$$\dot{e}_2 = -K_1 e_2 \tag{2.43}$$

where K_1 is the positive gain value. Putting this value in (2.42) we get:

$$\dot{\zeta}(e_2) = e_1(-K_1 e_1) \implies -K_1 e_1^2 \tag{2.44}$$

The equation shows that using the assumption the time derivative of the Lyapunov function is negative definite for all error signal values. Finally, the control law is calculated based on this assumption by comparing (2.40) and (2.43) and solving in for d.

$$d = \frac{\dot{x}_{1ref} + K_1 e_1 - \frac{R}{R_2 L} x_2 - \frac{R_2 r_L + R r_{co}}{R_2 L} x_1}{\left((\frac{r_i r_{c1} + r_L R_1}{R_1 L} + \frac{R_2 r_L + R r_{co}}{R_2 L}) x_1 + \frac{r_{in}}{R_1 L} x_2 + \frac{r_{c1}}{R_1 L} v_{in} + \frac{R}{R_2 L} x_2 \right)} \tag{2.45}$$

Hence, the final control input D is applied to the switching gates of the converter. The derivation is for a single stage; the control input for the second stage can be derived through the same method with a phase shift mathematical expressed as:

$$\phi_n = (n-1).\frac{360}{N} \tag{2.46}$$

where ϕ is the phase shift and n is the considered phase. N represents the total number of the stage. The final control input for n^{th} stage can be depicted as:

$$d_n = d + \phi(n) \tag{2.47}$$

The closed-loop control structure is given in the fig. 2.16 as below:

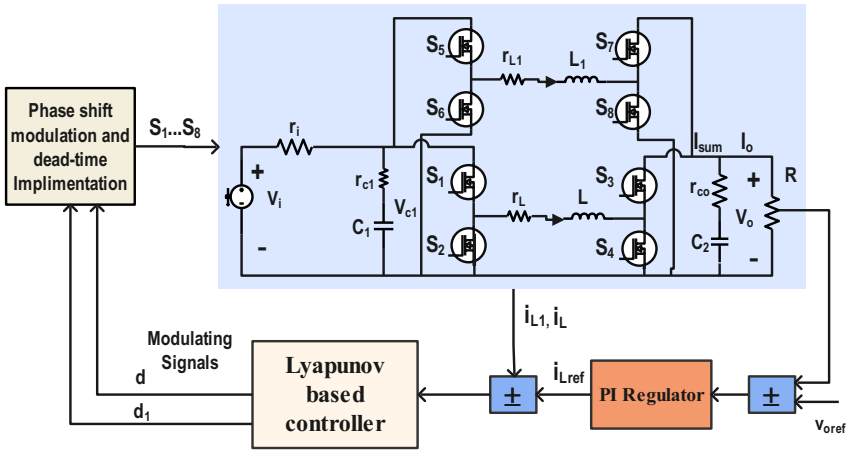

Figure 2.16: Closed-loop diagram of control structure

Table 2.2: System and Simulation parameters of IFSIBB

Parameter	**Values**
Inductors L_i	5 μH
Capacitance C_1, C_2	33 μF
Internal Resistance r_{c1}, r_{co}, r_{Li}	0.9, 1.9, 1 mΩ
Input Voltage V_i	35 V
Load Resistance R	5 Ω
Controller Parameters	
K_p , K_i	0.1, 10
Nonlinear Control parameter K_1	$1e^4$
Phase shift ϕ_1	180
Switching Frequency	$200kHz$

2.3.3 Simulation Results for IFSIBB

The two-stage FSIBB converter with a closed-loop controller is simulated in PLECS software. The simulation results are presented in the fig. 2.17 and the zoomed graphs are shown in Fig. 2.18. The simulation parameters are given in the table below:

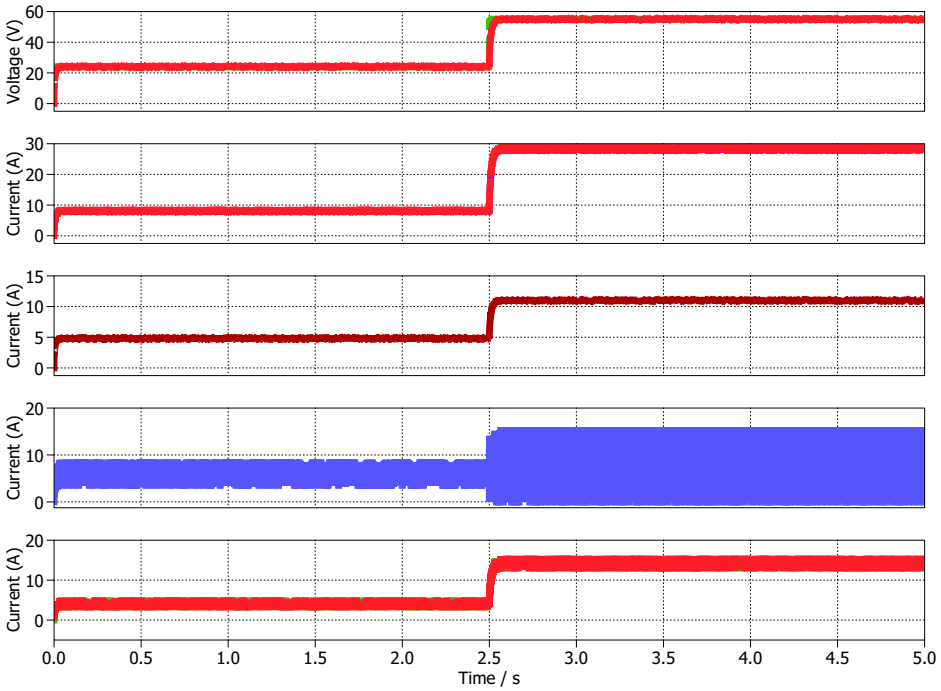

Figure 2.17: The closed-loop voltages and current response of the FSIBB Converter topology

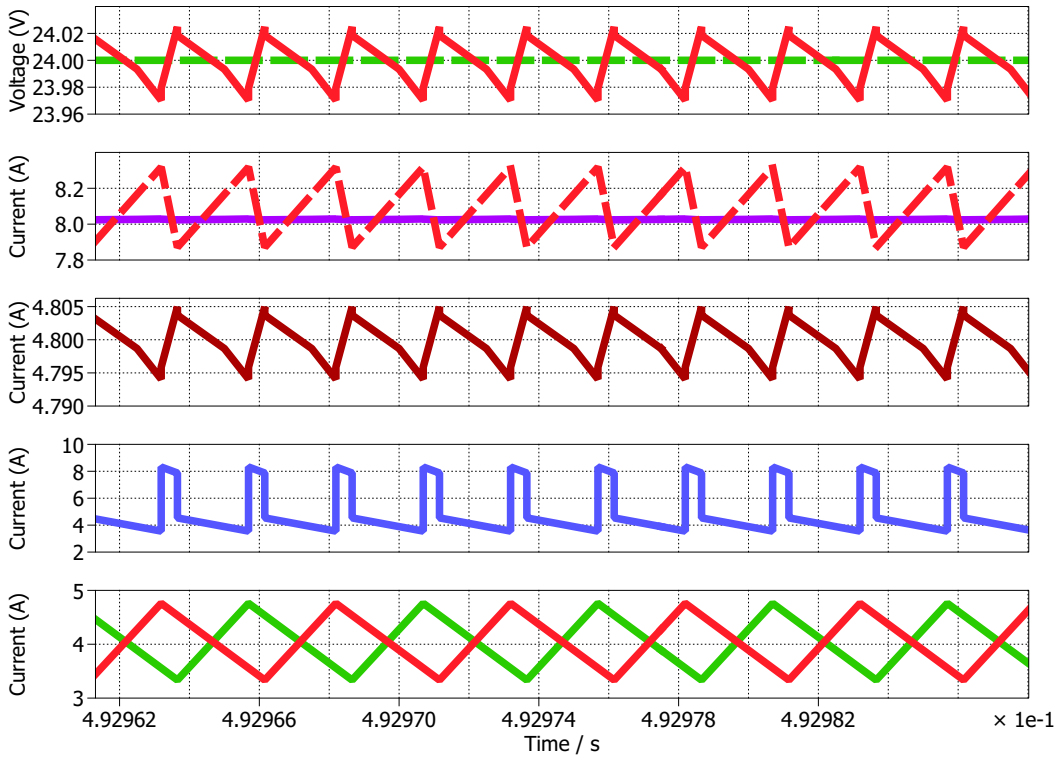

Figure 2.18: The Zoomed-in graph representation of voltage and currents waveforms

The fig. 2.17 has five plots of output voltage, summed inductors current, output current, total current before filter, and the current through each inductor, respectively. The results are shown to prove the proposed controller by showing the voltage and current tracking to their respective reference values and the output ripple behavior in a 2-stage FSIBB converter. The DC input voltage is $35V$ and the output voltage is tracked at 24 V and 55 V, respectively. The idea is to show the buck and boost operating mode of the power converter. It can be observed that the proposed control action tracks the voltage and current reference, and the trend of the voltage and current states can be studied in detail from the zoomed-in figure.
In fig. 2.18 the first plot shows the voltage response combined with the reference trajectory shown with a green-colored line, the output voltage is tracking the requested value with low ripple values. The second graph validates the current sharing control as the proposed nonlinear control action successfully achieves the reference current value requested by the out-loop. Similarly, the output current ripples show the advantage of a multi-stage FSIBB converter and also confirm the analysis carried out for multi-stage FSIBB. Lastly, the individual inductor currents $I_{1,2}$ are plotted together and a symmetric phase shift of 180^o can be observed through the last zoomed-in graph.

2.3.4 Real-time Experimental Results for IFSIBB

Controller Hardware in the Loop (C-HIL) tests are conducted to evaluate the real-time performance of the proposed controller method. Fig. 2.19 shows the C-HIL setup. The test setup can be explained as follows: 1. Host PC with SCADA panel, 2. Typhoon 404 device for real-time emulation of the power stage, 3. TI 28379D microcontroller for rapid control prototyping, 4. Oscilloscope for data acquisition. The clock frequency of the TI control board is 190 MHz and the switching frequency is considered to be 10 kHz. The converter parameters are recalculated for the 10 kHz switching frequency.

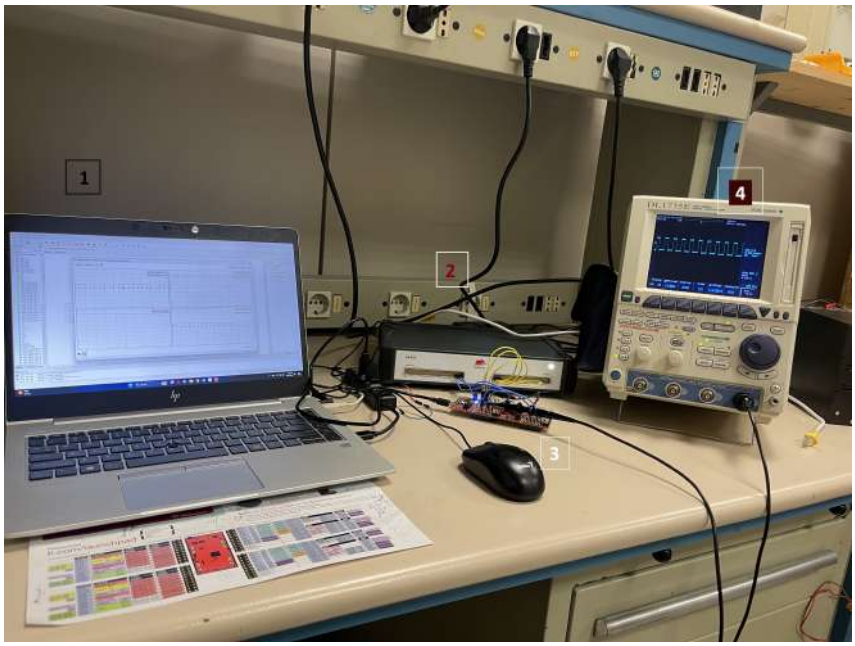

Figure 2.19: CHIL test Setup

The proposed control strategy is implemented using a TI microcontroller and tested with a typhoon HIL. The two cases are investigated to validate the control performance. In case one the output voltage reference is varied for three different values to see the transition between buck and boost mode while the input voltage is $32V$. Figs. 2.20 and 2.21 present the response of the output voltage and the sum of the inductor currents, respectively. The proposed controller can efficiently handle the mode transition and track the voltage reference. In the second case, the controller has been tested against varying load conditions.

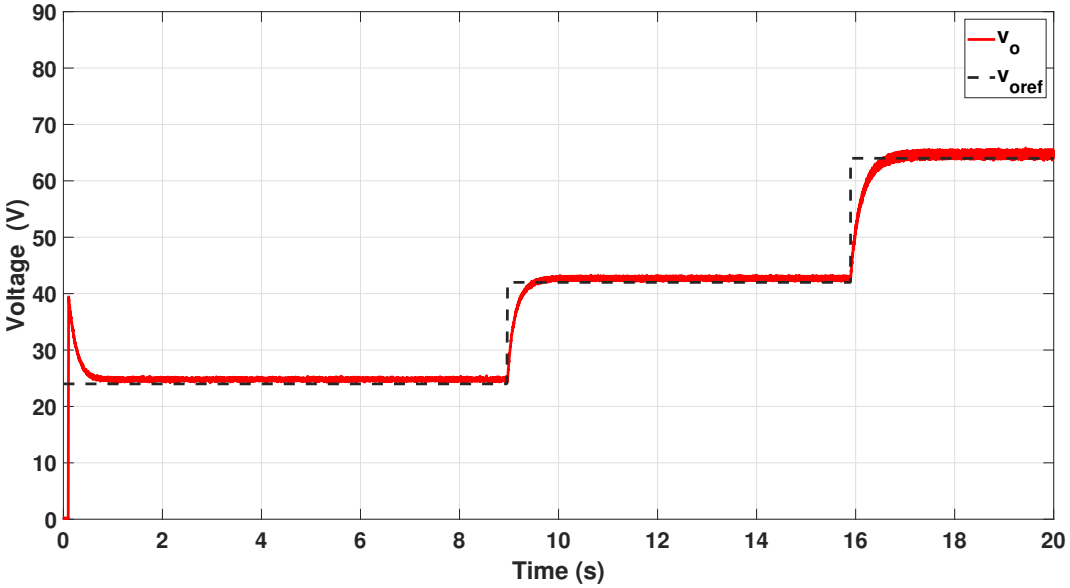

Figure 2.20: Case 1: Output Voltage response

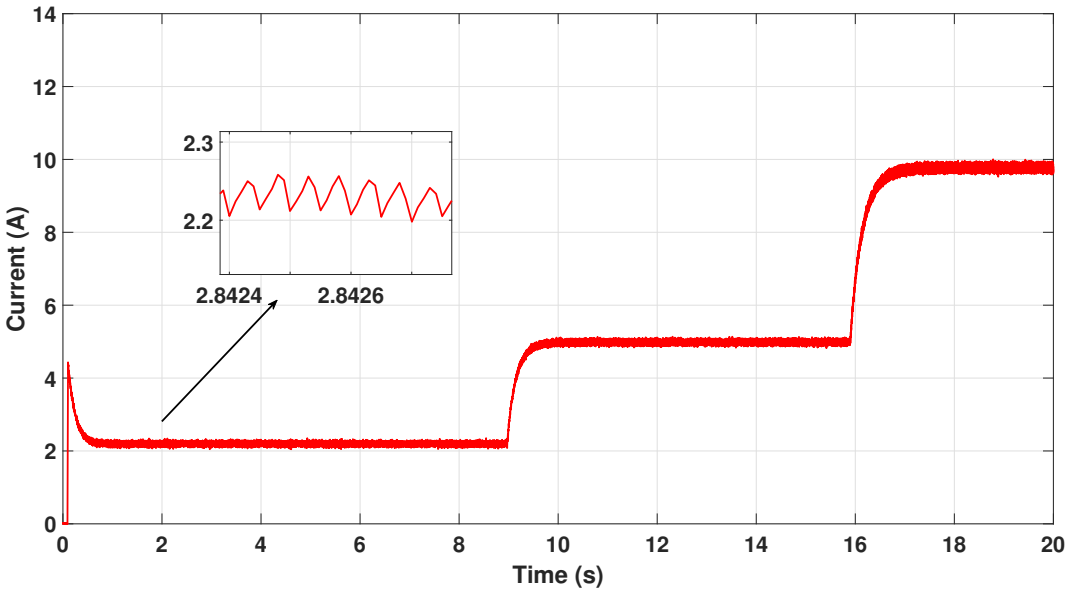

Figure 2.21: Case 1: Sum of inductor currents

The load power is varied between $250W$ and $300W$. The results are presented in fig. 2.22, 2.23 and 2.24, respectively. It can be observed that the output voltage is regulated to the desired reference of 65 V irrespective of the load changes, however, the small overshoot and undershoots can be seen due to the step change in load. The reference current is also achieved by balancing the current ratio between two stages, and the phase shift between the two stages can also be analyzed in the zoomed-in part of Fig. 2.24.

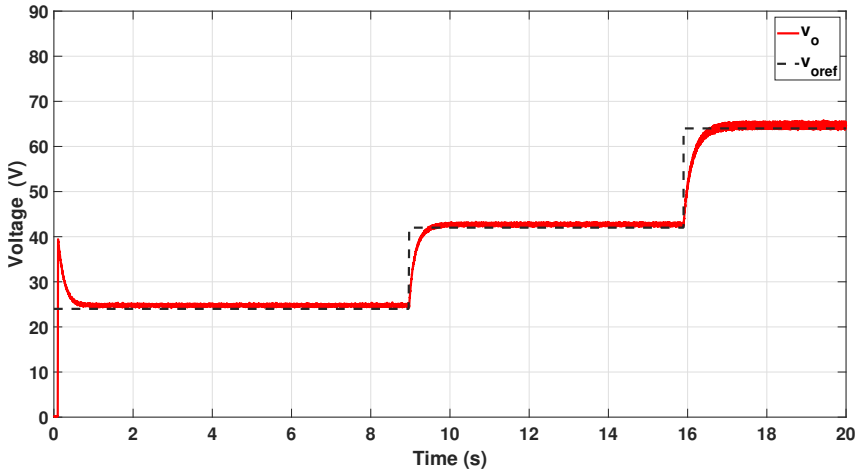

Figure 2.22: Case 2: Output Voltage response

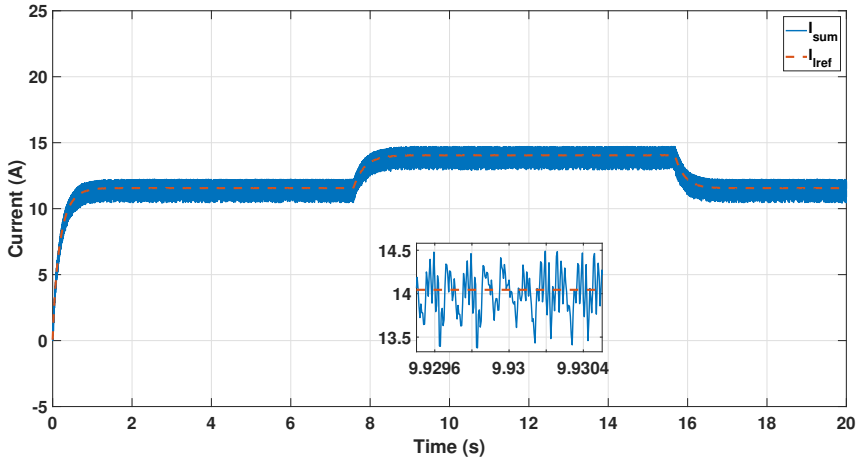

Figure 2.23: Case 2: Current reference tracking

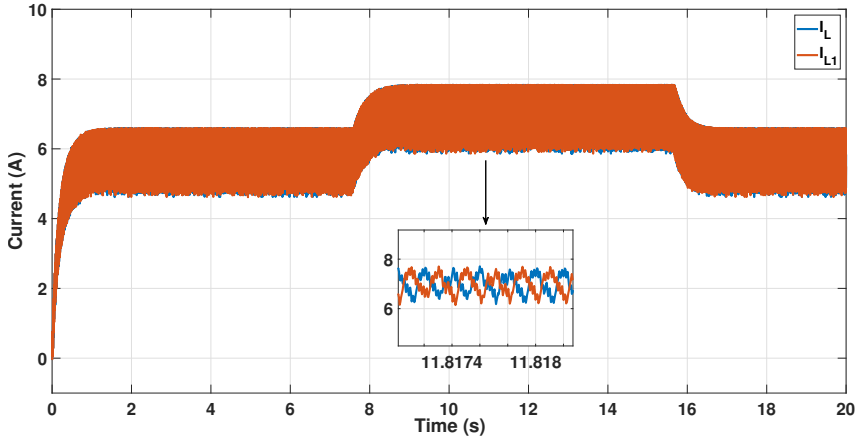

Figure 2.24: Case 2: Phase shifted currents of each inductor

2.4 Comparative Analysis

A comparative analysis is performed with the state-of-the-art linear PI controller, the first dual loop PI controller, and compared with the proposed strategy, and then direct current control PI is compared with direct current sliding mode control. The comparison is summarized in table 2.3. Figs.2.7 and 2.8 are the methodology

Table 2.3: Comparative analysis of proposed controller

Sr.	**Rise time**	**Overshoot/undershoot**	**Error**
PI control	9.915 ms	7.2% ,34.5%	0.512
Proposed Method	223.5 *us*	0.85%, 1.99%	0.041

proposed for comparative graphs with a state-of-the-art PI controller. The response of both controllers is plotted with the reference value to show the difference. It is evident that the proposed method has a fast rise time, fast convergence, fewer overshoots/undershoots, and negligible steady-state (S.S) error.

2.5 Summary

- The Importance of ESSs in the MG and the e-mobility sector is highlighted,
- A Brief introduction summarizing the latest literature review of the ESSs integration and controls is presented,
- Two converter topologies FSIBB and IFSIBB are studied for the bidirectional power flow,
- Nonlinear control-based dual-loop current and voltage control are derived for power converters
- The proposed methods are validated through numerical simulations and Real-time experimental tests.

2.6 Conclusion

Power converters are essential for energy storage devices as they provide a flexible control system. This chapter presents a study of two converters: a dual loop sliding mode controller with a PI regulator for the FSIBB converter and a two-stage interleaving FSIBB converter topology, each evaluated for their potential applications in ESS for modern microgrids. The dual-loop sliding-mode controller efficiently

operates the FSIBB converter in buck and boost modes. Lyapunov stability analysis confirmed the global stability of the closed-loop controller. Simulation using Simscape in MATLAB/Simulink with a 48 V battery pack demonstrated the effectiveness of the proposed control strategy. The comparative analysis highlighted the advantages of the dual loop controller over a traditional PI controller, and the real-time testing through HIL validated the theoretical design. This study underscores the potential of advanced nonlinear control algorithms to enhance stability and efficiency in power converters. The two-stage interleaving FSIBB converter topology was analyzed for its ability to integrate ESS within microgrids, focusing on the benefits of interleaving. The modulation scheme for interleaving FSIBB and a dual-loop control strategy based on the direct Lyapunov method were implemented to ensure smooth operation. Simulation in PLECS software demonstrated that the proposed controller could effectively share current across stages with symmetrical phase-shift modulation, achieving desired voltage and current regulation. Real-time testing using the TI 28379D launchpad and Typhoon HIL 404 device confirmed the controller's performance and reliability, with interleaving minimizing output ripples and achieving zero current states in the inductor. These findings support the use of multistage interleaving FSIBB in DC microgrid applications. In summary, the studies in this chapter highlight the importance of advanced control techniques and interleaved topologies to improve stability, efficiency, and reduction of ripples in power converters. Looking ahead, the FSIBB converter topology offers potential for hybrid energy storage systems in MG, with opportunities for further research into novel nonlinear controllers across different scenarios.

References

[1] A. Olabi, C. Onumaegbu, T. Wilberforce, M. Ramadan, M. A. Abdelkareem, and A. H. Al–Alami, "Critical review of energy storage systems," *Energy*, vol. 214, p. 118 987, 2021.

[2] A. Ajanovic, A. Hiesl, and R. Haas, "On the role of storage for electricity in smart energy systems," *Energy*, vol. 200, p. 117 473, 2020.

[3] S. Peyghami, F. Blaabjerg, and P. Palensky, "Incorporating power electronic converters reliability into modern power system reliability analysis," *IEEE Journal of Emerging and Selected Topics in Power Electronics*, vol. 9, no. 2, pp. 1668–1681, 2020.

[4] Z. Tang, Y. Yang, and F. Blaabjerg, "Power electronics: The enabling technology for renewable energy integration," *CSEE Journal of Power and Energy Systems*, vol. 8, no. 1, pp. 39–52, 2021.

[5] R. H. Lasseter, "Smart distribution: Coupled microgrids," *Proceedings of the IEEE*, vol. 99, no. 6, pp. 1074–1082, 2011. DOI: 10.1109/JPROC.2011.2114630.

[6] E. Fedele, A. Cervone, I. Spina, D. Iannuzzi, and A. Del Pizzo, "Multiobjective vector modulation for improved control of npc-based multi-source inverters in hybrid traction systems," *IEEE Journal of Emerging and Selected Topics in Power Electronics*, vol. 10, no. 6, pp. 7464–7474, 2022.

[7] A. Dannier, F. Di Bruno, F. Fiume, E. Fedele, and G. Brando, "Hairpin winding technology for electric traction motors: Design, prototyping, and connection rules," in *2022 International Conference on Electrical Machines (ICEM)*, IEEE, 2022, pp. 1170–1175.

[8] A. Dannier, E. Fedele, and M. Coppola, "Sizing approach of high torque density motors for aircraft application," in *2020 International Symposium on Power Electronics, Electrical Drives, Automation and Motion (SPEEDAM)*, IEEE, 2020, pp. 497–501.

[9] A. Dannier, E. Fedele, I. Spina, and G. Brando, *Doubly-fed induction generator (dfig) in connected or weak grids for turbine-based wind energy conversion system*, 2022.

[10] V. Di Dio, S. Favuzza, D. La Cascia, and R. Miceli, "Economical incentives and systems of certification for the production of electrical energy from renewable energy resources," in *2007 International Conference on Clean Electrical Power*, IEEE, 2007, pp. 277–282.

[11] A. O. Di Tommaso, F. Genduso, and R. Miceli, "Analytical investigation and control system set-up of medium scale pv plants for power flow management," *Energies*, vol. 5, no. 11, pp. 4399–4416, 2012.

[12] A. Di Tommaso, F. Genduso, R. Miceli, and G. R. Galluzzo, "Computer aided optimization via simulation tools of energy generation systems with universal small wind turbines," in *2012 3rd IEEE International Symposium on Power Electronics for Distributed Generation Systems (PEDG)*, IEEE, 2012, pp. 570–577.

[13] A. Del Pizzo, L. P. Di Noia, and E. Fedele, "A simple analytical model of static eccentricity for pm brushless motors and validation through fem analysis," *Energies*, vol. 13, no. 13, p. 3420, 2020.

[14] E. Fedele, A. Di Pasquale, D. Iannuzzi, and M. Pagano, "Integration of onboard batteries and supercapacitors based on the multi-source inverter for light rail vehicles," in *2022 International Power Electronics Conference (IPEC-Himeji 2022-ECCE Asia)*, IEEE, 2022, pp. 698–704.

[15] S. M. Kaplan, *Smart Grid: Modernizing electric power transmission and distribution; Energy independence, Storage and security; Energy independence and security act of 2007 (EISA); Improving electrical grid efficiency, communication, reliability, and resiliency; integrating new and renewable energy sources*. The Capitol Net Inc, 2009.

[16] R. A. Kaushik and N. M. Pindoriya, "A hybrid ac-dc microgrid: Opportunities & key issues in implementation," in *2014 International Conference on Green Computing Communication and Electrical Engineering (ICGCCEE)*, IEEE, 2014, pp. 1–6.

[17] S. A. Gorji, H. G. Sahebi, M. Ektesabi, and A. B. Rad, "Topologies and control schemes of bidirectional dc–dc power converters: An overview," *IEEE Access*, vol. 7, pp. 117 997–118 019, 2019.

[18] M. Veerachary and M. R. Khuntia, "Design and analysis of two-switch-based enhanced gain buck–boost converters," *IEEE Transactions on Industrial Electronics*, vol. 69, no. 4, pp. 3577–3587, 2021.

[19] O. Akın, Ç. Bilgin, S. Celik, and M. O. Gülbahçe, "Design of four-switch buck-boost converter for light electric vehicles: A cost and efficiency perspective," 2023.

[20] L. Tian, X. Wu, C. Jiang, and J. Yang, "A simplified real-time digital control scheme for zvs four-switch buck–boost with low inductor current," *IEEE Transactions on Industrial Electronics*, vol. 69, no. 8, pp. 7920–7929, 2021.

[21] L. L. Carralero, F. F. Costa, A. P. Tahim, *et al.*, "Pv emulator based on a four-switch buck-boost dc-dc converter," in *2019 IEEE 15th Brazilian Power Electronics Conference and 5th IEEE Southern Power Electronics Conference (COBEP/SPEC)*, IEEE, 2019, pp. 1–5.

[22] C.-W. Chen, K.-H. Chen, and Y.-M. Chen, "Modeling and controller design for a four-switch buck-boost converter in distributed maximum power point tracking pv system applications," in *2012 IEEE Energy Conversion Congress and Exposition (ECCE)*, IEEE, 2012, pp. 1663–1668.

[23] Q. Ullah, X. Wu, and U. Saleem, "Current controlled robust four-switch buck-boost dc-dc converter," in *2021 International Conference on Computing, Electronic and Electrical Engineering (ICE Cube)*, IEEE, 2021, pp. 1–6.

[24] Y. Wang, J. Lan, X. Huang, T. Fang, X. Ruan, and M. Dong, "An improved single-mode control strategy based on four-switch buck-boost converter," in *2020 IEEE Applied Power Electronics Conference and Exposition (APEC)*, 2020, pp. 320–325. DOI: 10.1109/APEC39645.2020.9124612.

[25] Q. Liu, Q. Qian, M. Zheng, S. Xu, W. Sun, and T. Wang, "An improved quadrangle control method for four-switch buck-boost converter with reduced loss and decoupling strategy," *IEEE Transactions on Power Electronics*, vol. 36, no. 9, pp. 10 827–10 841, 2021.

[26] X. Li, Y. Liu, and Y. Xue, "Four-switch buck–boost converter based on model predictive control with smooth mode transition capability," *IEEE Transactions on Industrial Electronics*, vol. 68, no. 10, pp. 9058–9069, 2020.

[27] Y. Bai, S. Hu, Z. Yang, Z. Zhu, and Y. Zhang, "Model predictive control for four-switch buck–boost converter based on tuning-free cost function with smooth mode transition," *IEEE Journal of Emerging and Selected Topics in Power Electronics*, vol. 10, no. 6, pp. 6607–6618, 2021.

[28] G. Bossi, A. Damiano, N. Campagna, V. Castiglia, R. Miceli, and A. Di Tommaso, "A hybrid storage systems for all electric aircraft," in *2021 IEEE 15th International Conference on Compatibility, Power Electronics and Power Engineering (CPE-POWERENG)*, IEEE, 2021, pp. 1–6.

[29] N. Campagna, V. Castiglia, A. Damiano, L. P. Di Noia, R. Miceli, and A. O. Di Tommaso, "A hybrid energy storage sizing for a vertical take-off and landing electric aircraft," in *IECON 2021–47th Annual Conference of the IEEE Industrial Electronics Society*, IEEE, 2021, pp. 1–6.

[30] A. U. Rahman, N. Campagna, A. Di Tommaso, R. Miceli, A. Damiano, and A. Floris, "Advanced control analysis of single inductor four switch non-inverting buck-boost converter for energy storage units," in *2023 International Conference on Clean Electrical Power (ICCEP)*, IEEE, 2023, pp. 267–272.

[31] F. Pellitteri, N. Campagna, R. Inguanta, and R. Miceli, "Application of a multiphase interleaved dc-dc converter for power-to-hydrogen systems," in *2023 IEEE 17th International Conference on Compatibility, Power Electronics and Power Engineering (CPE-POWERENG)*, IEEE, 2023, pp. 1–6.

[32] W. Yongqing, Y. Fei, H. Yaxin, and L. Kaixuan, "Research on the topology of multiphase interleaved bidirectional dc-dc converter for energy storage system," in *12th International Conference on Renewable Power Generation (RPG 2023)*, vol. 2023, 2023, pp. 466–470. DOI: 10.1049/icp.2023.2183.

[33] M. L. A. Caris, H. Huisman, and J. L. Duarte, "Harmonic elimination by adaptive phase-shift optimization in interleaved converters," in *2013 IEEE Energy Conversion Congress and Exposition*, 2013, pp. 763–768. DOI: 10.1109/ECCE.2013.6646779.

[34] S. Waffler, J. Biela, and J. W. Kolar, "Output ripple reduction of an automotive multi-phase bi-directional dc-dc converter," in *2009 IEEE Energy Conversion Congress and Exposition*, IEEE, 2009, pp. 2184–2190.

[35] A. Wibisono, M. Facta, and I. Setiawan, "An average current control method in multiphase interleaved bidirectional dc/dc converter connected on dc microgrids," in *2021 12th International Renewable Engineering Conference (IREC)*, IEEE, 2021, pp. 1–6.

[36] G. Mao, G. Zhou, H. Zhao, Y. Gao, P. P. Kubulus, and S. Munk-Nielsen, "Digital average current predictive control for multiphase interleaved dc–dc converters," *IEEE Transactions on Circuits and Systems II: Express Briefs*, vol. 70, no. 12, pp. 4519–4523, 2023. DOI: 10.1109/TCSII.2023.3294760.

Chapter 3

DC Microgrid: Adaptive Non-linear Perspective for EV Charging

3.1 Introduction

DC MGs have received significant attention in the energy sector in recent years due to their notable features: flexibility, efficient controlled power generation, and minimal maintenance costs [1]–[3]. With the considerable increase in the adoption of electric vehicles, concerns have emerged about the seamless integration of electric vehicles into conventional power networks. DC MG presents a viable alternative solution to address and potentially overcome these integration challenges. Furthermore, DC MGs combine various clean energy sources, including renewable energy sources and ESS, to offer emissions-free solutions [4], [5].

DC MGs present a promising alternative for empowering EMmobility by minimizing issues related to reactive power, the effect of the skin on transmission lines, and the high impedance. These MGs employ power electronics converters to interconnect power sources via a common bus, thereby forming a modern power system based on power electronics [6]. Given the involvement of multiple power converters, stochastic renewable energy sources, and dynamic loads, ensuring the stability and efficiency of DC MGs becomes paramount. Optimal energy management and control strategies [7] are imperative to facilitate uninterrupted charging of EVs and efficiently handling CPL [8].

In recent years, many multilayer control algorithms have been proposed for forecasting, power management, and converter control in DC MGs. The CPLs reduce the damping effect of the power converters in DC MGs that can result in system instability [9]. Furthermore, the inherently non-linear behavior of power converters [10] requires precise control mechanisms to ensure efficient operation. This chapter investigates the stability and control perspective of DC MGs for feeding CPLs

and charging EVs. Recently, a lot of research has been carried out to improve the efficiency of DC MGs. The droop control method [11] is a commonly employed technique to regulate the voltage of the DC bus and facilitate power sharing between ESSs. Addresses the challenges inherent in the methods of centralized control [12] by offering a decentralized solution [13]. Reference [14] recommends the utilization of an observer-based droop controller in DC MGs to enhance dynamic response while simultaneously reducing the need for additional current measurements. A proposed approach [15] involves the use of an adaptive droop controller followed by a sliding mode controller in a DC microgrid based on boost converter. However, these studies did not consider the problems raised by active loads, such as CPL and EV charging. Some studies [16], [17], specifically discussed the non-linearity of CPLs and tried to solve the problem with optimal control methods. Similarly, heuristic control methods [18], [19] are being explored for energy management in DC MGs. However, concerns arise due to the complexity of design and the high computational costs associated with these methods.

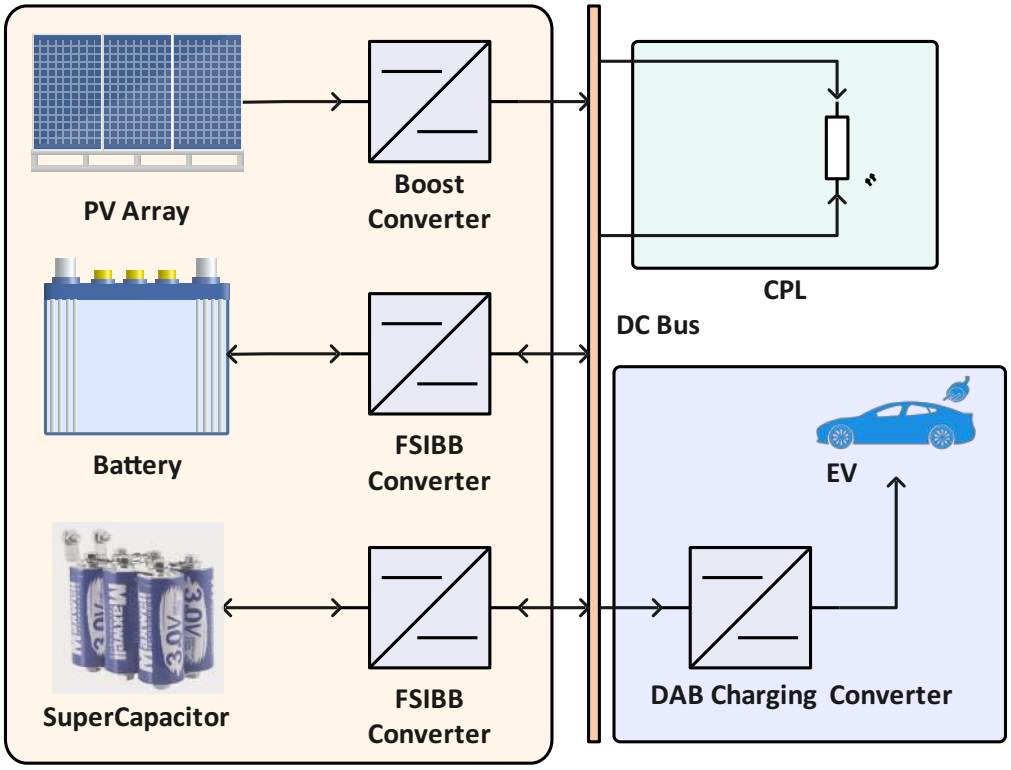

Figure 3.1: Structure of DC microgrid.

The attention of researchers is directed towards advanced DC-DC power converters [20], due to their high efficiency, wide operating range, and suitability for high voltage applications [21], [22]. However, they require advanced low-level switching controllers for smooth operation. Multiport and high efficiency bidirectional power converters are developed for electric vehicles and MG applications in [23], [24], these studies focus on the design and hardware testing of power converters specifically.

The stability and control strategy of the system have not been addressed in these articles. Linear control methods such as PI and LQR are considered state-of-the-art control methods for current and voltage regulation [25]. The control design is based on the linearized model of the system operating around its equilibrium point. However, the drawback of this linear control design emerges when the system faces significant disturbances that can impact its stability. Predictive controllers are proposed to optimally control the power converters in the DC microgrid [26], [27]. Given the nonlinearities inherent in power converters, certain nonlinear control algorithms are recommended to ensure DC microgrid stability. These algorithms offer rapid dynamic responses and possess the capability to effectively manage unknown disturbancesţtex26,x27,x28. The review exposed that these studies lack stability analysis in relation to EV integration and also exhibit drawbacks, including high computational costs, chattering effects, and reliance on high fixed gains.
This chapter focuses on the stability and control of a PV and ESS-based DC microgrid to supply power for EV charging and CPLs. The ESS, comprising batteries and supercapacitors, is employed to face the stochastic behavior of the PV system. It can be used not only for the supply of auxiliary services, but also to store surplus energy during low-load conditions. The regulation of DC bus voltage and the sharing of power among ESS is facilitated by implementing the decentralized extended droop control algorithm [28]. In addition, a sliding mode controller based on barrier function [29] is designed for power converters to ensure optimal power extraction. The main contribution of the proposed work can be encapsulated in points as follows:

- A two-layer control framework is proposed to improve the power-sharing, stability, and control effort of the DC microgrid feeding active loads such as EVs and CPLs since the integration and control of the EV charging system is not considered in most DC MG studies;
- Barrier-based SMC adaptive controller is developed for a large-scale system that not only provides the stability analysis but also overcomes the issues associated with traditional nonlinear control methods i.e chattering, high fixed gains;
- Detailed analytical stability analysis is conducted to ensure the global stability of the closed-loop system using Lyapunov theory;
- The proposed algorithm is compared with other linear and nonlinear control methods. The comparative analysis shows the performance of the proposed methods compared to the state-of-the-art methods.

The literature review can be summarized to show the novelty of the proposed work concerning the combination of different aspects in the table below. The literature review can be summarized to show the novelty of the proposed work concerning the combination of different aspects in the table below.

Table 3.1: Comparative analysis of proposed closed-loop system

Ref.	[28]	[30]	[31]	[32]	**Proposed**
Controller	PI	Deadbeat	SMC	Nonlinear	BSMC
CPL Test	YES	NO	-	NO	YES
EV Integration	NO	NO	NO	YES	YES
HESS Control	YES	YES	-	NO	YES
Large signal Stability	-	NO	YES	YES	YES

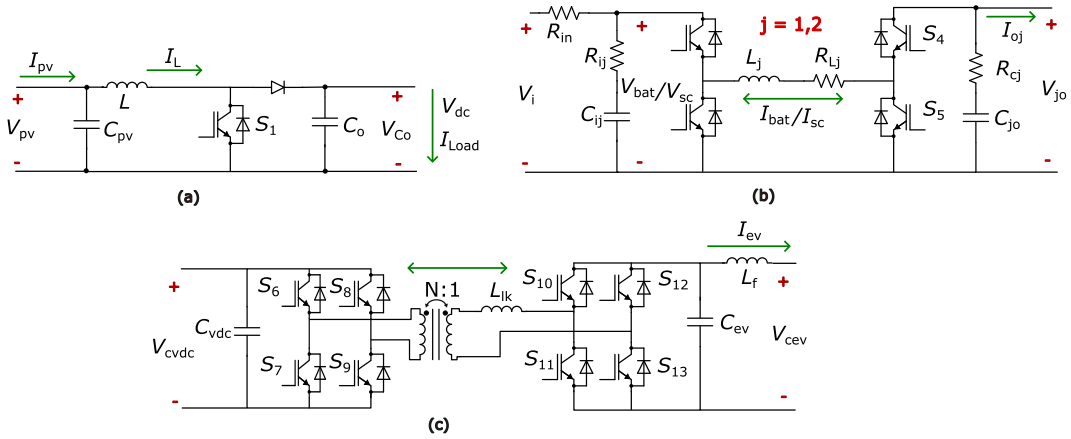

Figure 3.2: Schematic diagrams of the power converters used in DC microgrid (a) Boost converter for PV (b) Four-switches single inductor buck-boost (FSIBB) converter (c) Dual active bridge (DAB converter) for EV.

3.2 DC Microgrid Structure

The block diagram of the DC MG is presented in Fig. 3.1. The PV modules are connected to the DC bus through a simple boost converter to provide higher voltage. The FSIBB converter is investigated for integrating a battery and SC-based ESS. Finally, the integration of electric vehicle charging is managed by the DAB converter. The DC MG also provides the power supply to the CPLs.

3.2.1 PV System

The circuit diagram of the power converters deployed in the DC MG is presented in Fig. 3.2. Mathematical modeling of the system is crucial for understanding the behavior and designing the proper control system. Fig. 3.2 (a) displays the simple boost converter for PV panels. The photovoltaic system is considered the primary source of power generation and is intended to operate using MPPT. The average

state-space model [33] of the PV-boost module can be represented as:

$$\frac{dI_L}{dt} = \frac{1}{L}(-R \cdot I_L + V_{in} - D \cdot V_{dc}), \tag{3.1}$$

$$\frac{dV_{Co}}{dt} = \frac{1}{Co}(D \cdot I_L - I_{load}), \tag{3.2}$$

where I_L, V_{Co}, and I_{Load} represent the inductor current, output voltage, and load current respectively. Similarly, V_{in} and V_{dc} are the input voltage and DC bus voltage, where u denotes the duty cycle of the switch S. The PV current (I_{PV}) can derived through equation shown below:

$$I_{PV} = N_p I_{ph} - N_p I_o \left[e^{\frac{q(V_c + I_c \cdot R_s)}{N_s \cdot A \cdot K \cdot T}} - 1 \right], \tag{3.3}$$

where N_p represents the number of solar cells connected in a parallel arrangement, I_{ph} signifies the internal photon current, I_o denotes the saturation current, Q stands for the electron charge, V_c indicates the output voltage of the cell, I_c expresses the output current of the cell, N_s defines the number of cells connected in series, A symbolizes the ideality factor, K represents the Boltzmann constant, and T represents the temperature [34].

3.2.2 Energy Storage System

The ESS, comprising a combination of a battery and SC [35], combines the advantages of both components, offering enhanced storage capacity. Integrating an SC into the ESS aims to manage transient peaks during load changes due to its rapid discharge capability. The investigation into the FSIBB converter topology for the ESS in the DC MG is driven by its advantageous features over traditional buck-boost converters. Fig. 2.2 (b) shows the circuit diagram of the FSIBB converter deployed with ESS. The large-scale mathematical model of the FSIBB converter is developed by considering two modes of operation: 1) when S_1 and S_3 are conducting and 2) when S_2 and S_4 are ON. The advantages of FSIBB include a non-inverting output, a wide operating range, and an expanded range of operational modes [36]. The design equations for FSIBB can be written as

$$C_{jo} \geq \frac{V_{jo} D_j T_{sw}}{R \delta V_{jo}}, \tag{3.4}$$

$$L_j \geq V_i \frac{D_j T_{sw}}{\delta I_{L_j}}, \tag{3.5}$$

where D_j denotes the duty cycle, δV_o and δI_L are the desired ripple values for voltage and current and R represents the output load resistance. The average state-space

model can be derived as:

$$\begin{aligned}
\dot{x_1} &= \frac{1}{Lj}(-\frac{R_{ij}R_{cj}+R_{Lj}R_1}{R_1}x_1 + \frac{R_i}{R_1}x_2 + \frac{R_{cj}}{R_1}V_i),\\
\dot{x_2} &= \frac{1}{Cj}(-\frac{R_{ij}}{R_1}x_1 - \frac{1}{R_1}x_2 + \frac{1}{R_1}V_i),\\
\dot{x_3} &= \frac{1}{C_j}(\frac{-x_3}{R_1}).
\end{aligned} \tag{3.6}$$

for the second mode

$$\begin{aligned}
\dot{x_1} &= \frac{1}{Lj}(-\frac{R_{ij}}{R_1}x_1 + \frac{r_i}{R_1}x_3 + \frac{R_1}{V_i}),\\
\dot{x_2} &= \frac{1}{Cj}(-\frac{1}{R_1}x_2 + \frac{1}{R_1}V_i),\\
\dot{x_3} &= \frac{1}{C_j}(\frac{-x_3}{R_2} + \frac{R}{R_2}x_1),
\end{aligned} \tag{3.7}$$

whereas

$$R_1 = R_{in} + R_{ij},\ R_2 = R + R_{cj}$$

where $j = 1, 2$ for battery and SC respectively. The averaged model over one switch period can be calculated by finding the average matrices A, B, C, D by using the following expressions

$$\begin{cases}
A_{average} = A_{ON}.D_j + A_{OFF}.(1 - D_j)\\
B_{average} = B_{ON}.D_j + B_{OFF}.(1 - D_j)\\
C_{average} = C_{ON}.D_j + C_{OFF}.(1 - D_j)\\
D_{average} = D_{ON}.D_j + D_{OFF}.(1 - D_j)
\end{cases} \tag{3.8}$$

Hence the average state-space model can be obtained as follows:

$$\begin{cases}
\dot{x_k} = A_{average} \cdot x + B_{average} \cdot D_j\\
\dot{y_k} = C_{average} \cdot x + D_{average} \cdot D_j,
\end{cases} \tag{3.9}$$

As mentioned before, the FSIBB converter has two modes of operation buck and boost, the equation (3.8) calculates the average state-space matrices over a complete duty cycle. Equation 3.9 represents the general state-space form of the model [37]. Where $k = 1, 2....6$ for both battery and supercapacitor, respectively. $A_{average}, B_{average}, C_{average}, D_{average}$ are the calculated average value matrix, obtained by combining equations (3.6,3.7). For more clarity, it can be expressed as

$$[x_1, x_2, x_3, x_4, x_5, x_6]^T = [I_{bat}, V_{bat}, V_{1o}, I_{sc}, V_{sc}, V_{2o}]^T.$$

The system parameters are given in table 3.2.

Table 3.2: DC microgrid parameters and values.

PV system	
Parameter	**Values**
Number of panels (series * Parallel)	10*10
Capacitance C_{pv}, C_o	7 , 400 μF
Inductor L_{pv}	7.22 μH
Power at MPPT P_{pv}	21.315 kW
Energy Storage System (ESS)	
Battery nominal Voltage	100 V
Rate Capacity	100 Ah
Battery response time	0.1 s
Initial SoC battery	75 %
SuperCapacitor rate voltage	48 V
Number of capacitors in SC	6*8
Rate capacitance of SC	100 F
FSIBB Converter	
Input Resistance R_j	220 μ Ω
C_{ij} Input Capacitance	680 μF
Inductance value L_j	220 μ H
Internal Resistance R_{Lj}	1.4 mΩ
Output capacitance	200 μF

3.2.3 EV Charging Structure

The EV integration with the DC MG is reached through the DAB converter. Illustrated in Fig. 3.2 (c), the circuit diagram of the DAB converter features two full bridges and an isolating transformer, complemented by an inductor. Isolated DC-DC converters are gaining prominence as a result of their compliance with high-power applications. Their bidirectional power flow capability plays a pivotal role in the grid-to-vehicle (G2V) and V2G operations, facilitating efficient DC fast charging of EVs [38]. The DAB converter encompasses components such as C_{vdc}, the input side capacitor, L_{lk}, the inductor, and an output filter comprising C_{ev} and L_f. The expression for the output power of the DAB converter can be depicted as:

$$P_{ev} = \frac{NV_{Cev}V_{Cvdc}\phi(1-2|\phi|)}{f_{sw}L_{lk}}. \tag{3.10}$$

Here, P_{ev} indicates the output power of the DAB converter, while N, ϕ, and f_{sw} represent the number of turns of the transformer, the phase change, and the switching frequency, respectively. In the case of an ideal transformer, the number of turns can be expressed as:

$$N = \frac{V_{cev}}{V_{cvdc}}. \tag{3.11}$$

The mathematical model of the DAB converter can be derived by using the state-space average technique [32] and can be written as:

$$\begin{aligned}
\dot{x_7} &= -\frac{R}{L_{lk}}x_7 + \frac{T \cdot R \cdot N}{L_{lk}^2} \cdot \phi(1 - 2|\phi|)x_9, \\
\dot{x_8} &= \frac{1}{C_{ev}}x_7 + \frac{1}{R_{ev}C_{ev}}x_8 + \frac{V_g}{R_{ev}C_{ev}}, \\
\dot{x_9} &= \frac{N}{C_{vdc}}x_7 - \frac{1}{R_gC}x_9 + \frac{V_{ev}}{R_gC_{vdc}}.
\end{aligned} \tag{3.12}$$

ϕ serves as the control parameter employed for regulating the output power of the DAB through phase shift modulation. Here, R_g and R_{ev} denote the resistance on the MG side and the resistance on the EV side, respectively. The state variables of the system are defined as:

$$[x_7, x_8, x_9]^T = [I_{ev}, V_{cev}, V_{cvdc}]^T.$$

The current and voltage characteristics of CPL are illustrated in a mathematical expression given below

$$I_{load} = \frac{P_{CPL}}{V_{CPL}}. \tag{3.13}$$

The large signal model of the DC MG is represented by equations (3.1), (3.2), (3.8), and (3.12). This mathematical model serves as the foundation for analytically deriving control methodologies for the system. A comprehensive design analysis is conducted in the subsequent section.

3.3 Adaptive Control Algorithm

In this section, the adaptive control strategy is fully described. In particular, the first subsection focuses on droop-based supervisory control, responsible for power-sharing between the ESS and DC bus voltage regulation; the second subsection discusses the detailed derivation of the barrier-based nonlinear controller for power converters. Finally, the third subsection studies the closed-loop stability analysis using Lyapunov theory. The closed-loop PV system is designed to operate at MPPT. To achieve this condition, an MPPT controller is recommended to extract the maximum power, which is contingent upon temperature and irradiance values. As weather parameters influence PV power, the output PV power remains variable rather than constant.

Table 3.3: DAB-based charging interface.

EV Battery	
Parameter	**Values**
EV battery nominal voltage	400 V
EV battery capacity	80 kWh
Initial SoC of EV battery	60 %
EV battery response time	1 s
Battery type	Lithium-ion
DAB Converter	
Parameter	**Values**
Grid side capacitance C_{vdc}	$60e^{-6}$ F
Turns ratio of transformer	1 : 1
Inductor value L_{kl}	$1.3e^{-05}$ H
EV side capacitance C_{ev}	3.00 mF
Filtering Inductance L_f	$3.36e^{-05}$ H

The optimized linear regression [39] gives the expression to get the MPP using the temperature and irradiance value and expressed as

$$V_{mppt} = 332 + 1.34 \cdot T_{emp} - 0.00964 \cdot I_{irr}. \tag{3.14}$$

Here, V_{mppt}, T_{emp}, and I_{irr} represent the MPPT voltage, temperature value, and irradiance, respectively. The expression determines the maximum power point, while a PI controller tracks the reference value and attains maximum output power.

3.3.1 Decentralized Droop Control

The chapter introduces a two-layer control strategy focusing on power-sharing and converter switching to maintain system stability. The upper control layer is specifically developed to facilitate power distribution between the storage system and regulate the DC bus voltage. The primary objective of the ESS is to offer auxiliary support during power shortages. This objective can be effectively met with a well-designed energy management system. An enhanced droop control method is proposed due to its simplicity and good performance. The current request from ESS can be expressed as

$$I_{ESS} = I_{load} - I_{PV}. \tag{3.15}$$

The I_{ESS} can be shared between the battery and SC in such a way that high peak dynamics are managed by SC and base power is handled by the battery. The

expressions can be written as

$$\begin{aligned} I_{o1} &= G_1(s) \cdot I_{ESS}, \\ I_{o2} &= G_2(s) \cdot I_{ESS}, \end{aligned} \tag{3.16}$$

where

$$\begin{aligned} G_1(s) &= \frac{1}{1+\tau \cdot s}, \\ G_2(s) &= \frac{\tau \cdot s}{1+\tau \cdot s}. \end{aligned} \tag{3.17}$$

τ is the time constant which can be expressed as $\tau = \frac{1}{RC} \cdot G_1(s)$ and $G_2(s)$ represent the low and high pass filters respectively. The time constant τ should be greater than or equal to the battery response time so that the battery can respond according to droop control signals [28]. The V/I relationship of battery and SC can be expressed as:

$$V_{o1ref} = V_{vdcref} - R_{droop} \cdot I_{o1}, \tag{3.18}$$

where R_{droop} is the virtual resistance incorporated to regulate the DC bus voltage through the storage system. The R_{droop} can be expressed mathematically as [28]:

$$R_{droop} = \frac{V_{dcmax} - V_{vdcmin}}{I_{omax}}. \tag{3.19}$$

V_{vdcmin} and V_{vdcmax} are the maximum and minimum allowable DC bus voltage. I_{omax} is the maximum allowable current of the FSIBB converter. Contrary to the virtual resistance concept, the SC voltage reference is derived using a virtual capacitance method. The value of virtual capacitance for the particular case can be found by solving the time constant τ and R_{droop}. The expression of SC voltage reference can be formulated as:

$$V_{o2ref} = V_{dcref} - \frac{1}{C_s} \cdot I_{o2}. \tag{3.20}$$

Here, C_s represents the virtual capacitance, contributing to a quicker dynamic response than virtual resistance. The fundamental concept involves enhancing the traditional droop controller by integrating virtual capacitance, enabling it to effectively manage abrupt load variations while supporting DC bus voltage regulation. PI regulators are configured to generate the current reference for the battery and SC. The inner control loop is subsequently responsible for tracking the current reference and ensuring system stability.

3.3.2 Barrier based Nonlinear Controller

The significance of the low-level switching controller is pivotal for ensuring system stability. Its primary function involves controlling the converter and toggling it on and off to achieve the desired power output. Given the nonlinear characteristics inherent in power sources and converters, the proper design of this control algorithm is

crucial. To address this challenge, this study introduces a proposed barrier function-based adaptive nonlinear controller. This controller not only ensures system stability but also mitigates the overestimation of gains while resisting external disturbances. Fig.3.3 shows the flowchart representation of the adaptive control algorithm.

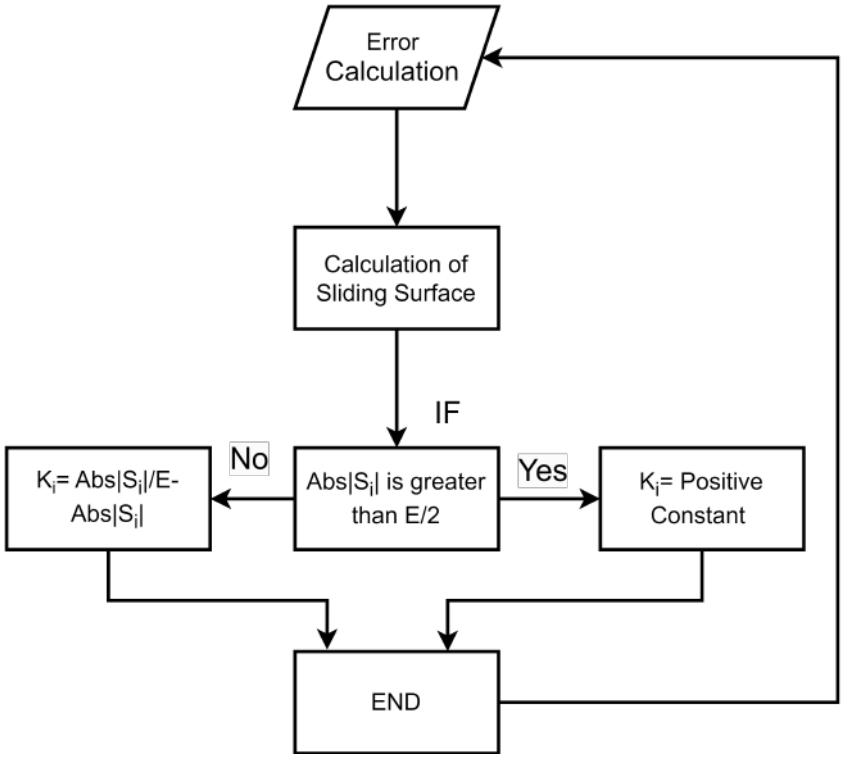

Figure 3.3: Flowchart representation of barrier-based adaptive gains

In this subsection, the derivation of the low-level controller is explained step by step. In the tracking controller, the error signals are the starting points, the error is defined as the difference between the actual and desired value of the state and it can be written as

$$\begin{aligned} e_1 &= x_{1ref} - x_1, \\ e_2 &= x_{4ref} - x_4, \end{aligned} \tag{3.21}$$

where the reference for the battery and SC current can be obtained by solving the equation (3.18) and (3.20) as:

$$\begin{aligned} x_{1ref} &= K_p(V_{o1ref} - x_3) + K_i \int_0^t (V_{o1ref} - x_3)dt, \\ x_{4ref} &= K_p(V_{o2ref} - x_6) + K_i \int_0^t (V_{o2ref} - x_6)dt. \end{aligned} \tag{3.22}$$

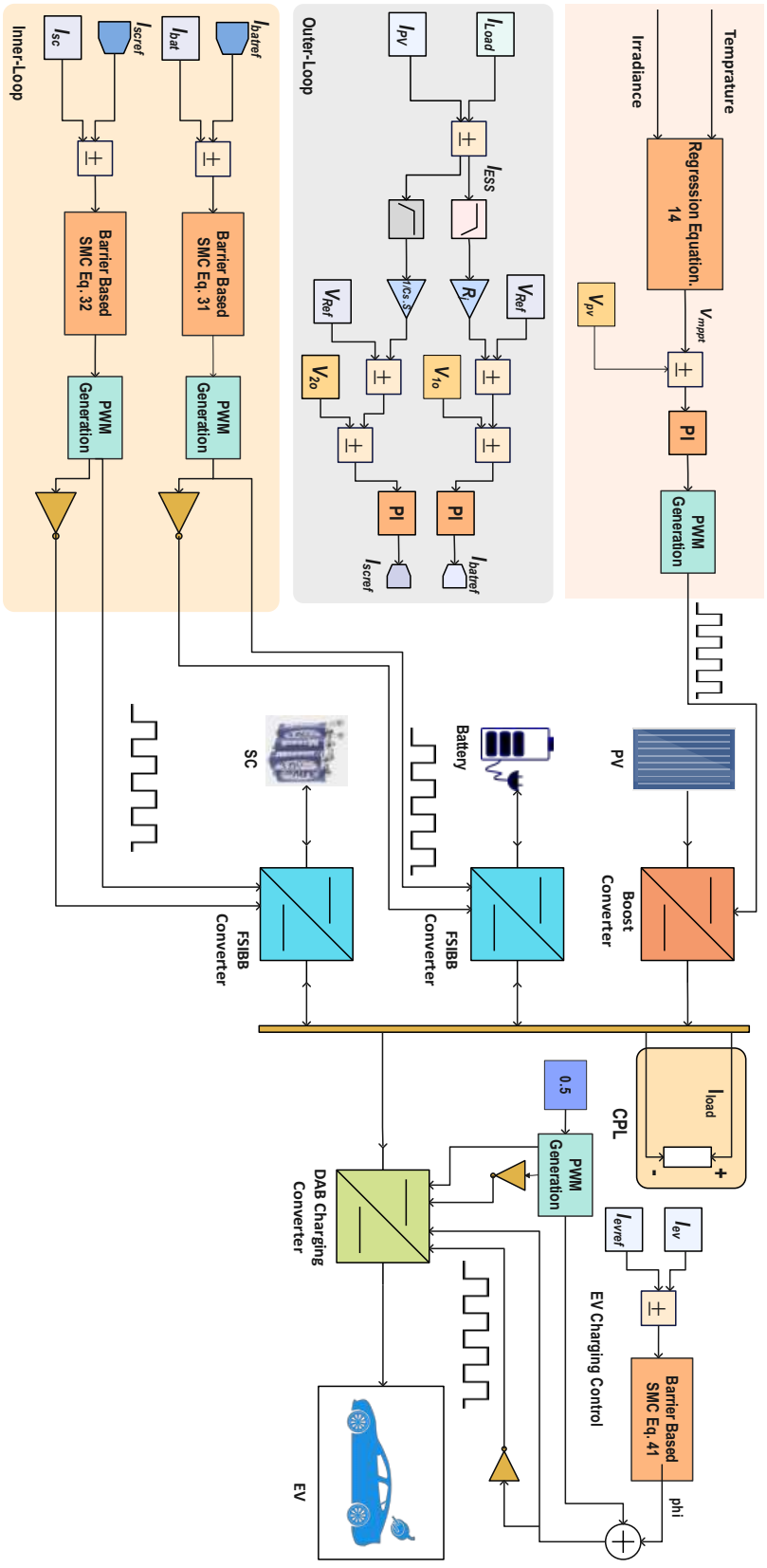

Figure 3.4: Proposed dual-loop control mechanism for DC microgrid.

Different sliding surfaces are selected to keep the controller fully decentralized,

the sliding surfaces are shown below:

$$S_1 = a_1 e_1, \tag{3.23}$$

$$S_2 = a_2 e_2. \tag{3.24}$$

Taking the time derivative of the equations above results

$$\dot{S_1} = a_1 \dot{e_1}, \tag{3.25}$$

$$\dot{S_2} = a_2 \dot{e_2}, \tag{3.26}$$

Here, a_1 and a_2 are the positive gains used to give the specific weight to the error signal, and $\dot{e_1}, \dot{e_2}$ gives the response of the error signals with time. It is possible to assume

$$\dot{S_i} = -k_i \left|S_i\right|^{0.5} sgn\left(\frac{S_i}{0.5}\right), \tag{3.27}$$

where $i = 1, 2, 3$, k_i denotes the controller gain which can be fixed or adaptive depending on the BF. The idea is to initially fix a gain that can bring the sliding surface $S_i(t)$ near zero $\epsilon/2$, the gain is changed to BF to keep the trajectory in the neighborhood of zero. The definition of the barrier function can be illustrated by theorems given in [29].

Definition of BF: It can be assumed that ϵ is fixed and has a value close to zero; then BF can be defined as a continuous function $k_i(y) : y \in]-\epsilon, \epsilon[\rightarrow k_i(y) \in]b, \infty[$ increasing on $[0, \epsilon]$.

- $\lim_{|y|\rightarrow\epsilon} k_i(y) = +\infty$
- $k_i(y)$ has a unique minimum at zero and $k_i(0) = i \geq 0$

The BF considered in this case is defined as

- The positive semidefinite BF is selected to derive the control law as: $K_i(y) = \frac{|y|}{\epsilon - |y|}$

Hence, the adaptive gains for S_i can be expressed mathematically as:

$$k_i(t, S_i(t)) = \begin{cases} k_a(t), \dot{k}_a(t) = \bar{k}|S(t)| & if \quad 0 \leq t \leq \bar{t}, \\ k(S(t)) & if \quad t \geq \bar{t}, \end{cases} \tag{3.28}$$

$$k_i(S(t)) = \frac{|S_i|}{\varepsilon - |S_i|}. \tag{3.29}$$

The equations (3.25) and (3.26) can be expanded as:

$$\dot{S_1} = a_1(\dot{x}_{1ref} - \dot{x_1}), \tag{3.30}$$

$$\dot{S_2} = a_2(\dot{x}_{4ref} - \dot{x_4}). \tag{3.31}$$

The value of $\dot{x_1}$ and $\dot{x_4}$ can be taken from equation (3.8), solving it for control variable $u_j, j = 1, 2$ gives:

$$D_1 = \frac{9.86e^3 x_1 a_1 + 4.46e^4 x_3 a_1 + a_1 \dot{x_{1ref}} - k_1 \left|S_1\right|^{0.5} sgn\left(\frac{S_1}{0.5}\right)}{6.69e^3 x_1 a_1 + 1.42e^4 x_2 a_1 + 31250 V_i a_1 + 4.04 x_3 a_1}, \tag{3.32}$$

$$D_2 = \frac{9.86e^3 x_4 a_1 + 4.46e^4 x_6 a_1 + a_1 \dot{x_{1ref}} - k_2 \left|S_i\right|^{0.5} sgn\left(\frac{S_1}{0.5}\right)}{6.69e^3 x_4 a_1 + 1.42e^4 x_5 a_1 + 31250 V_{isc} a_1 + 4.04 x_6 a_1}. \tag{3.33}$$

Hence, D_1 and D_2 are the control inputs applied to the FSIBB converters in ESS. The control inputs are the same in the diagonal of the H-bridge and inverse in the same leg switches. Similarly, the charging controller for EV charging is designed using the same method. However, for the EV charging controller, the direct current control method is adopted. The EV can be charged with a power level equal to $12kW$ or with a lower one to reduce the stress on the DC MG with normal charging. The DAB converter is used for interaction between the EV battery and DC MG, the error function for DAB current can be expressed as:

$$e_3 = x_{7ref} - x_7. \tag{3.34}$$

Taking the time derivative of the error error signal returns

$$\dot{e_3} = \dot{x}_{7ref} - \dot{x_7}. \tag{3.35}$$

Putting the value of $\dot{x_7}$ from DAB model given in equation (3.12), $\dot{e_3}$ can be expressed as:

$$\dot{e_3} = \dot{x}_{7ref} + \frac{R}{L_{lk}} x_7 - \frac{T \cdot R \cdot N}{L_{lk}^2} \cdot \phi(1 - 2|\phi|) x_9. \tag{3.36}$$

The sliding surface for control law derivation is assumed as:

$$S_3 = a_3 e_3 \Rightarrow \dot{S_3} = a_3 \dot{e_3}. \tag{3.37}$$

The sliding surface contains the error signal with a positive gain a_3. It means that the error trajectory would not converge easily to a chosen surface. Using the assumption given in equation (3.27) and putting the value of $\dot{e_3}$, it can be stated:

$$\begin{aligned} -k_3 \left|S_3\right|^{0.5} sgn\left(\frac{S_3}{0.5}\right) = \dot{x}_{7ref} + \frac{R}{L_{lk}} x_7 - \\ \frac{T \cdot R \cdot N}{L_{lk}^2} . \phi(1 - 2|\phi|) x_9. \end{aligned} \tag{3.38}$$

Solving it for control variable ϕ gives

$$\phi(1-2|\phi|) = \frac{L_{lk}^2}{T \cdot R \cdot N \cdot x_9}\Bigg(\dot{x}_{7ref} + \frac{R}{L_{lk}}x_7 + k_3 \left|S_3\right|^{0.5} sgn\left(\frac{S_3}{0.5}\right)\Bigg). \tag{3.39}$$

To simplify the solution, it can be rearranged as

$$\phi(1-2|\phi|) - T = 0 \Rightarrow \phi - 2\phi^2 - T = 0, \tag{3.40}$$

where T can be written as:

$$T = \frac{L_{lk}^2}{TRNx_9}\left(\dot{x}_{7ref} + \frac{R}{L_{lk}}x_7 + k_3 \left|S_3\right|^{0.5} sgn\left(\frac{S_3}{0.5}\right)\right). \tag{3.41}$$

Finally, the control law is obtained by solving the polynomial of equation (3.40) as:

$$\phi = \frac{-1-\sqrt{1-8T}}{-2},\ \phi = \frac{-1+\sqrt{1-8T}}{-2}. \tag{3.42}$$

The control variable ϕ is represented per unit value within the $-0.5 \leq \phi \leq 0.5$. This phase-shift angle is critical in modulating the power level within the DAB power converter. Consequently, in this scenario, it constitutes the ultimate control law employed for direct current regulation in the DAB converter.

3.3.3 Closed-loop Stability Analysis

Closed-loop system stability is essential for designing a large system controller. Lyapunov theory be used to provide insight stability analysis for the model-based controllers where large signal models are considered. The Lyapunov candidate function can be selected to start the stability analysis. The criteria for selecting a Lyapunov candidate can be summed in the following points:

- The Lyapunov candidate function V should be positive definite $V(S_i) \geq$ for all values of S_i,
- If $S_i \to 0$ then $V(S_i) \to 0$.

Based on theoretical rules, the Lyapunov function can be expressed mathematically as:

$$V = \frac{1}{2}S_1^2 + \frac{1}{2}S_2^2 + \frac{1}{2}S_3^2. \tag{3.43}$$

The Lyapunov candidate function accommodates all sliding surfaces that contain the error signals so that the stability of the DC MG can be determined. Lyapunov function is an energy function depicting the energy of the physical system. Taking

the time derivative of the Lyapunov candidate function, it gives

$$\dot{V} = S_1\dot{S}_1 + S_2\dot{S}_2 + S_3\dot{S}_3, \tag{3.44}$$

which can be simplified as:

$$\dot{V}(S_i) = S_i\dot{S}_i. \tag{3.45}$$

Putting the error e_1, e_2, e_3 and control input values from equations (3.32,3.33,3.42), the expression above take the form:

$$\dot{V}(S_i) = S_i(-k_i\,|S_i|^{0.5}\,sgn\left(\frac{S_i}{0.5}\right)), \tag{3.46}$$

where

$$|S_i|^{0.5} \geq 0,\ S_i(-k_i\,sgn\left(\frac{S_i}{0.5}\right)) \geq 0. \tag{3.47}$$

Remark 1: The function $S \cdot sgn(S)$ consistently produces a positive value due to the nature of the signum function, resulting in $+1$ for positive function values and -1 for negative ones. This signum function is the switching control that maintains the system on the desired trajectory. However, it is prone to chattering issues, which can be mitigated by making appropriate gain adjustments.
Finally, we get

$$\dot{V}(S_i) \leq 0,\ for\ all\ S_i \in \mathbb{R}. \tag{3.48}$$

As stated by the expression above, the time derivative of the Lyapunov function is negative definite which means that the closed-loop system is globally stable and all the error values should converge to the equilibrium point when time $t \to 0$.

3.4 Results and Discussion

The section discusses simulation studies and the results of the proposed method. Numerical simulations are performed to validate the proposed algorithms. In addition, the closed-loop system is tested under various conditions to evaluate the controller response. Subsequent subsections provide detailed discussions of the results.

3.4.1 Simulation Results

The DC MG system is simulated in the MATLAB / Simulink (R2023 b) environment using the simscape library. The simulation results are shown in Fig. 3.5 with 9 subfigures (a)-(l). A time-varying CPL is considered, which can be seen in Fig. 3.5a

and mathematically expressed as:

$$P_{CPL} = \begin{cases} 4.7\ kW, & if \quad 0s \leq t < 2.5s \\ 3.3\ kW, & if \quad 2.5\ s\ \leq t\ < 5s \\ 4.3\ kW, & if \quad 5s \leq t < 7.5s \\ 5.35\ kW, & if \quad 7.5s\ \leq t\ \leq 10s \end{cases} \tag{3.49}$$

Fig. 3.5b shows the PV voltage response with the MPPT controller. The figure illustrates two trajectories, where the red dotted line represents the desired maximum PowerPoint (MPP), and the blue line represents the response of V_{PV}. The temperature and irradiance values vary within the range of $20 - 35$ Celsius degrees and $700 - 1000W/m^2$, respectively. It is evident from the figure that the PV voltage can properly track its reference. Similarly, Fig. 3.5c represents the DC bus voltage response, one of the main aims of upper layer control is to regulate the DC link voltage to the desired value equal to $V_{dcref} = 400$. Since one graph shows both the reference line and the actual state value it can be verified that the DC bus voltage is regulated with little spikes at $t = 0,\ 2.5,\ 5,\ 7.5s$. These overshoots/undershoots are due to a time-varying load as mentioned in the equation (3.49). However, with the proposed control, the fluctuations are within the limits $\pm 4\%$.

The second interesting aspect to analyze is the response of the ESS. The control scheme is devised so that the battery supplies the base current, but exhibits a slow response. This sluggish response is effectively compensated for by the fast dynamic reaction of the SC. Graphs for battery and SC are presented in Figs. 3.5d and 3.5e, respectively. The SC provides a rapid dynamic response during load changes, complementing the slower response of the battery. In addition, the graphs illustrate the tracking of the battery and SC current in a zoomed-in area, showcasing the efficacy of the low-level adaptive non-linear controller. Figs. 3.5d and 3.5e depict the tracking of desired reference values (indicated by a red dotted line), confirming the stability of the system. The scope of the study also involves the integration and charging of EVs which can be controlled by deploying a direct current-controlled DAB converter. The charging current waveform is shown in Fig. 3.5f, to verify charging control, the electric vehicle is charged with two different current values $(25A,\ 30A)$. It can be seen that the EV charging current is tracking the different current levels which validates the charging control performance. The zoomed-in figure shows the steady-state performance of the advised control, and the graph shows that the controller has a steady-state error of $0.5A$. Similarly, Fig. 3.5g shows the charging power of the EV charger. The charging power level also changes with the change in charging current. The maximum charging power is $13.5kW$ for the $400V$ EV battery.

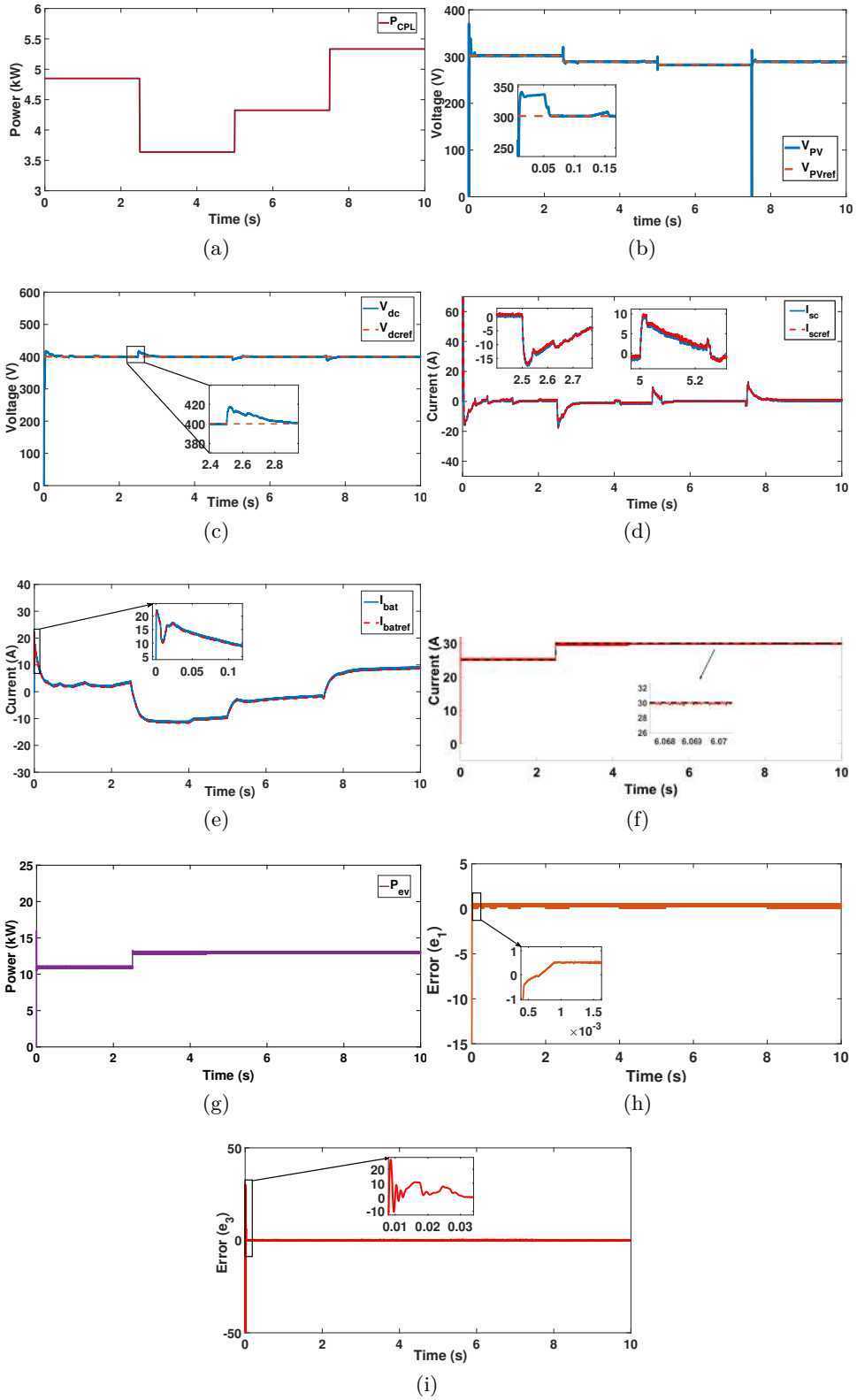

Figure 3.5: (a) Time-varying load power of CPL (b) PV voltage V_{pv} at MPPT (c) DC bus voltage (V_{dc}) response (d) SuperCapacitor Current (I_{sc}) response (e) Battery current (I_{bat}) in DC microgrid (f) Charging Current for EV in DC microgrid (g) EV charging power in DC microgrid (h) Plot of error (e_1) (i) Graph of EV current error (e_3).

Table 3.4: Parameters of proposed Controllers for testing

Enhanced Droop Control	
Parameter	**Values**
Time constant τ	0.5 s
Virtual Resistance R_{droop}	0.033 Ω
PI regulator for battery K_p	0.05
PI regulator for battery K_i	5
PI regulator for SC K_p	1
PI regulator for SC K_i	0.5
Adaptive Nonlinear Control	
Parameter	**Values**
$a_1,\ a_2,\ a_3$	1.00
ϵ	0.5
$k_1,\ k_2,\ k_3$	$5e^6,\ 5e^6,\ 7000$
Sliding surface S_i	0

The initial SoC of the EV battery is intentionally set to a low value of 60%. It is noticeable that when the charging power level varies within the range of $(25A-30A)$, the SoC trajectory also alters its behavior, indicating a rapid charging behavior. The Lyapunov stability analysis ensures the convergence of error signals to zero, Figs. 3.5h and 3.5i depict the error signal reaction to the applied control strategy, and the magnified portion shows the transient response of the error trajectory, however, when the control acts, the error signals converge to zero. From the error signal it can be concluded that the non-linear adaptive controller can remove the steady-state error and keep the system stable in different scenarios. The control parameters used to develop the control algorithm are listed in the table 3.4. The PI gains for the outer loop droop control are adjusted by using the error and trial method to avoid the complexity of the design. However, many methods can be found in the literature to tune the PI controller.

3.4.2 Robustness Test

The robustness test is conducted to evaluate the performance of the proposed controller in the presence of external disturbance. In this case, a time-varying disturbance is incorporated with an unknown upper bound. One of the advantages of barrier function-based nonlinear controllers is that they can mitigate the effect of disturbances and keep the system stable. The mathematical expression for the

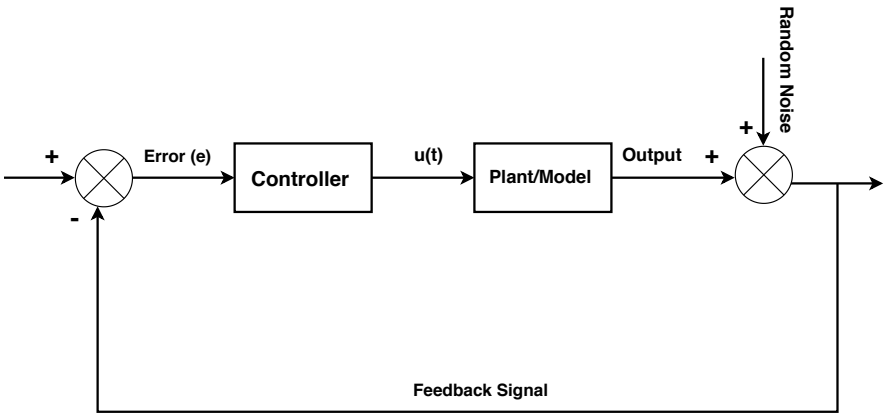

Figure 3.6: Closed-loop system with disturbance

time-varying disturbance can be written as:

$$d(t) = \begin{cases} 0.3sin(t), & if \quad 0 \leq t < \ 4.5s \\ 1.4sin(t), & if \quad 4.5s \leq t < 7.5s \\ 4.8sin(t), & if \quad t \geq 7.5s, \end{cases} \tag{3.50}$$

Fig. 3.7a, shows the graph of disturbance d, a sinusoidal function with varying amplitude. The response of DC bus voltage V_{dc} is plotted against disturbance d in fig.3.7b. The result proves the stability of the system as the DC bus voltage is regulated to 400. However, little effect of the disturbance can be observed after $t = 7.5$ which is in the limit of ± 4 due to the tight adaptive controller. The result shows the system stability and voltage regulation in the presence of unknown disturbances with unknown upper and lower bounds. The adaptive gains and the barrier-based control structure can significantly minimize the effect of unknown disturbance. Finally, Fig. 3.7c presents the response of sliding surface S_1 in the presence of disturbance. The magnified section of the figure depicts the effect of disturbance on the sliding surface, however, the important aspect to notice is that the amplitude of the disturbance at $t \ \geq 7.5s$ is 4.8 but the S_1 has a variation of value 0.3. In light of these results, it can be stated that the adaptive non-linear controller showed robustness against unknown disturbance and minimized the effect by keeping the trajectory on the desired sliding surface. Fig. 3.6 shows the block diagram of the system with the disturbance. In this chapter, the idea of barrier function-based adaptive control is used to manage unknown disturbances, and the disturbance signal is added to the DC bus. The idea is to test the system's robustness against an unknown disturbance signal with an unknown upper bound. So, a sinusoidal function with varying upper bounds has been considered.

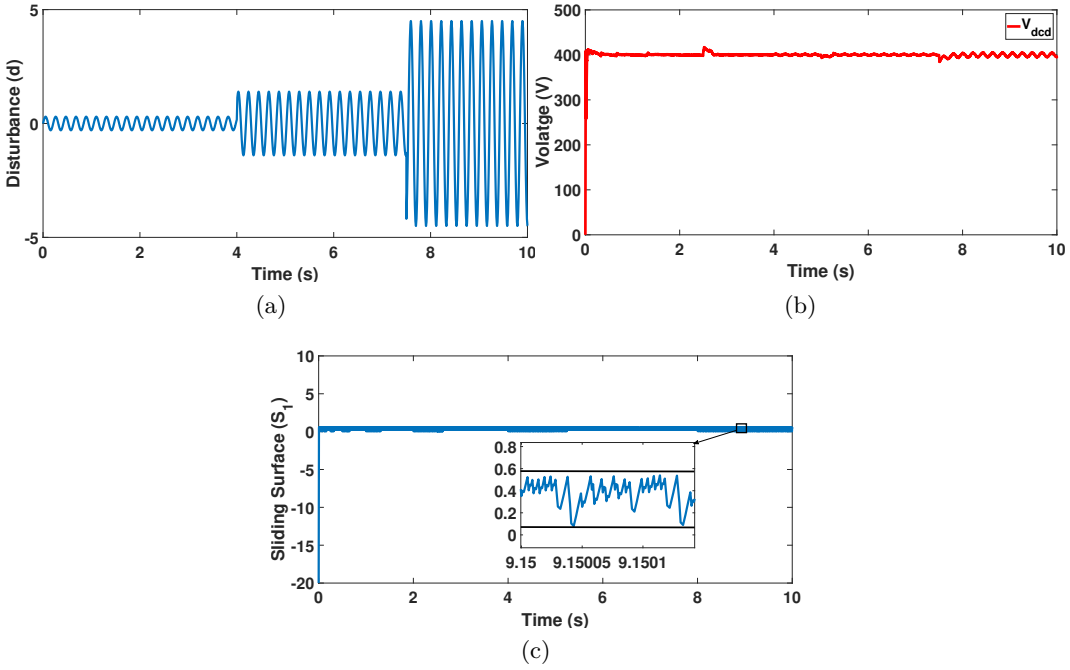

Figure 3.7: Robustness Test (a) Unknow time-varying disturbance d (b) Response of DC bus voltage against disturbance (c) Sliding surface S_1 response.

3.4.3 Comparative Analysis

The proposed controller is compared with state-of-the-art control algorithms such as PI, the Lyapunov method and traditional SMC.

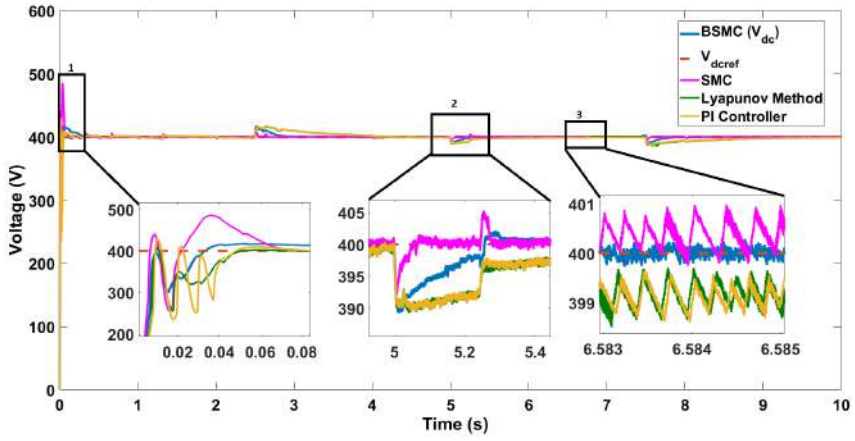

Figure 3.8: Comparative graph of different control methods

The regulation of the DC bus is selected as a criterion to compare different algorithms, and the comparative graph is presented in fig. 3.8. The three zoomed-in sections (1,2,3) depict the transient response, overshoot/undershoot, and steady-state behavior of the control methods. It can be seen that the proposed control method shows the optimal response while maintaining the minimum tracking error.

The proposed controller has fewer errors, overshoot / undershoot, and peak value compared to the others. Traditional SMC has a fast response, but also has the problem of chattering and high over/undershoots. The problem is mediated by the power rate reaching law and adaptive gains in the proposed method. Table 3.5 presents the comparative data of different controllers for a better understanding. The fixed and variable gains k_i of the adaptive nonlinear controller are plotted in the same graph and presented in Fig. 3.9.

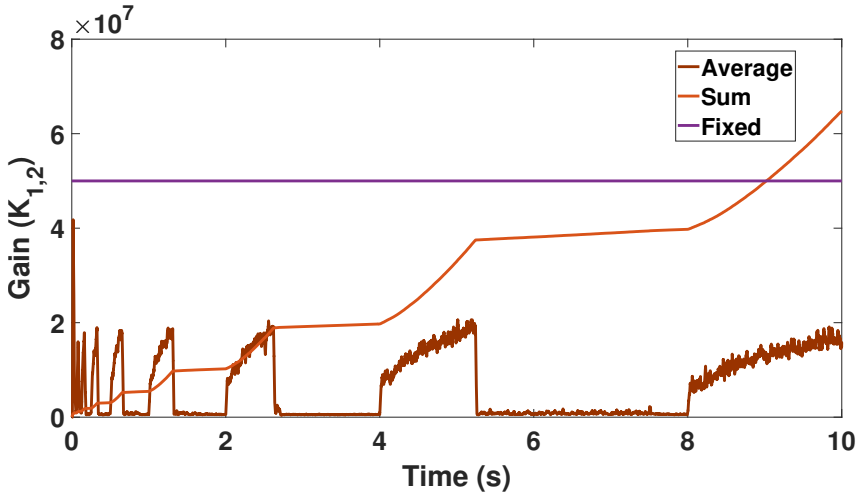

Figure 3.9: Comparative Analysis of different gains

Table 3.5: Comparative analysis of proposed controller

Sr.	Rise time	Over/undershoot	Error	Peak value
PI	6.525 ms	8.152% ,41.26%	1.1	429.8
Lyapunov	6.2 ms	7.2% ,39.26%	0.9	425.8
SMC	4.192 ms	9.787% , 36.617%	0.67	485.2
Proposed	5.237 ms	2.673%, 35.503%	0.095	417.2

3.4.4 Harware-in-the-loop (HIL) Tests

The high-fidelity HIL test is then performed to confirm the real-time performance of the proposed controller. The Typhoon HIL 404 emulator is used to instantiate the DC microgrid, using the FPGA cores of the device. The closed-loop controller operates in real time, utilizing system cores. The Typhoon HIL also provides the HIL SCADA, enabling real-time control over the operational system. The results can be visualized through an oscilloscope connected to the Typhoon HIL. For real-time analysis, varying CPLs are employed, with the initial SoC of the storage system

set to 75%. The assumed operating conditions include the PV system that operates under MPPT at a temperature of 25 C and a irradiance of 1000 W/m^2.

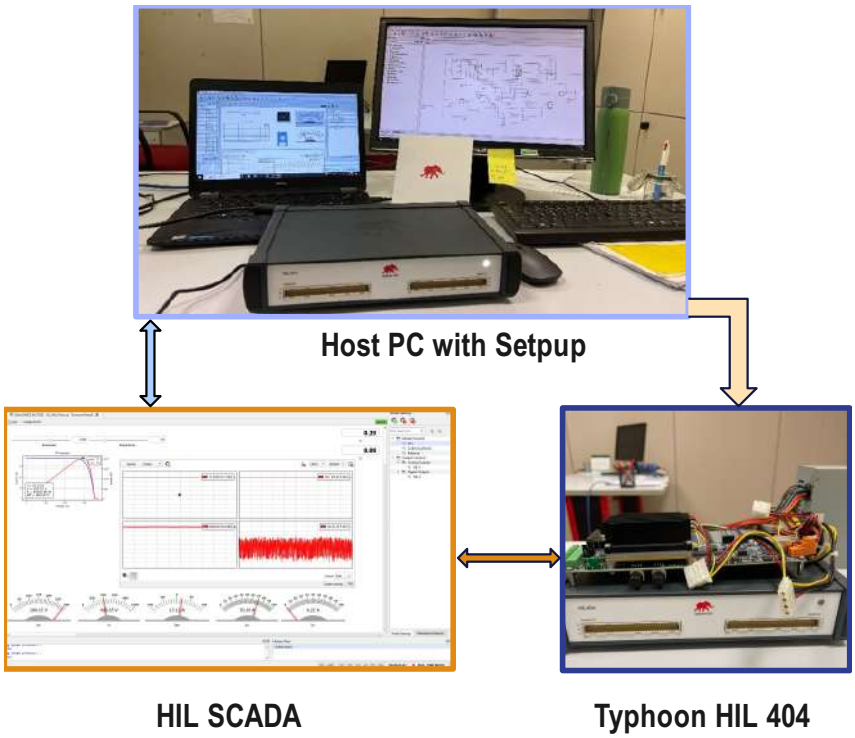

Figure 3.10: Hardware-in-Loop Setup for real-time testing.

The HIL results are shown in Fig. 3.11, Fig.3.11a shows the varying load profile, while Fig. 3.11b illustrates the MPPT working of the PV system at specific weather parameters. To verify the control objective, the DC bus voltage response is plotted in Fig. 3.11c, the reference value for the DC bus voltage is considered $400V$, the same as in simulation tests. The response of ESS is also reported in Fig. 3.11d and 3.11c, respectively. Lastly, Fig. 3.11e indicates the behavior of the charging current of the integrated EV. The reference value for the charging current is also kept the same as in the simulation $30A$, however, the reference value for the ESS is generated by the droop control of the top layer. The HIL set-up is illustrated in Fig. 3.10. The HIL results show that the controller performed up to the mark in real-time as well. The zoomed-in parts of the different subplots depict the transient behavior of the state variables. It can be verified that the DC bus voltage can be regulated to its desired value. Moreover, the effective charging and discharging of the battery and SC proves the power sharing concept depending on the dynamic response of the storage system. The SC can provide a fast response to cope with sudden load changes. The stable charging current for an electric vehicle verifies the idea of integrating electric vehicles with microgrids and also provides the supporting argument for the successful development of an electric vehicle charging controller.

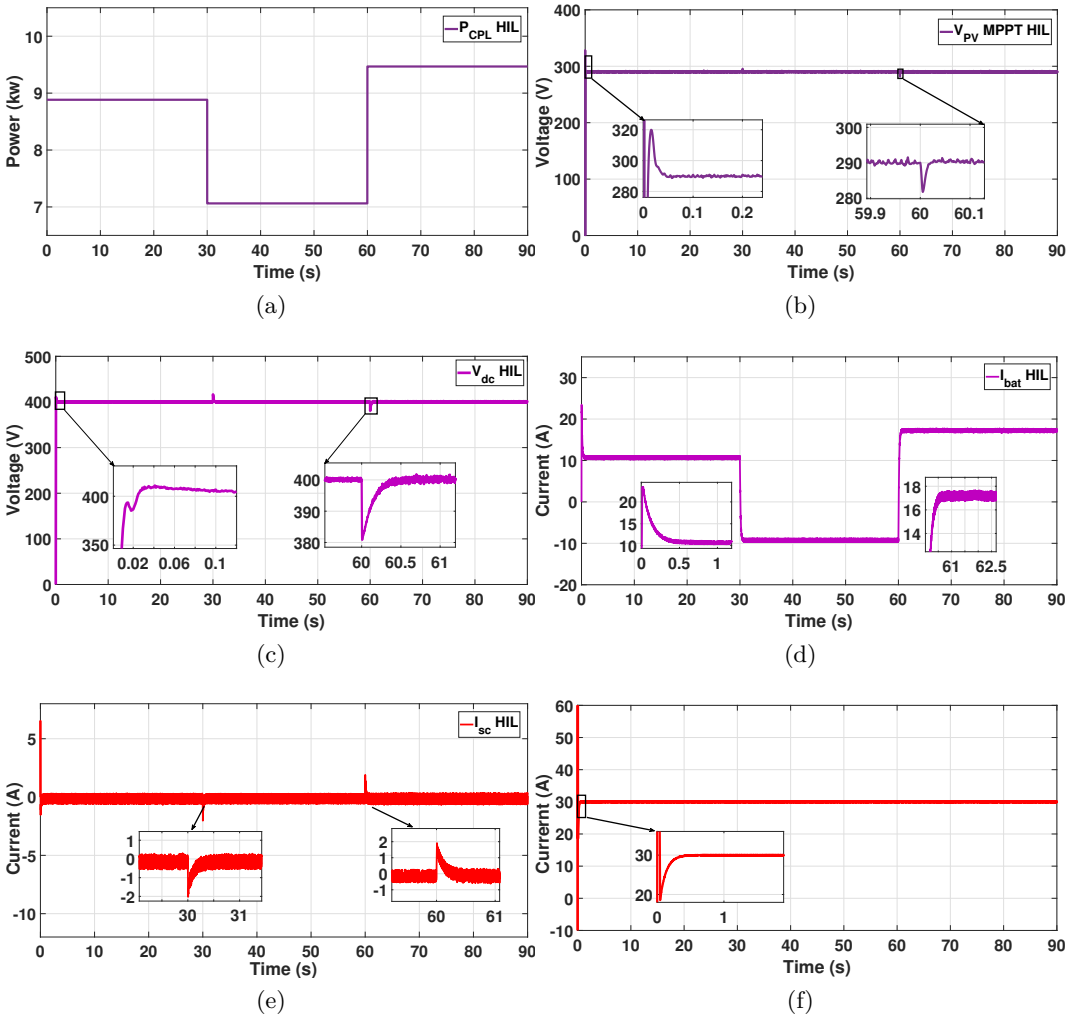

Figure 3.11: Hardware-in-loop based real-time results (a) Time-varying load power (b) PV voltage at MPPT in real-time (c) DC bus voltage response (d) Battery current response with charging and discharging (e) Super Capacitor current response (f) EV charging current in real-time.

3.5 Conclusion

The research introduces a two-layer control structure for optimal power sharing and a nonlinear switch controller for diverse power converters within a DC microgrid designed for e-mobility. This microgrid configuration integrates advanced converter topologies such as FSIBB and DAB, offering a broad operating range, bidirectional power flow, and seamless interaction with EVs. The chapter extensively discusses the mathematical analysis of the control design and closed-loop stability. Leveraging Lyapunov's theory, we explore the global stability of the system, affirming its stability under the proposed control measures. MATLAB/Simulink-based simulations are executed under various conditions to validate the controller performance. The results confirm that the primary control strategy effectively shares load power by

efficiently managing ESS charge and discharge cycles. Notably, the SC exhibits swift dynamic responses, compensating for the battery's slower dynamics, thereby confirming the efficacy of the enhanced droop control strategy. The adaptive nonlinear controller, evidenced by effective trajectory tracking with fast settling times and low steady-state, further substantiates the proposed approach's merit. Robustness testing confirms the self-compensation capability of the nonlinear controller, showcasing its resilience in managing unknown disturbances while minimizing controller gains. The proposed methodology prevents overestimation of gains and provides robustness against unforeseen disturbances without observer design. Comparison with state-of-the-art control methods concludes that the proposed controller has optimized response and also overcomes the issues related to traditional methods. Furthermore, HIL tests, executed using the Typhoon HIL 404 device, validate the real-time performance of the proposed controller. The real-time results provide the validity of the proposed method for practical implementations. This work will be expanded in future endeavors by incorporating advanced control algorithms and setting up a small-scale prototype. Furthermore, exploring the integration of DC microgrids and EVs with conventional power grids, coupled with robust control systems, presents an intriguing avenue for future research.

References

[1] F. S. Al Ismail, "Dc microgrid planning, operation, and control: A comprehensive review," *IEEE Access*, vol. 9, pp. 36 154–36 172, 2021.

[2] T. Dragičević, X. Lu, J. C. Vasquez, and J. M. Guerrero, "Dc microgrids—part i: A review of control strategies and stabilization techniques," *IEEE Transactions on power electronics*, vol. 31, no. 7, pp. 4876–4891, 2015.

[3] T. Dragi, X. Lu, J. C. Vasquez, and J. M. Guerrero, "Dc microgrids—part ii: A review of power architectures, applications, and standardization issues," *IEEE transactions on power electronics*, vol. 31, no. 5, pp. 3528–3549, 2015.

[4] H. Masrur, M. Shafie-Khah, M. J. Hossain, and T. Senjyu, "Multi-energy microgrids incorporating ev integration: Optimal design and resilient operation," *IEEE Transactions on Smart Grid*, vol. 13, no. 5, pp. 3508–3518, 2022.

[5] R. H. Ashique, Z. Salam, M. J. B. A. Aziz, and A. R. Bhatti, "Integrated photovoltaic-grid dc fast charging system for electric vehicle: A review of the architecture and control," *Renewable and Sustainable Energy Reviews*, vol. 69, pp. 1243–1257, 2017.

[6] L. E. Zubieta, "Are microgrids the future of energy?: Dc microgrids from concept to demonstration to deployment," *IEEE Electrification Magazine*, vol. 4, no. 2, pp. 37–44, 2016.

[7] F. Gao, R. Kang, J. Cao, and T. Yang, "Primary and secondary control in dc microgrids: A review," *Journal of Modern Power Systems and Clean Energy*, vol. 7, no. 2, pp. 227–242, 2019.

[8] J. Liu, W. Zhang, and G. Rizzoni, "Robust stability analysis of dc microgrids with constant power loads," *IEEE Transactions on Power Systems*, vol. 33, no. 1, pp. 851–860, 2017.

[9] S. Singh, A. R. Gautam, and D. Fulwani, "Constant power loads and their effects in dc distributed power systems: A review," *Renewable and Sustainable Energy Reviews*, vol. 72, pp. 407–421, 2017.

[10] L. Benadero, R. Cristiano, D. J. Pagano, and E. Ponce, "Nonlinear analysis of interconnected power converters: A case study," *IEEE Journal on Emerging and Selected Topics in Circuits and Systems*, vol. 5, no. 3, pp. 326–335, 2015.

[11] D. Regulated, "Supervisory control of an adaptive-droop regulated dc microgrid with battery management capability," 2013.

[12] M. Saleh, Y. Esa, and A. Mohamed, "Centralized control for dc microgrid using finite state machine," in *2017 IEEE Power & Energy Society Innovative Smart Grid Technologies Conference (ISGT)*, IEEE, 2017, pp. 1–5.

[13] A. Tah and D. Das, "An enhanced droop control method for accurate load sharing and voltage improvement of isolated and interconnected dc microgrids," *IEEE Transactions on Sustainable Energy*, vol. 7, no. 3, pp. 1194–1204, 2016.

[14] X. Li, L. Guo, S. Zhang, *et al.*, "Observer-based dc voltage droop and current feed-forward control of a dc microgrid," *IEEE Transactions on Smart Grid*, vol. 9, no. 5, pp. 5207–5216, 2017.

[15] M. Mokhtar, M. I. Marei, and A. A. El-Sattar, "An adaptive droop control scheme for dc microgrids integrating sliding mode voltage and current controlled boost converters," *IEEE Transactions on Smart Grid*, vol. 10, no. 2, pp. 1685–1693, 2017.

[16] L. Herrera, W. Zhang, and J. Wang, "Stability analysis and controller design of dc microgrids with constant power loads," *IEEE Transactions on smart grid*, vol. 8, no. 2, pp. 881–888, 2015.

[17] Z. Karami, Q. Shafiee, S. Sahoo, M. Yaribeygi, H. Bevrani, and T. Dragicevic, "Hybrid model predictive control of dc–dc boost converters with constant power load," *IEEE Transactions on Energy Conversion*, vol. 36, no. 2, pp. 1347–1356, 2020.

[18] R. R. Deshmukh, M. S. Ballal, and H. M. Suryawanshi, "A fuzzy logic based supervisory control for power management in multibus dc microgrid," *IEEE Transactions on Industry Applications*, vol. 56, no. 6, pp. 6174–6185, 2020.

[19] N. Chettibi, A. Mellit, G. Sulligoi, and A. M. Pavan, "Adaptive neural network-based control of a hybrid ac/dc microgrid," *IEEE Transactions on Smart Grid*, vol. 9, no. 3, pp. 1667–1679, 2016.

[20] V. Chapparya, A. Dey, and S. P. Singh, "A novel non-isolated boost-zeta interleaved dc-dc converter for low voltage bipolar dc micro-grid application," *IEEE Transactions on Industry Applications*, 2023.

[21] Z. Xiao, W. Lei, G. Gao, X. Zhang, and L. Hu, "Dual-terminal voltage feedforward based direct power control scheme and stability analysis of dual active bridge converter in dc microgrid systems," *IEEE Transactions on Power Electronics*, vol. 38, no. 4, pp. 4475–4492, 2022.

[22] D. Das, M. J. Hossain, S. Mishra, and B. Singh, "Bidirectional power sharing of modular dabs to improve voltage stability in dc microgrids," *IEEE Transactions on Industry Applications*, vol. 58, no. 2, pp. 2369–2377, 2022.

[23] H.-S. Lee and J.-J. Yun, "High-efficiency bidirectional buck–boost converter for photovoltaic and energy storage systems in a smart grid," *IEEE Transactions on Power Electronics*, vol. 34, no. 5, pp. 4316–4328, 2019. DOI: 10.1109/TPEL.2018.2860059.

[24] S. R. Khasim, C. Dhanamjayulu, and S. M. Muyeen, "A single inductor multiport power converter for electric vehicle applications," *IEEE Access*, vol. 11, pp. 3367–3385, 2023. DOI: 10.1109/ACCESS.2023.3234105.

[25] Q. Xu, N. Vafamand, L. Chen, T. Dragičević, L. Xie, and F. Blaabjerg, "Review on advanced control technologies for bidirectional dc/dc converters in dc microgrids," *IEEE Journal of Emerging and Selected Topics in Power Electronics*, vol. 9, no. 2, pp. 1205–1221, 2020.

[26] M. M. Mardani, M. H. Khooban, A. Masoudian, and T. Dragičević, "Model predictive control of dc–dc converters to mitigate the effects of pulsed power loads in naval dc microgrids," *IEEE Transactions on Industrial Electronics*, vol. 66, no. 7, pp. 5676–5685, 2018.

[27] Y. Yu, G.-P. Liu, and W. Hu, "Coordinated distributed predictive control for voltage regulation of dc microgrids with communication delays and data loss," *IEEE Transactions on Smart Grid*, vol. 14, no. 3, pp. 1708–1722, 2022.

[28] Q. Xu, X. Hu, P. Wang, *et al.*, "A decentralized dynamic power sharing strategy for hybrid energy storage system in autonomous dc microgrid," *IEEE transactions on industrial electronics*, vol. 64, no. 7, pp. 5930–5941, 2016.

[29] S. Laghrouche, M. Harmouche, Y. Chitour, H. Obeid, and L. M. Fridman, "Barrier function-based adaptive higher order sliding mode controllers," *Automatica*, vol. 123, p. 109 355, 2021.

[30] B. Wang, U. Manandhar, X. Zhang, H. B. Gooi, and A. Ukil, "Deadbeat control for hybrid energy storage systems in dc microgrids," *IEEE Transactions on Sustainable Energy*, vol. 10, no. 4, pp. 1867–1877, 2019. DOI: 10.1109/TSTE.2018.2873801.

[31] V. Kumar, S. R. Mohanty, and S. Kumar, "Event trigger super twisting sliding mode control for dc micro grid with matched/unmatched disturbance observer," *IEEE Transactions on Smart Grid*, vol. 11, no. 5, pp. 3837–3849, 2020.

[32] M. J. Carrizosa, A. Iovine, G. Damm, and P. Alou, "Droop-inspired nonlinear control of a dc microgrid for integration of electrical mobility providing ancillary services to the ac main grid," *IEEE Transactions on Smart Grid*, vol. 13, no. 5, pp. 4113–4122, 2022.

[33] M. H. Rashid, *Power electronics handbook*. Butterworth-heinemann, 2017.

[34] S. S. Zehra, A. U. Rahman, and I. Ahmad, "Fuzzy-barrier sliding mode control of electric-hydrogen hybrid energy storage system in dc microgrid: Modelling, management and experimental investigation," *Energy*, vol. 239, p. 122 260, 2022.

[35] V. Castiglia, N. Campagna, A. O. Di Tommaso, *et al.*, "Modeling, simulation, and characterization of a supercapacitor in automotive applications," *IEEE Transactions on Industry Applications*, vol. 58, no. 2, pp. 2421–2429, 2022.

[36] A. U. Rahman, N. Campagna, A. Di Tommaso, R. Miceli, A. Damiano, and A. Floris, "Advanced control analysis of single inductor four switch non-inverting buck-boost converter for energy storage units," in *2023 International Conference on Clean Electrical Power (ICCEP)*, IEEE, 2023, pp. 267–272.

[37] J. Mahdavi, A. Emaadi, M. Bellar, and M. Ehsani, "Analysis of power electronic converters using the generalized state-space averaging approach," *IEEE Transactions on Circuits and Systems I: Fundamental Theory and Applications*, vol. 44, no. 8, pp. 767–770, 1997.

[38] S. Shao, L. Chen, Z. Shan, *et al.*, "Modeling and advanced control of dual-active-bridge dc–dc converters: A review," *IEEE Transactions on Power Electronics*, vol. 37, no. 2, pp. 1524–1547, 2021.

[39] M. Arsalan, R. Iftikhar, I. Ahmad, A. Hasan, K. Sabahat, and A. Javeria, "Mppt for photovoltaic system using nonlinear backstepping controller with integral action," *Solar energy*, vol. 170, pp. 192–200, 2018.

Chapter 4

DC Microgrid: A Cascade Nonlinear Control of Interleaving Converters for Power to Hydrogen System

4.1 Introduction

The transition towards RES leads to several benefits due to the opportunity to decentralize energy production, thus reducing transmission line power losses and providing energy to remote and rural areas. Regarding the technological challenges related to the increasing use of RES, HESS, and MG are the most attractive solutions to manage the electrical energy arising from renewable sources [1], [2]. HESS promises to collect energy to be subsequently used when solar, wind, and other available RES cannot provide enough power to the load [3]. The hybrid solution aims at properly modulating energy or power density according to the users requirements: for example, batteries and fuel cells guarantee high energy density and therefore can provide long-term demand, whereas supercapacitors offer high power density, thus supporting short-term power peaks [4]. As far as MG is concerned, they implement the local platform to which RES, HESS, and loads are connected, thanks to the fundamental support of electrical converters [5], [6]. The recent advancements in the design and control of power electronics specifically of AC-DC converters have contributed to the increasing presence of DC loads concerning AC loads, thus giving the significantly beneficial possibility to implement DC MGs [7]. DC microgrids improve energy efficiency by eliminating conversion losses between AC and DC, which is ideal for renewable energy sources like solar panels and batteries that naturally generate DC. They also reduce infrastructure costs, enhance reliability through islanded operation, and offer scalability for integrating more energy sources or loads

in the future [8]. The DC microgrid can be connected to the conventional power grids for a hybrid or grid-connected solution [9]. On the other hand, the hydro-

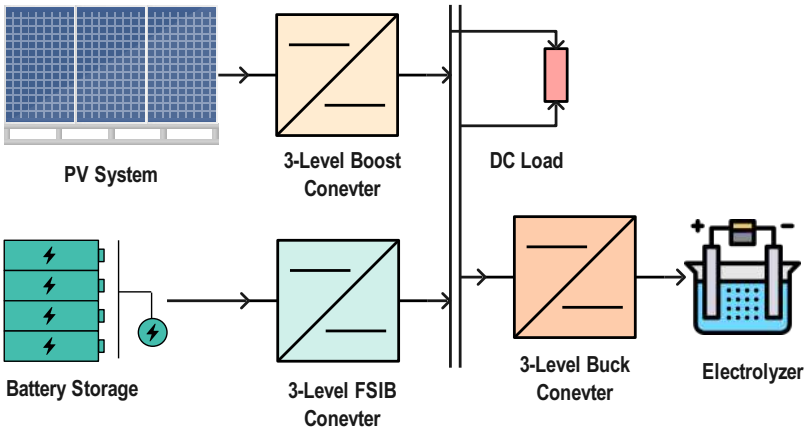

Figure 4.1: The Power-to-Hydrogen system in DC microgrid.

gen energy system stands poised to revolutionize the energy industry. Extensive research and development efforts have been dedicated to advancing hydrogen production through electrolyzer [10], [11]. However, it is crucial to note that hydrogen production necessitates a significant power input for the chemical process [12]. Renewable energy sources (RES), particularly solar and wind energy, have emerged as promising candidates for powering hydrogen production processes. Integrating these renewable resources with electrolysis technologies holds tremendous potential for enabling sustainable and environmentally friendly hydrogen production at scale [13], [14]. Hydrogen fuel is also getting attention in the e-mobility sector in the form of fuel-cell electric vehicles due to their long driving range and zero carbon emission [15], [16]. In this scenario, power converters play a vital role in all these modern power system technologies i.e. EVs and MGs. High penetration of power converters also raised the question related to stability and proper control of the system [17], [18]. Advanced power converters can sufficiently increase efficiency and safety with high power transfer [19]. The multilevel interleaving converter topology gained attention due to low output ripples, high power applications, and ease of configuration in case of fault [20]. The basic principle of interleaving converters can be defined as identical converters connected in parallel working with different phase shifts [21]. Interleaving converter topology reduces output ripple and improves efficiency, enabling fault-tolerant systems, which leads to more compact designs, better thermal management, and enhanced reliability in real systems [22]. However, the topology requires a more sophisticated control system for these advantages. Different control methods have recently been proposed for Interleaving power converters [23]. This chapter investigates the cascaded lyapunov-based control of multiple interleaving converters to power an electrolyzer for hydrogen production and to feed the constant power loads in a DC microgrid. The DC microgrid can be termed a multi-agent system

in which different renewable energy sources, power-converting units, and loads act according to their dynamics. One of the key control problems in the DC microgrid is to develop a decoupled control strategy to enhance the overall performance and stability of the system [24]. Previously, a single interleaving topology and control system for different applications was studied in most studies. However, the interactive system with multiple interleaving converters has not been studied in depth [25], [26]. Traditionally, linear controllers based on the PI algorithm are advised for the Interleaving power converters [27], [28]. Linear controllers are designed using the linearized model which does not guarantee stability in large systems with multiple agents involved. In most studies, only one converter with a single input and single out is studied lacking of a large system stability analysis. In [29] a finite control set model predictive control is advised for symmetric and asymmetric interleaving converters. The proposed control optimally deals with the balancing between different phases. However, the computational cost can be an obstacle to large-scale implementation. Nonlinear control theory also provides a decent solution for controlling and maintaining the system's large signal stability. Some nonlinear control algorithms are also proposed for the different interleaving converter topologies in [30]–[32]. These studies proposed sliding mode-based backstepping and observer-based control for interleaving converter topology but considered only symmetric boost converter in stand-alone conditions. Moreover, issues such as the chattering effect of sliding mode control, the complexity of backstepping control, and extensive observer design can be improved. This chapter investigates three types of interleaving power converters in a DC MG. To solve the control problem a simplified cascaded lyapunov-based hybrid controller is developed. The contribution of this study can be summed up in points as follows:

- A large-scale mathematical model of the DC microgrid with interleaving power converters is developed.
- A cascaded Lyapunov-based hybrid controller for a DC microgrid system involving different interleaving converters is derived and advised.
- The large signal stability analysis of the system is carried out using the Lyapunov theory. Moreover, the current balancing approach is also used to minimize the output ripples.
- The proposed control scheme is verified through numerical simulation and real-time control prototyping.

Table 4.1: Comparative analysis of proposed closed-loop system.

Ref.	[33]	[34]	[35]	**Proposed**
Controller	PI	DPI	SMC	PI+NL
CPL Test	NO	NO	-	YES
Converter Topology	Quadratic	Traditional	TLIBC	Interleaving
HESS Control	-	YES	-	YES
Large signal Stability	-	NO	YES	YES

Table 4.1 presents the comparative analysis of the proposed method with some closely existing studies in the literature.

4.2 Microgrid System Description

Fig. 4.1 shows the overall structure of the system integrating RES, BESS, load, and electrolyzer load. Three-level DC-DC converters are deployed with each power source for power sharing between the source and the DC Bus. The composition of a DC microgrid consists of a PV panel used as the main power source and the battery as a backup, which also compensates during different power generation scenarios. The parameters of PV and battery storage systems are shown in the table below.

Table 4.2: DC microgrid parameters and values.

PV system	
Parameter	**Value**
Number of panels (series * Parallel)	4*4
Number of cells per module	60
Open circuit voltage Voc	36.3 V
Short-circuit current Isc	7.84 A
Capacitance C_{pv}, C_{o1}	10 , 500 μF
Inductor $L_{1,2,3}$	5e-4 H
Maximum Power P_{max}	3.410 kW
Battery Storage System (BSS)	
Battery nominal Voltage	120 V
Rate Capacity	120 Ah
Battery response time	10 s
Initial SoC battery	80 %

Fig. 4.2 shows the discharge characteristics of the battery model. The lithium-

ion battery model has been used for analysis in this study. The graph is plotted during the different current discharge values against the time value shown on the x-axis. The electrolyzer is used as a potential application for the accessive energy to convert electrical energy into hydrogen fuel. Renewable DC MG provides the power for the electrolysis process through an interleaving buck converter. The electrolyzer dynamic equivalent electrical circuit model is considered to test the proposed method against dynamic behavior. In Fig. 4.3, the electrical behavior of the system is represented by two RC branches (R_a, C_a) for the anode side and (R_c, C_c) for the cathode side. These branches effectively model the dynamic responses of the anode and cathode under transient conditions. The presence of these branches captures the intricate charge storage and transfer processes that occur within the electrochemical system during transient operation.

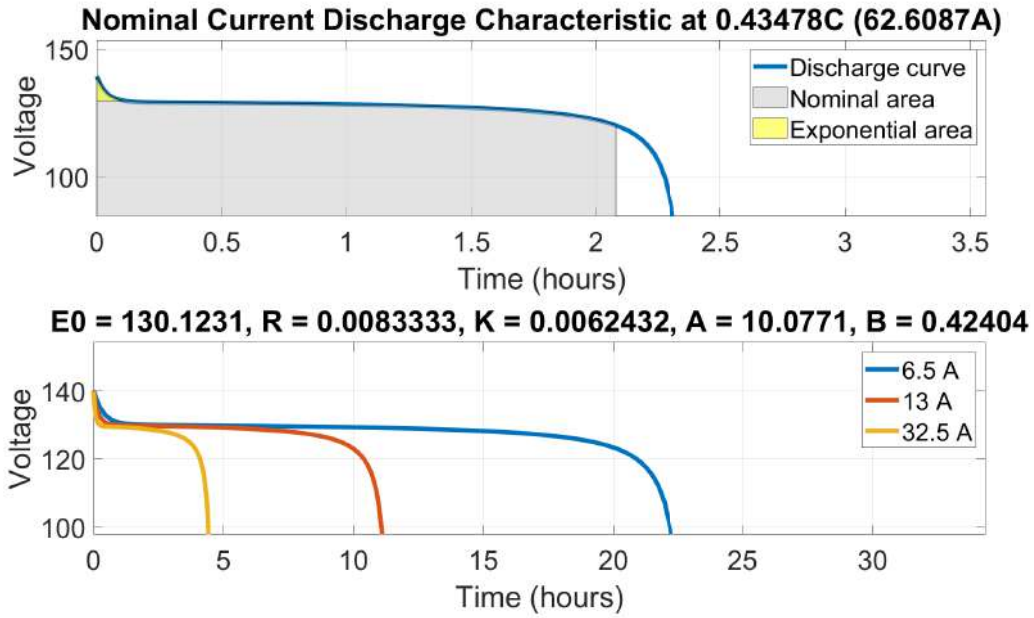

Figure 4.2: Battery charging and discharging curves.

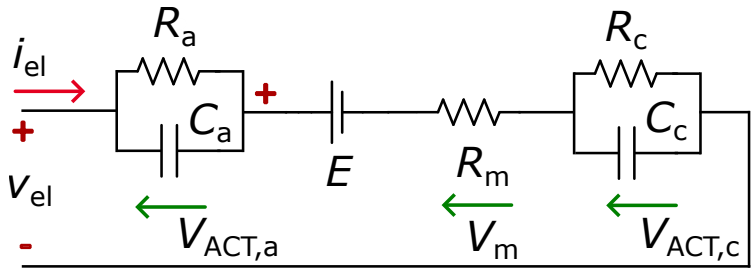

Figure 4.3: The equivalent electrical circuit of electrolyzer model.

In addition to the RC branches, the resistor R_m models the ohmic losses that occur in the membrane. This resistor accounts for the voltage drop that arises due to the membrane's inherent resistance to ion transport. Meanwhile, The overall

DC voltage is represented as the reversible voltage (E), which signifies the energy converted into hydrogen during the electrochemical reaction. The elemental parameters of the system, such as R_a, C_a, R_c, C_c and R_m, are essential for characterizing its performance under both steady-state and dynamic conditions. A least-squares regression technique is employed to estimate these parameters accurately. This method allows calculating the time constant associated with the transient behavior of the system, providing insight into how quickly the system responds to changes in operational conditions [35].

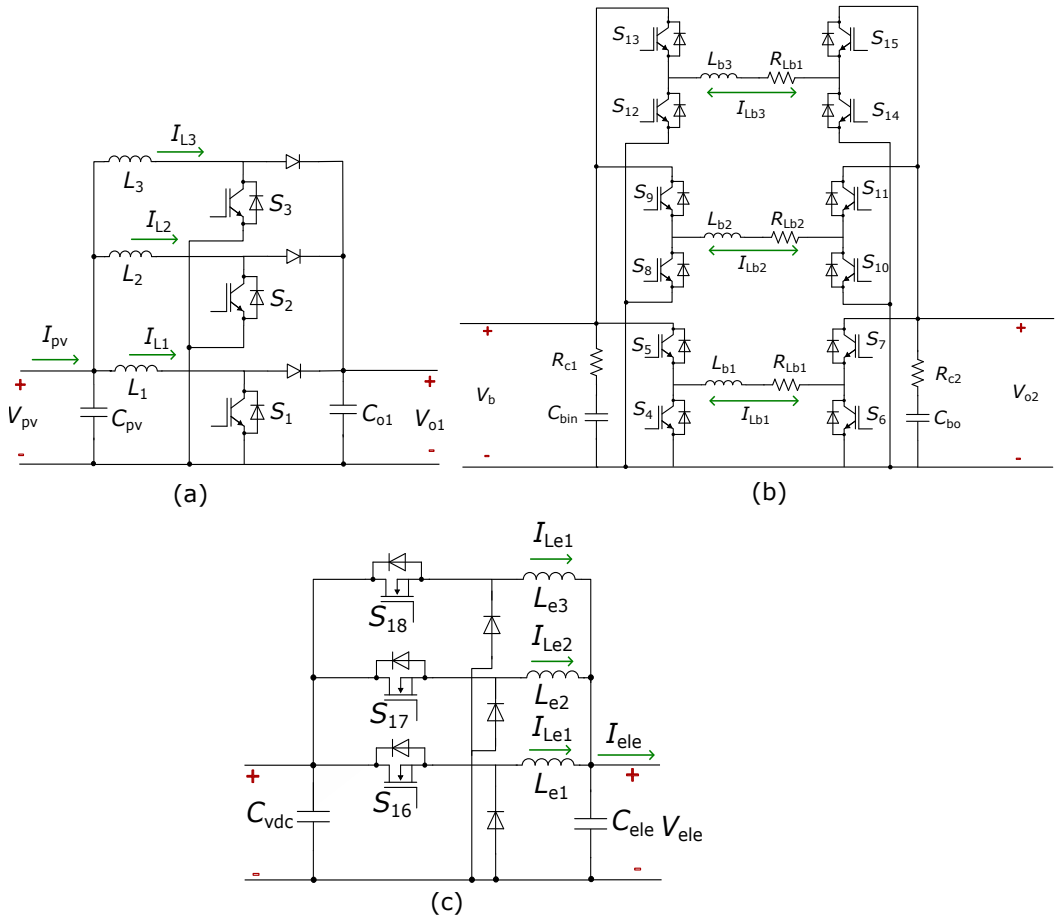

Figure 4.4: The three-level interleaving power converters in DC microgrid (a) three-level boost converter for PV system (b) Three-level IFSIBB Converter for Battery storage system (c) Three-level buck converter for electrolyzer system.

4.3 Interleaving Power Converter Topologies and Modeling

Fig. 4.4 presents the interleaved three-level power converters. In particular, Fig. 4.4a shows a three-level boost converter connected to the PV system, the basic working principle of the converter is the same as a traditional boost converter however in this topology the power can be transferred through all three inductors si-

multaneously. Similarly, IFSIBB and interleaving buck are advised for battery and electrolyzer systems and depicted in Fig. 4.4b and Fig. 4.4c, respectively. The switches $S_1, ...S_{18}$ control the system to acquire the desired current and voltages. The nonlinear dynamic model of the system is developed by considering converter topology and microgrid structure. The mathematical analysis is derived using KCL and KVL over one complete duty cycle. The average mathematical model of the proposed DC can be represented below:

$$
\begin{aligned}
\dot{x}_1 &= \frac{1}{C_{pv}}(I_{pv} - \sum_{i=1}^{N} x_{1i}),\\
\dot{x}_{2i} &= \frac{1}{L_i}(-(1-u_i)x_3 + V_{pv}),\\
\dot{x}_3 &= \frac{1}{C_{o1}}(\sum_{i=1}^{N}(1-u_i)x_{1i} - \frac{x_3}{R}),\\
\dot{x}_{4i} &= \Big((P_1+P_2)x_{4i} + \frac{R_i}{R_1 L}x_5 +\\
&\quad + \frac{r_{c1}}{R_1 L}V_b + \frac{R}{R_2 L}x_5\Big)\cdot ub_i\\
&\quad - \frac{R}{R_2 L}x_6 - \frac{R_2 r_{Li} + R r_{c2}}{R_2 L}x_{4i},\\
\dot{x}_5 &= \frac{1}{R_1 C_{bin}}V_b - \frac{1}{R_1 C_{bin}}x_5 - \frac{R_i}{R_1 C_{bin}}\sum_{i=1}^{N} x_{4i}\cdot ub_i,\\
\dot{x}_6 &= \frac{R}{R_2 C_{bo}}x_5 - \frac{1}{R_2 C_{bo}}x_6 - \frac{R}{R_2 C_{bo}}\sum_{i=1}^{N} x_{4i}\cdot ub_i,\\
\dot{x}_{7i} &= \frac{1}{L_{ei}}\Big(x_8 + v_{dc}\cdot ue_i\Big),\\
\dot{x}_8 &= \frac{1}{C_{ele}}\Big(\sum_{i=1}^{N} x_{7i} - \frac{x_8}{R}\Big).
\end{aligned}
\tag{4.1}
$$

Where $i = 1, 2, 3$ represents each phase of the interleaving converters. Eq. 4.1 presents the 8^{th} order averaged state-space model further used for the control derivation. Where

$$R_1 = R_i + R_{c1},\ R_2 = R + R_{c2}$$

are the sum of internal resistance. The state $x_1 ... x_8$ shows the input PV voltage, interleaving boost converter current, output voltage of PV-Boost module, Input Voltage of IFSIBB converter, Current of IFSIBB, output voltage of IFSIBB converter, Inductor current of interleaving buck, and output voltage for electrolyzer. u_i, ub_i, and ue_i are the system's control inputs. The model-based control derivation is explained in the section below.

4.3.1 Backstepping Control Algorithm

Backstepping control is a nonlinear control method that's great for handling complex systems with dynamic behaviors. It works by designing control laws through the system's dynamics step by step, which helps manage nonlinearities and uncertainties effectively. This makes it useful for systems like renewable energy setups, where things can be unpredictable. Backstepping control adapts to changing conditions and disturbances, making it robust and reliable. Plus, it provides a clear framework for designing controllers, making it easier to understand and implement. To avoid putting lengthy derivation of each controller, the basic algorithm is presented as follows. Let's consider a second-order generic model as:

$$\begin{cases} \dot{\theta_1} = \theta_2 \\ \dot{\theta_2} = u \end{cases} \tag{4.2}$$

The error signal for the first control loop can be written as:

$$e_1 = \theta_{1ref} - \theta_1 \tag{4.3}$$

Taking the time derivative of the error signal it becomes:

$$\dot{e_1} = \dot{\theta}_{1ref} - \dot{\theta}_1 \tag{4.4}$$

Putting the value of $\dot{\theta_1}$, the equation takes the following form:

$$\dot{e_1} = \dot{\theta}_{1ref} - \theta_2 \tag{4.5}$$

Considering the Lyapunov function for stability as:

$$V = \frac{1}{2}(e_1)^2 \implies \dot{V} = e_1\dot{e_1} \tag{4.6}$$

To be sure about the system's stability following assumption is considered:

$$\dot{e_1} = -c_1 e_1 \tag{4.7}$$

where c_1 is the positive gain of the controller. Based on this assumption the eq. 4.5 can be written as:

$$-c_1 e_1 = \dot{\theta}_{1ref} - \theta_2 \tag{4.8}$$

$$\theta_2 = \dot{\theta}_{1ref} + c_1 e_1 = \alpha \tag{4.9}$$

Here the α is the reference for the second step of the backstepping controller. So the second error becomes:

$$e_2 = \alpha - \theta_2 \implies \theta_2 = \alpha - e_2 \tag{4.10}$$

Updating Error

The error updating is a very important step to follow, to ensure the stability of the system. Putting the above value of α_2 in eq.4.5, we get:

$$\dot{e_1} = \dot{\theta}_{1ref} - \dot{\theta}_{1ref} - c_1 e_1 + e_2 \tag{4.11}$$

So the Lyapunov function became,

$$\dot{V} = -c_1 e_1^2 + e_1 e_2 \tag{4.12}$$

Second Step

This is the final step to obtain the control input u, taking the time derivative of eq. 4.10, we get:

$$\dot{e}_2 = \dot{\alpha} + u \tag{4.13}$$

Embedding the second error function and calculation of the combined Lyapunov function gives:

$$\dot{V}_c = -c_1 e_1^2 + (e_1 + \dot{e_2}) e_2 \tag{4.14}$$

To make the time derivative of the Lyapunov function negative definite, we considered,

$$e_1 + \dot{e_2} = -c_2 e_2 \tag{4.15}$$

Putting Value of $\dot{e}_2$ and solving it for control input u gives:

$$u_{eq} = -e_1 - \dot{\alpha} - c_2 e_2 \tag{4.16}$$

for robustness, a switching control action can be added to get the final control action:

$$u_{sw} = k \left| e \right|^{\beta} sgn \left(\frac{e}{\gamma} \right) \tag{4.17}$$

$$u = u_{eq} + u_{sw} \tag{4.18}$$

Using this approach the control inputs u_i, ub_i, ue_i are derived for the proposed model and shown below:

$$\begin{aligned} u_i = (\frac{L_i}{x_2})(x_{1ref} + c_2 e_2 + \frac{x_2}{L_i} + \frac{V_{pv}}{L} + \dot{\alpha_1} \\ + \frac{e_1}{C_{pv}} - k_1 \left|e_2\right|^{\beta} sign\left(\frac{e_2}{\gamma}\right)) \\ \dot{ub_i} = \frac{ub_i}{\alpha_2}\Big(c_4 e_4 + \frac{1}{p(ub_i - 1)} T(e3, e4) \\ -\dot{x_6} - (P(ub_i) + 1)e_3 - k_2 \left|e_4\right|^{\beta} sign\left(\frac{e_4}{\gamma}\right))\Big) \\ ue_i = \Big(\frac{Le_i}{Vdc}\Big(c_6 e_6 + \frac{c_5}{C_{ele}} + \dot{\alpha_3} + \frac{x_8}{L_{ele}} - \\ k_3 \left|e_6\right|^{\beta} sign\left(\frac{e_6}{\gamma}\right)\Big)\Big) \end{aligned} \tag{4.19}$$

where $c_{1..6}$ are the positive gains of the proposed control signals. β, γ are the weighting factors of the switching control to reduce the chattering effect of the controller. P and (e_3, e_4) represent the sum of resistance and error functions respectively. the control input for the i^th stage can be derived through the same method with a phase shift modulation mathematical expressed as:

$$\phi_n = (n-1).\frac{360}{N} \tag{4.20}$$

where ϕ is the phase shift and n is the considered phase. N represents the total number of the stage.

Stability Analysis

The closed-loop stability analysis can be conducted by using the Lyapunov theory. The time derivative of the combined Lyapunov function is given in eq. 4.14 as follow:

$$\dot{V_c} = -c_1 e_1^2 + (e_1 + \dot{e_2})e_2 \tag{4.21}$$

Putting the value of the controllers given in eq. 4.19, the final Lyapounv function will be:

$$\dot{V_c} = \sum_{i=1}^{6} e_i(-a_1 \left|e_i\right|^{\alpha} sign\,(\,\frac{e_i}{\rho_1})) \tag{4.22}$$

where

$$\begin{aligned} e_i\, sign\,(\,\frac{e_i}{\rho_1}) \geq 0 \; for\; all\; e_i \in R \\ a_1 |e_i|^{\alpha} \geq 0 \end{aligned}$$

So this concludes that

$$\dot{V}_c < 0 \; for \; all \; e_i \in R \tag{4.23}$$

This analysis shows that the closed-loop controller is globally stable. The negative definite Lyapunov function confirms the convergence of the error function to the equilibrium point.

4.3.2 Cascaded Lyapunov-based Hybrid Controller

Designing a proper control system is crucial to achieving efficient performance from all the sources and coordinates of the system. The overall control objectives can be subdivided into the following points:

- MPPT working of PV system and droop control design for DC bus voltage regulation,
- Cascased Lyapunov-based hybrid control for current and voltage control and current balancing in Interleaving converters,
- Stability analysis of large-scale closed-loop system.

The closed-loop PV system is designed to operate at Maximum Power Point Tracking (MPPT). An MPPT controller is recommended to extract the maximum power, contingent upon temperature and irradiance values to achieve this condition. As weather parameters influence PV power, the output PV power remains variable rather than constant [36], [37]. The optimized linear regression [37] gives the expression to get the MPP using the temperature and irradiance value and expressed as

$$v_{mppt} = 332 + 1.34 \cdot T_{emp} - 0.00964 \cdot I_{irr}. \tag{4.24}$$

Here, v_{mppt}, T_{emp}, and I_{irr} represent the MPPT voltage, temperature value, and irradiance, respectively. Where the constant numeric coefficients represent the parameters of the regression equation. The expression determines the maximum power point, while the proposed cascaded controller tracks the reference value and attains maximum output power.

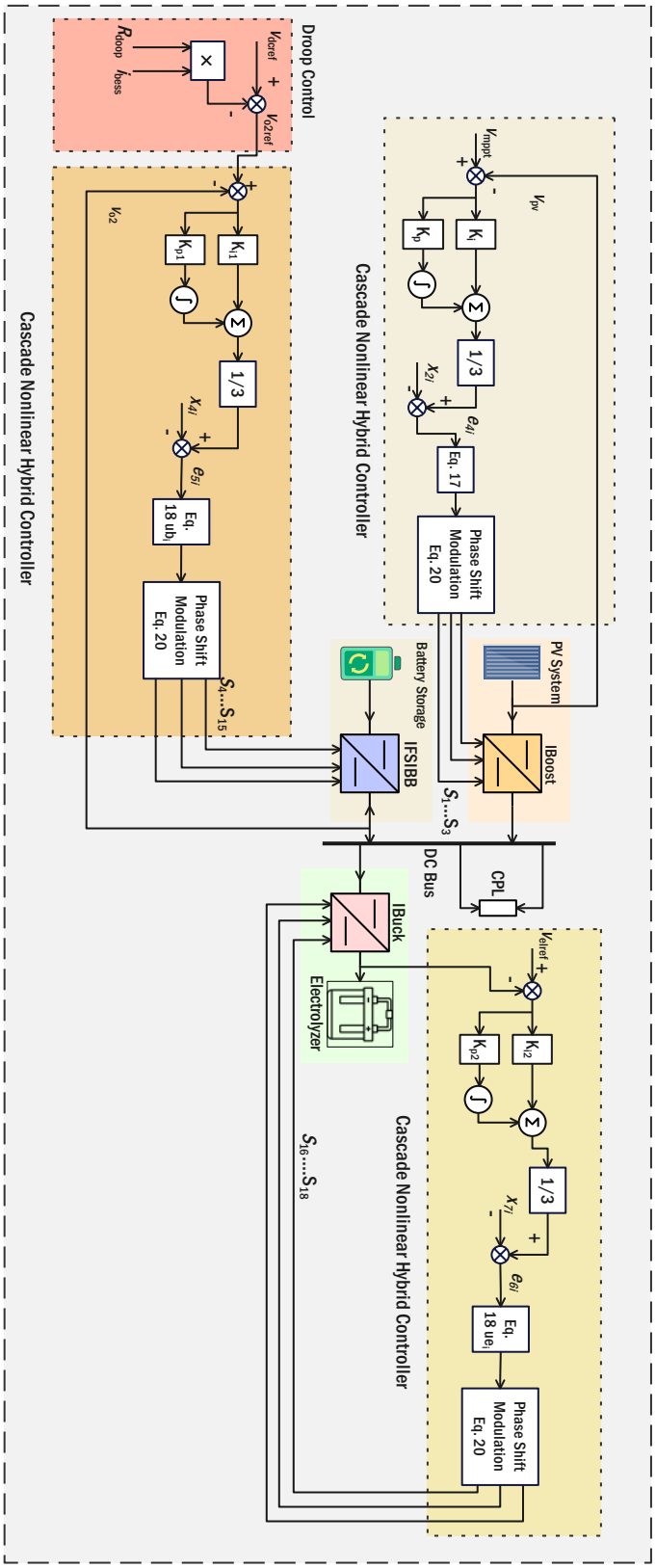

Figure 4.5: Proposed closed-loop control structure.

The traditional droop control method is proposed due to its simplicity and good performance for DC bus voltage regulation. The current request from the battery energy storage system (BESS) can be expressed as

$$i_{bess} = i_{load} - i_{pv}. \tag{4.25}$$

The output voltage reference for the IFSIBB converter can be expressed as:

$$v_{o2ref} = v_{vdcref} - R_{droop} \cdot i_{bess}. \tag{4.26}$$

where R_{droop} is the virtual resistance incorporated to regulate the DC bus voltage through the storage system. The R_{droop} can be expressed mathematically as [38]:

$$R_{droop} = \frac{v_{dcmax} - v_{vdcmin}}{i_{bmax}}. \tag{4.27}$$

v_{vdcmin} and v_{vdcmax} are the maximum and minimum allowable DC bus voltage. i_{bmax} is the maximum allowable current of the IFSIBB converter. The droop control algorithm aims to regulate DC bus voltage through BESS. Fig. 4.5 shows the overall closed-loop control structure to better illustrate control strategy. The low-level cascaded control of power converters is derived and explained below.

4.3.3 Switching Control Algorithm

Lyapunov's theory provided a systematic way to approach the system stability in the time domain analysis. The theory has a wide range of applications in different fields including intelligent energy systems. The so-called Lyapunov redesign is known as a nonlinear control method which is purely based on Lyapunov theory. It works by designing control laws through the system dynamics step by step, which helps manage nonlinearities and uncertainties effectively. This makes it useful for systems like renewable energy setups and microgrids, where things can be unpredictable. Lyapunov-based control adapts to changing conditions and disturbances, making it robust and reliable. Plus, it provides a clear framework for designing controllers, making it easier to understand and implement. In this chapter, a cascaded lyapunov-based hybrid controller is advised for multilevel power DC-DC converters operating in a DC MG. The term cascaded indicates the presence of two control loops (*i.e.* voltage loop and current loop working in a cascaded form). The outer control loop is designed using a linear PI regulator and the inner loop is derived using Lyapunov theory, illustrating the hybrid control concept. The error functions for the outer

loop can be defined as:

$$\begin{cases} e_1 = v_{mppt} - x_1, \\ e_2 = v_{boref} - x_6, \\ e_3 = v_{eleref} - x_8. \end{cases} \tag{4.28}$$

The role of the voltage loop is to track the desired voltage while generating the current reference. The mathematical expression for the designed PI regulator is expressed as:

$$\begin{aligned} x^*_{2iref} &= \frac{1}{3}\left[K_{p1}(e_1) + K_{i1}\int_0^t (e_1)\right], \\ x^*_{4iref} &= \frac{1}{3}\left[K_{p2}(e_2) + K_{i2}\int_0^t (e_2)\right], \\ x^*_{7iref} &= \frac{1}{3}\left[K_{p3}(e_3) + K_{i3}\int_0^t (e_3)\right]. \end{aligned} \tag{4.29}$$

where $x^*_{2iref}, x^*_{4iref}, x^*_{7iref}$ indicate the reference values for IBoost, IFSIBB, and IBuck, respectively. The inner-loop current controller is derived using the Lyapunov redeign theorem. The theorem also provides information about the stability of nonlinear time-varying systems. The system is stable if the following theorem is justified [39].

Lemma 1: The nonlinear time-varying system is stable if

$$\begin{cases} V(0) = 0, \\ \alpha(||e||) < V(e) < \beta(||e||), \\ \dot{V}(e) = -\gamma(||e||), \\ \lim_{t\to\infty} V(t) \implies ||e|| \longrightarrow \infty. \end{cases} \tag{4.30}$$

where $V(e)$ is the Lyapunov candidate function and the idea behind taking the Lyapunov candidate as a function of the error signal is to determine the system stability in terms of tracking. The variables α, β, γ always have a positive definite value. The inner loop error functions are defined as:

$$\begin{cases} e_{4i} = x^*_{2iref} - x_{2i}, \\ e_{5i} = x^*_{4iref} - x_{4i}, \\ e_{6i} = x^*_{7iref} - x_{7i}. \end{cases} \tag{4.31}$$

Considering the following Lyapunov function:

$$\begin{aligned} V(e_{4,5,6}) &= \frac{1}{2}e_{4i}^2 + \frac{1}{2}e_5^2 + \frac{1}{2}e_6^2, \\ V(e_{4,5,6}) &= V_1 + V_2 + V_3, V(e) = E^T P E. \end{aligned} \tag{4.32}$$

where the P matrix represents the eigenvalues of the system. The Lyapunov function is then solved to obtain the switch control law. For the simplification, it is here solved for the e_{4i} and the methodology can be extended to all error functions of the inner loop. From equation (4.32), V_1 is given by:

$$V_1 = \frac{1}{2}e_{4i}^2. \tag{4.33}$$

Taking the time derivative of the Lyapunov function V_1 and putting the value of e_{4i} from the equation (4.31):

$$\dot{V}_1 = e_{4i}(\dot{e}_4). \tag{4.34}$$

To make the time derivative of the Lyapunov function, it can be assumed:

$$\dot{e}_4 = -c_1 e_{4i}. \tag{4.35}$$

However as from the equation (4.31) it is evident that the time derivative of e_{4i} presented as:

$$\dot{e}_{4i} = \dot{x}_{2ref}^* - \dot{x}_2. \tag{4.36}$$

Comparing equations (4.35) and (4.36):

$$-c_1 e_{4i} = \dot{x}_{2ref}^* - \dot{x}_2. \tag{4.37}$$

Putting value of $\dot{x}_2$ the above expression takes the following form:

$$-c_1 e_{4i} = \dot{x}_{2ref}^* - \frac{1}{L_i}(-(1-u_i)x_3 + V_{pv} \tag{4.38}$$

Solving equation (4.38) for control input u_i, it is obtained that:

$$u_i = \frac{L_i}{x_3}\left[\dot{x}_{2ref}^* + \frac{x_3}{L_i} + c_1 e_{4i} + V_{pv}\right]. \tag{4.39}$$

Using this approach the control inputs ub_i, ue_i are derived for the proposed model and shown below:

$$\begin{aligned} ub_i &= T \cdot \left[\frac{R}{R_2 L} x_6 + \right. \\ &\left. + \frac{R_2 r_{Li} + R r_{c2}}{R_2 L} x_{4i} + \dot{x}_{4iref} + c_2 e_{5i} \right], \\ ue_i &= \frac{L_{ei}}{v_{dc}} \left[\dot{x}_{7iref} - \frac{x_8}{L_{ei}} + c_3 e_{6i} \right]. \end{aligned} \tag{4.40}$$

where

$$T = \frac{1}{\left((P_1 + P_2) x_{4i} + \frac{R_i}{R_1 L} x_5 + \frac{r_{c1}}{R_1 L} V_b + \frac{R}{R_2 L} x_5 \right)} \tag{4.41}$$

and $c_{1..3}$ are the positive gains of the proposed control signals. P_1 and P_2 represent the sum of internal resistances of passive components in IFSIBB. The control input for the i^{th} stage can be derived through the same method with a phase shift modulation mathematical expressed as:

$$\phi_n = (n-1).\frac{360}{N}. \tag{4.42}$$

where ϕ is the phase shift and n is the considered phase. N represents the total number of the stage.

4.3.4 Stability Analysis

The closed-loop stability analysis can be conducted by using the Lyapunov theory. The time derivative of the combined Lyapunov function is given in (4.32) as follow:

$$\dot{V}(t)_(e_4, e_5, e_6) = \dot{V}(t)_1 + \dot{V}(t)_2 + \dot{V}(t)_3. \tag{4.43}$$

$$\dot{V}(t)_(e_4, e_5, e_6) = e_{4i}\dot{e}_{4i} + e_{5i}\dot{e}_{5i} + e_{6i}\dot{e}_{6i}. \tag{4.44}$$

Putting the value of the controllers given in equations (4.39) and (4.40), the final Lyapunov function is:

$$\dot{V}(t) = -c_1 e_{4i}^2 - c_2 e_{5i}^2 - c_3 e_{6i}^2. \tag{4.45}$$

where

$$\begin{aligned} e_{4i,5i,6i}^2 \geq 0 \quad \forall\ e_i \in \mathbb{R} \\ c_{1,2,3} \geq 0 \end{aligned}$$

So this concludes that

$$\dot{V}_c < 0 \quad \forall\ e_i \in \mathbb{R}. \tag{4.46}$$

This analysis shows that the closed-loop controller is globally stable. The negative definite Lyapunov function confirms the convergence of the error function to the equilibrium point.

4.4 Results and Discussion

In the first step, the closed-loop system with the cascaded Lyapunov-based controller is simulated using Simscape Electrical using MATLAB/Simulink. Both dynamical models of electrolyzer with interleaving buck converter and DC load are connected with DC MG for controller analysis.

4.4.1 Numerical Simulations

The stack voltage of the electrolyzer is considered to be 24 V. The generic Lithium-Ion battery model is implemented with an initial state of charge (SoC) of 80%. The DC bus reference is selected to be 220 V. The design parameters for DC MG and controller design are presented in tables 4.3 and 4.4, respectively. Two types of loads are considered to test the performance of the proposed method: electrolyzer and time-varying DC loads. The main control objectives are DC bus voltage regulation during different load conditions, MPPT of the PV system, Optimal powering of the Electrolyzer unit, Battery charging and discharging, and current sharing in all converter topologies.

Table 4.3: Parameters of Power Converting Units.

IBoost Converter	
Parameter	**Value**
Capacitance C_{pv}, C_{o1}	100 , 500 μF
Inductor $L_1 = L_2 = L_3$	5 mH
DC bus voltage reference	220 V
FSIBB Converter	
Input Resistance R_i	220 μ Ω
C_{ij} Input Capacitance	60 μF
Inductance value $L_{b1} = L_{b2} = L_{b3}$	2.2 mH
Internal Resistance $R_{Lb1} = R_{Lb2} = R_{Lb3}$	1.4 mΩ
Output capacitance C_{bo}	60 μF
IBuck Converter	
DC grid side capacitance C_{dc}	500 μF
Inductor $L_{e1} = L_{e2} = L_{e3}$	5 mH
Electrolyzer side capacitance C_{ele}	500 μF

Fig. 4.6a shows the graphical representation of the time-varying load power. To analyze the first control objective the DC bus voltage response can be seen in fig. 4.6b. The black dotted line shows the reference trajectory and the purple color waveform is the actual v_{dc}. It is evident that DC bus voltage is regulated to the reference values with some over/undershoots which are justified due to sudden load change however, the controller can bring the trajectory back to the reference value.

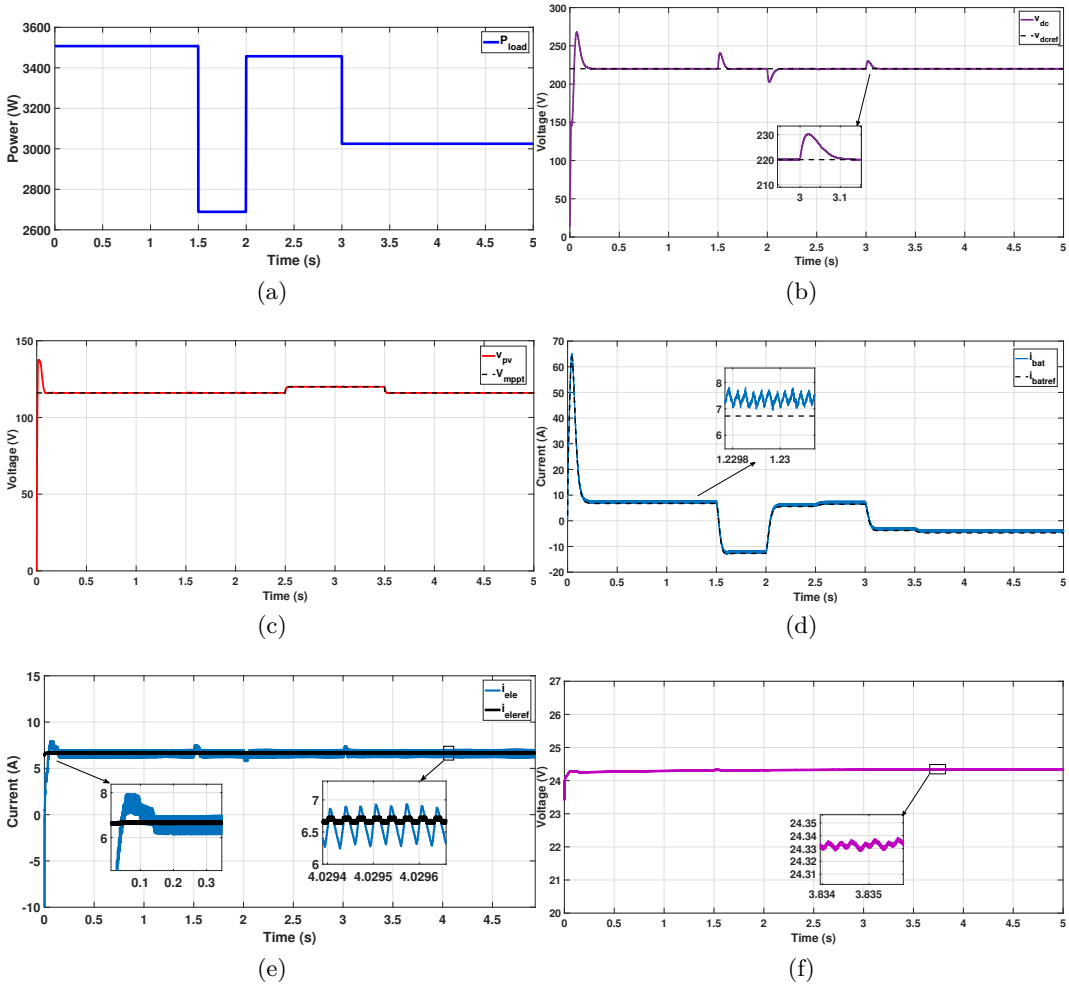

Figure 4.6: Simulation results of the closed-loop system (a) Time-varying load profile (b) DC Bus voltage regulation (c) v_{pv} behavior under MPPT (d) Battery current graph (e) Electrolyzer Current i_{ele} (f) Voltage across Electrolyzer v_{ele}.

The exact overshoot behavior can be seen in the zoomed-in part of the fig. 4.6b. The strategy imposes the MPPT controller for the PV-Boost system. It is advised to get the maximum possible outcome of the PV panel. Fig. 4.6c shows the v_{pv} graph, the MPPT algorithm calculates the maximum voltage, and a dual-loop voltage controller is designed using the cascaded Lyapunov method. The graph confirms the achievement of v_{mppt}. Two different values for temperature and irradiance are used to test the performance under different weather conditions. The graph shows

that the controller can track the MPPT in different conditions.

Table 4.4: Parameters of proposed Controllers for testing.

Enhanced Droop Control	
Parameter	**Value**
Time constant τ	0.5 s
Virtual Resistance R_{droop}	0.033 Ω
Proportional gain for IFSIBB K_{p1}	0.01
Integral gain for IFSIBB K_{i1}	5
Proportional gain for IBoost K_{p2}	0.1
Integral gain for IBoost K_{i2}	50
Proportional gain for IBuck K_{p3}	1
Integral gain for IBuck K_{i3}	10
Lyapunov-based Controller	
Parameter	**Value**
Controller gain for IBoost c_1	2000
Controller gain for IFSIBB c_2	2000
Controller gain for IBuck c_3	3000
Switching frequency f_{sw}	10 kHz

The droop controller is responsible for generating the reference value for the battery storage system, to keep the DC bus voltage stable by providing the auxiliary services. The battery current reference can be positive and negative depending on the load demand. Battery current response is shown in fig.4.6d. Both charging and discharging modes can be observed, the zoomed-in part of the figure shows the steady-state response of the system with little tracking error. Figs. 4.6e, 4.6f depicts the current and voltage graphs across the electrolyzer, respectively. The output voltage of the interleaving buck converter must be equal to the stack voltage of the electrolyzer. The cascaded controller gives the possibility to control both the voltage and the current simultaneously. The graphs show the tracking of both voltage and currents to their desired value. The proper regulation ensures the seamless integration of hydrogen production units. Zoomed-in section of fig.4.6e highlights the transient and steady-state response of the i_{ele} tracking. In interleaving converters, balancing the current between different phases is very important. The tracking of PV current, battery current, and electrolyzer current is already shown, however, it is also important to visualize these current waveforms in each leg. Figs. 4.7a, 4.7b, and 4.7c illustrate the x_{2i}, x_{4i}, and x_{7i} in each inductor of interleaved converter. The results show that the current balancing between different phases is achieved

using phase-shift modulation with the proposed controller. As shown in the figures, the modulation strategy has considered the symmetric phase shift.

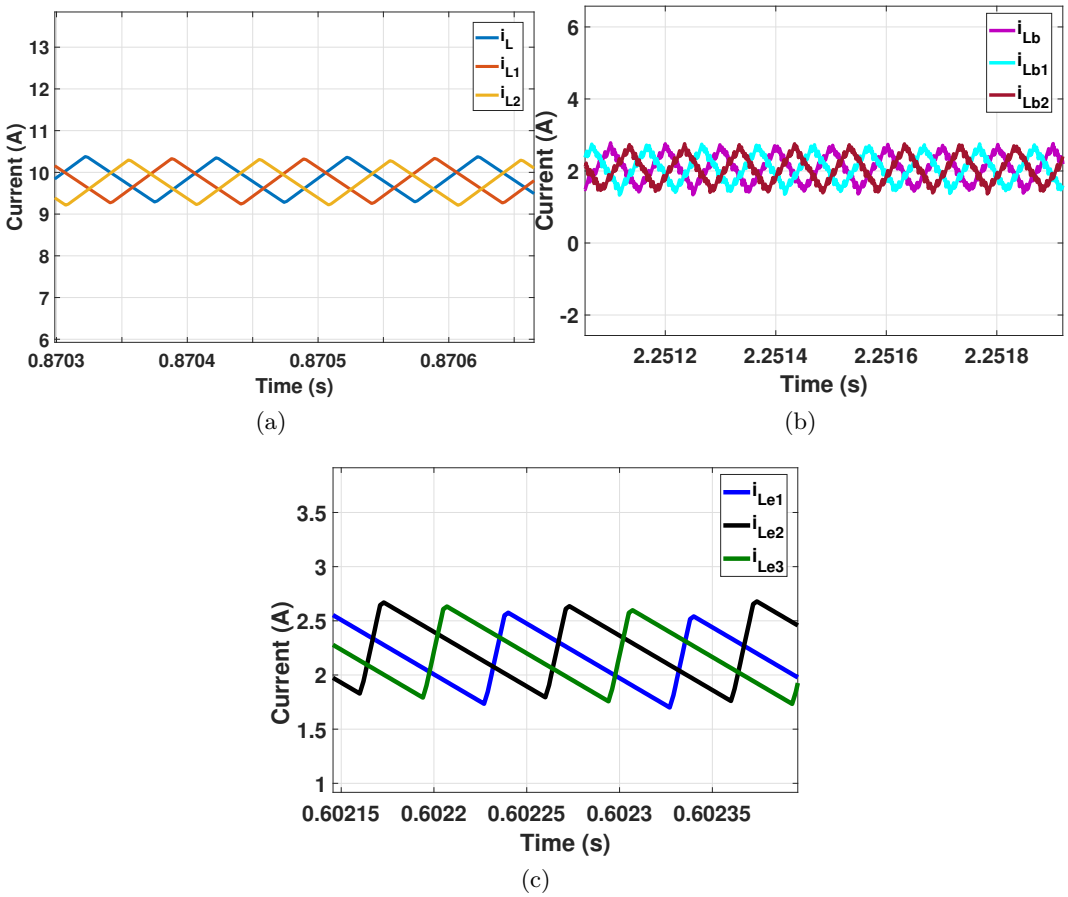

Figure 4.7: Current in different phases of interleaving converters (a) PV panel current through each phase of interleaving boost (b) Battery current through each phase of interleaving IFSIBB converter (c) Electrolyzer current through each phase of interleaving buck converter.

4.5 CHIL Experimental Results

The proposed control scheme is further tested with a C-HIL test bench for real-time verification. The power converters and control parameters are selected the same as considered in the simulation tests. Fig. 4.8 shows the C-HIL setup for experimental testing. The description for the hardware setup is provided as follows:

1. SCADA panel to control and observe different conditions in real time,
2. Host PC for designing schematics and control codes,
3. Two C2000 TI microcontrollers LAUNCHXL-F28379D for real-time control prototyping ,

4. Typhoon 404 real-time emulator for system emulation programmed through the schematic editor.

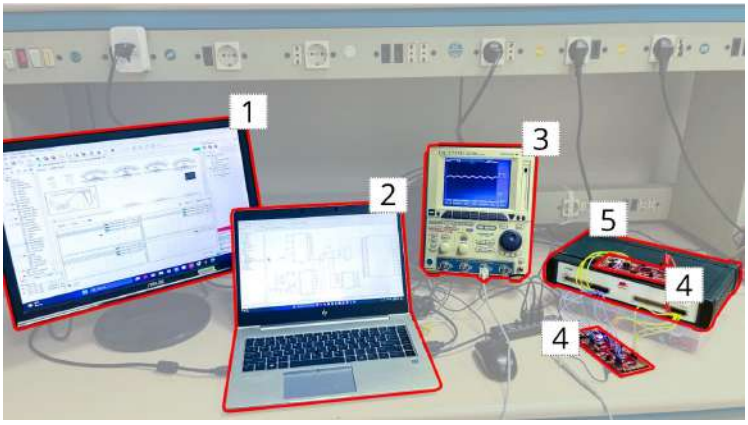

Figure 4.8: C-HIL based experimental test bench.

In C-HIL experiments, the proposed control algorithm is tested under two different load scenarios: DC load variation and electrolyzer load variation. The results and discussion for both cases are given in the following subsections.

4.5.1 DC Load Variation

In this case, a time-varying load is considered to evaluate the performance of the control algorithm, while the electrolyzer load remains connected continuously. Fig. 4.9 presents the results of inductor current through each captured through the oscilloscope. The zoomed-in plots of the oscilloscope provide the flexibility to see the inductor current through the signal inductor phase. The results are presented in Fig. 4.10. The following considerations can be observed. Fig. 4.10a illustrates the graph of the DC bus voltage under varying load conditions. In this figure, the blue line represents the actual response of the DC bus voltage, while the red dotted line denotes the reference value. It can be observed that the DC bus voltage, v_{dc}, remains stable across different load conditions. However, transient overshoots and undershoots occur during abrupt load changes. The zoomed-in section of Fig. 4.10a highlights the steady-state response, demonstrating that v_{dc} successfully tracks the reference value of 220 V. This indicates the robustness of the controller in maintaining voltage stability under dynamic load variations. The battery current response is another critical aspect to examine. A simple droop control strategy is employed to generate the charging and discharging current references. The tracking plot of the battery current during both charging and discharging events is shown in Fig. 4.10b. The Battery Energy Storage System (BESS) plays a vital role in supporting the system during high-load conditions by discharging and storing energy during low-load conditions by charging. The results clearly show that the proposed controller effectively tracks both the charging and discharging current references. While transient

overshoots are present, the controller promptly brings the current trajectory back to the desired reference value, indicating a fast response to sudden changes in load demand. This confirms the effectiveness of the droop control method in managing the energy flow between the BESS and the load, ensuring system stability.

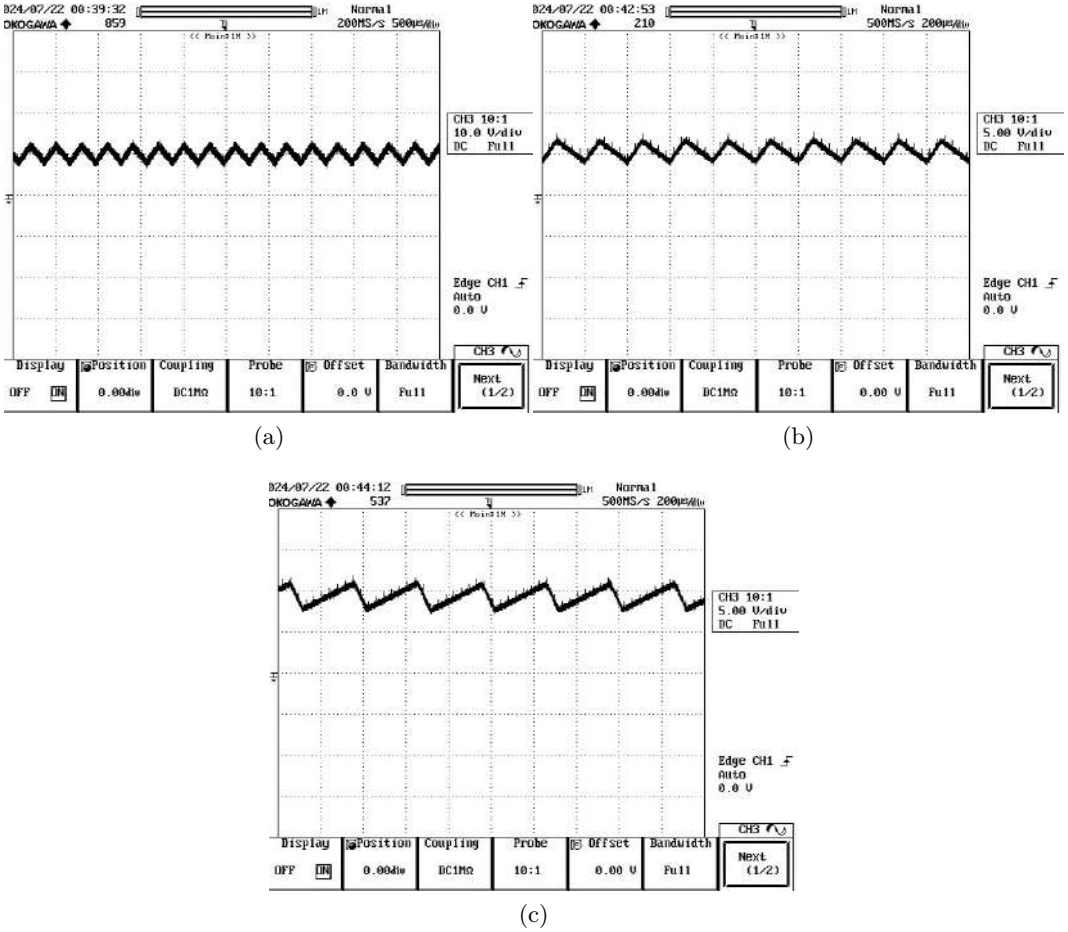

Figure 4.9: C-HIL experimental results (a) Current through the single inductor in IBoost (b) Current through the single inductor in IFSIBB (c) Current through the single inductor in IBuck.

Fig. 4.10c depicts the current supplied to the electrolyzer system. In this scenario, a constant controlled current is provided to power the electrolyzer, ensuring uninterrupted operation for hydrogen production. The case assumes an uninterrupted power supply to the hydrogen generation system, which is essential for maintaining production efficiency. The results show that the electrolyzer current remains stable and tracks the required trajectory throughout the test by employing the proposed switching controller. This confirms that the controller is not only effective in managing dynamic load conditions but also in ensuring stable operation of auxiliary systems like the electrolyzer. One of the key aspects analyzed in this study is the balancing of inductor current through each inductor with a proper phase shift,

aimed at minimizing current ripple in the three power converters. The current waveforms through each phase of the IBoost, IFSIBB, and IBuck converters are shown in Figs. 4.10d, 4.10e, and 4.10f, respectively. The results indicate that the currents remain balanced with the prescribed phase shifts regardless of the load variations. This balancing of inductor currents, achieved through interleaving, effectively reduces the current ripple across the converters, improving efficiency and reducing electromagnetic interference (EMI).

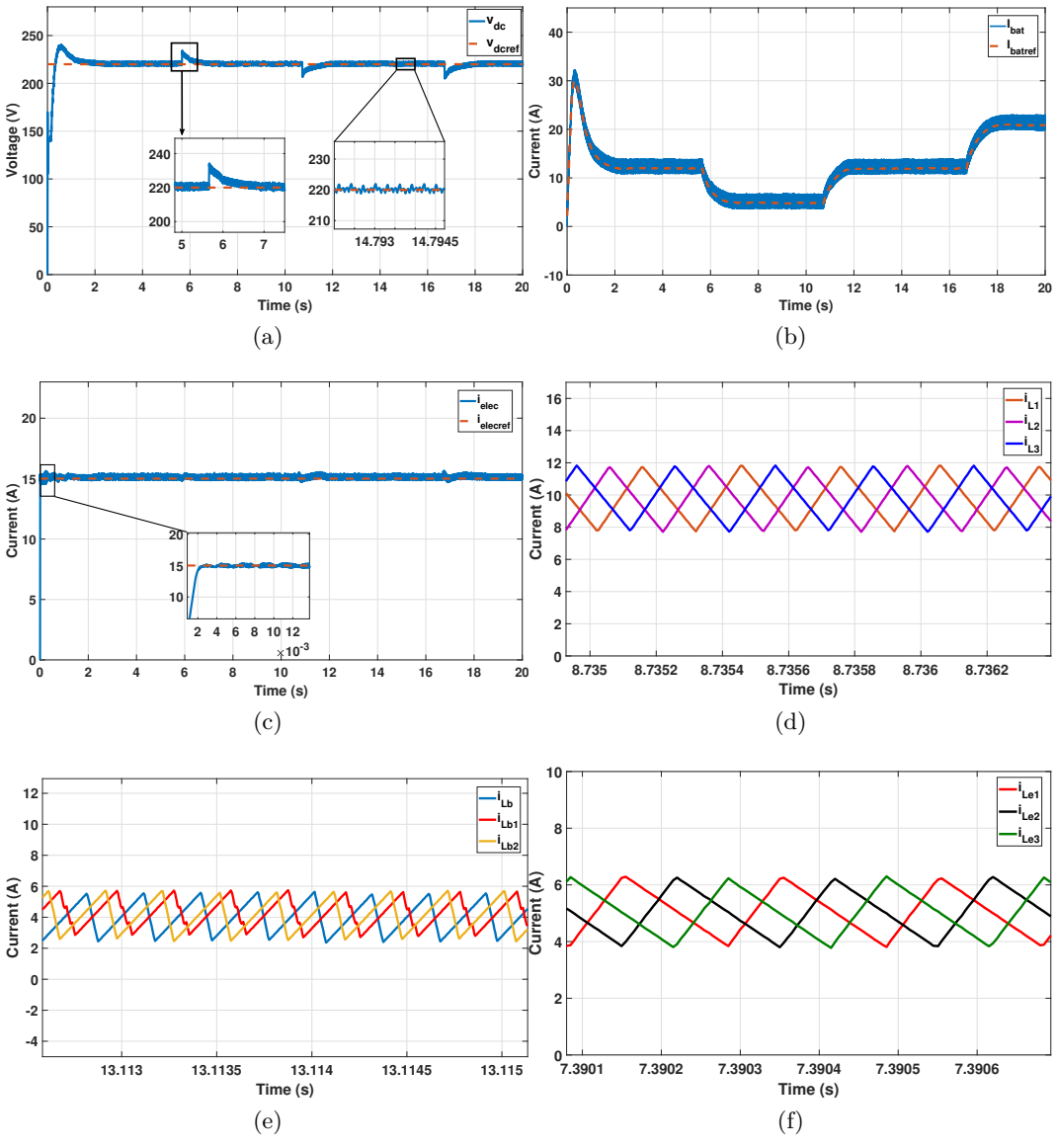

Figure 4.10: Experimental Results Case:1 (a) v_dc tracking under different conditions (b) Battery current charging and discharging under different loads (c) Electrolyzer current Response (d) Current through L_1,L_2,L_3 with phase shift (e) Current through L_{b1},L_{b2},L_{b3} with phase shift (f) Current through L_{e1},L_{e2},L_{e3} with phase shift.

The proposed control algorithm thus demonstrates its capability in regulating output voltage and current and enhancing power converters' performance by min-

imizing ripple, which is a significant benefit in modern power electronics systems. The overall analysis shows that the proposed control strategy offers high performance in terms of voltage stability, efficient current tracking for both the BESS and electrolyzer systems, and the successful balancing of converter currents. Despite the occurrence of transient overshoots and undershoots during sudden load variations, the controller exhibits a fast response, ensuring that system stability is quickly restored. These results underline the robustness and adaptability of the control algorithm, making it well-suited for applications involving dynamic load conditions and multiple power converters operating in parallel.

4.5.2 Electrolyzer Load Current Variation

In this case, the electrolyzer load current is varied to evaluate the performance of the proposed controller under dynamic conditions. Fig. 4.11 presents the results obtained in this case. One key aspect to analyze in this case is the system's stability, which can be observed through the regulation of the DC bus voltage, as shown in Fig. 4.11a. The results demonstrate that the proposed controller effectively maintains stable DC bus voltage despite the variations in the electrolyzer load. This stability is crucial for ensuring that all components connected to the DC bus operate efficiently, as voltage fluctuations could otherwise lead to inefficiencies or damage.

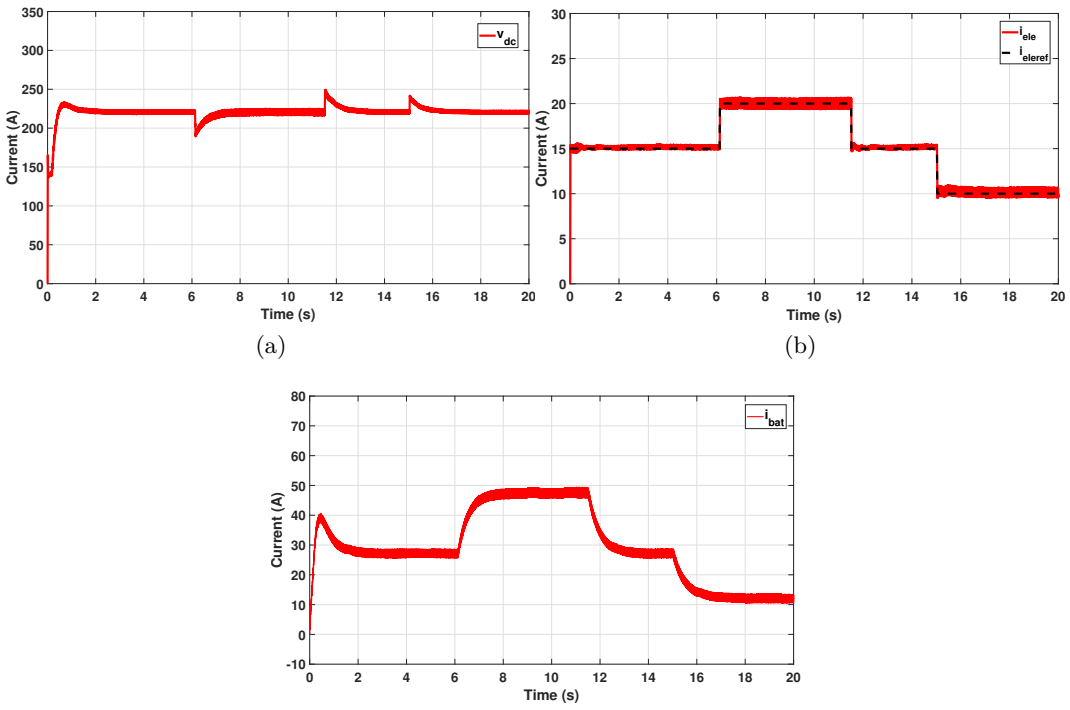

Figure 4.11: C-HIL Experimental Results Case 2: (a) v_{dc} under varying electrolyzer load (b) Electrolyzer current tracking (c) Battery response under varying electrolyzer load.

When the electrolyzer load current is varied, it introduces a time-varying reference for the electrolyzer charging current. The ability of the controller to track this reference in time is critical to system performance. Fig. 4.11b illustrates the tracking of i_{ele}, showing that the controller can follow the reference current of the electrolyzer with high accuracy. The ability to accurately track this reference is essential to ensure that the electrolyzer operates within its optimal range, preventing undercharging or overcharging, which could reduce system efficiency and negatively impact the electrolyzer's lifespan. Furthermore, Fig. 4.11c, when analyzed together with Figs. 4.11a and 4.11b, provide deeper insights into the system performance during high electrolyzer load periods. From the 6-second mark onward, when the electrolyzer load is increased, the battery discharge current rises accordingly. This increase in battery discharge compensates for the additional demand placed on the system by the electrolyzer, helping to stabilize the DC bus voltage. The fact that the controller automatically increases battery discharge in response to higher electrolyzer loads indicates its robustness in balancing multiple energy resources within the microgrid. This coordinated control action ensures that the system can handle fluctuations in demand without compromising voltage stability. In summary, the results from Case 2 show that the proposed controller successfully handles the electrolyzer load variations while maintaining DC bus voltage stability. The precise tracking of the reference time-varying for the electrolyzer current, as depicted in Fig. 4.11b, and the increased battery discharge in response to higher electrolyzer loads, illustrated in Fig. 4.11c, emphasize the controller's ability to manage energy flow efficiently and ensure reliable microgrid operation.

4.6 Conclusion

This chapter presented a cascaded Lyapunov-based hybrid control approach for three-phase interleaving power converters in a DC microgrid, aimed at efficiently supplying power to an electrolyzer. The proposed controller demonstrated robust performance under various operating conditions, including time-varying load scenarios and continuous operation of the electrolyzer. Using the strengths of both linear and nonlinear control methods, the controller ensured effective current sharing between phases while maintaining stable DC bus voltage. The outer voltage loop, controlled by a PI regulator, and the inner current loop, driven by a Lyapunov-based nonlinear method, worked in tandem to provide precise control over the system. This hybrid control approach not only maintained the stability of the system but also minimized the output ripples and enhanced the overall efficiency of the microgrid. The simulation and controller hardware-in-the-loop (C-HIL) results validated the controller's capability to manage system dynamic behavior under real-time conditions. The seamless coordination between the converters and the energy storage system highlights the effectiveness of the proposed method in balancing energy flow

within the DC microgrid. Future work can explore fault-tolerant schemes and optimal phase shift algorithms for asymmetric conditions and extend the control strategy to larger, multimode microgrids integrating renewable energy sources.

References

[1] F. S. Al-Ismail, "Dc microgrid planning, operation, and control: A comprehensive review," *IEEE Access*, vol. 9, pp. 36 154–36 172, 2021.

[2] V. Di Dio, S. Favuzza, D. La Cascia, and R. Miceli, "Economical incentives and systems of certification for the production of electrical energy from renewable energy resources," in *2007 International Conference on Clean Electrical Power*, IEEE, 2007, pp. 277–282.

[3] A. Muhtadi, D. Pandit, N. Nguyen, and J. Mitra, "Distributed energy resources based microgrid: Review of architecture, control, and reliability," *IEEE Transactions on Industry Applications*, vol. 57, no. 3, pp. 2223–2235, 2021.

[4] S. Hajiaghasi, A. Salemnia, and M. Hamzeh, "Hybrid energy storage system for microgrids applications: A review," *Journal of Energy Storage*, vol. 21, pp. 543–570, 2019.

[5] A. Frances, R. Asensi, O. Garcia, R. Prieto, and J. Uceda, "Modeling electronic power converters in smart dc microgrids—an overview," *IEEE Transactions on Smart Grid*, vol. 9, no. 6, pp. 6274–6287, 2017.

[6] J. Rocabert, A. Luna, F. Blaabjerg, and P. Rodriguez, "Control of power converters in ac microgrids," *IEEE transactions on power electronics*, vol. 27, no. 11, pp. 4734–4749, 2012.

[7] S. A. Q. Mohammed and J.-W. Jung, "A state-of-the-art review on soft-switching techniques for dc–dc, dc–ac, ac–dc, and ac–ac power converters," *IEEE Transactions on Industrial Informatics*, vol. 17, no. 10, pp. 6569–6582, 2021.

[8] S. Beheshtaein, R. M. Cuzner, M. Forouzesh, M. Savaghebi, and J. M. Guerrero, "Dc microgrid protection: A comprehensive review," *IEEE Journal of Emerging and Selected Topics in Power Electronics*, 2019.

[9] S. Pannala, N. Patari, A. K. Srivastava, and N. P. Padhy, "Effective control and management scheme for isolated and grid connected dc microgrid," *IEEE Transactions on Industry Applications*, vol. 56, no. 6, pp. 6767–6780, 2020.

[10] X. Wang, J. Huang, Z. Xu, C. Zhang, and X. Guan, "Real-world scale deployment of hydrogen-integrated microgrid: Design and control," *IEEE Transactions on Sustainable Energy*, 2024.

[11] A. G. del Valle, P. García-Linares, and A. Martí, "Optimizing hydrogen production: A comparative study of direct and indirect coupling between photovoltaics and electrolyzer," *Energy Conversion and Management*, vol. 315, p. 118 751, 2024.

[12] D. Guilbert, S. M. Collura, and A. Scipioni, "Dc/dc converter topologies for electrolyzers: State-of-the-art and remaining key issues," *International Journal of Hydrogen Energy*, vol. 42, no. 38, pp. 23 966–23 985, 2017.

[13] G. Hu, C. Chen, H. T. Lu, *et al.*, "A review of technical advances, barriers, and solutions in the power to hydrogen (p2h) roadmap," *Engineering*, vol. 6, no. 12, pp. 1364–1380, 2020.

[14] Y. Lin and L. Fu, "A study for a hybrid wind-solar-battery system for hydrogen production in an islanded mvdc network," *IEEE Access*, vol. 10, pp. 85 355–85 367, 2022.

[15] A. Khaligh and Z. Li, "Battery, ultracapacitor, fuel cell, and hybrid energy storage systems for electric, hybrid electric, fuel cell, and plug-in hybrid electric vehicles: State of the art," *IEEE transactions on Vehicular Technology*, vol. 59, no. 6, pp. 2806–2814, 2010.

[16] O. Hegazy, J. Van Mierlo, and P. Lataire, "Analysis, modeling, and implementation of a multidevice interleaved dc/dc converter for fuel cell hybrid electric vehicles," *IEEE transactions on power electronics*, vol. 27, no. 11, pp. 4445–4458, 2012.

[17] F. Pellitteri, M. Cellura, F. Guarino, R. Miceli, and L. Schirone, "A comparison of different dc-dc converters for energy storage management in nearly-zero energy buildings," in *2020 9th International Conference on Renewable Energy Research and Application (ICRERA)*, IEEE, 2020, pp. 505–509.

[18] B. L. Nguyen, M. Panwar, R. Hovsapian, K. Nagasawa, and T. V. Vu, "Power converter topologies for electrolyzer applications to enable electric grid services," in *IECON 2021–47th Annual Conference of the IEEE Industrial Electronics Society*, IEEE, 2021, pp. 1–6.

[19] T. Dragičević, S. Vazquez, and P. Wheeler, "Advanced control methods for power converters in dg systems and microgrids," *IEEE Transactions on Industrial Electronics*, vol. 68, no. 7, pp. 5847–5862, 2020.

[20] F. Pellitteri, N. Campagna, R. Inguanta, and R. Miceli, "Application of a multiphase interleaved dc-dc converter for power-to-hydrogen systems," in *2023 IEEE 17th International Conference on Compatibility, Power Electronics and Power Engineering (CPE-POWERENG)*, IEEE, 2023, pp. 1–6.

[21] Y. Wang, O. Lucia, Z. Zhang, S. Gao, Y. Guan, and D. Xu, "A review of high frequency power converters and related technologies," *IEEE Open Journal of the Industrial Electronics Society*, vol. 1, pp. 247–260, 2020.

[22] M. A. Alharbi, M. S. Dahidah, S. A. Ali, S. A. Ethni, and V. Pickert, "Ripple-free multiphase interleaved stacked converter for high-power applications," *IEEE Transactions on Power Electronics*, vol. 37, no. 12, pp. 14 770–14 780, 2022.

[23] A. R. Nikhar, S. Apte, and R. Somalwar, "Review of various control techniques for dc-dc interleaved boost converters," in *2016 International Conference on Global Trends in Signal Processing, Information Computing and Communication (ICGTSPICC)*, IEEE, 2016, pp. 432–437.

[24] F. S. Al-Ismail, "Dc microgrid planning, operation, and control: A comprehensive review," *IEEE Access*, vol. 9, pp. 36 154–36 172, 2021.

[25] M. A. Alharbi, M. S. Dahidah, S. A. Ali, S. A. Ethni, and V. Pickert, "Ripple-free multiphase interleaved stacked converter for high-power applications," *IEEE Transactions on Power Electronics*, vol. 37, no. 12, pp. 14 770–14 780, 2022.

[26] S. Zhuo, L. Xu, Y. Huangfu, A. Gaillard, D. Paire, and F. Gao, "Robust adaptive control of interleaved boost converter for fuel cell application," *IEEE Transactions on Industry Applications*, vol. 57, no. 6, pp. 6603–6610, 2021.

[27] G. Tsolaridis and J. Biela, "Interleaved hybrid control concept for multiphase dc-dc converters," in *2017 IEEE Energy Conversion Congress and Exposition (ECCE)*, IEEE, 2017, pp. 3069–3076.

[28] A. R. Nikhar, S. Apte, and R. Somalwar, "Review of various control techniques for dc-dc interleaved boost converters," in *2016 International Conference on Global Trends in Signal Processing, Information Computing and Communication (ICGTSPICC)*, IEEE, 2016, pp. 432–437.

[29] M. Aguirre, S. Vazquez, A. M. Alcaide, *et al.*, "Period control approach finite control set model predictive control switching phase control for interleaved dc/dc converters," *IEEE Transactions on Industrial Electronics*, 2023.

[30] X. Hao, I. Salhi, S. Laghrouche, Y. Ait-Amirat, and A. Djerdir, "Backstepping supertwisting control of four-phase interleaved boost converter for pem fuel cell," *IEEE Transactions on Power Electronics*, vol. 37, no. 7, pp. 7858–7870, 2022.

[31] S. Zhuo, L. Xu, Y. Huangfu, A. Gaillard, D. Paire, and F. Gao, "Robust adaptive control of interleaved boost converter for fuel cell application," *IEEE Transactions on Industry Applications*, vol. 57, no. 6, pp. 6603–6610, 2021.

[32] A. U. Rahman, N. Campagna, A. Di Tommaso, R. Miceli, A. Damiano, and A. Floris, "Advanced control analysis of single inductor four switch non-inverting buck-boost converter for energy storage units," in *2023 International Conference on Clean Electrical Power (ICCEP)*, IEEE, 2023, pp. 267–272.

[33] S. A. Gorji, "Reconfigurable quadratic converters for electrolyzers utilized in dc microgrids," *IEEE Access*, vol. 10, pp. 109 677–109 687, 2022.

[34] N. Naseri, S. El Hani, K. El Harouri, and H. Mediouni, "Primary and secondary control of an autonomous solar microgrid based power-to-x: Renewable hydrogen conversion," *International Journal of Hydrogen Energy*, vol. 47, no. 58, pp. 24 421–24 438, 2022.

[35] B. Yodwong, D. Guilbert, W. Kaewmanee, M. Phattanasak, M. Hinaje, and G. Vitale, "Improved sliding mode-based controller of a high voltage ratio dc–dc converter for electrolyzers supplied by renewable energy," *IEEE Transactions on Industrial Electronics*, 2023.

[36] A. O. Di Tommaso, F. Genduso, and R. Miceli, "Analytical investigation and control system set-up of medium scale pv plants for power flow management," *Energies*, vol. 5, no. 11, pp. 4399–4416, 2012.

[37] S. S. Zehra, A. U. Rahman, and I. Ahmad, "Fuzzy-barrier sliding mode control of electric-hydrogen hybrid energy storage system in dc microgrid: Modelling, management and experimental investigation," *Energy*, vol. 239, p. 122 260, 2022.

[38] Q. Xu, X. Hu, P. Wang, *et al.*, "A decentralized dynamic power sharing strategy for hybrid energy storage system in autonomous dc microgrid," *IEEE Transactions on Industrial Electronics*, vol. 64, no. 7, pp. 5930–5941, 2017. DOI: 10.1109/TIE.2016.2608880.

[39] S. R. Sanders and G. C. Verghese, "Lyapunov-based control for switched power converters," *IEEE Transactions on Power Electronics*, vol. 7, no. 1, pp. 17–24, 1992.

Chapter 5

DC Microgrid: AI-based Control of Grid-Connected EV Charging Station

5.1 Introduction

Renewable energy sources (RESs), such as photovoltaic (PV) and wind energy systems, are gaining tremendous attention in power due to their clean energy generation and unlimited energy supply. Moreover, they are actively addressing the common issues of conventional power systems [1]. The concept of RESs and an energy storage unit-based microgrid (MG) gradually replaced traditional power generation methods over time. MGs can be installed remotely to provide an instant energy solution for a specific area or industry. The concept of demand-based small-scale power generation is termed distributed generation (DG) [2]. Furthermore, MGs have two modes of operation: islanded and grid-connected modes. Currently, it is not possible to replace an entire conventional power system; therefore, it is imperative to focus on the combination of DG and primary power grid, that is, microgrids connected to the grid [3].

Recently, an immense amount of work has been done to study and analyze the integration of renewable energy systems in grid-connected mode. mainly, energy management [4], control [5], and correction of the power factor [6] of DG systems connected to the grid have been discussed. In this chapter, a grid-connected microgrid has been considered where the power generation and consumption in the utility grid have been observed. MGs require proper control and management algorithms to improve their work efficiency as a multi-agent system. The MG control level has been divided into two main categories: supervision and distributed control [7]. The supervisory control deals with the energy management unit (EMU) of MG and is mainly designed to maximize the share of power between power sources and consumers [8]. On the other hand, local controllers, such as PI or linear voltage

regulators, are used to get the desired power from specific power sources [9].
In [10], a slap swarm-based energy management algorithm has been proposed for a DC system connected to the grid. This work presented that efficiency and fuel economy improved using a novel EMU. However, an increased computational cost can be a drawback of such algorithms. Model predictive control (MPC) has also been used as an energy management tool for a long time. An online MPC-based optimization method for an energy storage system in a DC MG has been proposed in [11]. The high computational time, complexity, and stochastic nature of the power sources create difficulty for MPC to handle an advanced control and management problem.
Fuzzy logic control has also been used as a supervisory control in DGs and MGs. In [12], a fuzzy-based energy management strategy has been proposed for an isolated DC microgrid. Similarly, fuzzy-based energy management has also been designed for fuel cell-based electric vehicles (EV) in [13], in which the results showed that the fuel economy of the vehicles has improved by managing the power from the energy storage system. Fuzzy logic-based control is receiving attention due to its simplicity and efficiency, which is based on rules and requires accurate human knowledge regarding the system. Recently, some algorithms based on artificial intelligence have also been developed to make the system more intelligent and efficient [14]-[15]. In general, MGs display non-linear behavior due to the stochastic nature of RESs and the interconnection of different power sources. Therefore, the state-of-the-art PI regulators are replaced by droop control methods [16]. Moreover, the poor voltage regulation in droop control has been improved by applying nonlinear distributed controllers to MG [17], [18]. Most of the previously proposed MGs have constant or controllable loads, i.e., residential or utility loads.
In this chapter, neurofuzzy-based energy management of grid-connected MG has been proposed to charge electric vehicles. This system is designed to charge a maximum of four EVs at a time in which each EV consists of an uncontrollable stochastic load. EV is a very remarkable concept for the reduction of environmental pollution. However, it also creates many problems for power networks, such as power losses, high tariffs, and network instability [19]. The management strategy has been drafted so that the maximum power demand is met by the RESs and storage devices, while additional power is provided to the main grid. The novelty of the work can be summarized as follows:

- Photovoltaic systems, fuel cell-based grid-connected systems have been proposed to charge EVs, while batteries and supercapacitor are used as storage devices.

- An algorithm based on maximum power point tracking (MPPT) has been presented based on artificial neural networks to extract maximum power from the photovoltaic system.

- Fuzzy-based energy management unit has been implemented to allow optimal power sharing under different scenarios.

5.2 Structure of Microgrid

The microgrid considered in this work is presented in Fig. (5.1). This system is made up of a photovoltaic panel connected with a DC-DC bidirectional boost converter, a HESS which is comprised of an SC and a battery; both connected with DC-DC buck-boost converters, a fuel cell (FC) connected with a DC-DC boost converter, and electric vehicles connected as load with the DC bus. This MG works in a grid-connected mode, which means that if the RESs and HESS do not meet the load demand, then the additional power is supplied by the grid. In contrast, if the RESs generate excess power, it is provided back to the main grid. The modeling of the microgrid is explained in detail as follows.

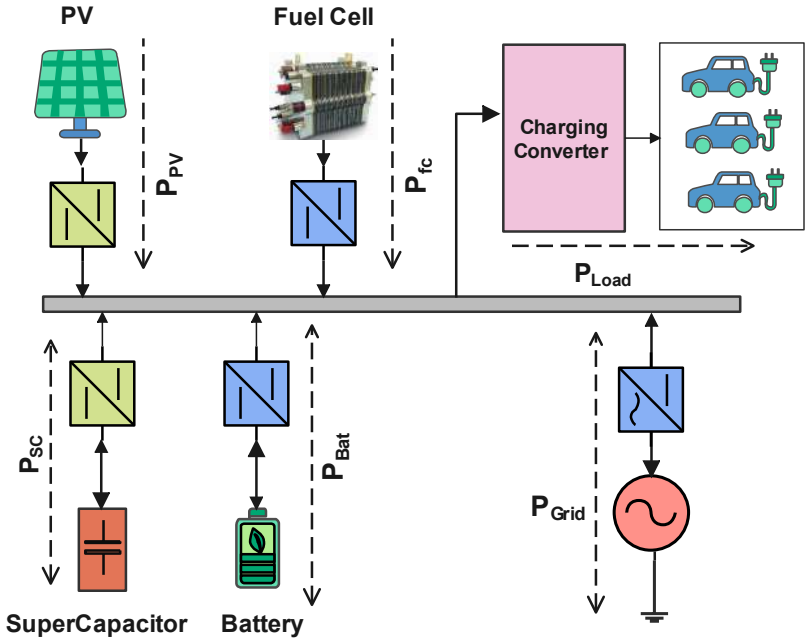

Figure 5.1: Structure of grid-connected microgrid

5.2.1 PV Energy System

The primary source of energy generation in this work is the PV energy system. The power obtained from the PV panel depends on the temperature and the irradiance; therefore, it is essential to track the maximum power point (MPP) at which the PV panel generates its maximum power. As illustrated in Fig. (5.1), the PV panel has

been connected with a DC-DC bidirectional boost converter to increase the output voltage to meet load demand without compromising the efficiency of the system. The average model of the voltage and current of this system after applying the electrical theorems can be given as:

$$\frac{dV_{PV_i}}{dt} = \frac{I_{PV}}{C_1} - \frac{I_{L1}}{C1}u_1 \tag{5.1}$$

$$\frac{dI_{PV}}{dt} = \frac{V_{C1}}{L1}u_1 - \frac{V_{C_2}}{L1}(1-u_1) \tag{5.2}$$

$$\frac{dV_{PV_o}}{dt} = \frac{I_{L1}}{C_2}(1-u_1) - \frac{V_{C2}}{R_1C_2} \tag{5.3}$$

Eq. (5.1) is formulated using the electrical configuration of the PV panel with the converter, which consists of two capacitors C_1, C_2, an inductor L_1 and u_1 which is the converter control input.

5.2.2 Fuel Cell

In this proposed microgrid, FC is considered an auxiliary power source as it works alongside the PV system to fulfill the load demand. In this device, the energy is generated through a chemical reaction between hydrogen and oxygen, which takes place with the help of an electrolyte. The output voltage of the FC can be given as:

$$V_{FC} = E - (V_{act} + V_{ohm} + V_c) \tag{5.4}$$

In eq. (5.4), V_{FC}, E, V_{ohm}, V_{act} and V_c is the output voltage of the FC, Nerst instantaneous voltage, ohmic voltage drop, fuel cell's activation voltage drop and voltage drop inside the FC respectively. Since FC is a non-rechargeable device, a uni-directional DC-DC boost converter has been connected for the regulation of voltage according to the load of the electric vehicles. The average current of the FC can be given as:

$$\frac{dI_{FC}}{dt} = \frac{-R_2}{L_2}I_{FC} + \frac{1}{L_2}V_{FC} - \frac{1-u_2}{L_2}V_{DC} \tag{5.5}$$

In eq. (5.5), L_2 and R_2 represent the inductor and resistor of the DC-DC boost converter connected with the FC in the proposed configuration. Moreover, V_{DC} represents the DC bus voltage and u_2 is the control input to this converter which regulates V_{DC}.

5.2.3 Hybrid Energy Storage System

Battery and supercapacitor (SC) based hybrid energy storage system (ESS) has been considered as illustrated by fig. 5.1. The ESS is a backup to accommodate the stochastic nature of RESs and the load demand. However, the availability of the ESS depends on its state of charge (SoC). The expressions for the SoCs of battery

and SC are given as follows:

$$SoC_B = SoC_{Bini} - \frac{1}{C_n} \int_0^t I_B \, dt \tag{5.6}$$

$$SoC_{SC} = SoC_{SCini} - \frac{1}{C_n} \int_0^t I_{SC} \, dt \tag{5.7}$$

where SoC_{Bini}, SoC_{SCini} are the initial values of SoCs, while C_n denotes the capacity of each source. It is important to check the SoCs of the energy storage system to continue their operation within the safe limits without compromising their efficiency. The proposed energy management strategy incorporates the SoCs of ESS as input parameters for its optimization, discussed in the following section.

5.3 Energy Management Strategy

The energy management strategy (EMS) has two main objects, MPPT and power-sharing between ESS and the main grid. The PV power generation depends upon the weather parameters, i.e., temperature and irradiance. Weather parameters have a stochastic behavior therefore, an artificial neural network (ANN) based algorithm has been used to find out the possible maximum output from the PV system. The

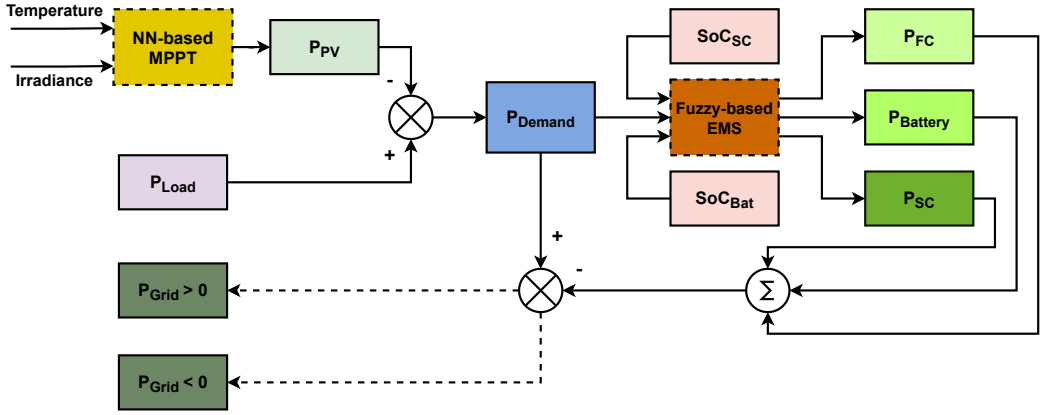

Figure 5.2: Graphical representation of proposed strategy

ANN toolbox is used to develop the neural network for the PV system. The input-output curve fitting app and the Levenberg-Marquardt algorithm have been used to adjust the parameters in MATLAB (2020a).

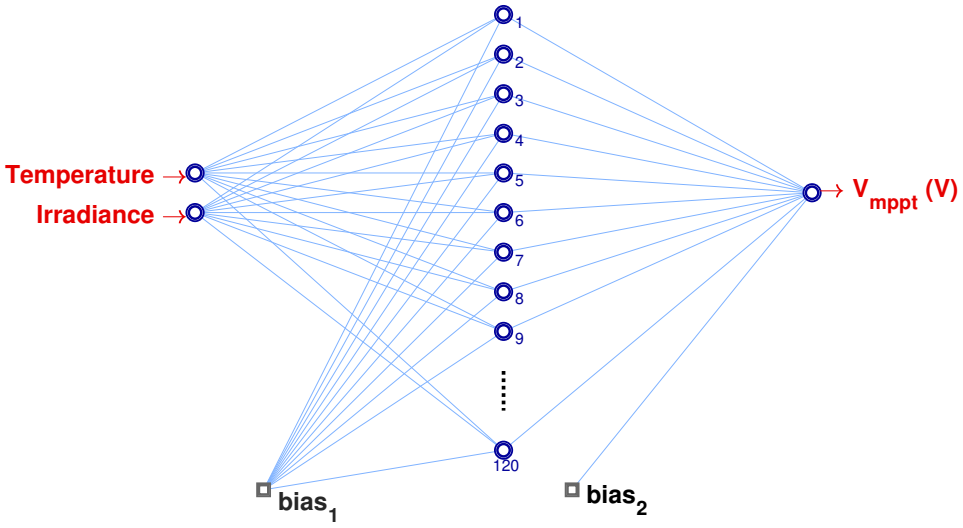

Figure 5.3: Structure of proposed neural network

Fig. 5.3 shows the structure diagram of the proposed ANN having two inputs (temperature, irradiance) and a single output (maximum voltage). It contains one hidden layer with some hidden neurons and one output layer. Uniformly distributed random temperature values between 15 ° C and 45 ° C were used as input. Similarly, random values between 0-1000 W/m^2 have been considered for irradiance. After obtaining the training data, the neural network has been trained and deployed to get the maximum power point. Fig. 5.4 presents the graph between errors and epochs along with the training, test, and validation graphs. It can be seen that mean square error (MSE) has the best validation performance at 1000 epochs. The approximate value of MSE is zero, which validates the performance of the developed neural network.

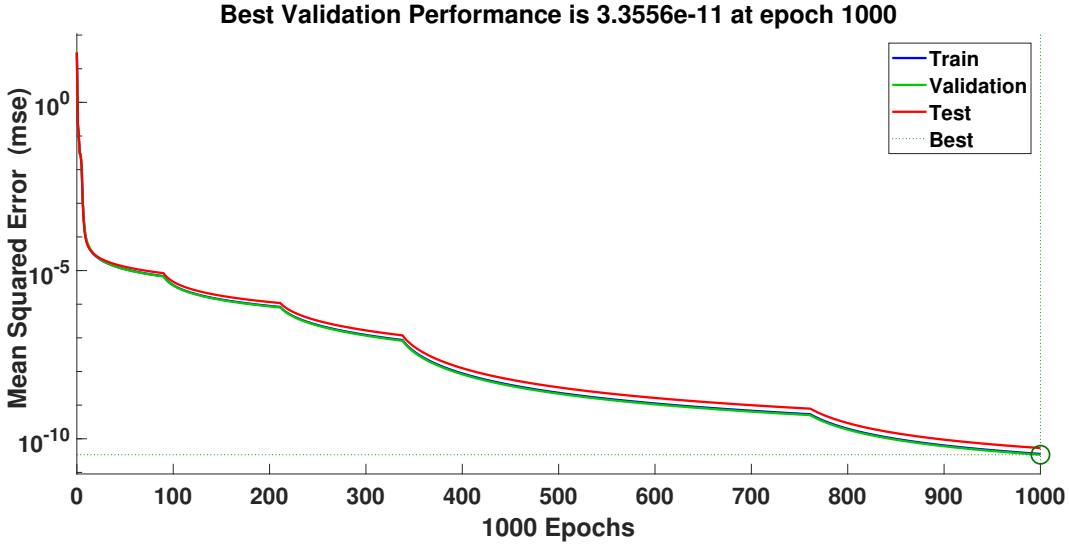

Figure 5.4: Performance evaluation of designed ANN

For energy management between power sources, grid, and load, a fuzzy logic-

based EMS has been designed with three input variables such as power demand P_D, SoC of battery SoC_B, and SoC of SC SoC_{SC}. Similarly, three output variables have been designed as FC power P_{FC}, battery power P_B and SC power P_{SC}. The balance between the required and generated power can be expressed as follows.

$$P_{Load} = P_{PV} + P_{ESS} + P_{FC} + P_{Grid} \tag{5.8}$$

$$P_{Load} - P_{PV} = P_{ESS} + P_{FC} + P_{Grid} \tag{5.9}$$

$$P_{Demand} = P_{ESS} + P_{FC} + P_{Grid} \tag{5.10}$$

Eq. (5.10) refers to the power demand that must be met by the ESS, FC and the grid. Now, grid power can be expressed as:

$$P_{Grid} = P_{Demand} - P_{ESS} - P_{FC} \tag{5.11}$$

From eq. (5.11), it can be observed that the grid power can be either positive or negative, which means that the power can be taken from the grid or supplied to the grid, which has been illustrated in fig. (5.2).
The output of the designed fuzzy system is generated according to the set of the designed fuzzy rule base, and the number of rules for this system has been calculated as:

$$Number\ of\ rules = x * y * z \tag{5.12}$$

In eq. (5.12), x, y, and z represent the membership functions of the three input variables of the system. According to this equation, the authors have formulated thirty-six rules which decide the output powers. A block diagram illustrating the working of the proposed EMS has been shown in fig. (5.2). The output from this EMS is the reference powers provided by the FC, battery, and SC according to their SoCs and electric vehicle load demand. A sample of rules formulated for the EMS of FHEV has been shown in table 5.1 and has been discussed in detail as follows:

- **Input 1: Power demand**
  The first input to the fuzzy inference system is the power demand which is the resultant power between power obtained from the PV energy system and load power. Considering eq. (5.10), the power demand can either be positive or negative. Positive power demand depicts that the required load power is more than the power generated by the PV energy system. In contrast, negative power demand shows that the PV energy system fails to fulfill the load demand. In both cases, power can be taken from the main grid to fulfill the load demand, charge the battery and SC according to their SoCs, or be supplied back to the main grid. This input variable has four membership functions displayed as

Negative, *Low*, *Medium* and *High* in fig. (5.5).

Table 5.1: Sample Fuzzy-based EMS rules

$\mathbf{P}_D$	$\mathbf{SoC}_B$	$\mathbf{SoC}_{SC}$	$\mathbf{P}_{FC}$	$\mathbf{P}_B$	$\mathbf{P}_{SC}$
N	L	H	I	CF	I
N	H	M	I	I	CF
L	M	H	DP	DP	DF
L	H	L	DP	DF	I
M	L	H	DF	I	DF
M	M	L	DF	DF	I
H	L	H	DF	I	DF
H	H	M	DF	DF	DF

CF, DF, CP and DP represent $Charged_{fully}$, $Discharged_{fully}$, $Charged_{partially}$ and $Discharged_{partially}$ respectively.

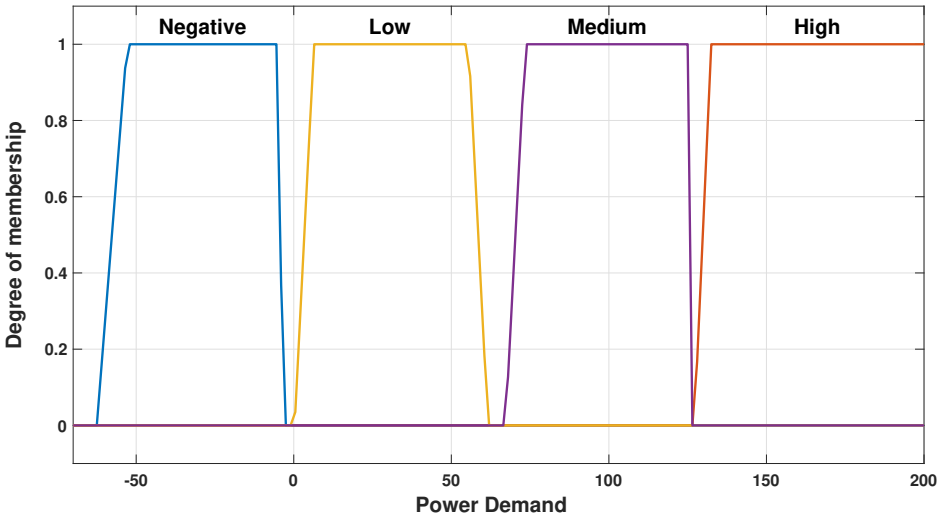

Figure 5.5: EMS input 1: Power Demand

- **Input 2: Battery state of charge**
  In this strategy, the second input variable is the SoC of the battery which has three membership functions *Low*, *Medium*, and *High*. Since it is a rechargeable device, it can charge or discharge itself according to the power demand and its SoC.

- **Input 3: Supercapacitor state of charge**
  The third input of the fuzzy inference system is the SoC of SC which is capable of providing peak power due to its high power density. The SC can

charge or discharge itself instantly and has three membership functions as Low, $Medium$, and $High$.

- **Output 1: Battery power**
  The first output variable of the designed EMS is the battery power which has five membership functions as $Charged_{fully}$, $Charged_{partially}$, $Idle$, $Discharged_{partially}$ and $Discharged_{fully}$ as displayed in fig (5.6). The battery can charge, remain idle, or discharge according to the designed fuzzy rules to charge electric vehicles. The surface response for the battery power with the SoC of battery and power demand as the two inputs have been displayed in fig. (5.7) in which the battery power corresponding to its SoC and power demand can be observed in various time intervals.

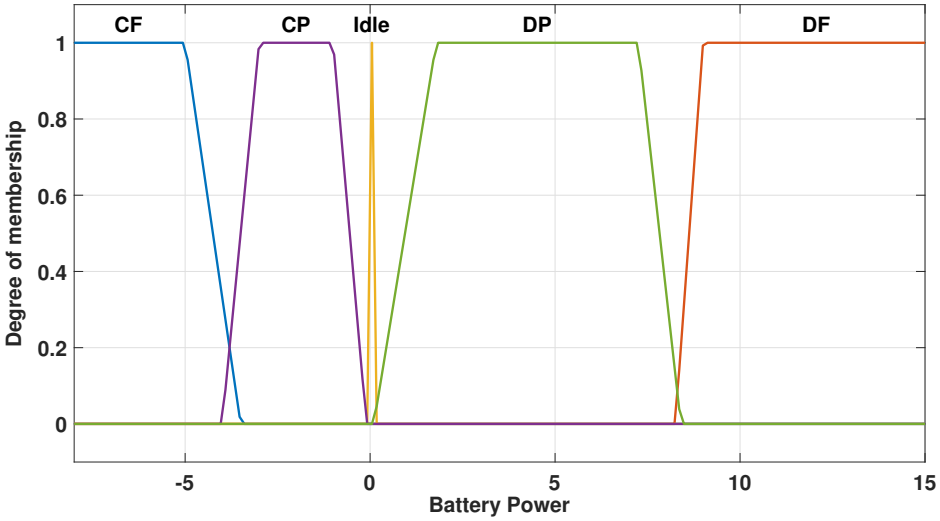

Figure 5.6: EMS output 1: Battery Power

- **Output 2: Fuel cell power**
  The output power from the FC is the second output from the EMS, which is determined by the SoCs of the battery, SC, and load demand. This output variable has been divided into three membership functions as $Idle$, $Discharged_{partially}$, and $Discharged_{fully}$. Since FC is a non-rechargeable device, it can discharge itself according to the respective inputs of the fuzzy inference system.

- **Output 3: Supercapacitor power**
  The last output variable of the EMS is the SC power which depends on the SoC of SC and the power demand. Similar to the second output variable, this variable has also been divided into five membership functions as $Charged_{fully}$, $Charged_{partially}$, $Idle$, $Discharged_{partially}$ and $Discharged_{fully}$. SC charge remains idle or discharged accordingly. Moreover, the surface response for the

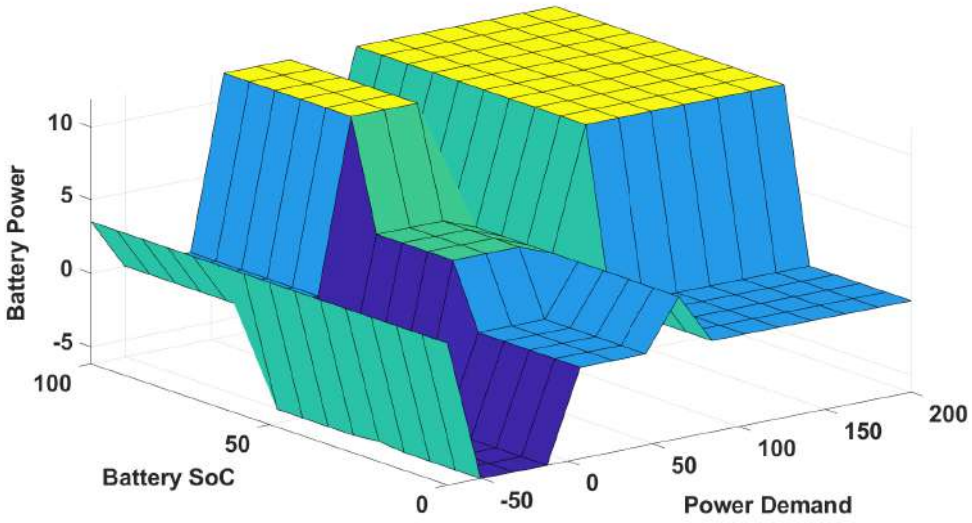

Figure 5.7: EMS surface response for battery power

SC power with its SoC and the corresponding power demand as the two inputs has been displayed in fig. (5.8). In this graph, the response of SC power under varying SoC and power demand can be evaluated.

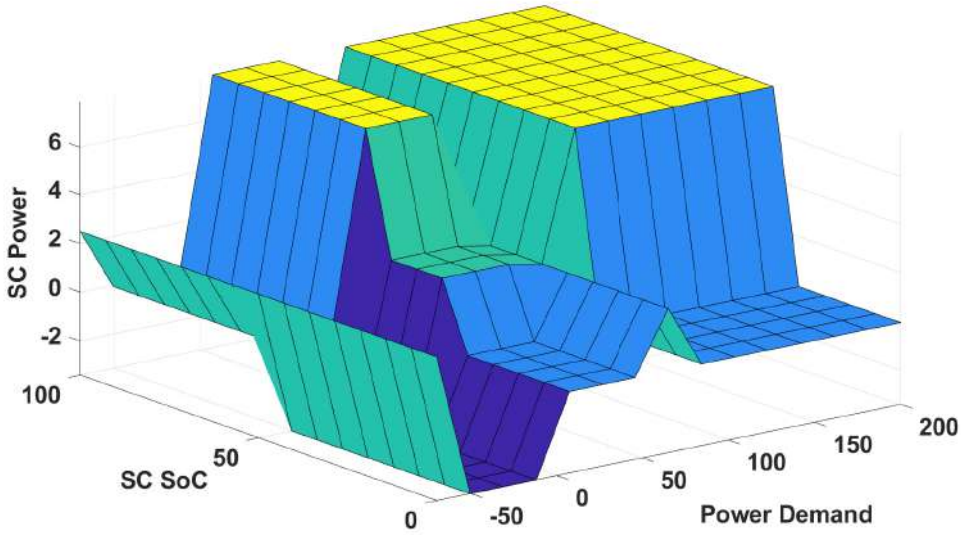

Figure 5.8: EMS surface response for SC power

5.4 Results and Discussion

MATLAB/Simulink-based numerical simulations have been carried out to validate the proposed method. This section contains detailed results in graphs and a brief

discussion of the findings. In this chapter, neurofuzzy-based EMU has been adopted to extract maximum power from the PV system and optimally share the power between different power sources. The proposed strategy has been well explained in Section 5.3. The proposed MG system is designed to provide the power for an EV charging station to power the e-mobility sector. There are different models of electric vehicles on the market and they have different charging topologies. On-board vehicle charging (OBC) is one of the methods in which an AC power supply is used to charge the vehicle; charging can be done through publicly available AC charging points or through an AC supply at home [20]. However, the concept of DC fast charging for electric vehicles is becoming trendy due to the shorter charging time. The DC fast charging ports are commercially available and do not require OBC. The power required for EV charging depends on the miles driven. Generally, EVs get 3-4 miles / kWh [21], which has also been considered for the simulations performed.

Assumption: The considered MG will provide power to a charging station having four DC fast charging ports [22], and each port can charge the vehicle between 20-25 kW. Based on this assumption, 1-4 EVs can be charged using the DC fast charger at once. Fig. 5.9 shows the graph of the load profile of the charging station. A

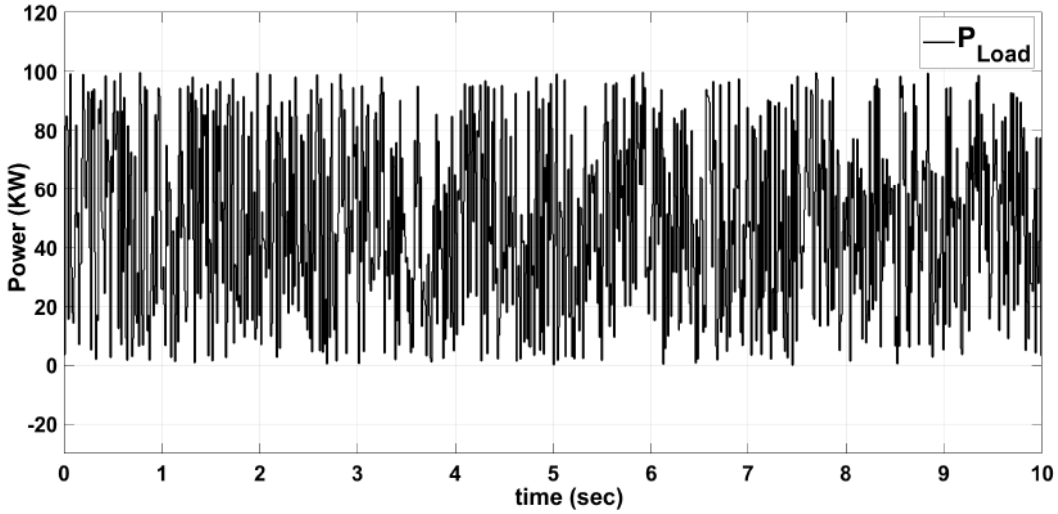

Figure 5.9: Load power of charging station P_{Load}

uniformly distributed varying load profile between 0-100 kW has been considered and the load value is varied between no load to full load condition. The load profile depicts the stochastic nature of the electric vehicle's charging, which shows the idea behind varying load is to test the validity of the proposed algorithm under different conditions. The PV system is the primary power-generating source. The maximum output power of the PV system is displayed in fig. 5.10. It can be observed that PV power is not constant and the variations are due to the changes in temperature and irradiance. The response of the PV system is the same for all values of load power

because it cannot provide power more than its maximum output. The difference between load power and PV power has been termed as P_{Demand} and can be written as:

$$P_{Demand} = P_{Load} - P_{PV} \tag{5.13}$$

Fig. 5.11 illustrates the demand power response in which it can be observed that

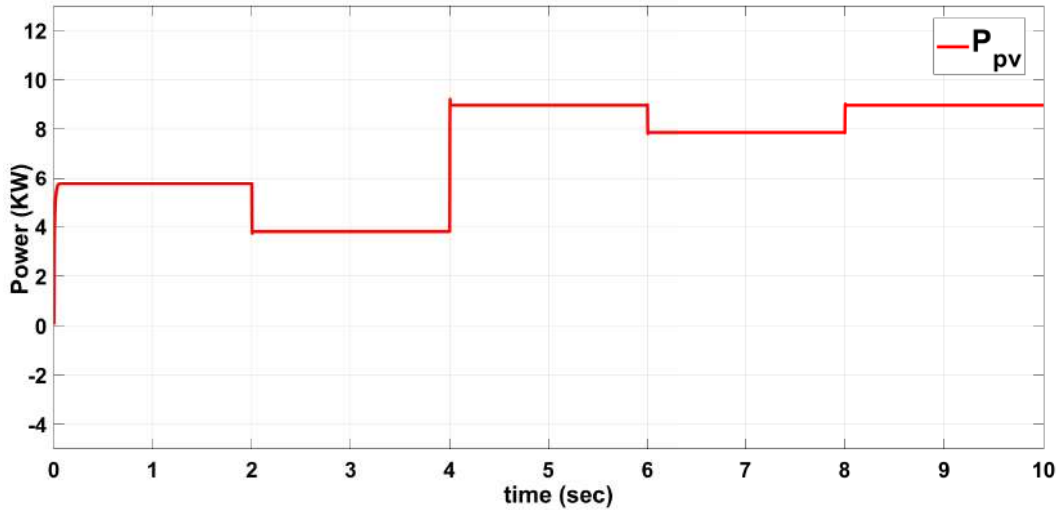

Figure 5.10: Maximum extracted power from PV system P_{PV}

P_{Demand} has both positive and negative values. Positive value means $P_{Load} > P_{PV}$ so the remaining load requirement is managed by using the FC, ESS, and main grid while in case of negative peaks, $P_{PV} > P_{load}$ so extra PV power can be stored in the ESS. As discussed in the previous section, the proposed EMS has two inputs;

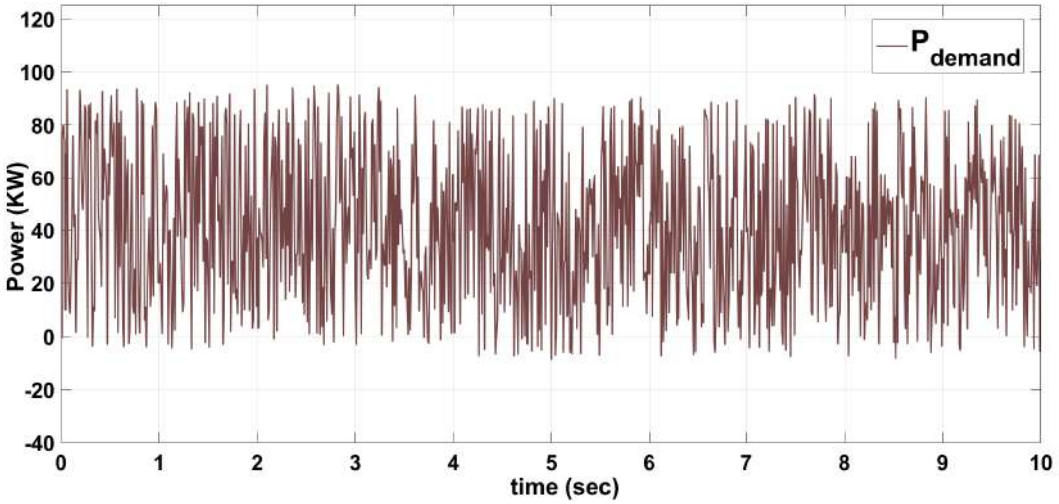

Figure 5.11: Difference between P_{load} and P_{pv}

P_{Demand} and the SoC of ESS. Based on these parameters, it decides the charging and discharging of ESS.

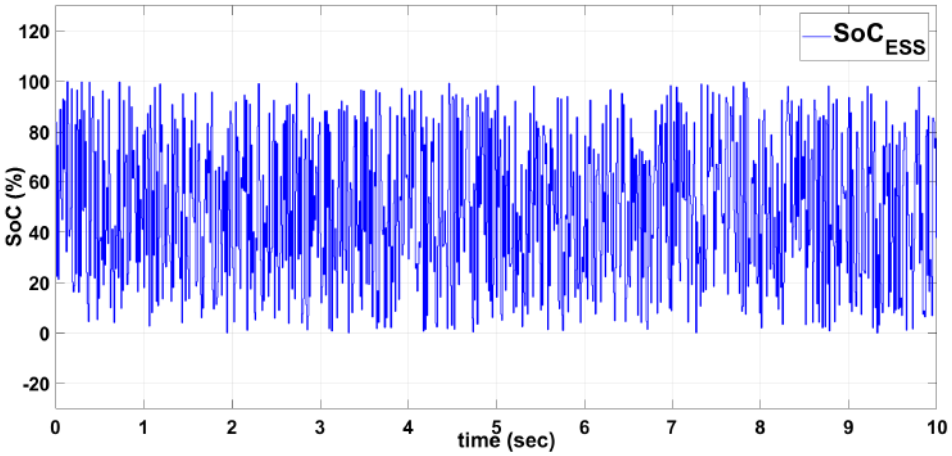

Figure 5.12: SoC of energy storage system (ESS)

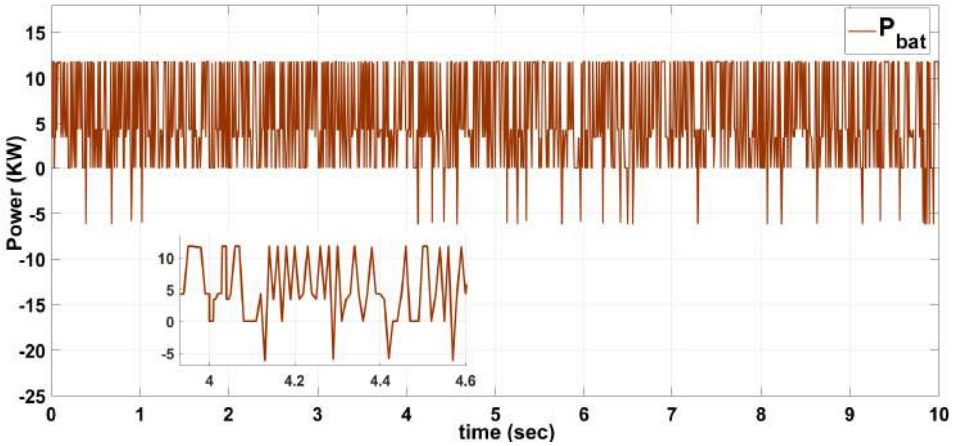

Figure 5.13: Battery power P_{Bat} based on SoC

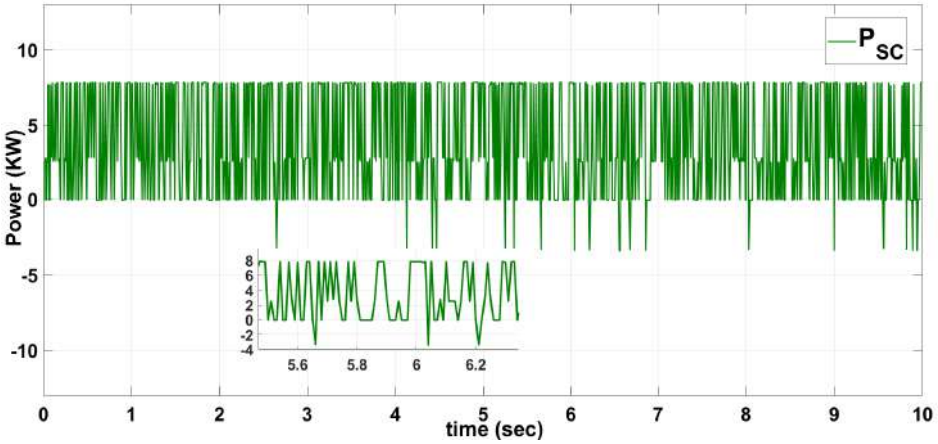

Figure 5.14: Supercapacitor power P_{SC} based on SoC

The SoC (%) of ESS can take any value between 0-100 as displayed in fig. 5.12 in which a uniformly distributed signal between 0-100 is considered to check the

response of the management system under all conditions. Figs. 5.13 and 5.14 show the optimal powers of battery and SC respectively. The response of each storage can be analyzed through the zoomed-in view of the graphs. Charging, discharging, and idle conditions can be verified through the signals that correspond to the proposed EMS's efficient performance. The ESS has been used to overcome the stochastic nature of the renewable energies. The EMS has been designed in such a way that in the case of SoC $< 30\%$, the ESS will not work and can only be charged for its operation in the safe limit. The responses of the battery and SC powers demonstrate the efficient functioning of the proposed algorithm. In the proposed strategy, during low P_{Demand}, ESS is used to meet the requirement to improve the hydrogen fuel economy. However, FC provides the power to meet power demand during medium- to high-peaks. Fig. 5.15 shows the FC power; the discharging, partial discharging, and idle state of the FC can be observed in the zoomed-in section of this figure. The term partial discharge has been included in fuzzy rules to further improve the hydrogen fuel economy. Finally, the power of the main grid can be calculated using the power balance equation given in the previous section. This calculation is important to find the improvement in the power consumption and generation due to the designed EMS. Fig. 5.16 presents the grid power response in which it is evident that grid power has both positive and negative peaks. The positive value of the grid represents the power taken from the grid to meet the demand for the load, while the negative power shows that the power is supplied to the grid by the MG during low load conditions. It can be observed by looking at fig. 5.9 and 5.16 that the MG contributed well to reducing the grid power consumption. Moreover, the power injected into the utility grid during low load conditions can improve the tariff.

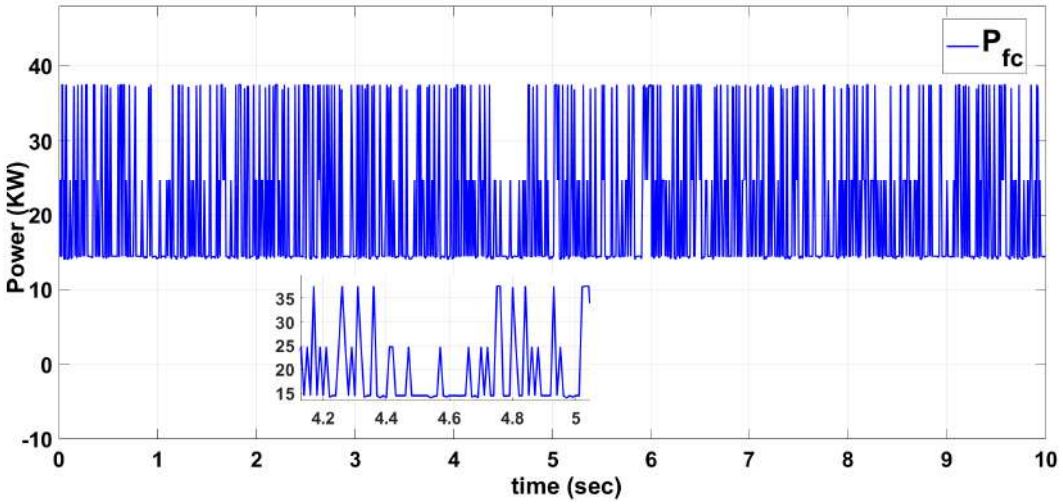

Figure 5.15: Optimal power contributed by fuel cell P_{FC}

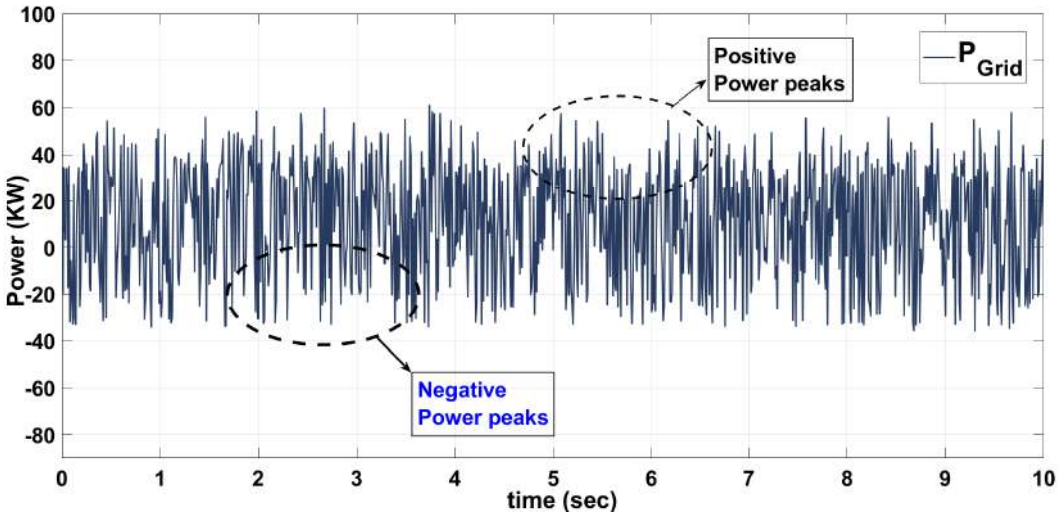

Figure 5.16: Calculated utility grid power P_{Grid}

5.5 conclusion

In this chapter, a PV-FC-based grid-connected microgrid has been considered to power the electric vehicle charging station. To improve the reliability and fuel economy of the FC, battery and supercapacitor-based ESS have also been used. The grid-connected topology has been investigated to minimize the power consumption of the utility grid through renewable energy and storage devices. This chapter proposes a neurofuzzy-based energy management strategy for optimal power sharing during stochastic and uncontrollable loads of electric vehicles. The ANN-based algorithm has been recommended to obtain the maximum power output of the photovoltaic system. In addition, a fuzzy rule-based system has been developed to get the maximum output from the battery, supercapacitor, and FC. Through the MATLAB/Simulink simulations, it is evident that the proposed EMS optimally shared the power between storage devices depending on SoCs and load demand by avoiding their complete discharging to enhance their useful life. This outcome demonstrates not only the efficiency of the power-sharing model, but also its adaptability to fluctuating loads, a key challenge in microgrid management, thus contributing to both sustainable energy usage and extended storage life. Furthermore, the observed negative power of the grid has verified the significant contribution of renewable energy and storage systems to the main grid, indicating that such systems can actively reduce grid dependency and lower operating costs over time. In future work, this work will be extended to design an advanced controller for power sources using actual data from electric vehicles, which promises to further enhance the accuracy and applicability of the proposed EMS. This extension will allow for a more responsive and predictive system that can adapt in real-time to varying charging demands, environmental conditions, and grid requirements. Furthermore, integrating machine

learning techniques, such as reinforcement learning, can optimize controller adaptability, leading to even more efficient power management strategies that respond dynamically to evolving electric vehicle ecosystems.

References

[1] W. Strielkowski, L. Civín, E. Tarkhanova, M. Tvaronavičienė, and Y. Petrenko, "Renewable energy in the sustainable development of electrical power sector: A review," *Energies*, vol. 14, no. 24, p. 8240, 2021.

[2] S. Kakran and S. Chanana, "Smart operations of smart grids integrated with distributed generation: A review," *Renewable and Sustainable Energy Reviews*, vol. 81, pp. 524–535, 2018.

[3] H. Abdelgawad and V. K. Sood, "A comprehensive review on microgrid architectures for distributed generation," in *2019 IEEE Electrical Power and Energy Conference (EPEC)*, IEEE, 2019, pp. 1–8.

[4] M. A. Hossain, H. R. Pota, S. Squartini, and A. F. Abdou, "Modified pso algorithm for real-time energy management in grid-connected microgrids," *Renewable energy*, vol. 136, pp. 746–757, 2019.

[5] S. A. Gorji, H. G. Sahebi, M. Ektesabi, and A. B. Rad, "Topologies and control schemes of bidirectional dc–dc power converters: An overview," *IEEE Access*, vol. 7, pp. 117 997–118 019, 2019.

[6] M. Aourir, A. Abouloifa, I. Lachkar, C. Aouadi, F. Giri, and J. M. Guerrero, "Nonlinear control and stability analysis of single stage grid-connected photovoltaic systems," *International Journal of Electrical Power & Energy Systems*, vol. 115, p. 105 439, 2020.

[7] F. Gao, R. Kang, J. Cao, and T. Yang, "Primary and secondary control in dc microgrids: A review," *Journal of Modern Power Systems and Clean Energy*, vol. 7, no. 2, pp. 227–242, 2019.

[8] J.-O. Lee, Y.-S. Kim, and S.-I. Moon, "Novel supervisory control method for islanded droop-based ac/dc microgrids," *IEEE Transactions on Power Systems*, vol. 34, no. 3, pp. 2140–2151, 2018.

[9] S. H. Qazi and M. W. Mustafa, "Improving voltage profile of islanded microgrid using pi controller," *International Journal of Electrical and Computer Engineering*, vol. 8, no. 3, p. 1383, 2018.

[10] S. Ferahtia, A. Djeroui, H. Rezk, A. Houari, S. Zeghlache, and M. Machmoum, "Optimal control and implementation of energy management strategy for a dc microgrid," *Energy*, vol. 238, p. 121 777, 2022.

[11] U. R. Nair and R. Costa-Castelló, "An analysis of energy storage system interaction in a multi objective model predictive control based energy management in dc microgrid," in *2019 24th IEEE International Conference on Emerging Technologies and Factory Automation (ETFA)*, IEEE, 2019, pp. 739–746.

[12] S. S. Zehra, A. U. Rahman, and I. Ahmad, "Fuzzy-barrier sliding mode control of electric-hydrogen hybrid energy storage system in dc microgrid: Modelling, management and experimental investigation," *Energy*, vol. 239, p. 122 260, 2022.

[13] A. U. Rahman, S. S. Zehra, I. Ahmad, and H. Armghan, "Fuzzy supertwisting sliding mode-based energy management and control of hybrid energy storage system in electric vehicle considering fuel economy," *Journal of Energy Storage*, vol. 37, p. 102 468, 2021.

[14] A. Rosato, M. Panella, R. Araneo, and A. Andreotti, "A neural network based prediction system of distributed generation for the management of microgrids," *IEEE Transactions on Industry Applications*, vol. 55, no. 6, pp. 7092–7102, 2019.

[15] Y. Du and F. Li, "Intelligent multi-microgrid energy management based on deep neural network and model-free reinforcement learning," *IEEE Transactions on Smart Grid*, vol. 11, no. 2, pp. 1066–1076, 2019.

[16] Y. Sun, X. Hou, J. Yang, H. Han, M. Su, and J. M. Guerrero, "New perspectives on droop control in ac microgrid," *IEEE Transactions on Industrial Electronics*, vol. 64, no. 7, pp. 5741–5745, 2017.

[17] A. Iovine, S. B. Siad, G. Damm, E. De Santis, and M. D. Di Benedetto, "Nonlinear control of a dc microgrid for the integration of photovoltaic panels," *IEEE Transactions on Automation Science and Engineering*, vol. 14, no. 2, pp. 524–535, 2017.

[18] S. S. Zehra, A. U. Rahman, H. Armghan, I. Ahmad, and U. Ammara, "Artificial intelligence-based nonlinear control of renewable energies and storage system in a dc microgrid," *ISA transactions*, 2021.

[19] S. Deb, K. Tammi, K. Kalita, and P. Mahanta, "Impact of electric vehicle charging station load on distribution network," *Energies*, vol. 11, no. 1, p. 178, 2018.

[20] I.-O. Lee, "Hybrid pwm-resonant converter for electric vehicle on-board battery chargers," *IEEE Transactions on Power Electronics*, vol. 31, no. 5, pp. 3639–3649, 2015.

[21] T. S. Bryden, G. Hilton, A. Cruden, and T. Holton, "Electric vehicle fast charging station usage and power requirements," *Energy*, vol. 152, pp. 322–332, 2018, ISSN: 0360-5442. DOI: https://doi.org/10.1016/j.energy.2018.03.149. [Online]. Available: https://www.sciencedirect.com/science/article/pii/S0360544218305589.

[22] Andersen, *What power do i need to charge my electric vehicle?: Andersen ev*, Oct. 2020. [Online]. Available: https://andersen-ev.com/charging-academy/what-power-do-i-need-to-charge-my-electric-vehicle/.

Part II

Study of EV Electrification and EV Chargers

Chapter 6

Energy Storage Systems for Electric Vehicles

6.1 Introduction

The storage devices have a wide range of applications in DC MGs and the e-mobility sector as discussed in the first part of the thesis. The technology can be used for electric vehicle propulsion systems. Energy storage devices (ESDs) are receiving attention in green energy research due to the uncertain nature of renewable energies. ESDs are actively used as auxiliary sources to provide backup in electrical networks [1], [2]. This study investigated the role and importance of HESS in fuel cell-based hybrid electric vehicles (HEVs) through proper control and management. HEVs will play an important role in the development of future green cities. In previous studies, different HEV models have been investigated, such as battery-only electric vehicles [3], fuel cell-based electric vehicles (FHEV) [4], and hybrid vehicles with internal combustion engines (ICE) [5]. Previous studies show that the fuel cell-based model overcomes the issues of low driving range and CO_2 emission. However, to minimize the use of hydrogen fuel, ESDs can be used as backup units [6]. ESDs provide two benefits for e-mobility applications; backup during high speed to reduce fuel consumption and storage of energy during regenerative braking. The selection of proper ESD according to the requirements of a particular system is also a challenging research field. In [7], [8] battery and supercapacitor have been used as ESD. Later, in the literature, a novel battery / supercapacitor-based HESS has been proposed that highlights the benefits of this combination such as more storage capacity, high current and power density, and long backup time [9].

6.2 Types of HEVs

The internal combustion engine (ICE) is the primary component of traditional vehicles, which is based on fossil fuels for operation. Despite advances over time, issues

remain due to fossil fuel dependency. A significant drawback of fossil fuels is their contribution to greenhouse gas emissions. In 1898, Dr. Ferdinand Porsche, from Germany, introduced the concept of the hybrid vehicle. A hybrid vehicle combines more than one power source, which can include any combination of ICE, fuel cell (FC), supercapacitor (SC), and battery. These vehicles can recover energy through regenerative braking, which also improves fuel efficiency. Hybrid vehicles are generally classified into three main types based on the combination of power sources.

ICE Based Hybrid Vehicles

In this configuration, a combination of an internal combustion engine (ICE) and an energy storage unit (ESU) is used. ICE serves as the main power source, while the ESU is used to store energy, particularly capturing energy through regenerative braking. The ESU can consist of either a battery or a supercapacitor (SC) and may sometimes use both. This setup improves the efficiency of the ICE and reduces fuel costs [10]. A plug-in hybrid electric vehicle (PHEV) represents a variant of hybrid electric vehicles (HEVs) that utilizes external power from the grid to recharge its ESU. In contrast, the ESU in standard HEVs is recharged by the electric motor during regenerative braking and under light load conditions. Currently, all hybrid vehicles on the market are based on an ICE [11]. The distinction between HEVs and PHEVs is illustrated in fig. 6.1.

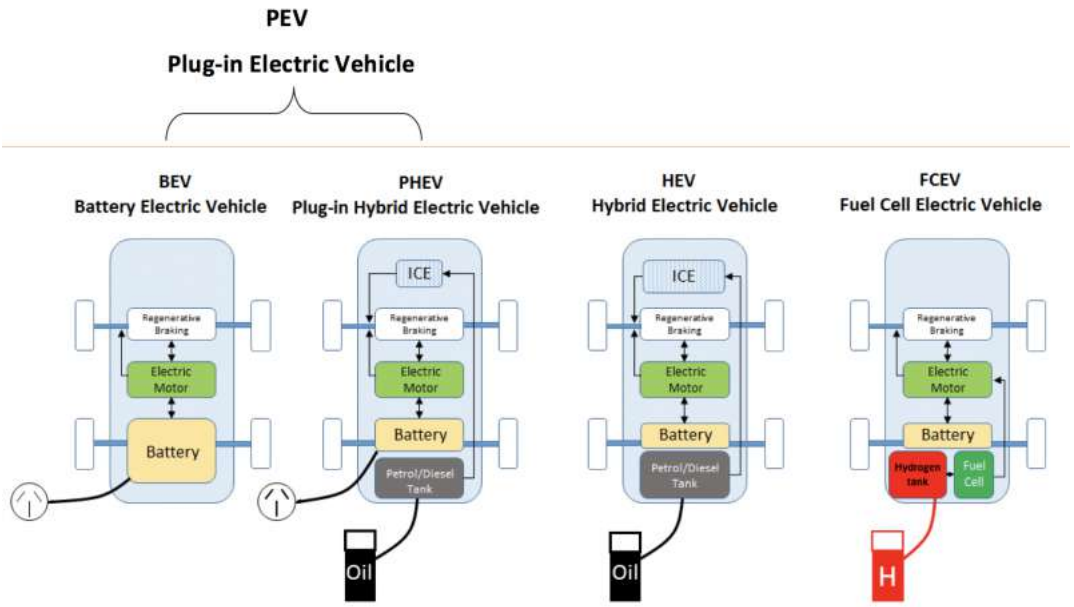

Figure 6.1: Comparative figure of different HEVs

Battery Based Hybrid Vehicle

The battery-only model uses a battery pack to power the electric motor of the vehicle. Its operating principle is straightforward: batteries are charged from an

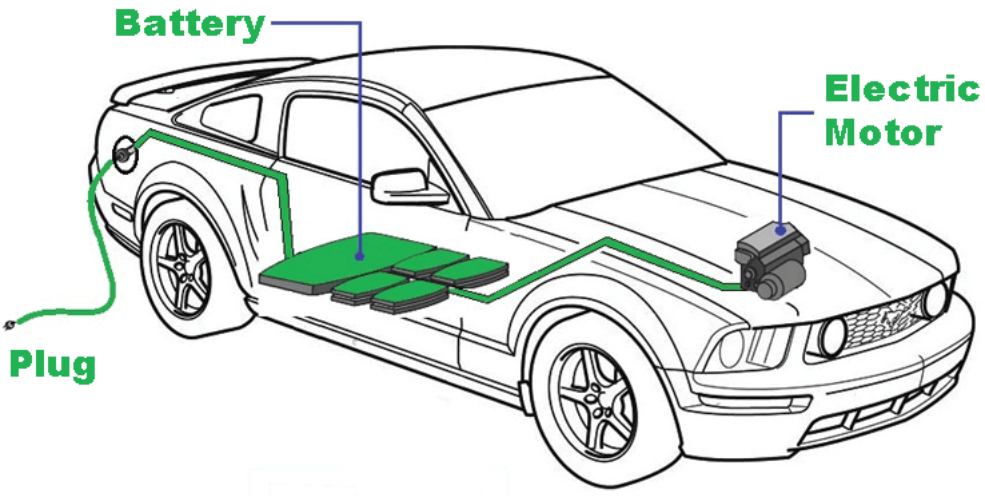

Figure 6.2: BEV Model

external power source and then discharged to drive the vehicle. Essentially, this model functions as a type of plug-in hybrid electric vehicle (PHEV). In this model, supercapacitors can be used in conjunction with batteries. The main advantages of battery electric vehicles (BEVs) include zero emissions, high efficiency, independence from crude oil, and broad commercial availability. However, they also come with some drawbacks, such as limited range, high upfront costs, and the need for accessible electric grid charging infrastructure. A brief review of BEVs is provided in [12].

Fuel Cell based HEV

A fuel cell generates electricity through a chemical reaction between hydrogen and oxygen in the presence of an electrolyte. This process offers significant advantages, including clean energy production and high efficiency. Various types of fuel cells exist, each with unique characteristics, and can be combined with other power sources in a hybrid configuration [13]-[14]. Fuel cells present a promising alternative to fossil fuels because of their high efficiency and zero emissions. In fuel-cell hybrid electric vehicles (FHEVs), the fuel cell acts as the primary power source, though it may not meet all load requirements independently. To support this, energy storage units (ESUs), typically comprising supercapacitors and batteries, are integrated alongside the fuel cell. Proton Exchange Membrane Fuel Cells (PEMFCs) are the most commonly used in hybrid electric vehicles (HEVs), offering benefits such as high power density, rapid start-up, zero emissions, and solid electrolyte [15]. FHEVs often incorporate different hybrid energy storage systems (HESS) [16]–[18]. Moreover, the use of HESS is not only limited to the e-mobility sector, but is also widely used in renewable energy and smart grids [19].

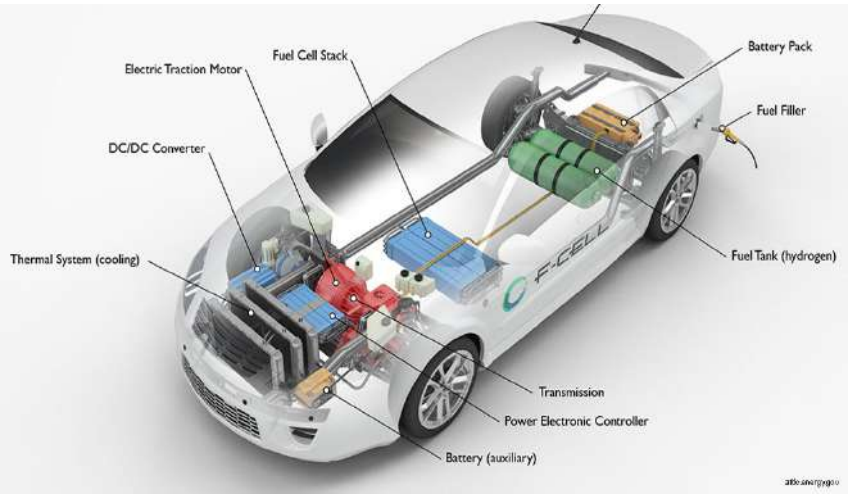

Figure 6.3: FHEV Diagram

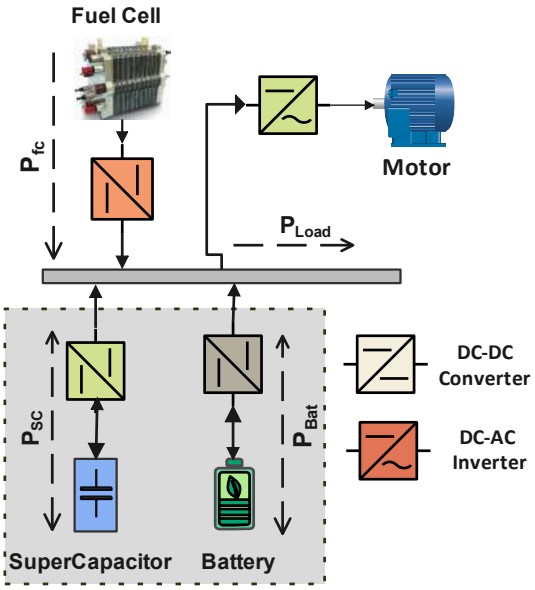

Figure 6.4: Overall structure of the vehicle model

All power sources require power electronics units, such as power converters, to share the power with the DC bus, which is used to run the electric motor. The power converters are very important to improve the efficiency of the system. Many converter topologies have been proposed for EVs such as cascade power converters, multi-converters, and multi-port power converters. Generally, bi-directional power converters are used with HESS to charge and discharge ESDs as they allow power flow in both directions [20]–[22]. To improve the efficiency of the system, the energy management and control of HESS play a very important role. The automation of HESS can be categorized into two sub-parts, energy management for power sharing between sources (master level control) and switching control to get the desired power from sources (slave level control). In [23], a real-time energy management algorithm

has been developed and followed by a speed controller. Similarly, a predictive management strategy has been proposed based on the velocity of the electric vehicle [24]. In [25], the optimal control method has been recommended for the control and power sharing of HESS. However, studies lack the development of sophisticated low-level controllers for power electronics units. Recently, some advanced distributed controllers based on sliding mode control (SMC) and model predictive control (MPC) have been studied. The results showed that advanced algorithms can outperform traditional PI controllers [26]–[28].
In a nutshell, some of the key issues found through the literature survey are; complex and high computational energy management algorithms, the discontinuous nature of advanced local controllers, and no test result against advanced driving cycles i.e. Worldwide Harmonized Light Vehicle Test Procedure (WLTP). The novelty of this work can be summarized as follows:

- A fuzzy rules-based heuristic algorithm is proposed for power distribution in HESS,
- Nonlinear controls theory based terminal synergetic, controller is developed for power converting units of EV model to overcome the discontinuous nature of SMC,
- Global stability analysis of the closed-loop system is carried out by using Lyapunov theory,
- The proposed algorithm is tested against a standard WLTP driving cycle using MATLAB/Simulink

Fig. 6.4 shows the overall structure of the FHEV having three power sources connected to the DC bus through power converters.

6.3 System Description and Modeling

In this chapter, battery and supercapacitor-based HESS are considered to provide auxiliary services in FHEV. The power electronics unit has multiple converter topology; each power source is connected to the DC bus through a dedicated converter. A fuel cell (FC) provides the prime power through a boost converter. The dynamic mathematical model [29] of the FC can be illustrated as follows:

$$\dot{\theta_1} = -(1-d_1)v_o - \frac{r_1}{l_1}\theta_1 + \frac{v_{fc}}{l_1} \tag{6.1}$$

$$\dot{\theta_4} = (1-d_1)\frac{\theta_1}{C} - \frac{i_1}{C} \tag{6.2}$$

where θ_1, v_{fc} and θ_4 are FC current, FC voltage and DC bus voltage respectively. r_1,l_1, and C represent the resistance, inductance, and capacitance of the boost con-

verter.

Fig. 6.5 shows the schematic diagram of HESS. The battery is considered one of the most reliable energy storage devices. Usually, lithium-ion batteries are used for EVs due to their less weight, long life span, and high power [30]. Applying Kirchhoff's voltage law on a battery circuit with a buck-boost converter the dynamic equation for battery current is derived as:

$$\dot{\theta_2} = \frac{v_{bat}}{l_2} - \frac{r_2}{l_2} - d_{23}\frac{\theta_4}{l_2} \tag{6.3}$$

$$d_{23} = [K(1-d_2) - (K-1)d_3] \tag{6.4}$$

where θ_2 and v_{bat} represents the battery current and voltage. The buck-boost converter has two modes of operation, buck (charging) and boost (discharging). d_{23} is the averaged duty cycle of the power converter having two switches S_1 and S_2.

A supercapacitor (SC) is also getting attention as a storage device that can rapidly provide power. It has the characteristics of fast charging and discharging. In Evs, supercapacitors can provide power during startup situations and can also handle the peak loads by providing instant power. The SC shares the same structure of the power converter as of battery. So, the mathematical equations for SC can also be obtained by applying KVL as:

$$\dot{\theta_3} = \frac{v_{sc}}{l_3} - \frac{r_3}{l_3} - d_{45}\frac{\theta_4}{l_3} \tag{6.5}$$

$$d_{45} = [K_1(1-d_4) - (K_1-1)d_5] \tag{6.6}$$

where $\dot{\theta_3}$ and v_{sc} are SC current and voltage. d_{45} denoted the averaged duty cycle input of the SC connected converter.

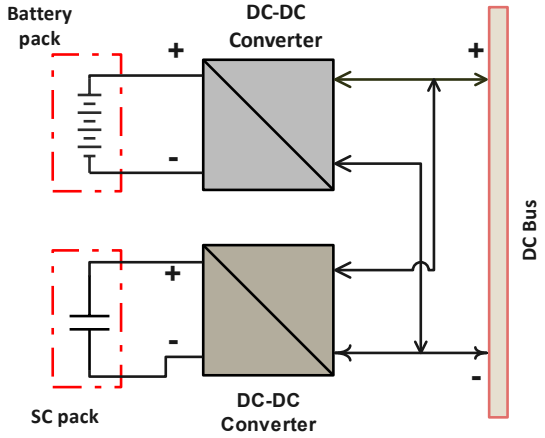

Figure 6.5: Hybrid energy storage system

Finally, a state-space averaged model of the system is obtained by applying

Kirchhoff's current law at the output node.

$$i_o = i_1 + i_2 + i_3 \tag{6.7}$$

as

$$i_2 = d_{23}\theta_2, \quad i_3 = d_{45}\theta_3$$

so

$$i_1 = i_o - d_{23}\theta_2 - d_{45}\theta_3 \tag{6.8}$$

where i_1, i_2, and i_3 are the output currents of three power converters attached with FC, battery, and SC respectively. Putting the value of i_1 in (6.2), the final expression for the DC bus voltage is given below.

$$\dot{\theta_4} = (1 - d_1)\frac{\theta_1}{C} - \frac{i_o}{C} + \frac{d_{23}\theta_2}{C} + \frac{d_{45}\theta_3}{C} \tag{6.9}$$

Hence, the equations (6.1), (6.3), (6.5), and (6.9) represent the averaged state-space model of the fuel cell electric vehicle.

6.4 Hierarchical Control Strategy

In this chapter, a master-slave control strategy is proposed for the automation of HESS in e-vehicles. The master level control algorithm is proposed by using a heuristic fuzzy rule-based approach and can be termed a management unit. The main idea is to optimally share the power between different sources of HESS during different scenarios. The terminal synergetic-based nonlinear controller is developed to follow the master-level control by tracking the desired trajectory. The working principle of the slave-level controller is to generate the duty cycle for power converters to follow the master-level control. The explanation of the proposed algorithms is given below.

6.4.1 Master control

Optimal power sharing is a real problem in multi-power source systems. A master-level control strategy is proposed to manage the power distribution between HESS. The fuzzy toolbox is used to develop the fuzzy rule-based heuristic algorithm. Mamdani fuzzy interface is used in MATLAB, the proposed master control has three inputs and two outputs. The three inputs can be defined as:

Load Power:

The first input is the load power required by the vehicle motor. The membership function for the load power is characterized as, $Negative$, Low, $Medium$, and $High$. All rules are developed taking into account these conditions.

State of charge (SoC) of Battery:

The strategy is also based on the SoCs of ESDs. SoC is an important factor in the management of HESS because the power provided by HESS depends on SoC. The SoC can vary between $1 - 100$. The membership function is classified as Low, $Medium$, and $High$. The SoC of the battery can be expressed as follows:

$$SoC_{BAT} = SoC_{Binital} - \frac{1}{C_n} \int_0^t \theta_2 \, dt \tag{6.10}$$

where C_n denotes the capacity of the power source.

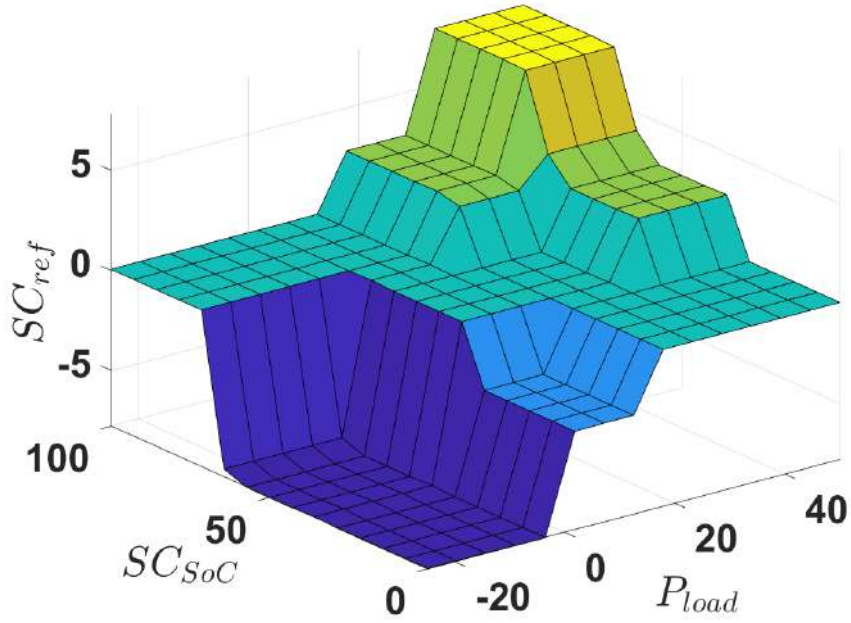

Figure 6.6: Surface graph of desired battery power

SoC of SC:

Similarly, the SoC of SC is also considered to decide the optimal power sharing. The SoC of SC will be used to determine the reference value. The same membership function is considered for SC as of battery.

$$SoC_{SC} = SoC_{Binital} - \frac{1}{C_n} \int_0^t \theta_2 \, dt \tag{6.11}$$

The output of the master level control is the optimal power signal for the battery and SC. Fig. 6.6 shows the surface plot of the battery reference value based on the SoC of the battery and the power load. The surface illustrates the rules developed based on input parameters. Similarly, fig.6.7 represents the output reference power value for SC SoC and load power.

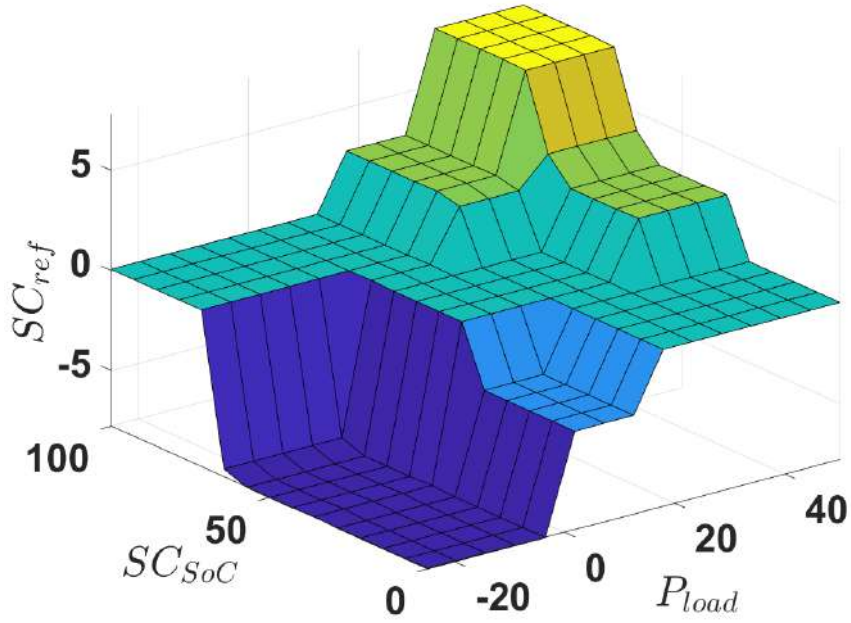

Figure 6.7: Surface graph of desired battery power

The simple rules of the proposed algorithm are given in Table6.1.

Table 6.1: Sample of heuristic fuzzy rules for FHEV

Rule no.	$\mathbf{P}_{load}$	$\mathbf{SoC}_{bat}$	$\mathbf{SoC}_{sc}$	$\mathbf{I}_{batref}$	$\mathbf{I}_{scref}$
1.	N	L	H	CF	I
2.	L	H	L	DP	CP
3.	M	H	M	DF	I
4.	H	H	M	DF	DF

CF, DF, CP and DP represent $Charged_{fully}$, $Discharged_{fully}$, $Charged_{partially}$ and $Discharged_{partially}$ respectively.

6.4.2 Slave Level Control

Terminal synergetic control (TSC) strategy is used for low-level monitoring purposes. The synergetic controller is simple as compared to other nonlinear controllers such as SMC. In synergetic control, we define a macro variable that contains tracking errors of states. The number of variables in the design procedure depends on the number of control inputs. In this section, the design of the controller is explained step by step.

For a tracking controller, error signals are very important. The error signals for

HESS tracking are defined as follows.

$$e_1 = \theta_2 - \theta_{2ref} \tag{6.12}$$

$$e_2 = \theta_3 - \theta_{3ref} \tag{6.13}$$

where θ_{2ref} and θ_{3ref} are the reference current values distributed by master level control for battery and SC respectively. They can be illustrated by the following equations.

$$\theta_{2ref} = \frac{P^*_{bat}}{v_{bat}} \tag{6.14}$$

$$\theta_{3ref} = \frac{P^*_{sc}}{v_{sc}} \tag{6.15}$$

where P^*_{bat} and P^*_{sc} are the output of master level control. The terminal approach is getting attention in advanced control theory due to finite time convergence. The dynamic equation for the TSC is

$$T_1\dot{\zeta_1} + \zeta_1 = 0 \tag{6.16}$$

where ζ_1 is the macro variable containing the error signal as

$$\zeta_1 = e_1 + G_1\Big(\int_0^t (e_1)\Big)^{p/q} \tag{6.17}$$

where p, q, T_1 and G_1 are the positive constant. The variables p and q always satisfy the condition $1 \leq p/q \leq 2$. Taking the time derivative of (6.17) and putting the value of $\dot{\theta_2}$ from (6.3), we can solve the above equation for control input d_{23}.

$$d_{23} = \frac{l_2}{\theta_4}\left[\frac{v_{bat}}{l_2} - \frac{r_2}{l_2} - \dot{\theta_{2ref}} + G_1(p/q)e_1 + \frac{\zeta_1}{T_1}\right] \tag{6.18}$$

d_{23} is the duty cycle applied to the buck-boost converter of the battery as the control input. Similarly, for SC another macro variable with the same specifications is considered as

$$\zeta_2 = e_2 + G_2\Big(\int_0^t (e_1)\Big)^{p/q} \tag{6.19}$$

Considering the standard dynamic equation

$$T_i\dot{\zeta_i} + \zeta_i = 0 \tag{6.20}$$

$$i = 1, 2, 3$$

Solving the dynamic equation using eqs.(6.5), (6.19) for the SC in the same way will give

$$d_{45} = \frac{l_3}{\theta_4}\left[\frac{v_{sc}}{l_3} - \frac{r_3}{l_3} - \dot{\theta_{3ref}} + G_2(p/q)e_2 + \frac{\zeta_2}{T_2}\right] \tag{6.21}$$

As we have two control inputs for the battery and SC converter. Finally, the control input for FC trajectory tracking and DC bus voltage regulation can be obtained by defining error as follows

$$e_3 = \theta_1 - \theta_{1ref} \tag{6.22}$$

$$e_4 = \theta_4 - \theta_{4ref} \tag{6.23}$$

where

$$P^*_{fcref} = P_{load} - P_{bat} - P_{sc} \tag{6.24}$$

$$\theta_{1ref} = \frac{P^*_{fcref}}{v_{fc}} \tag{6.25}$$

Considering the following manifold for FC and DC bus voltage

$$\zeta_3 = e_3 + G_3\Big(\int_0^t (e_3)\Big)^{p/q} + e_4 \tag{6.26}$$

Now, using eqs. (6.1), (6.20) and (6.26) and solving for control input d_1, we get

$$\begin{aligned} d_1 = \Big(\frac{l_1 C}{C\theta_4 + \theta_1 l_1}\Big)\Big[&\frac{\theta_4}{l_1} - \frac{r_1}{l_1}\theta_1 \\ &+ \frac{v_{fc}}{l_1} - \dot{\theta_{1ref}} + \frac{\theta_1}{C} \\ &- \frac{i_o}{C} + \frac{\theta_2}{C}d_{23} + \frac{\theta_3}{C}d_{45} + \frac{\zeta_3}{T_3}\Big] \end{aligned} \tag{6.27}$$

The three control inputs d_1, d_{23}, and d_{45} are the duty cycle signals generated by the slave level controller to track the optimal reference values. The stability analysis of the closed-loop system is given below by using the Lyapunov theory.

6.4.3 Stability Analysis

The error e_i $(i = 1, 2, 3, 4)$ will converge to zero, through which the states will follow the desired trajectory due to TSC. Considering the following Lyapunov function

$$V_i = \frac{1}{2}(\zeta_i(e_i))^2 \tag{6.28}$$

Taking the time derivative of (6.28) gives

$$\dot{V_i} = \zeta_i(e_i)\dot{\zeta}_i(e_i) \tag{6.29}$$

putting the value ζ_i from (6.20) in equation above, it takes the following form

$$\dot{V}_i = \zeta_i(e_i)\frac{-\zeta_i(e_i)}{T_i} \tag{6.30}$$

By simplifying and rearranging the (6.30), we get

$$\dot{V}_i = -\frac{2}{T_i}V_i \tag{6.31}$$

where in (6.31) $V_i = V_{oi}$, so final expression can be written as

$$\dot{V}_i = -\frac{2}{T_i}V_{oi} < 0 \tag{6.32}$$

where $i = 1, 2, 3$ for three macro variables and V_{oi} is the value of V_i at time $t = 0$ can be termed as condition. The time deviation of the Lyapunov function is negative definite according to (6.32), which means that the closed-loop system will be stable while the controller brings the error signals to zero and ensures the finite-time convergence of the states to their desired value.

6.5 Simulation Results and Discussion

Finally, the proposed methodology is tested using MATLAB/Simulink. The WLTP class 3 speed profile is considered for the vehicle driving test. WLTP is the standard test used for vehicle driving testing according to European law. The speed profile of the vehicle driving cycle is shown in Fig.6.8. The proposed control algorithm is simulated for 1800 seconds to verify its validity against each driving speed and scenario. The power required to run the vehicle for the WLTP cycle can be calculated using the following mathematical expression.

$$P_{load} = \frac{1}{0.75}\left[0.5p_a v_t^2 AC_x + M_g C_r + M\frac{dv_t}{dt}\right]v_t \tag{6.33}$$

where v_t denotes the speed of the vehicle, and other parameters are given below in Table 6.2.

Table 6.2: Specifications of vehicle parameters

Parameter	**Values**
Car mass M	1070Kg
Passenger weight (x 2)	65+70 kg
Aerodynamic drag coefficient (C_x)	0.18
Rolling resistance coefficient(C_r)	0.0048
Front Area (A)	$1.75m^2$

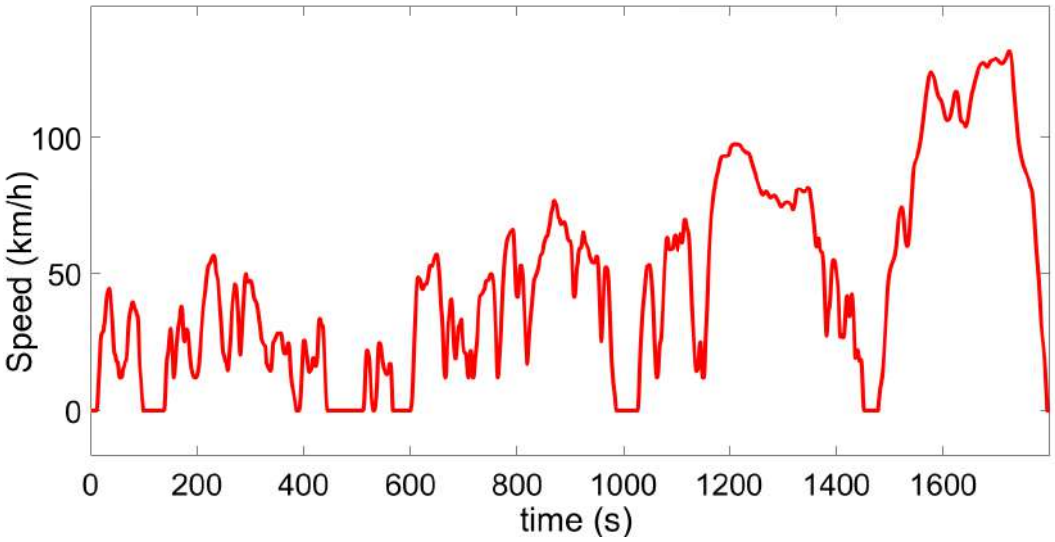

Figure 6.8: Speed profile of e-vehicle under WLTP

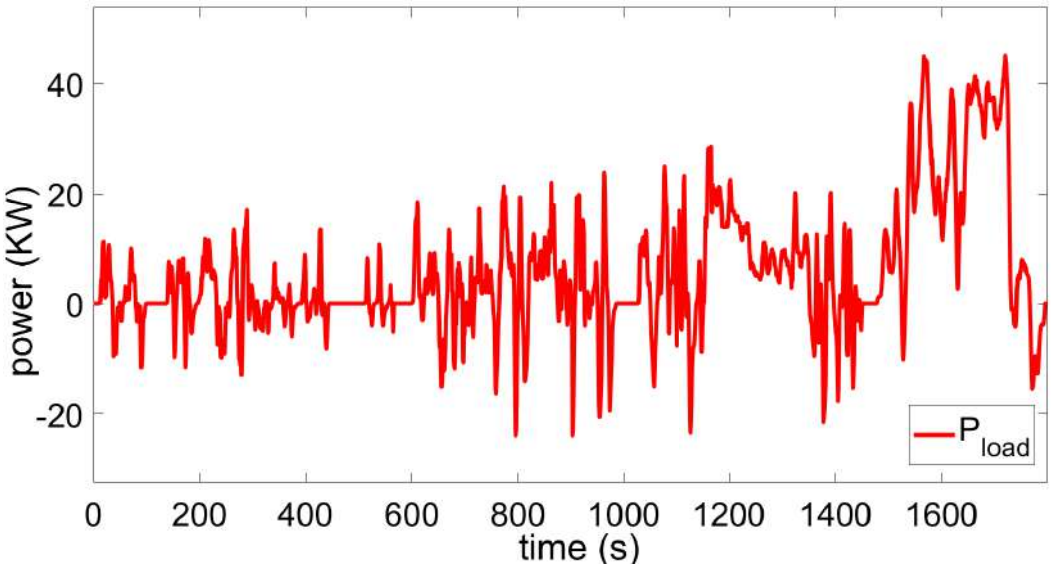

Figure 6.9: Load power under WLTP

Fig. 6.9 shows the graph of load power calculated according to the change of vehicle speed in WLTP. HESS will charge or discharge to meet the load requirements according to the SoC presented in Fig. 6.10. The initial SoC is assumed 50% and 85% for SC and battery respectively. Based on SoC of HESS and P_{load}, optimal reference values are generated by master-level control which is tracked by slave-level control. Figures 6.11, 6.12, and 6.13 present the comparative graph between the reference value advised by master control and the actual state (i_{fc}, $i_{bat,sc}$) response. The black dotted line and red solid line represent the optimal trajectory and the actual system response respectively. It can be observed from the results that the TSC-based slave level controller is tracking the desired value nicely. The convergence

of battery and SC current can be seen in the zoomed-in view of Fig. 6.11 and 6.12.

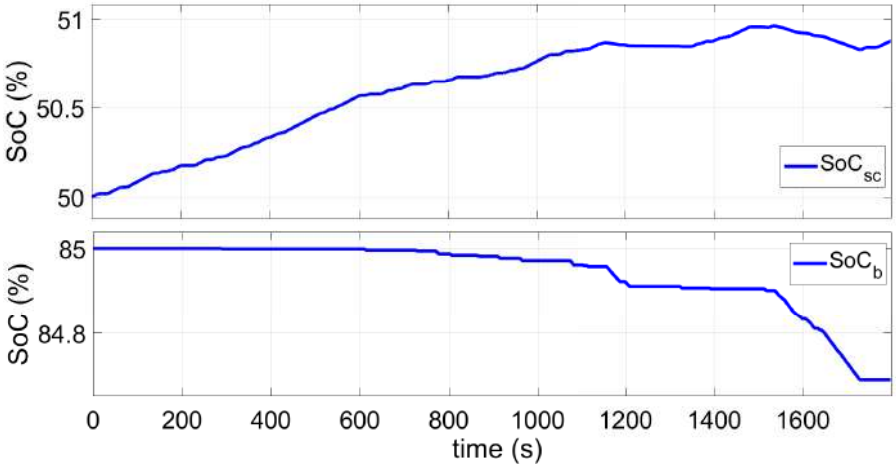

Figure 6.10: SoCs of HESS

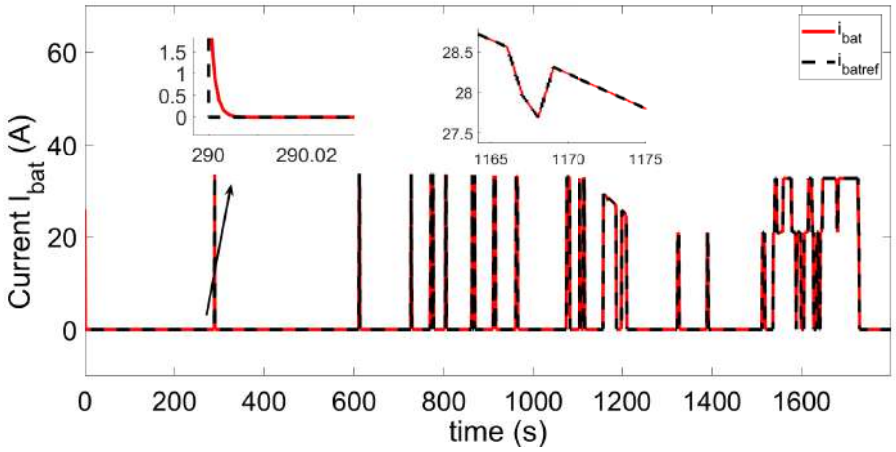

Figure 6.11: Tracking of battery current by TSC

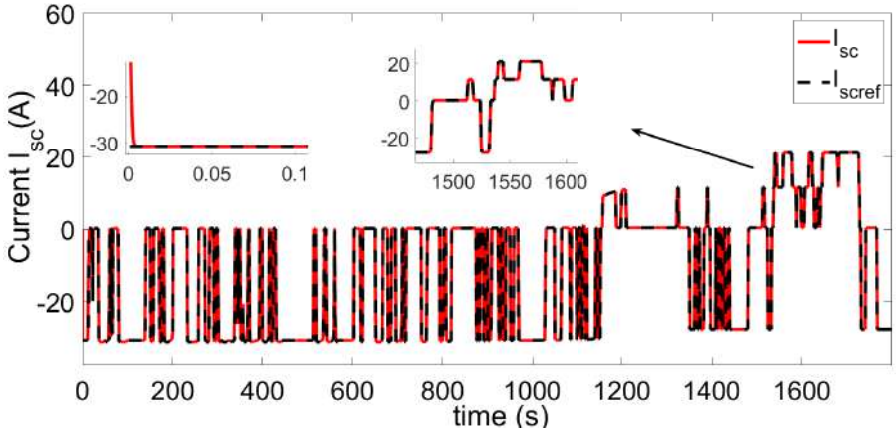

Figure 6.12: Tracking of SC by TSC

Moreover, the charging and discharging of HESS according to the SoC also validates the rules-based management. In fig 6.13, it is evident that the fuel cell is working as the primary source. The zoomed-in part of the figure shows the tracking of the FC current to its reference value with a very low steady-state error. Finally, Fig. 6.14 shows the DC bus response, the reference value for the bus voltage is set to 400 V.

The controller showed satisfactory performance in bus voltage regulation. However, transient response and some overshoots can be observed in the zoomed-in part of Fig. 6.14. The overshoots are due to a high nonlinear time-varying load profile but these spikes are within safe limits.

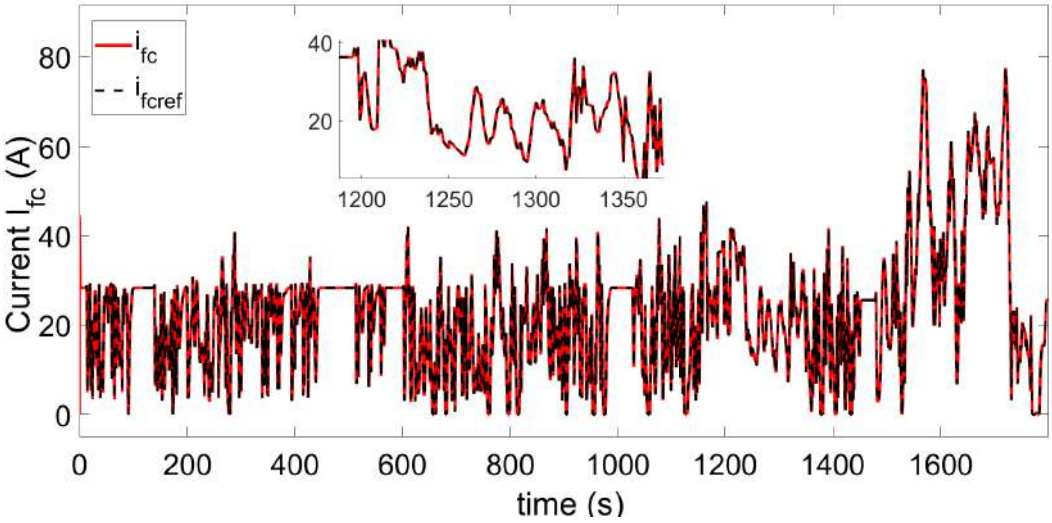

Figure 6.13: Tracking of FC by TSC

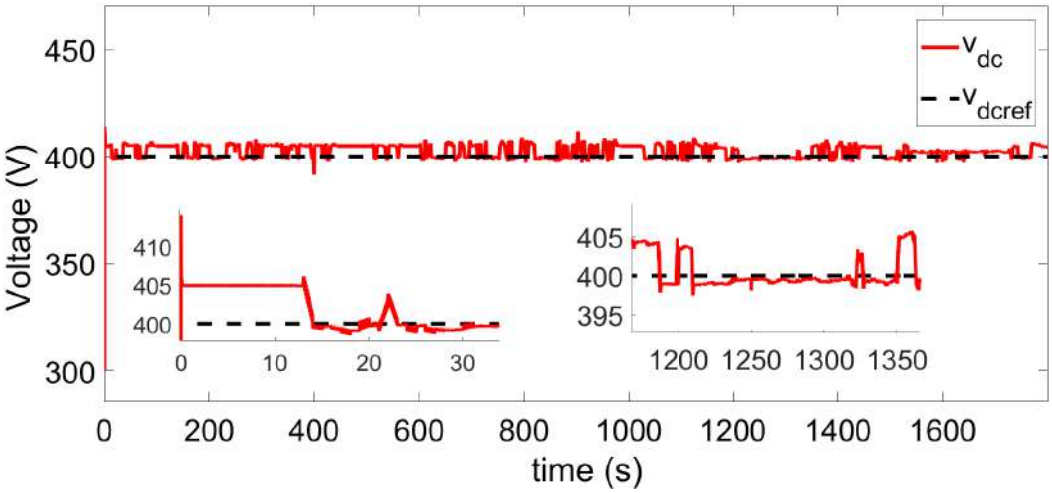

Figure 6.14: DC bus voltage regulation

6.6 Conclusion

This chapter studies the control of HESS by keeping the SoCs in the count. The HESS is considered for fuel cell-based electric vehicle. A two-stage control algorithm makes the system stable and more efficient. The results showed that fuzzy rule-based master control handled the split of power between sources depending on the load required and SoCs. So, the use of hydrogen fuel will decrease as the maximum capacity of the storage system is used. The TSC algorithm is used to develop the slave-level controller to track the optimal trajectory. The results obtained from the MATLAB implementation clearly show the validity of the proposed controller. In summary, the study concluded that the proposed two-stage control strategy performed very well in solving the control and management problem of such hybrid systems.

References

[1] J. Liu, L. Jian, W. Wang, Z. Qiu, J. Zhang, and P. Dastbaz, "The role of energy storage systems in resilience enhancement of health care centers with critical loads," *Journal of Energy Storage*, vol. 33, p. 102 086, 2021.

[2] A. Kalair, N. Abas, M. S. Saleem, A. R. Kalair, and N. Khan, "Role of energy storage systems in energy transition from fossil fuels to renewables," *Energy Storage*, vol. 3, no. 1, e135, 2021.

[3] M. Adaikkappan and N. Sathiyamoorthy, "Modeling, state of charge estimation, and charging of lithium-ion battery in electric vehicle: A review," *International Journal of Energy Research*, vol. 46, no. 3, pp. 2141–2165, 2022.

[4] A. U. Rahman, S. S. Zehra, I. Ahmad, and H. Armghan, "Fuzzy supertwisting sliding mode-based energy management and control of hybrid energy storage system in electric vehicle considering fuel economy," *Journal of Energy Storage*, vol. 37, p. 102 468, 2021.

[5] A. Gerlach, N. Förster, H. Rottengruber, and R. Leidhold, "Efficient control of internal combustion engines for electric power generation without throttle actuator," in *IECON 2016-42nd Annual Conference of the IEEE Industrial Electronics Society*, IEEE, 2016, pp. 1802–1807.

[6] Q. S. Wei, X. Zhang, B.-H. Kim, and B. S. Oh, "Experimental investigation of supercapacitor based regenerative energy storage for a fuel cell vehicle equipped with an alternator," *International Journal of Hydrogen Energy*, vol. 47, no. 3, pp. 1954–1964, 2022.

[7] M. Carignano, V. Roda, R. Costa-Castelló, L. Valiño, A. Lozano, and F. Barreras, "Assessment of energy management in a fuel cell/battery hybrid vehicle," *IEEE access*, vol. 7, pp. 16 110–16 122, 2019.

[8] H. El Fadil, F. Giri, J. M. Guerrero, and A. Tahri, "Modeling and nonlinear control of a fuel cell/supercapacitor hybrid energy storage system for electric vehicles," *IEEE Transactions on Vehicular Technology*, vol. 63, no. 7, pp. 3011–3018, 2014. DOI: 10.1109/TVT.2014.2323181.

[9] H. Fathabadi, "Novel fuel cell/battery/supercapacitor hybrid power source for fuel cell hybrid electric vehicles," *Energy*, vol. 143, pp. 467–477, 2018.

[10] C. C. Chan, "The state of the art of electric, hybrid, and fuel cell vehicles," *Proceedings of the IEEE*, vol. 95, no. 4, pp. 704–718, Apr. 2007, ISSN: 0018-9219. DOI: 10.1109/JPROC.2007.892489.

[11] S. Overington and S. Rajakaruna, "A novel model of internal combustion engine for high efficiency operation of hybrid electric vehicles and power systems," in *2014 Australasian Universities Power Engineering Conference (AUPEC)*, Sep. 2014, pp. 1–6. DOI: 10.1109/AUPEC.2014.6966489.

[12] H. E. Dance, "The electric battery vehicle," *Journal of the Institution of Electrical Engineers*, vol. 61, no. 323, pp. 1100–1108, Oct. 1923. DOI: 10.1049/jiee-1.1923.0141.

[13] H. Fathabadi, "Fuel cell hybrid electric vehicle (fchev): Novel fuel cell/sc hybrid power generation system," *Energy Conversion and Management*, vol. 156, pp. 192–201, 2018, ISSN: 0196-8904. DOI: https://doi.org/10.1016/j.enconman.2017.11.001. [Online]. Available: http://www.sciencedirect.com/science/article/pii/S019689041731035X.

[14] K. Rajashekara, "Hybrid fuel-cell strategies for clean power generation," *IEEE Transactions on Industry Applications*, vol. 41, no. 3, pp. 682–689, May 2005, ISSN: 0093-9994. DOI: 10.1109/TIA.2005.847293.

[15] M. A. Laughton, "Fuel cells," *Engineering Science and Education Journal*, vol. 11, no. 1, pp. 7–16, Feb. 2002, ISSN: 0963-7346. DOI: 10.1049/esej:20020102.

[16] Wenzhong Gao, "Performance comparison of a fuel cell-battery hybrid powertrain and a fuel cell-ultracapacitor hybrid powertrain," *IEEE Transactions on Vehicular Technology*, vol. 54, no. 3, pp. 846–855, May 2005, ISSN: 0018-9545. DOI: 10.1109/TVT.2005.847229.

[17] H. El Fadil, F. Giri, J. M. Guerrero, and A. Tahri, "Modeling and nonlinear control of a fuel cell/supercapacitor hybrid energy storage system for electric vehicles," *IEEE Transactions on Vehicular Technology*, vol. 63, no. 7, pp. 3011–3018, Sep. 2014, ISSN: 0018-9545. DOI: 10.1109/TVT.2014.2323181.

[18] M. S. Khan, I. Ahmad, H. Armaghan, and N. Ali, "Backstepping sliding mode control of fc-uc based hybrid electric vehicle," *IEEE Access*, vol. 6, pp. 77 202–77 211, 2018, ISSN: 2169-3536. DOI: 10.1109/ACCESS.2018.2879881.

[19] A. Olabi and M. Abdelkareem, *Energy storage systems towards 2050*, 2021.

[20] A. Affam, Y. M. Buswig, A.-K. B. H. Othman, N. B. Julai, and O. Qays, "A review of multiple input dc-dc converter topologies linked with hybrid electric vehicles and renewable energy systems," *Renewable and Sustainable Energy Reviews*, vol. 135, p. 110 186, 2021.

[21] S. Chakraborty, H.-N. Vu, M. M. Hasan, D.-D. Tran, M. E. Baghdadi, and O. Hegazy, "Dc-dc converter topologies for electric vehicles, plug-in hybrid electric vehicles and fast charging stations: State of the art and future trends," *Energies*, vol. 12, no. 8, p. 1569, 2019.

[22] H. Al-Sheikh, O. Bennouna, G. Hoblos, and N. Moubayed, "Power electronics interface configurations for hybrid energy storage in hybrid electric vehicles," in *MELECON 2014-2014 17th IEEE Mediterranean Electrotechnical Conference*, IEEE, 2014, pp. 122–126.

[23] L. Zhang, X. Ye, X. Xia, and F. Barzegar, "A real-time energy management and speed controller for an electric vehicle powered by a hybrid energy storage system," *IEEE Transactions on Industrial Informatics*, vol. 16, no. 10, pp. 6272–6280, 2020.

[24] C. Zhai, F. Luo, and Y. Liu, "A novel predictive energy management strategy for electric vehicles based on velocity prediction," *IEEE Transactions on Vehicular Technology*, vol. 69, no. 11, pp. 12 559–12 569, 2020.

[25] C. Zheng, W. Li, and Q. Liang, "An energy management strategy of hybrid energy storage systems for electric vehicle applications," *IEEE Transactions on Sustainable Energy*, vol. 9, no. 4, pp. 1880–1888, 2018.

[26] L. Wang, Y. Wang, C. Liu, D. Yang, and Z. Chen, "A power distribution strategy for hybrid energy storage system using adaptive model predictive control," *IEEE Transactions on Power Electronics*, vol. 35, no. 6, pp. 5897–5906, 2019.

[27] A. U. Rahman, I. Ahmad, and A. S. Malik, "Variable structure-based control of fuel cell-supercapacitor-battery based hybrid electric vehicle," *Journal of Energy Storage*, vol. 29, p. 101 365, 2020.

[28] H. Armghan, I. Ahmad, N. Ali, M. F. Munir, S. Khan, and A. Armghan, "Nonlinear controller analysis of fuel cell–battery–ultracapacitor-based hybrid energy storage systems in electric vehicles," *Arabian Journal for Science and Engineering*, vol. 43, no. 6, pp. 3123–3133, 2018.

[29] S. A. Gorji, H. G. Sahebi, M. Ektesabi, and A. B. Rad, "Topologies and control schemes of bidirectional dc–dc power converters: An overview," *IEEE Access*, vol. 7, pp. 117 997–118 019, 2019.

[30] A. Ranjan and S. B. Bodkhe, "Modified energy management strategy for hess in electric vehicle," in *2021 9th IEEE International Conference on Power Systems (ICPS)*, IEEE, 2021, pp. 1–6.

Chapter 7

Market Study EV Chargers for Smart Communities

7.1 Introduction

This part of the research has been carried out in collaboration with EOSS Prysmian Palermo. The company works on data-driven power flow, Wallbox chargers for EV charging, and energy management in smart communities. The main goal of this research is to develop a comparative analysis of available DC fast chargers in the market for the development of a "Wallbox" for EV integration. Prysmian's asset monitoring systems and electronics are centered on advanced diagnostic tools such as PRY-CAM technology, which detects and analyzes partial discharge in electrical assets. This system supports monitoring conditions both online and offline without interruptions of service. Using high-frequency sensors and cloud-based data analytics, PRY-CAM enables real-time data acquisition and fault prediction, which are critical to minimizing system downtime and ensuring the longevity of the electrical network. The solutions also include integrated electronics for smart grid applications, enabling seamless energy flow management and enhanced fault detection in power distribution networks. Their monitoring systems are designed to handle high-voltage environments, using IoT connectivity to provide remote access and control. By combining robust hardware with sophisticated data analytics platforms, Prysmian optimizes decision-making processes for preventive and predictive maintenance in power transmission and distribution systems [1].

The main aim is to analyze the integration of a DC fast charger with the existing PRY-CAM device and other energy sources to provide a controller and efficient energy solutions. The different scenarios, configurations, and market analyses of the chargers have been studied to provide insight into the suitable budget for the DC fast charger.

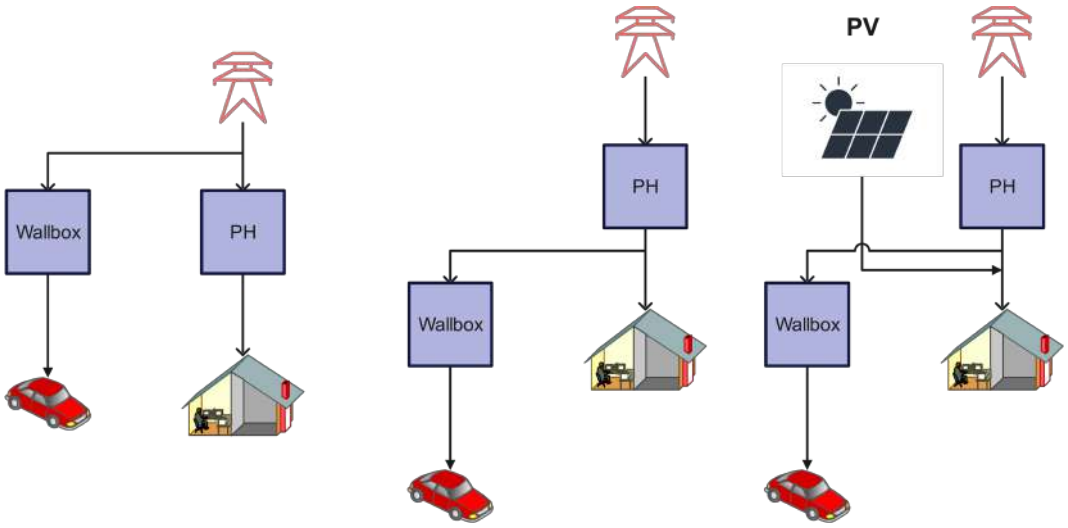

Figure 7.1: Possible Configuration for Wallbox

7.2 Type of EV Chargers

Due to the rapid growth of EVs in the market, EV chargers are also an important field to escalate the penetration of EVS in the market. Different types of EV chargers are available to charge an EV according to the power rating and standards. The EV charger market can be categorized as follows:

7.2.1 AC fast charger

AC fast charging systems are versatile and essential for both private and public EV charging infrastructures. They are based on different voltage levels and power outputs to suit various use cases.

Key Features of AC Fast Charging

- **Power Range:** Delivers between 7 kW and 22 kW, depending on the type of charger and the setup.
- **Voltage Requirements:** Operates on 240V single-phase or 400V three-phase connections.
- **Compatibility:** Universally compatible with electric vehicles as the onboard charger handles the AC to DC conversion.
- **Charging Speed:** Typically adds 25–75 km (15–45 miles) of range per hour of charging.

Residential AC Chargers

- **Power Output:** Typically ranges between 7 kW and 11 kW.

- **Connection Type:** Uses a 240V single-phase AC supply.
- **Applications:** Installed at homes for private EV owners. Often wall-mounted for easy use.
- **Charging Time:** Takes about 6–8 hours to fully charge a standard EV with a 50 kWh battery.
- **Advantages:**
  - Convenient for overnight charging.
  - Affordable installation compared to DC fast chargers.
- **Limitations:**
  - Slower charging speeds compared to public three-phase AC or DC chargers.
  - Requires a dedicated circuit to prevent overloading of household electricity systems.

Public AC Chargers

- **Power Output:** Typically up to 22 kW, using a three-phase AC supply for higher charging speeds.
- **Applications:** Installed in parking lots, shopping malls, workplaces, and public charging hubs.
- **Charging Time:** Adds about 100–130 km (60–80 miles) of range per hour of charging. Full charge in 3–4 hours for most EVs.
- **Advantages:**
  - Faster than residential chargers due to the three-phase power supply.
  - Suitable for mid-trip charging or workplace charging during working hours.
- **Limitations:**
  - Infrastructure costs can be higher than for residential installations.
  - Requires proper parking and power infrastructure to accommodate multiple vehicles.

7.2.2 DC fast charger

DC fast chargers are classified according to their power output and application. They are commonly used in public charging stations along highways and urban centers. Some of the key points of DC fast chargers are:

- **Power Range:** Typically between 50 kW and 350 kW, with some ultra-fast chargers exceeding 400 kW.
- **Voltage Requirements:** Operates at higher voltage levels, usually between 400V and 800V, with future systems aiming at 1,000V.
- **Charging Speed:** Capable of delivering 80% charge in 20–40 minutes for most EVs.
- **Direct Current Supply:** Bypasses the EV's onboard charger, supplying DC power directly to the battery.

Types of DC Fast Chargers

- **Standard DC Chargers (50 kW):**
  - Common at public stations for moderate-speed charging.
  - Suitable for EVs with smaller battery capacities or lower fast-charging limits.
  - Adds approximately 150 km (90 miles) of range in about 30 minutes.
- **High-Power DC Chargers (150 kW to 350 kW):**
  - Designed for newer EVs with large battery capacities.
  - Provides faster charging, adding up to 300 km (190 miles) of range in 20–30 minutes.
  - Operates on 800V systems, reducing heat loss and improving efficiency.
- **Ultra-Fast DC Chargers (350 kW and above):**
  - aimed at next-generation electric vehicles with ultra-fast charging capabilities.
  - Adds approximately 400 km (250 miles) of range in less than 15 minutes for compatible vehicles.
  - Requires advanced cooling systems and high-capacity infrastructure.

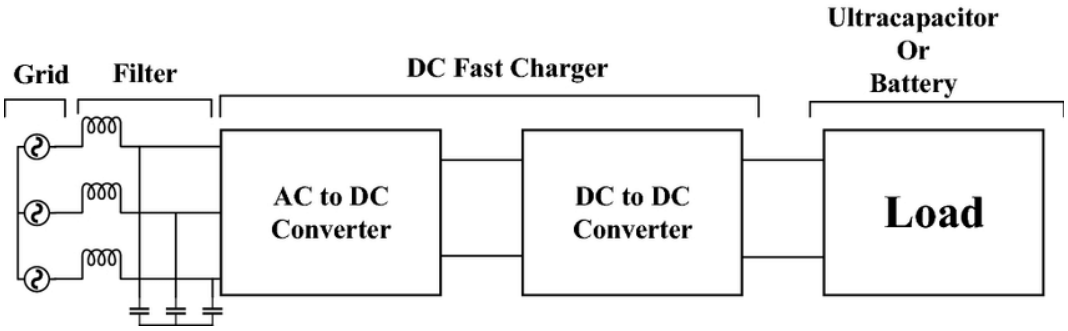

Figure 7.2: Schematic diagram of DC fast charger

Advantages of DC Fast Charging

- **High-Speed Charging:** Reduces charging time significantly compared to AC systems.
- **Long-Distance Viability:** Essential for highway charging stations and long-haul EV travel.
- **Direct Battery Charging:** Bypasses onboard limitations for faster energy transfer.

Limitations

- **High Infrastructure Costs:** Installation and maintenance are expensive due to high power requirements.
- **Vehicle Compatibility:** Not all electric vehicles can use high-power DC fast chargers.
- **Battery Degradation:** Frequent use can accelerate battery wear over time.
- **Energy Demand:** Requires robust electrical infrastructure to support high power levels.

7.3 DC Fast Charger Configurations and Topology

DC fast chargers are receiving attention due to their utmost advantages. However, there are some limitations and technical issues that must be taken into account to produce new technical products. Power converters are considered the backbone of this technology, as energy conversion is the most important part of the transfer of power from the grid to the vehicle battery. Fig. 7.2 shows the schematic block diagram of the DC fast charging system. Isolated DC-DC converters like DAB, LLC, and multilevel DAB provide better performance and safe solutions due to their applications in high power transfer. As illustrated in Fig. 7.3, the circuit

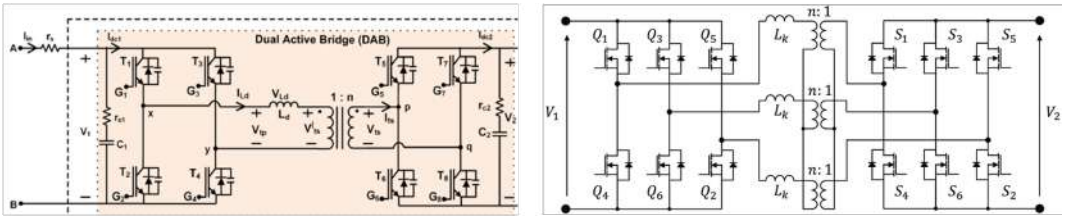

Figure 7.3: Some general power converters for DC fast charger

diagram of the DAB converter features two full bridges and an isolating transformer, complemented by an inductor. Isolated DC-DC converters are gaining prominence due to their compliance with high-power applications. Their bidirectional power flow capability plays a pivotal role in the grid-to-vehicle (G2V) and V2G operations, facilitating efficient DC fast charging of EVs [2]. The DAB converter encompasses components such as C_{vdc}, the input side capacitor, L_{lk}, the inductor, and an output filter comprising C_{ev} and L_f. The expression for the output power of the DAB converter can be depicted as:

$$P_{ev} = \frac{NV_{Cev}V_{Cvdc}\phi(1-2|\phi|)}{f_{sw}L_{lk}}. \tag{7.1}$$

Here, P_{ev} indicates the output power of the DAB converter, while N, ϕ, and f_{sw} represent the number of turns of the transformer, the phase change, and the switching frequency, respectively. In the case of an ideal transformer, the number of turns can be expressed as:

$$N = \frac{V_{cev}}{V_{cvdc}}. \tag{7.2}$$

The mathematical model of the DAB converter can be derived by using the state-space average technique [3] and can be written as:

$$\begin{aligned}
\dot{x_1} &= -\frac{R}{L_{lk}}x_1 + \frac{T\cdot R\cdot N}{L_{lk}^2}\cdot\phi(1-2|\phi|)x_3,\\
\dot{x_2} &= \frac{1}{C_{ev}}x_1 + \frac{1}{R_{ev}C_{ev}}x_2 + \frac{V_g}{R_{ev}C_{ev}},\\
\dot{x_3} &= \frac{N}{C_{vdc}}x_1 - \frac{1}{R_gC}x_3 + \frac{V_{ev}}{R_gC_{vdc}}.
\end{aligned} \tag{7.3}$$

ϕ serves as the control parameter employed for regulating the output power of the DAB through phase shift modulation. Here, R_g and R_{ev} denote the resistance on the MG side and the resistance on the EV side, respectively. The state variables of the system are defined as:

$$[x_1, x_2, x_3]^T = [I_{ev}, V_{cev}, V_{cvdc}]^T.$$

The DC fast charger also needs to be standardized to be widely used in the market. Fig 7.4 shows the standard CCS combo two and the types and power ratings of

Table 7.1: Market price analysis of EV chargers

Sr.	Power Rating	Price (€)	Type	Range
Tritium [4]	50 kW	13-16 K	DC	High
Xcharge [5]	50 KW +	15+ K	DC	High
HICONIC [6]	50 KW +	up to 80 K	DC	High
ABB Terra [7]	22 kW	9 K	DC	Medium
Dcbel R16 [8]	16 kW	5 K	DC	Medium
ABB AC [7]	22.2 kW	740	AC type 2	Low
Tesla Wallbox [9]	11 kW	340	AC	Low

different DC fast chargers.

Figure 7.4: Standard port for DC fast charger

7.4 Benchmark Market Study of EV chargers

The market study of the market for electric vehicle chargers is an important aspect of developing the new product and its integration into smart energy communities. The technology not only provides the integration of clean energy but can also act as an energy source in V2G operations. The comparative market and technical study highlights the following key points.

- The price is directly proportional to the power rating and charging current,
- The DC fast charger often costs more than due to advanced infrastructure,
- The application depends on the power range of the charger and the installation configuration is also different.

The DC Fast Chargers represent a breakthrough achievement in the field of infrastructure development for electric vehicles, introducing high-speed charging solutions to car owners' needs in a widely developing mobile world. In contrast to AC chargers, which depend on an onboard converter in the vehicle for AC-to-DC transformation, DC fast chargers feed electricity directly to the vehicle's battery in DC form. This allows them to provide much higher power, which can dramatically reduce charging times to 20-40 minutes for most electric vehicles. These have become quite indispensable in many fields. For example, public charging stations are highly dependent on DCFCs for urban commuters and apartment dwellers who have no home charging options. Situated in highly trafficked areas such as shopping centers and transit hubs, they are a quick and convenient way to top off battery levels. Technologically, DC fast chargers fall into a few distinct types, tailored according to specific regional or manufacturer standards. CHAdeMO, developed in Japan, supports bidirectional charging, enabling V2G applications. The combined charging system, widely adopted in Europe and North America, uses a single port for AC and DC charging, providing flexibility to the user. Tesla's supercharger network is notable for the extremely fast charging capability available exclusively for Tesla vehicles. Meanwhile, GB/T, predominant in China, enables unique connector designs for the huge EV market. The new emerging trends in DCFC technology are towards modularity and scalability. The development of HPC above 350 kW will enable future models with larger batteries, capable of ultrarapid charging. Other critical evolvements are integration with renewable energy sources, such as solar and wind, which enhance the sustainability of charging networks. The main challenges in deploying these advanced chargers are related to the need for strong heat management systems due to the heat generated during high-power charging and due to challenges in grid stability when there is sudden high-power demand. Other studies have accentuated innovative ideas, such as the use of DC-DC bidirectional converters and the utilization of high-capacity lithium iron phosphate cells, which enhance effectiveness and dependability.

Type of charger	Price range	Usage
DC fast Charging station 30KW – 350 KW	13000 euro-85000 euro	Commercial Buildings Highways Hospital Areas
DC Fast charging wall box 12KW – 24 KW	5000 euro-13000 euros	Both commercial and Home usage Industries Community areas
DC Wall Box Connectors Type 2 level charging	500 euros – 1000 euros	Home Workplace Parking Apartments

Figure 7.5: The DC fast charging types and applications

7.5 Impact on Energy Communities

The comparative analysis of the EV chargers provides insight into the selection of EV wallbox for homes and communities. At Prysmian, an OMHERO device has been developed that can be installed in homes and industry for smart energy monitoring. Fig. 7.6 shows the OHMERO device. The feature of the device can be listed as:

- Real-time measurement of parameters,
- Voltage drop test,
- Earth loop impedance test,
- Residual Current Circuit Breaker test.

Figure 7.6: OMHERO device

7.5.1 Results and Discussion

The real-time data of the energy consumption is obtained through the OMHERO device and three different configurations have been studied.

1. Only Grid supply
2. Grid + PV
3. Grid + PV + Wallbox

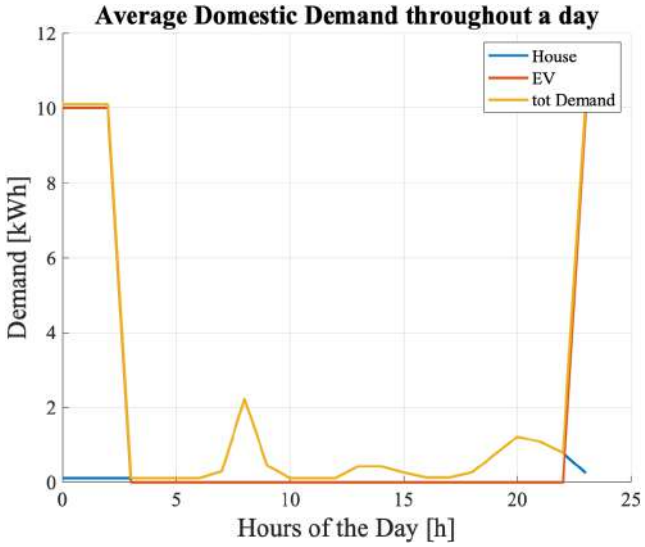

Figure 7.7: Total and individual load plots for average domestic use

Fig. 7.7 presents the average load demand for 24 hours, the load is the house load, the EV load in the presence of the EV charger, and the total load demand.

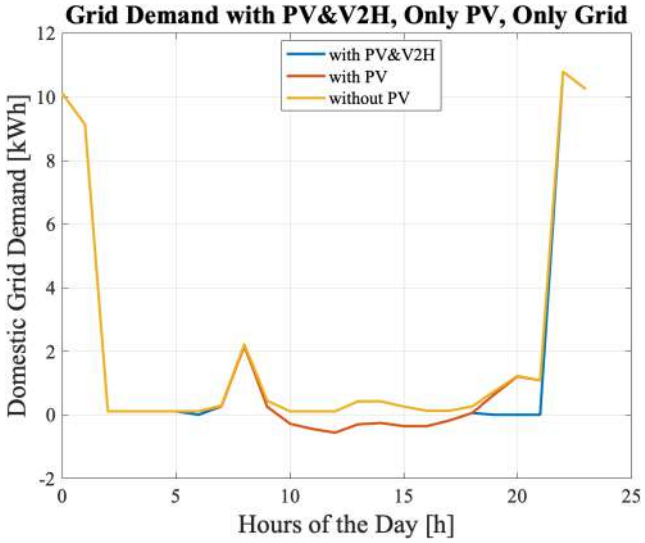

Figure 7.8: Grid load in three different scenarios

As in these cases, there are two types of load, domestic load and EV load. Photovoltaic and electric vehicle can also act as active power sources in different load scenarios, so the load on the grid is not the same in all three cases. Fig. 7.8, shows the load on the grid in different working scenarios and it can be observed that in the presence of V2H and PV, the load demand on the grid is reduced.

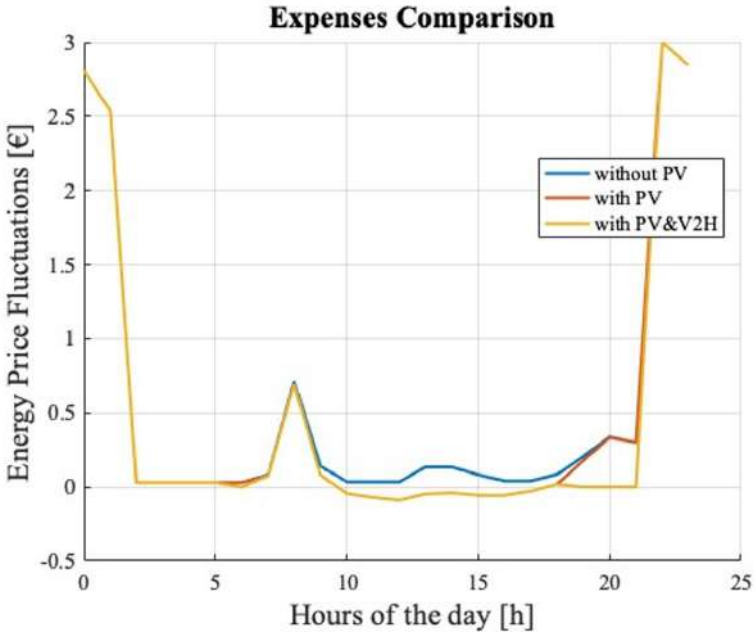

Figure 7.9: Total and individual load plots for average domestic use

Fig. 7.9, presents an expense comparison of the three cases in terms of economic tariff. The configuration with V2H and photovoltaic has a lower price compared to others and the analysis shows that on average 15 % of the total energy expense can be reduced. In summary, the analysis shows that with the help of proper energy management and control, the use of EV wallbox and photovoltaic systems can make electricity more cheap and more reliable.

7.6 Summary

- The introduction about the company and field of research is discussed,
- Technology used for EV charging stations is studied and comparative market analysis is presented,
- Impact of using wallbox and Pv in future smart communities is analyzed through data acquired by "OMHERO"

References

[1] *OMHERO | Prysmian — prysmian.com*, https://www.prysmian.com/en/markets/asset-monitoring-systems-and-electronics/omhero, [Accessed 02-12-2024].

[2] S. Shao, L. Chen, Z. Shan, *et al.*, "Modeling and advanced control of dual-active-bridge dc–dc converters: A review," *IEEE Transactions on Power Electronics*, vol. 37, no. 2, pp. 1524–1547, 2021.

[3] M. J. Carrizosa, A. Iovine, G. Damm, and P. Alou, "Droop-inspired nonlinear control of a dc microgrid for integration of electrical mobility providing ancillary services to the ac main grid," *IEEE Transactions on Smart Grid*, vol. 13, no. 5, pp. 4113–4122, 2022.

[4] *On a Mission to Electrify Transportation | Welcome to Tritium — tritiumcharging.com*, https://tritiumcharging.com/, [Accessed 02-12-2024].

[5] *C7EU — xcharge.com*, https://www.xcharge.com/device/C7EU, [Accessed 02-12-2024].

[6] *EV Charger, Electric Vehicle Charging Station Design & Manufacturer | Hiconics — hiconics-global.com*, https://www.hiconics-global.com/ev-charger/, [Accessed 02-12-2024].

[7] https://new.abb.com/ev-charging/terra-dc-wallbox, [Accessed 02-12-2024].

[8] https://www.dcbel.energy/uk/blog/2023/06/13/dcbels-residential-bidirectional-dc-charger-first-to-achieve-certification-in-the-us/, [Accessed 02-12-2024].

[9] *Wall connector*, https://shop.tesla.com/it_it/product/wall-connector, [Accessed 02-12-2024].

Conclusions

This research explores innovative control strategies for power converters within DC microgrids, focusing on their role in optimizing energy storage systems (ESS) and supporting applications such as e-mobility and electrolyzer power supply. The study investigates a dual loop sliding mode controller and a two-stage interleaving FSIBB converter topology, both designed to improve stability, efficiency, and ripple reduction in microgrid systems. Through Lyapunov stability analysis, the global stability of the proposed control strategies is confirmed, and simulations in MATLAB/Simulink, coupled with real-time hardware-in-the-loop (HIL) testing, validate the effectiveness of these methods. The dual-loop controller outperforms traditional PI controllers in both buck and boost modes, showcasing enhanced system dynamics, better load management, and minimized output ripples, making it highly suitable for modern microgrid applications.

Further advancements were made by introducing a two-layer control structure that incorporates an adaptive nonlinear switch controller, aimed at optimizing power sharing and ensuring seamless bidirectional energy flow within DC microgrids. The approach demonstrated excellent performance in the efficient management of ESS charge and discharge cycles. Through simulation and HIL testing, the nonlinear controller proved its robustness, exhibiting fast dynamic responses and the ability to self-compensate for disturbances without overestimating controller gains. This performance surpasses conventional control methods, offering significant advantages in managing unpredictable disturbances and improving overall system reliability. The real-time test results bolster the potential of this control strategy for practical implementation in systems that integrate electric vehicles (EVs) and ESS, ensuring stable operation under varying load and environmental conditions.

In addition, the research introduces a cascaded Lyapunov-based hybrid control approach for three-phase interleaving power converters, specifically designed for the efficient power supply of electrolyzers within DC microgrids. This hybrid control strategy successfully combines linear and non-linear control techniques, allowing for precise current sharing between phases and stable DC bus voltage regulation. By minimizing output ripples and improving overall efficiency, the system achieves reliable operation under dynamic load conditions. Simulation results, along with controller hardware-in-the-loop (C-HIL) testing, confirm the viability of the proposed

approach, demonstrating its ability to coordinate energy flow effectively across multiple components within the microgrid.

A key focus of this work was also on the control of Hybrid Energy Storage Systems (HESS), particularly for fuel cell-based electric vehicles. A two-stage control algorithm was developed to optimize the power split between sources based on load requirements and the state of charge (SoC) of the storage system. The fuzzy rule-based master controller efficiently managed the power distribution, thus reducing hydrogen fuel consumption by utilizing the full capacity of the energy storage system. The slave-level controller, designed using the TSC algorithm, tracked the optimal power trajectory, further enhancing system efficiency. MATLAB simulations confirmed the effectiveness of this two-stage control strategy in the management of HESS, demonstrating its potential for hybrid systems and fuel cell applications. Lastly, significant advances and insights gained during the industrial period showcased innovative solutions and their practical implications. The analysis of EV charging systems and real-time data underscores the transformative potential of integrating EV wallbox and PV systems for sustainable energy communities, offering a foundation for further technological and market development. Collectively, the findings of this research underline the importance of advanced control algorithms and multistage converter topologies in enhancing the performance of DC microgrids. The proposed solutions not only improve the efficiency, stability and resilience of power converters but also offer practical solutions for integrating renewable energy sources, energy storage systems, and e-mobility infrastructure. Moving forward, these methods could be expanded to larger-scale, multi-node microgrids, with potential applications in fault-tolerant schemes, optimized phase shift algorithms for asymmetric conditions, and broader integration with conventional power grids. This work paves the way for future innovations in microgrid design, promising improved energy management and increased system resilience in diverse applications.

La borsa di dottorato è stata cofinanziata con risorse del
Programma Operativo Nazionale Ricerca e Innovazione 2014-2020 (CCI 2014IT16M2OP005),
Fondo Sociale Europeo, Azione I.1 "Dottorati Innovativi con caratterizzazione Industriale"

UNIONE EUROPEA
Fondo Sociale Europeo